Micromechanical Investigations of Foundation Structures-Granular Soil Interactions

Zuhair Kadhim Jahanger

Submitted in accordance with the requirements for

the degree of Doctor of Philosophy

The University of Leeds

Institute of Particle Science and Engineering (IPSE)

School of Chemical and Process Engineering (SCAPE)

May 2018

The candidate confirms that the work submitted is his own and that appropriate credit has been given where reference has been made to the work of others.

Preface

The research work presented in the Thesis has been performed in the Discipline of Civil Engineering, Faculty of Engineering in School of Chemical and Process Engineering at University of Leeds under supervision of Associated Professor **Dr. S. Joseph Antony** and **Professor Elaine Martin** from August 2014 to May 2018. During the term of candidature, a number of papers were published which are listed below:

1. Jahanger, Z.K., Antony, S.J. and Richter, L. 2016. Displacement patterns beneath a rigid beam indenting on layered soil. *In: Proceedings of 8th Americas Regional Conference of International Society for Terrain-Vehicle Systems*, Michigan, USA, paper No.67.

2. Jahanger, Z.K. and Antony, S.J. 2016. Finite Element Modelling of Displacement Fields in Granular Systems. Presentation slides at *GM3 Geo-mechanics: From micro to macro- UK 13th Travelling Workshop* at University College London (UCL), London.

3. Jahanger, Z.K. and Antony, S.J. 2017a. Application of Digital Particle Image Velocimetry in the Analysis of Scale Effects in Granular Soil. *In: Proceedings of 19th International Conference on Soil Mechanics and Dynamics*, 19(7) part X, Rome, pp.1134-1139.

4. Jahanger, Z.K. and Antony, S.J. 2017b. Application of Particle Image Velocimetry in the Analysis of Scale Effects in Granular Soil. *International Journal of Civil, Environmental, Structural, Construction and Architectural Engineering*. 11(7), pp.832-837.

5. Jahanger, Z.K., Sujatha J. and Antony, S.J. 2018a. Local and global granular mechanical characteristics of grain-structure interactions. *Indian Geotechnical Journal*, doi.org/10.1007/s40098-018-0295-5.

6. Jahanger, Z.K., Antony, S.J., Martin, E. and Richter, L. 2018b. Multi-methodological investigations on the interaction of rigid beam indenting on a dense granular layer overlying loose granular soil, *Journal of Terramechanics*, 79, pp.23-32.

To my dedicated parents, in memory of my grandparents

Dedicated to my wife, son and daughters

Acknowledgements

First, I would like to thank Almighty Allah for his generous mercy over me and for giving me the strength to finish this research project. Secondly, I would like to express my sincerest thanks to my supervisor **Dr. S. Joseph Antony** for his unending help and invaluable assistance, support and guidance from the initial to the final level of my research. His unlimited availability and encouragement made my research life smooth and rewarding. In addition, I would like to appreciate my co-supervisor, **Professor Elaine Martin** for her helpful advice.

I am thankful to the Ministry of Higher Education and Scientific Research (MOHESR) in the Republic of Iraq and University of Baghdad for doctorate scholarship (Grant No. 2075 in 15-05-2013).

I was delighted to have valuable discussion with **Dr. Raul Fuentes** in Civil engineering, **Dr. David Harbottle**, and **Dr. Xiaodong Jia** in School of Chemical and Process Engineering in some critical stages of this research work at university of Leeds. Their guidance is really appreciated. I was delighted to have valuable discussion with **Dr. Joana Fonseca** from School of Mathematics, Computer Science & Engineering, Civil Engineering at City University of London.

I would like to thank Mr. Tony Wiese for his very valuable cooperation in strength of material laboratory, Mr. Steve Caddick, Mr. Graham Brown (Mechanical Workshop Managers) and his colleagues in the mechanical workshop for helping for the fabrication of planar box and other related stuff, Mr. Adrian Eagles and Camille Hammersley in Metrology laboratory for helping to measure the surface roughness of the materials in School of Mechanical Engineering. I would also like to thank Mr. Michael Marsden for helping to use the soil laboratory in School of Civil Engineering at University of Leeds.

Many thanks to the staff of the School of Chemical and Process Engineering for the kind advice and able support I received through my studies. I am also thankful to my friends and colleagues at University of Leeds and at University of Baghdad.

I owe my deepest gratitude to Israa Khazaali (wife), for her unflagging love and support and encouragement. Finally, yet importantly, I am grateful to my gorgeous children; Ali (son), Zahraa (daughter) and Zainab (baby girl) who have constantly reminded me that life without a challenge is going to be boring.

This document could not have been produced without the help of everyone mentioned above and their expertise, knowledge and input has been invaluable.

Abstract

In the geotechnical engineering applications, precise understandings are yet to be established on the local displacement fields of the soil grains and the evolution of failure envelopes in strip footing structures interacting with different soil profiles. Several theoretical and experimental approaches have been used to measure the ultimate bearing capacity of homogeneous and layered soil systems in the past, but with a significant level of differences depending on the failure envelopes of the soils assumed. The ultimate bearing capacity refers to the ability of the soil to sustain the maximum load on the footing before the soil collapses. Finite element method (FEM) could help to study such large-scale problems but depends on the continuum assumption and the type of the constitutive relation of the soil. This research contributes new advancements on both the experimental and computational fronts in the field of soil-strip footing structure interactions under plane strain condition: (i) experimentally digital particle image velocimetry (DPIV) is used to measure the grain-scale (local scale) displacement fields, and they are used to characterise the failure envelopes of key footing-granular soil interaction problems. For the first time, such outcomes are generated in terms of the relative density of the sand, interference effects of the strip footings, accounting for the layering characteristics of sand and under static and cyclic loading environments. The experimental results are compared with corresponding finite element analysis and a good level of agreements are reported between them and (ii) in the finite element analysis (FEA), it was shown that, using an inbuilt (/existing) model of constitutive relation of sand does not produce the displacement fields of sand grains (local scale) that are comparable with DPIV outputs. Hence, a new approach of using the global experimentally-derived constitutive relations are represented as an input in the FEM simulations. The localised subsoil deformations from FEM are validated experimentally using DPIV outputs. It is worth mentioning that, such an approach results an excellent level of agreements between the above said experimental and finite element analysis approaches at both local and global scales. Furthermore, using the displacement fields obtained using DPIV, where applicable the existing theories for calculating the ultimate bearing capacity of the strip footing on layered sand are refined for achieving a better accuracy of the predictions. The computational and the experimental approaches developed in this research programme provide a strong basis in terms of methodology and findings for analysing other complex soil profiles in the ground-structure interactions in future.

Table of Contents

List of Figures

Lists of Tables

Nomenclature

ALE	Arbitrary Lagrangian-Eulerian	
AoI	Area of interest	pixel
AoR	Angle of repose	degree
a	Diameter of the triaxial sample	mm
B	Width of the footing	mm
B'	Projection of slip lines on the surface of the bottom layer	mm
c	Cohesion, or apparent cohesion of the soil	kPa
C	c×D= Total cohesion along vertical plane through footing edge	kPa/m
CBR	California bearing ratio test	%
CCT	Colour coding technique	
C_C	Coefficient of curvature	
CEUC	Coefficient of elastic uniform compression of sand	
C_f	Cohesive force in Meyerhof's UBC equation	kPa
CPT	Cone penetration test	
C_U	Uniformity coefficient	
C_1	Depth factor	
C_2	Time factor	
C_{I1I2}	Cross-correlation function	
DEM	Discrete Element Method	
D_f	Depth of footing embedment	mm
DIC	Digital image correlation	
DP	Drucker-Prager model	
DPIV	Digital particle image velocimetry	
DSLR	Digital single-lens reflex camera	
DSSP	Dynamic Studio Software Platform	
DST	Direct shear test	
D_r	Relative density of the soil	%
D_{50}	Mean grain size of the soil	mm
d	Depth of the region M under the footing (**Figure 7.4**)	mm
d_1 and d_2	Points of tangency of the inner and outer spirals (**Figure 2.4**)	
E	Modulus of elasticity	MPa
E_i	Initial tangent modulus	MPa
EDP	Extended Drucker-Prager Model	
E_s	Equivalent modulus of elasticity in soil layer	MPa

e	In-place void ratio of the tested soil	
e_{max}	Maximum void ratio of the soil in loosest condition	
e_{min}	Minimum void ratio of the soil in densest condition	
F	Friction force in Meyerhof BC equation	kPa
F	EDP linear yield criterion	
f	Empirical constant correlating soil stiffness (E_s) with q_c (**Eq. 2.2**)	
FS	Safety factor, $q_s = q_{ult}$/FS	
FEM	Finite Element Method	
G	Shear stiffness	MPa
G_s	Specific gravity of the solids	
H	Thickness of the top layer of sand	mm
HSC	High speed camera	
h	Height of the sand sample in triaxial test	mm
I_1	Interrogation area-image input 1	
I_2	Interrogation area-image input 2	
IA	Interrogation areas	$Pixel^2$
ISO	Linear isotropic elastic material model	
$I_1(I,J)$	Intensity distribution of the reference image	
$I_2(I,J)$	Intensity distribution of the deformed image	
Iε	Strain influence factor at midpoint of soil layer	
K	Bulk modulus	MPa
Kp	Coefficient of passive earth pressure of the top layer of sand	
K_s	Coefficient of punching shearing resistance	
LSV	Laser speckle velocimetry	
MC	Mohr-Coulomb model	
MDD	Maximum dry density in Proctor test	
MISO	Multi isotropic hardening plasticity material model in ANSYS	
M_s	Mass of the tested dry sand	kg
N_c	Bearing capacity factor due to soil cohesion	
N_q	Bearing capacity factor due to surcharge stress	
N_γ	Bearing capacity factor due to unit weight of soil	
OMC	Optimum moisture content	%
PLT	Plate loading test	
PIV	Particle Image Velocimetry	
P_p	Total passive earth pressure	kPa
$P_{ult\ layered}$	Ultimate force for footing on layered soil	kPa

p'	Mean effective stress	kPa
q	Load per unit area	kPa
q	Deviatoric Cauchy stress tensor	kPa
$\bar{q}$	Surcharge load at footing level	kPa
q′	Net applied pressure	kPa
q_{all}	Allowable bearing capacity of the soil	kPa
q_c	Cone resistance	MPa
q_{ci}	Cone resistance for layer i	MPa
q_s	Static load	kPa
Q	Linear plastic flow potential	
Qu	Ultimate load per unit length of the footing in Myerhof BC Eq.	kPa
q_{ult}	Ultimate bearing capacity of soil, the ultimate bearing capacity refers to the ability of the soil to sustain the maximum load on the footing before the soil collapses	kPa
$q_{ult\ 1}$	Ultimate bearing capacity of the top soil	kPa
$q_{ult\ 2}$	Ultimate bearing capacity of the bottom soil	kPa
$q_{ult\ cyc}$	Cyclic ultimate bearing capacity of the soil	kPa
$q_{ult\ layered}$	Ultimate bearing capacity for footing on layered soil	kPa
R	Roundness of the grains	
S	Spacing distance between adjacent footings	mm
S	Settlement at footing structure-soil level	mm
S_{all}	Allowable settlement	mm
S_c	Primary consolidation settlement	mm
SCL	Stress control loading	
S_{opt}/B	Optimum interference space	
S_{cyc}	Cyclic loading settlement	mm
s_c	Shape factor in BC Eq. for shapes of footing	
S_e	Elastic settlement	mm
S_h	Horizontal displacement component	mm
$S_{opt.}$	Optimum spacing for maximum interference effects	mm
SPT	Standard penetration test	blows
S_s	Secondary consolidation settlement	mm
S_u	Ultimate vertical settlement of the footing	mm
s_u	Shear strength of the clay	kPa
S_R	Resultant velocity and or displacement	mm/s
S_t	Total settlement	mm
S_v	Vertical displacement component	mm

$\{s\}$	Deviatoric stress in DP model	kPa
S_{sph}	Sphericity of the particle	
UBCR	Ultimate Bearing Capacity Ratio	mm/s
V	Velocity between successive images	mm^3
V_{mould}	Volume of compaction mould	mm^3
W	Weight of the lifted soil mass and weight of the footing	kg
w_c	Water content= weight of water/weight of solid	%
z	Depth of the soil from the footing soil interface	mm
α	Angle of plastic wedge vertices intersecting the horizontal	degree
α	Material pressure sensitive parameter in DP model	
α1	Average inclination with vertical of forces Cf	degree
α_1	Flow potential referred to dilation angle in DP model	
β	Angle of the slip surface	degree
$\beta 1$	Average inclination with vertical of forces F	degree
γ	Unit weight of the soil	kN/m^3
γ_d	Dry density of the soil	kN/m^3
$\gamma_{d\ min.}$	Minimum dry density	kN/m^3
γ_w	Density of water at 20°C	kN/m^3
γ_{max}	Maximum shear strain rate	kN/m^3
γ_{wet}	Wet bulk density	kN/m^3
γ′	Effective unit weight of the soil	kN/m^3
γ_1	Unit weight of the top soil layer	kN/m^3
γ_2	Unit weight of the bottom soil layer	kN/m^3
Δt	Time between successive images	s
Δx	Movement in x direction between successive images	mm
Δy	Movement in y direction between successive images	mm
Δz	Thickness of soil layer	mm
δ_{bw}	Roughness of the side wall footing interface	µm
δ_p	Roughness of the Perspex wall	µm
$\delta p'$	Increment in mean stress	
δq	Increment of deviator stress	
$\delta\varepsilon_s$	Increment of shear strain	
$\delta\varepsilon_v$	Increment of volumetric strain	
δ	Roughness angle of the material	µm
ε_a	Axial strain	
ε_{pl}	Plastic strain	

ε_{vol}	Volumetric strain	
ε_z	Vertical strain	
$\dot{\varepsilon_h}$	Horizontal strain rate	s^{-1}
$\dot{\varepsilon_v}$	Vertical strain rate	s^{-1}
θ	Angle of total passive earth pressure	degree
λ	Distance of sand heap from the centre of the footing	mm
λ_{max}	Location of sand heap attaining max. height from footing centre	mm
ν	Poisson's ratio	
ξq	Efficiency factor for surcharge load	
$\xi\gamma$	Efficiency factor for unit weight of soil	
σ	Mean normal stress	kPa
σ_r	Cell pressure	kPa
σ_y	Yield stress of material which can be fed as multi-yield via MISO	kPa
σ_1	Main principal stress	kPa
σ_2	Intermediate principal stress	kPa
σ_3	Minor principal stress	kPa
τ	Shear stress and or shear strength	kPa
ϕ	Angle of internal friction of the soil	degree
ϕ_1	Angle of internal friction of the top soil layer	degree
ϕ_2	Angle of internal friction of the bottom soil layer	degree
ϕ_{cr}	Residual angle of internal friction of the soil	degree
ϕ_{mob}	Mobilized shear strength	degree
ϕ_{Peak}	Peak angle of internal friction of the soil	degree
ϕ_{ps}	Angle of internal friction from plane strain test	degree
ϕ_{tr}	Angle of internal friction from triaxial test	degree
ψ	Dilatancy angle of the soil	degree
ω_z	Vorticity	

Chapter 1 Introduction

1.1 General

Micromechanical studies of foundation structures-granular soil interaction have been used frequently to analyse deformable soils, in civil engineering. The mechanical behaviour of granular soil is different from that of conventional solid, liquid and gaseous state of matter (Jaeger et al., 1996). However, the study of granular materials can improve our understanding within a wide range of industrial sectors, where many unsolved challenges remain, such as the particulars of soil mechanics (Zhou, 2011). Therefore, micromechanical techniques have been used extensively to establish a solution for numerous stability problems in geomechanics such as measuring (i) the bearing capacity of the foundations on a single layer under static loading (ii) the bearing capacity of two adjacent foundations under a static loading (iii) the bearing capacity of the foundation on layered soil under the static load, and (iv) the bearing capacity of the foundation on a single dense layer under cyclic loading. Bearing capacity is capacity of the soil to sustain the loads applied to the soil (Das, 2016). Micromechanical studies are based on deformations at the grain level, associated under the ultimate load with the settlement of the footing at a macro scale, which enables quantifying the magnitude of the strain of the collapse load for different soil stiffness, such as single and layered soil systems.

Presently, there is a lack of experiments that show the failure envelope of granular soils of specific relative density interacting with foundation structures, such as a strip footing. Much of the knowledge of footing design is based on vast theoretical calculations or empirical data from experiments and in site tests. However, soil deformation remains unclear, and usually it cannot be accurately measured in field tests, since generally only the footing pressure and its settlement are measured. This limited knowledge of soil deformations and internal shearing mechanisms therefore leads to complications when verifying engineering calculations. In order to solving the different problems considered in this thesis, Particle Image Velocimetry (PIV) as well as the Finite Element Method (FEM) were performed. Qualitative and quantitative assessments of sand deformation with high spatial resolution during a footing compression test are obtained using digital particle image velocimetry (DPIV). Emphasis is given on the effects of relative density on load-settlement responses and failure mechanisms, in terms of their displacement field

and shear strain rate. Furthermore, FEM simulations corresponding to a strip footing compression test on a sand of different relative densities were also employed to access its capability in making qualitative and quantitative predictions. In sand-structure interaction problems, FEM based outputs of the displacement profiles in the sand bed to a level of accuracy of what happens in real experiments (e.g. using DPIV methodology here) is possible to obtain, if the input parameters of constitutive relations are also characterised realistically and fed as input in the FEM simulations. It is worth stating that, FEM simulations, when they work reliably are much more suited to simulate real-scale soil-structure interaction problems in future.

The objective of this thesis is to develop a new approach to use the experimentally characterised stress-strain curve from the DPIV-based experiments as input to the FEM simulations and to validate the FEM based subsoil displacement fields using the DPIV methodology. The performance of foundation structures-soil system interactions, as well as the effects of the relative density (D_r) on the load-displacement behaviour and failure envelopes, towards solving a few stability problems such strip footing-sand interactions.

1.2 Motivation for the Current Research

1.2.1 The Methods DPIV and FEM

In order to ascertain the deformations at both the localised and grain levels for foundation structures-soil system interaction, as well as the effect of the overall foundation system's stiffness (packing densities) on the load-displacement behaviour for various geotechnical stability problems, DPIV along with FEM have been deployed. Due to significant developments in the resolution of high definition cameras, they have become quite widespread in research (Willert and Gharib, 1991). Due to the simplicity of their implementation and the relative ease in obtaining results, high definition cameras are widely used in DPIV applications (Albaraki and Antony, 2014). Likewise, the Discrete Element Method (DEM) is a grain scale numerical method for modelling the macro scale behaviour of the granular material such as soil and rocks. DEM has been used more frequently in structure-soil interaction studies (Zhou, 2011). DEM provides the ability to probe the discrete nature of granular media more efficiently. However, the simulation of large-scale granular systems, such as those required in foundation structures-sand interaction (millions of particles using sand grains having an average size of 0.37 mm

used in the current study) is computationally challenging and expensive. Therefore, FEM is widely used due its simplicity in implementation and ease in obtaining results (Potts and Zdravković, 2001). The current study is based on the DPIV method, in which displacement components of the individual grains in different relative densities are tracked to trace the failure envelope.

1.2.2 Local and Global Granular Mechanical Characteristics of Grain-Structure Interactions

In order to systematically probe deformations at the grain level in the sand of different packing densities of the strip footing resting on single layers of loose, medium-dense and dense sand have been used. Increasing soil mass density improves the strength and stability of soil masses. A number of studies have been conducted to analyse problems involving the deformation field on single layer sand (Liu and Iskander, 2004; Murthy et al., 2012; Chen et al., 2017). No rigorous studies seem to be available that deal with the characteristics of foundation structures-granular soil interactions. However, experimental results on the role of the relative density of sand for all three major types (loose, medium-dense and dense) on their geomechanical characteristics using DPIV have not yet been probed systematically. This is addressed here using two-dimensional DPIV as the strip footing is considered as plane strain condition in which the movement in the z-direction of the sand would be very small and neglected in plane-strain geotechnical engineering problems. Detailed experimental characterisations of the sand material are made using a range of experiments. The aim is firstly to compare the variation of displacement fields measured in sand packing, using DPIV with a FEM analysis. Thereafter, the variations of fundamental mechanical features at both local and global scales are studied in detail, using DPIV for strip footing interacting with sand packing of different relative densities in a systematic manner.

1.2.3 Interference Effects on Displacement Fields in Strip Footing-Sand Interaction

Usually, the foundations of buildings, which is the lower part of the that transfer the load to the soil, in reality are closely spaced and are not very regularly isolated, due to design considerations and space restrictions. Therefore, interference between two closely spaced footings behaves different from that of a single isolated footing. The footing is the type

of foundation transfer the load from the column or wall to the soil. Numerous theoretical and experimental studies have been carried out to measure the effects of interference on the ultimate bearing capacity and settlement of the adjacent footings. The ultimate bearing capacity refers to the ability of the soil to sustain the maximum load on the footing before the soil collapses. Stuart (1962) used a theoretical approach that considered a limit equilibrium method to study the case of two footings at the surface of a sand. In this analysis, unlike previous theories that dealt with a single rough base strip foundation ($\delta = \phi$), a non-symmetrical triangular trapped wedge was considered below the base of the footing. A number of numerical methods have also been applied by different researchers (Kumar and Ghosh, 2007; Ghazavi and Lavasan, 2008; Kumar and Kouzer, 2008; Lee et al., 2008; Lavasan and Ghazavi, 2014). Other researchers have used small-scale model tests (Stuart, 1962; Das and Larbi- Cherif, 1983; Kumar and Saran, 2003; Kumar and Bhoi, 2009; Lavasan and Ghazavi, 2012). All these studies reveal that at close spacing the ultimate bearing capacity increases substantially when compared to that of a single footing. These results, however, do indicate a certain optimum spacing (S_{opt}/B) as has been observed for rough base footings ($\delta = \phi$). However, for smooth footings ($\delta = 0$), as seen in the work of Stuart (1962), the ultimate bearing capacity increases with a decrease in interference spacing. In the current thesis, towards obtaining a more rigorous understanding of the deformation fields and failure mechanisms of sand, pairs of relatively rough strip footings ($\delta/\phi = 0.25$) will be used systematically for different packings densities of sand.

1.2.4 Interaction of Strip Footing-Layered Soil Systems

Layered soil profiles can either be naturally occurring or man-made. With the growing populations of our towns and cities, the availability of new land is a premium for human habitations. There is an increasing demand to construct buildings on loose soils, which were previously considered unsuitable for construction (Jahanger et al., 2010). Loose sand packings have high compressibility and low shear strength (Terzaghi et al., 1996). Constructing a suitable layer of strong granular material on weak soil improves strength and decreases the overall compressibility. Accordingly, Terzaghi's theory (Terzaghi, 1943) of the ultimate bearing capacity given by $q_{ult}=0.5\gamma BN\gamma$, where γ, B and $N\gamma$ are unit weight of the soil (bulk density), the width of the footing and bearing capacity factors of the soil applied to surface strip footing on homogeneous granular sand are not applicable to layered granular sand. The most widely used methods to calculate the bearing capacity

of layered soil are the projected area method (Yamaguchi, 1963) and the punching shear failure method (Meyerhof, 1974). The measured angle of the slip failure surface β significantly depends on the thickness of the top dense sand layer. β passes through the footing edge and is inclined clockwise from the vertical. These studies (Yamaguchi, 1963; Meyerhof, 1974; Terzaghi et al., 1996) form the basis behind the motivation of this case of my current work. For the current study, a new methodology is presented, based on the experimental measure of β for the layered soil system considered here.

1.2.5 Local Scale Displacement Fields in Footing-Sand Interactions under Cyclic Loading

The cyclic behaviour of granular soil has become a critical issue for many civil engineering applications, particularly in pavement constructions, storage tank foundations (which involves a large amount of filling and discharging), railway ballast, and earthquake zones. Although Iraq is secure from seismic hazards, seismic events indicate otherwise. Regions, which were once described as non-hazardous seismic areas, today observe increased seismic action, such as Baghdad in Iraq. There are an increasing number of earthquakes in Iraq due to many natural and man-made effects, such as drilling oil wells nearby residential areas. However, in order to compute the ultimate bearing capacity and the settlement of a single strip footing under cyclic loading, a few theoretical and experimental studies have been conducted (Kempfert et al., 2010; Tafreshi et al., 2011; El Sawwaf and Nazir, 2012; Asakereh et al., 2013). Therefore, very little information is available in the literature for performing an analysis of the failure mechanisms and deformation properties of foundation structures dense granular soil. In this thesis, micromechanical study of foundation structures granular soil interactions under cyclic loading have been performed to analyse the significant effects that different types of cyclic loading have on dense granular soil-foundation-structures. Three different cyclic loading types were adapted in this study. DPIV and FEM were used to introduce the effects of cyclic loading on the failure mechanism. The salient objective is to model the cyclic behaviour of model strip footings supported on a dense sand layer, and to study the cumulative settlements due to cyclic loading. The broader aim is to study the relationships between the quasi-static and the cyclic failure mechanisms and settlements of the cyclically loaded model footings. The current study contributes data with the intention to reduce this knowledge gap.

1.3 Scope of the Thesis

The research focus on understanding the local and global geomechanical properties of key structure-soil interaction problems under quasi-static and cyclic loading condition, using DPIV and FEM simulations coherently. The methodologies complement each often used in the investigations. Experimentally based user-defined constitutive relations got from the footing compression test are applied in the FEM analysis and the results are validated experimentally using DPIV. The results from the DPIV cannot provide stress measurements, therefore by validated the suitability of using the user-defined constitutive relations got from the footing compression test in FEM helps to overcome this by validated the FEM with DPIV measurement of displacement. The research structure presented in this thesis is illustrated in work plan (flow chart) in **Figure 1.1**. The DPIV and FEM are the core, which present the central work. These lead to introduce the concept of the foundation structure-granular soil interactions. Then, the experimental characterisation of the physical properties of the sand are presented, the key foundation-granular soil interactions are discussed, and a literature review is carried out on the key subjects, knowledge gap, development of local and global mechanical properties, along with an analysis to establish the links between local and global (macro) scale properties, ending with the thesis conclusions, and a consideration for the subjects that influence this study. The content of this thesis is divided into nine chapters, which are outlined below.

Chapter 1 is an introduction, which introduces the problem addressed in this thesis and presents an overview of the thesis structure and the overall aims of the study. This includes how the thesis will make an original contribution to knowledge.

The limitations of the continuum approach for the foundation structures-soil interaction problems are presented and detailed in **Chapter 2**. This includes a review of the behaviour and the properties of granular soils of different densities under vertical axial compression loading, along with limitations and challenges that have risen. Details of previous studies and a review of the challenges associated with the foundation structures-soil interaction problems are also presented. The principle of PIV and FEM is introduced. The relevant aspects of soil mechanics that relate to the deformation of foundation-soil under vertical compression, quasi-static and cyclic are also discussed in **Chapter 2**.

Chapter 3 involves the experimental characterisation of the physical properties of the sand, and the deformation of foundation soil under vertical compression, quasi-static and cyclic is discussed.

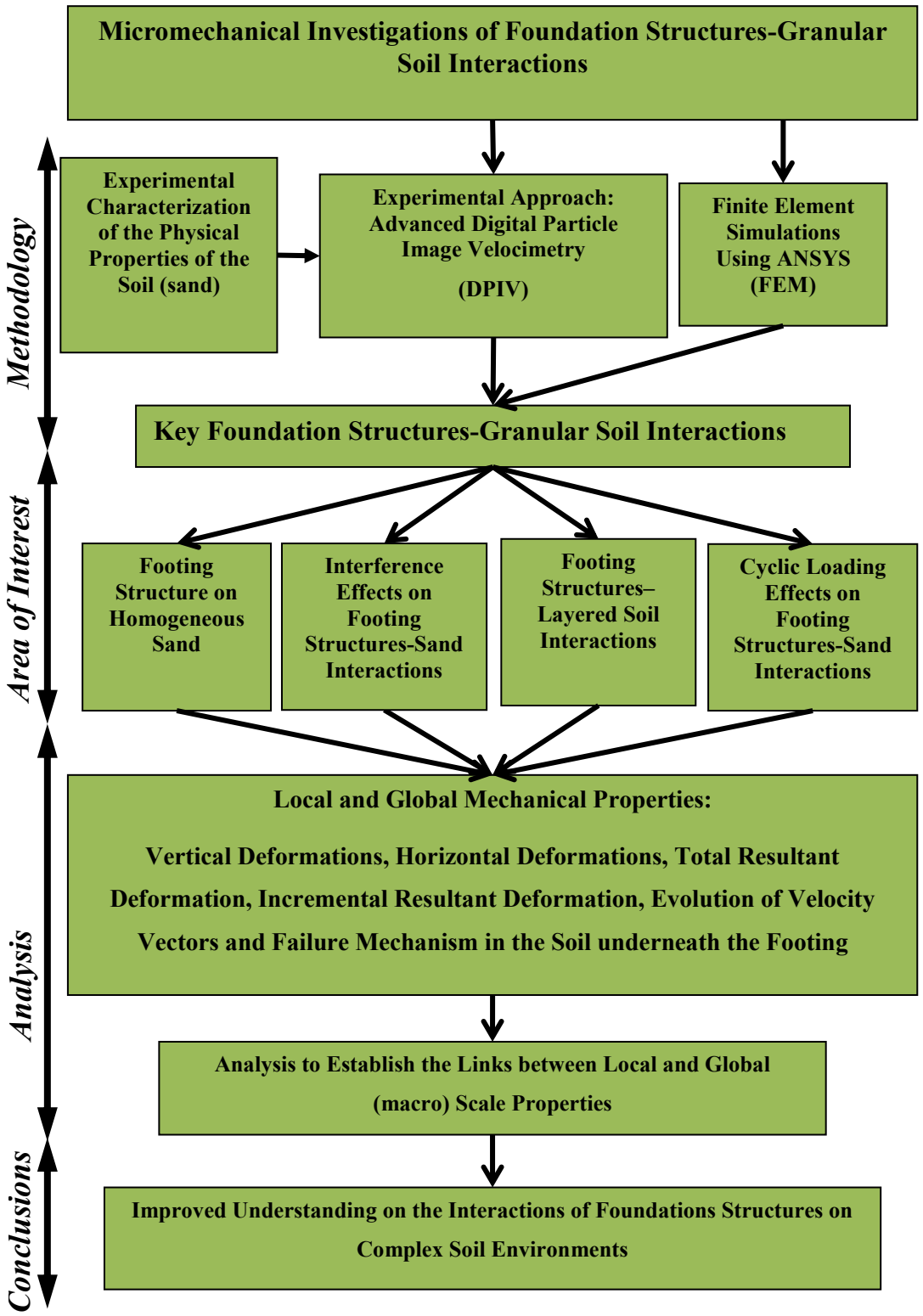

Figure 1.1 Flow chart diagram showing work plan for PhD research

The materials used in this research, their properties and steps followed in the preparation of specimens, box models and the footings model have been used in the study. A description of the equipment is presented and how it has been used.

Chapter 4 describes the research methodology used in the current study. The fundamental principle of the DPIV method, and the primary research tools used for finding solutions for this geotechnical problem, are described. ANSYS, the finite element software used, is also introduced.

The experimental results that cover the effects of packing densities on the local and global footing structures-sand interactions are presented in **Chapter 5**. The impact of the packing densities of sand, as well as the width of the relatively rough rigid footing on the measured displacement in the sand, which was obtained at the footing–soil level interface using DPIV, are also evaluated and discussed. These are compared to the FEM results.

Chapter 6 presents the influence of the interference phenomenon on the bearing capacity of soil beneath two closely relatively rough footings under plane-strain conditions on the surface of sand packings. The effects of the spacing of the footings on the variation of ultimate bearing capacity and failure mechanisms have been systematically studied using experimental model tests. Deformation patterns of the zone of plastic flow (active and passive zones) in sand at different load levels have been compared with the results obtained from the numerical data, as well as with those available in literature.

Multi-methodological investigations on the interaction of footing resting on a strong granular layer overlying weak granular soil are introduced in **Chapter 7**. The effect of a change in thickness of the strong top layer on the overall layer bearing capacity of the layered is evaluated. Likewise, the impact of the angle of slip surface for different thickness of the top layer, measured using DPIV, on the overall bearing capacity is also explicitly evaluated. A new equation to calculate the bearing capacity of layered soil has been derived based on the measured angles of slip surface, which is compared to the experimental results, as well as the literature.

Chapter 8 describes the crucial effects of the cyclic behaviour of granular material in seismic areas. This has a significant effect on the soil layer under the foundations of a building. Thus, the effects of three types of cyclic loadings on the behaviour of dense sand have been studied. The influence of cyclic loading on deformation patterns and the failure modes of sand are reviewed.

Chapter 9 summarises the content of this thesis, highlights its relevance, and provides recommendations for future works related to the foundations on granular layers.

Chapter 2 Literature Review

2.1 General

The foundation system of a building, in reality, comprises not only of a footing structure, but also of the supporting soil, such as granular soil, fine soil and/or a mixture of both. The foundation system consists of different parts that interact with each other, which requires a thorough understanding in order to produce the most economical design (Das, 2016). Numerous techniques are available for estimating the bearing capacity of the soil and the settlement of the shallow foundation on the granular homogeneous or layered soil. However, the predictions of the settlements of the footing differ considerably between the individual methods that depend on the types of the footing and the deformation of the soil, like granular sand. Geotechnical engineers often have to work with the foundation soil as it is found, only attempting improvements to the uppermost material.

Granular materials have long been a subject of considerable importance within mechanics and mathematics. Coulomb, in 1776, pioneered work into the failure conditions on a retaining wall with granular materials (Das, 2011). Since then, each method has been based on the developer's theory on the theoretical and semi-empirical correlation, and most analysis involves homogeneous soils at a macro scale, which connects the applied stresses on the footing to the strains or the deformation of the soil. This macroscale is a good way to develop a general understanding of the footing structures-granular soil interactions. More recently, efforts have been made to study particulates at the microscopic level, where granular soil is considered an assembly of discrete grains interacting with each other at a grain scale. Researchers have made effort to bridge the gap between the micro and macro scale modelling of granular materials.

The exploration of the actual mechanisms involved in the behaviour of granular materials is dominated by an assembly of particles, rather than a continuum. The most popular approach to model the mechanical behaviour of granular materials is the discrete element method (DEM). However, the simulation of large-scale granules systems, such as the need in footing structures-sand interactions (hundreds of millions of particles of sand size of D_{50} =0.37 mm) is computationally challenging and expensive. Particle Tracking Velocimetry (PTV) is another optical method based on tracking individual grains, but it also involves higher computational costs. Therefore, kinematically admissible and

mathematically correct theories to describe the complex behaviour of granular media such as PIV and/or the FEM have been recognised as valuable methodologies for the researchers in this field. Hence, this study deals with the foundation structures-sand interactions under axial vertical compression loading, and it is important therefore to focus on the behaviour and the properties of granular soils of different densities under compression load conditions, using the latest technology, such as DPIV and FEM.

2.2 Types of Soil in Geotechnical Engineering Applications

Soil is a non-homogeneous mix, which possesses a wide range of physical properties (Das, 2016). Soil from a geotechnical point of view is divided into three main types: cohesionless (coarse-grained soil, granular soil), cohesive (fine-grained soil) and organic (peats). Peats are derived from the decaying process of plants and animals. The mechanical and chemical weathering processes of the rocks produce granular and cohesive soils, respectively. Some of these soils have specific names according to their sizes, such as gravel, sand, silt, clay, etc. Granular soils are comprised of sediments or individual particles (solids) of varying sizes and voids (Jaeger et al., 1996). These solids are in contact, and voids between grains fill the gap with water in some voids, and air in the rest of the void space.

Recently, shear properties at the micro scale have been studied in the granular artificial medium. These studies have shown that load transmission occurs via inter-particle contacts in a non-homogeneous manner (Radjai et al., 1998). Also, the shear resistance in the granular bed is achieved from a minority of about 30% of the grains, which are called strong force chains, whereas the other grains contribute less, and are called weak force chains (Antony, 2007). This means the granules are not a continuum medium, where force is transmitted through interconnected points or chain-like structures called force chains. In geotechnical engineering, the transmissions of interaction strength between the soil and the foundation material have been investigated in several construction projects (Das, 2016). These investigations regard the soil as a continuum material. However, further understanding is required to discover the role of shear strength interaction between natural soils-foundation structures, which are subjected to real loading conditions. Granular materials, such as sand, gravel and rock, are largely inhomogeneous and discontinuous in nature. Thus, the constitutive relationship cannot be easily formulated.

Complications accordingly arise in numerical modelling, such as large deformation in soil and bifurcation problems.

2.2.1 Background of Sand as Cohesionless Materials

Granular materials have been classified second to water in their importance to humanity's many actions and activities (Duran, 2000; 2012). Granular materials are simply defined as an aggregate of discrete particles in contact and surrounded by air voids (Oda and Iwashita, 1999). These cohesionless granular materials can move and alter their arrangement individually, or as aggregates, depending on their initial relative density and loading condition. However, its localised scale (meso scale) performance is discontinuous, non-homogeneous and isotropic (Oda and Iwashita, 1999). Their mechanical behaviour is different from usual solid, liquid and gaseous matter states (Jaeger et al., 1996). One challenge is that particles can behave like a solid (in a sand pile), a liquid (when poured from a silo) or a gas (when strongly agitated) (Albaraki, 2015). The micro-scale behaviour of granular particles significantly influences its macro-scale behaviour and challenges the existing physics laws (Jaeger et al., 1996).

Under loading conditions, granular material assemblies can produce and build up a force chain between the particulates, in order to support their bulk packing and underlying structure (Antony, 2007; Majmudar et al., 2007). These forces chains have a significant influence on the bulk behaviour of the granular material assembly, such as ultimate bearing capacity and shear banding (Majmudar et al., 2007). Ultimate bearing capacity is the largest load that the subsoil underneath the footing can sustain. In dense granular packing, the forces between grains are transferred through contacts between the grains and builds up a skeleton pattern within the granular (birefringent) assembly (Majmudar et al., 2007). Majmudar et al. (2007) reported that forces between grains have spatial correlations depending on their macroscopic loading, such shear or compression loadings. The inter-particle contact points show multi-fringe colours depending on the magnitude of the transmitted load at these contacts (Antony, 2007; Majmudar et al., 2007). Radjai et al. (1998) reported that the average contact force of a sheared assembly is bimodal. Also, the strong force chains (load bearing network) is able to carry a force magnitude higher than the average force (deviatoric load), whereas the other grains have contributed less and are called the weak force chains (Radjai et al., 1998; Antony, 2007). These studies have shown that load transmission occurs via inter-particle contacts in a non-

homogeneous manner (Radjai et al., 1998) and the shear resistance is achieved from a minority of about 30% of the load-bearing network in the granular media.

The complex and unpredictable temporal and spatial behaviour of the granular material assemblies is greatly influenced by the inter-particle force chain pattern (Albaraki, 2015). Therefore, due to this dependence on grain arrangement, the inter-particle force chain will distribute in a complex, non-uniform manner, even under uniform loading conditions (Majmudar and Behringer, 2005; Antony, 2007). Hence, the force is transmitted between grains in a non-homogeneous way.

2.3 Relevance of Strip Footing in Geotechnical Engineering

The foundation is the lowest part of a structure, which transfers the load of the building structure to the soil or rock, without being overstressed. Overstressing the soil results in either shear failure or excessive deformation of the soil. The soil may be below water, such as a bridge or a marine structure, although most foundations are placed on soil or rock near the ground surface. Thus, the depth of footing embedment (D_f) depends on many factors, such as frost action, soil volume change (shrinkage and swell due to drying and wetting), adjacent footing and property lines, ground water level, underground utilities (defects, such as faults and caves) and building codes (Liu and Evett, 2004). Foundations can be classified into two main categories: shallow and deep foundations. Foundations are categorised according to the ratio of D_f/B. This ratio is less than four for shallow foundations and greater than four for deep foundations (Das, 2006). Safety against the bearing capacity failure of the soil under the foundation and tolerable settlement is essential criteria for any safe foundation design. In foundation engineering designs, an ultimate bearing capacity (q_{ult}) and an allowable settlement (S_{all}) are used as design control parameters (Liu and Evett, 2004; Bowles, 1996). q_{ult} equals the maximum failure applied load per unit area of the footing (kN/m^2). S is the settlement at footing structure-soil level.

2.3.1 Ultimate Bearing Capacity (UBC)

The ultimate bearing capacity refers to the ability of the soil to sustain the maximum load on the footing before the soil collapses. Geotechnical engineers must ensure that the load per unit area of the footing does not exceed the ultimate bearing capacity of the soil, which

can lead to excessive vertical movement in the ground (deformation), causing shear failure in the soil. Foundation design is based on q_{ult} and S_{all}, however, only one of these should control the design, depending on the soil profile and the loading condition. The design of footings on sand is usually done based on using either of the criteria, viz., based on the ultimate bearing capacity or the maximum allowable settlement of sand. Soils under the ultimate load fail due to excessive settlement of the footing. This settlement increases as the applied load increases. Theoretical and/or Experimental analyses are used to determine the ultimate bearing capacity. The experimental analysis is achieved by conducting a full-scale loading test, plate loading test (PLT), laboratory scale model footing loading test and/or centrifuge tests. The theory of plasticity and FEM are widely used for theoretical analyses. These methods typically assume that the soil is homogeneous under the footing, and that the stress profile shows linear elastic decreasing with the depth. However, the properties of soil are far from this assumption. Granular materials, such as sand, gravel and rock, are largely inhomogeneous and discontinuous in nature. Moreover, the accuracy of results depends on the assumptions involved in the determination of the q_{ult}.

Depending mainly on the density of the soil, three types of failure mode have been identified, as illustrated in **Figure 2.1**. General shear failure occurs below footing supported by dense sand or stiff clay soils that are relatively incompressible and reasonably strong. The failure surface starts around the corner of the footing, then gradually extend downward and outwards. A heap shows on the free surface around the footing. This is the most common mode of failure. Local shear failure happens for footing resting on medium-dense sand or a medium-stiff clay soils with relatively large displacement. The development of failure surface initiates from the edges of the footing and end within the soil mass. This mode is an intermediate between general and punching shear failure. Punching shear failure takes place in loose sand or soft clay with large displacement and high compressibility. Shear failure forms directly under the edges of footing, where the failure surface cannot further propagate. Therefore, three types of failure under ultimate loads:

- General shear failure.
- Local shear failure.
- Punching shear failure.

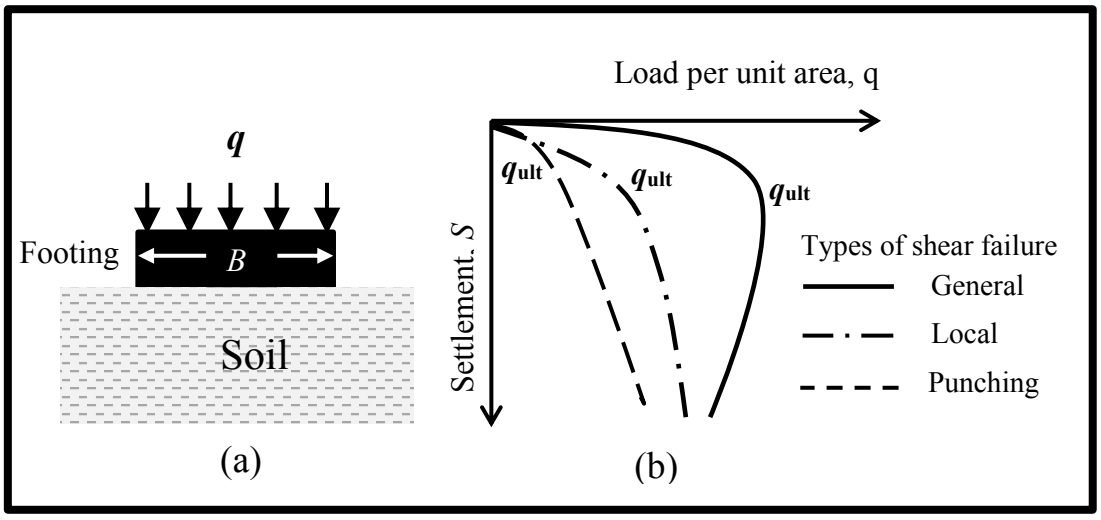

Figure 2.1 Ultimate bearing capacity of soil for a shallow foundation (a) model footing (b) load-settlement curves of different bearing capacity failure modes

2.3.2 Settlement of the Footing

Ultimate bearing capacity and tolerable settlement are the basic requirements for a good foundation (Liu and Evett, 2004; Fang, 1991). The settlement often controls the design for larger foundation widths (Das, 1999), and in many cases, the displacement of the sand controls the design of the footing (Bowles, 1996).

Building loads, dynamic forces, changes in water table, adjacent excavation work (etc), are among the possible causes of the settlement of the footing. However, the major cause of the settlement results from the compressive deformation of the soil by the building load (Liu and Evett, 2004). Most of the settlement of foundations on sand occurs by the end of the building construction. Therefore, the rate of the load application does not affect the settlement of the sand, as with clay. The settlement of the footing on sand almost controls design, rather than the ultimate bearing capacity (Liu and Evett, 2004). The total settlement under any foundation should not exceed S_{all} when considering the features of good structure serviceability, such as stability and functionality. The settlement of the footing on sand is predicted by empirical methods, using the modulus of elasticity (E) from in situ tests, such as the standard penetration test (SPT), plate loading test (PLT) and cone penetration test (CPT); these all depend on relative density (D_r) (Fang, 1991).

Geotechnical engineers must use a safety factor (FS) to minimize q_{ult} to an allowable bearing capacity (q_{all}). However, for small width footing, the bearing capacity controls the design, while for larger width of footing, the allowable settlement controls the design (Das, 1999). The allowable settlement is recommended as 50mm, and 35-65mm for

isolated and raft foundations, respectively (Bowles, 1996, p.339). The settlement of a foundation is divided into three types.

- Elastic settlement (S_e) in mm.
- Primary consolidation settlement (S_c) in mm.
- Secondary consolidation settlement (S_s) in mm.

Thus, the total settlement (S_t) is equal to the sum of any of the above, depending on the soil and the structure lifetime, which is expressed as:

$$S_t = S_e + S_c + S_s \tag{2.1}$$

Elastic settlement is related to the deformation of dry soil and saturated soils, without any moisture change. Fine-grained soil, such as silt and clay, undergo consolidation settlement under the water table level. A time lag is required between the load application and the settlement of the footing due to the low permeability that delays the expulsion of water from the voids of the soil. At the end of consolidation settlement process, the secondary settlement emerges as a result of plastic distorting the soil fabric (Das, 1999). Hence, the load-settlement relationship is a function of any foundation design. Therefore, it is important to identify the load-settlement relationship when measuring the stress in the soil and its deformation during the load application on the foundation. Most of these relationships assume that the soil is a homogeneous, semi-infinite, elastic medium (Schmertmann et al., 1978).

There are numerous techniques available for estimating the settlement of a shallow foundation. Each procedure is based on the developer's theories on the theoretical equations (elastic theory) and semi-empirical correlation. Therefore, the predicted settlements differ considerably between the individual methods (Fang, 1991). The most famous method that is used to estimate the settlement of the footing is notably Schmertmann's method (Lee et al., 2008). Schmertmann et al. (1978) have proposed a semi-empirical strain influence factor, which is a mixture of rational and empirical bases, to measure the immediate settlement of the sand layer, as shown in **Figure 2.2**.

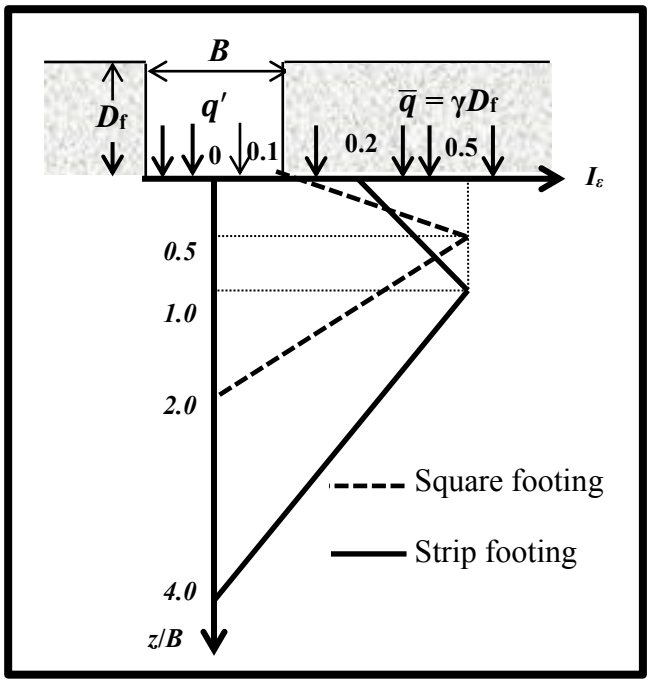

Figure 2.2 Variation of the strain influence factor, I_ε

According to this method, the settlement equation is given as:

$$S = C_1 C_2 (q' - \bar{q}) \sum_0^{Z_i} \frac{I_\varepsilon \Delta_z}{E_s} \qquad (2.2)$$

Where

C_1 = Depth factor = $(1 - 0.5\frac{\bar{q}}{q' - \bar{q}})$,

C_2 = Time factor = [1+0.2log (time in years/0.1)] ≥ 1.0,

q' = Net applied pressure (kPa),

$\bar{q}$ = Surcharge load at the footing level = γD_f, (kPa),

γ = Unit weight of the soil (kN/m^3),

I_ε = Strain influence factor at midpoint of soil layer,

Δz = Thickness of the soil layer (mm), and

E_s = Equivalent modulus of elasticity in the soil layer (MPa).

E_s can be determined by an unconfined test, a triaxial test, SPT, and CPT (Bowles, 1996, p.313). $E_s = f\, q_{ci}$, f = empirical constant correlates soil stiffness (E_s) with q_c (O'Loughlin and Lehane, 2010).

Since using this approach (Schmertmann et al., 1978), designers have tended to change the value of f to provide calculations in keeping with local experience. The Schmertmann's method is based on strain profiles along the footing centre line obtained from the laboratory scale model footing tests carried out at low stress levels, and from linear elastic finite element analyses. Four strain measurements were made at different levels in the sand beneath the footing. However, DPIV measurements can be approximately 100 points under the footing centre line. Therefore, vertical strain profiles could be obtained by differentiating the vertical displacement that is obtained along the footing centre line, as qualitatively illustrated in **Figure 2.3**. The strain profiles are qualitatively similar to the results of Schmertmann et al. (1978). This is to be expected due to the same stress level and soil stiffness in the 1g tests. Then, consistent with **Equation 2.3**, the vertical strain (ε_z) is given as:

$$\varepsilon_z = \frac{S}{\Delta z} = \frac{q' I_\varepsilon}{E_s} \tag{2.3}$$

Where

S = Settlement (mm), and

Δz, q', I_ε, and E_s as defined before.

For discrete *z/B* levels below the footing, with stiffness modulus E_s, the value of I_ε varies when deducing the most consistent relationship between E_s and strain level for q' levels typically greater than 100 kPa, by rearrange the **Equation 2.4** as follows:

$$I_\varepsilon = \frac{E_s}{q'} \varepsilon_z \tag{2.4}$$

I_ε = Strain influence factor,

E_s = Equivalent modulus of elasticity in the soil layer (MPa).

q' = Net applied pressure (kPa), and

ε_z = vertical strain.

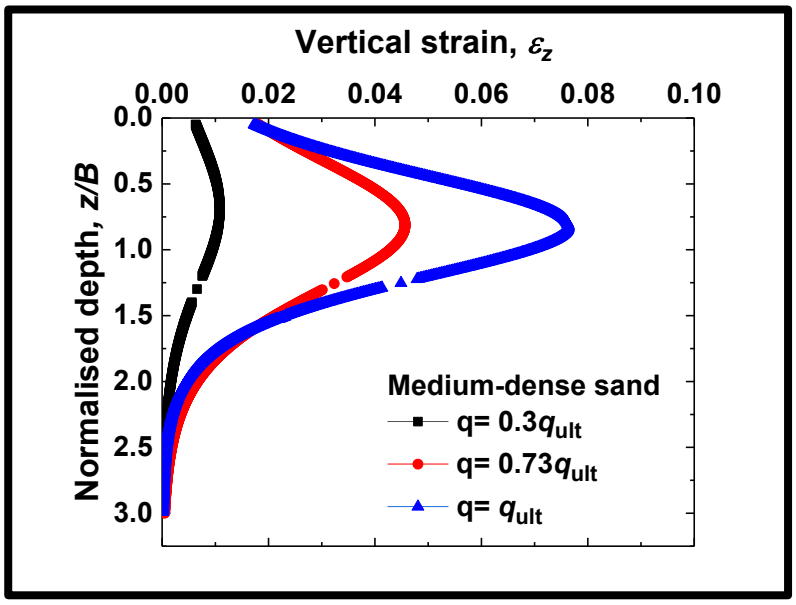

Figure 2.3 Qualitative vertical strain profiles (Schmertmann et al., 1978)

2.3.3 Interaction Effects of Adjacent Footings

Foundations in the field are rarely isolated and interfere with each other due to design considerations and space restrictions. Therefore, the mechanical behaviour of footing interference behaves differently from that of a single isolated footing. The use of the conventional bearing capacity equation of a single foundation, which was developed by Terzaghi (1943) to calculate the bearing capacity of the foundation, does not take into account the effect of interfering with each other. Consequently, comprehensive theoretical methods have been applied in the literature to calculate the interference effect by changing the edge to edge spacing (S) between the adjacent footings.

Stuart (1962) was the first to study the effect of interference on the ultimate bearing capacity of neighbouring rough and smooth strip footings. The ultimate bearing capacity refers to the ability of the soil to sustain the maximum load on the footing before the soil collapses. The shapes of different selected failure surfaces were assumed a combination of straight line and logarithmic spiral arc. Stuart (1962) assumed a non-symmetrical triangle wedge (Scalene triangle) in the sand below the two closely spaced strip footings (**Figure 2.4 b)**. The point of tangency of the inner and outer spirals moves from (d) under the centre of the footing to (d_1) which is closer to the centre of the group (line of symmetry). The outer spiral contact at the point (d_2), blocking occur and the pair acts as a single footing.

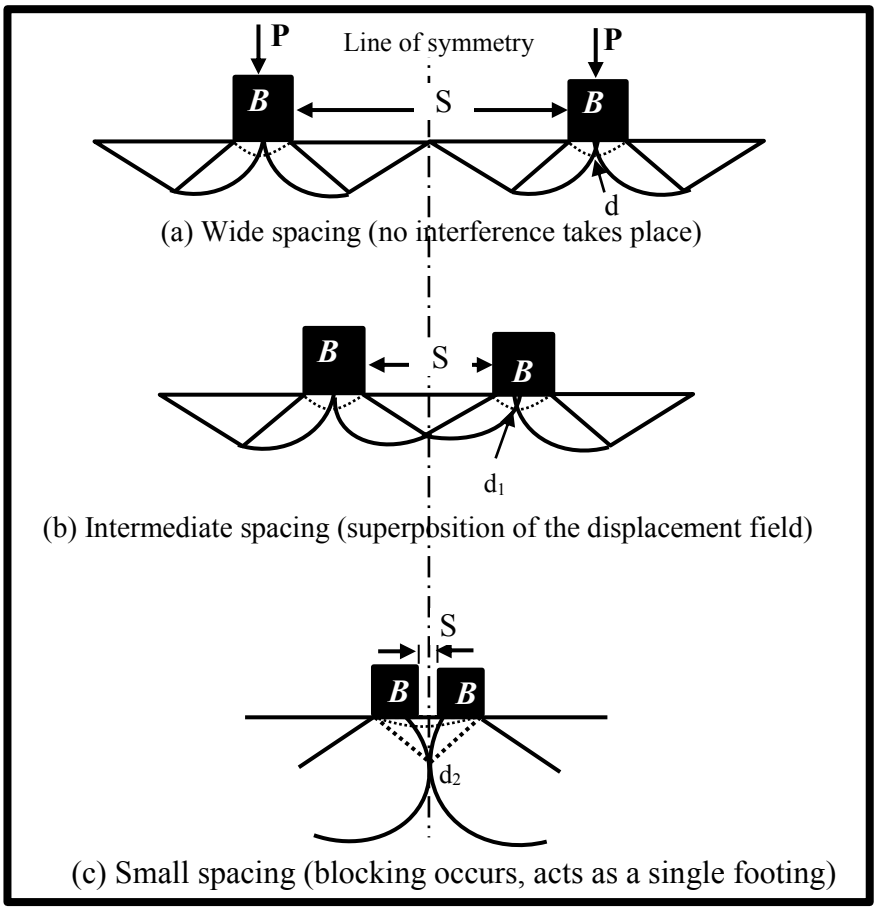

Figure 2.4 Different scenarios of the failure surfaces in sand beneath adjacent strip footings (Reproduced from Stuart, 1962)

Stuart (1962) used a theoretical approach by considering a limit equilibrium method (which is a graphical method based on the predefined Terzaghi's failure mechanism) to calculate the interference effects on ultimate load between two foundations. Stuart (1962) presented the efficiency factors of footings with interference in terms of the unit weight of the soil (ξ_γ) and for the surcharge load (ξ_q), resulting from interference. The efficiency factors are the ratio of the measured bearing capacity of the soil (due to coefficients of the bearing capacity N_γ and N_q according to Terzaghi, 1943) of interfering footing of width B to that of single footing having the same value of B for a given unit weight of soil and the surcharge load respectively. Stuart (1962) unlike previous studies of a single rough base strip foundation ($\delta=\phi$), anon-symmetrical trapped wedge was considered below the base of the footings with interference in the cohesionless soil. For a smooth footing ($\delta=0$), the ultimate bearing capacity increases to its maximum value with a decrease in interference spacing to zero when the two footing touch each other, rather than before they touch, as with the rough base footing (i.e. ($\delta=\phi$)), as shown in **Figure 2.5**. In the case of footings on cohesive soils where $\phi=0$ as reported by Stuart (1962), the

footings with interference did not exhibit any change in bearing capacity as they approached each other because the blocking (interpenetrate of passive zones) does not occur underneath the footings. The development of the failure surfaces as two foundations approach each other on the cohesive and the cohesionless soils have been explained (Stuart, 1962). Later, by using a failure mechanism similar to that used by Stuart (1962), many researchers have employed the method of stress characteristics to obtain a solution for the bearing capacity, accounting for the interference of two strip footings.

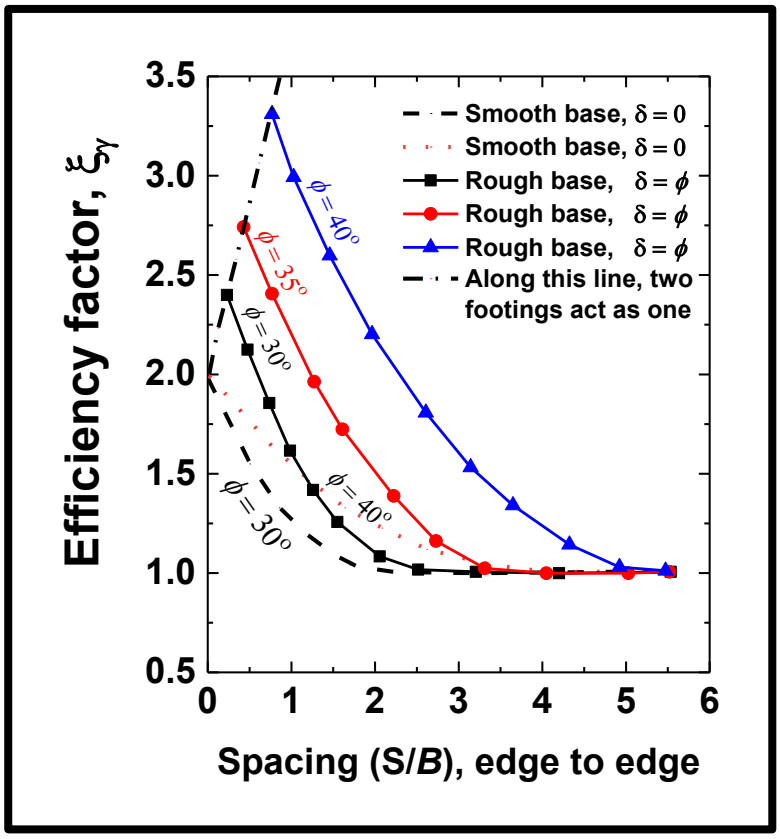

Figure 2.5 Efficiency factor for a pair of footings on sand (Reproduced from Stuart, 1962)

In addition, in order to study the effect of the interference of two closely spaced footings on unreinforced, reinforced cohesionless and cohesive soils, a number of studies were conducted by many researchers (Das and Larbi-Cherif, 1983; Al-Ashou et al., 1994; Kumar and Saran, 2003; Griffiths et al., 2006; Lavasan and Ghazavi, 2012).

Das and Larbi-Cherif (1983) also performed a series of small model tests to study the interference effect on the ultimate bearing capacity of rough strip footing resting on sand with a relative density of 54%. The results are qualitatively consistent with the theoretical study given by Stuart (1962). However, the values of ξ_γ and ξ_q have big differences

quantitatively for S/B <3.0. Furthermore, at S/B=0, the normalized ultimate settlement (S_u) by the width of the footing (S_u/B) was about 0.6 – 0.7 then S_u/B gradually decreases to 0.27 with an increase in spacing at S/$B \geq 4.5$. Similar trend for the settlement of the footings at ultimate shear failure was reported by Saran and Agarwal (1974). They stated that the settlement of the footing decreases as the spacing between the footings increases.

Kumar and Ghosh (2007) have studied the effect of spacing of two closely spaced rough strip footings on their bearing capacity due to the unit weight component of soil, choosing two different possible failure mechanisms (mechanism 1 and 2) using the method of stress characteristics which is a numerical method based on stress calculation. Mechanism 1 was assumed a quadrilateral trapped wedge below the base of each footing, whereas a non-symmetrical triangular wedge was taken below the base of each footing in mechanism 2. The results have shown a significant influence of interference on the failure mechanism and deformation pattern. Using mechanism 1, it was noted that the maximum value of $\xi\gamma$ occurs at zero clear spacing between the two footing and then decreases continuously with an increase in spacing. While, using mechanism 2, the maximum value of ξ_γ has noticed before touching of the footings when S/B = S_{opt}/B; then $\xi\gamma$ decreases with an increase in the spacing between the two footings. They have argued that mechanism 1 provides conservative results than mechanism 2 compared to the theory of Stuart (1962).

Kumar and Bhoi (2009) have studied the interference effect on the ultimate bearing capacity of two closely spaced strip foundations rested on the surface of dry sand of different relative densities using small-scale model tests. Unlike the usual experimental approaches that presented in the literature by using two adjacent footings (e.g. Stuart 1962; Das and Larbi- Cherif, 1983 in their experiments), they have used a single footing. Thus, a full symmetry in between the two footing has simulated using a smooth vertical rigid glass. As a result, the horizontal displacements have been prevented along this glass wall; therefore, it seems that zero shear stresses need to be checked along this symmetry wall barrier. The value of ξ_γ increases with the increase of angle of internal friction (ϕ) of the soil. The interference of footings makes a substantial increase in their bearing capacity and the bearing capacity becomes higher with the relative density. These observations are in a good agreement qualitatively with the literature; however, significant differences reported quantitatively. Hence, same results can be seen clearly in the theoretical work of Kumar and Kuozer (2008) who have assumed that the soil behaves symmetrically around the proposed axis of symmetry. Therefore, the need to do further

research with two footings experiment is become essential to understand more about the whole soil deformations around the adjacent footing under different loading level.

Lavasan and Ghazavi, 2012 have investigated the ultimate bearing capacity and settlement of the adjacent rough square and circular footing models on unreinforced and reinforced sand. Its relative density was about 40%. The ultimate bearing capacity and settlement of the adjacent footings on unreinforced sand were maximized due to the occurrence of blocking (superposition of the displacement field) of neighbour footings at about S_{opt}/B =0.5 and S_{opt}/B =0.0 for square and circular footing pairs respectively. Thus, the behaviour of two identical adjacent foundations depends on the shape of the footing and the spacing between them as well.

All these studies reveal that at close spacing the ultimate bearing capacity increases substantially when compared to that of a single footing. They reported that at close spacing of less than the width of the footing *B,* the ultimate bearing capacity increases substantially when compared to that of a single footing. These results, however, do indicate a certain optimum spacing (S_{opt}/B) as has been observed for rough base footings ($\delta = \phi$). However, for smooth footings ($\delta = 0$), as seen in the work of Stuart (1962), the ultimate bearing capacity increases with a decrease in interference spacing. The influence of the size of the elastic wedge in Prandtl's mechanism used in theoretical solution on the overestimation of bearing capacity of single footings was later proven by Das (1999) and Zhu et al. (2001). Das (1999) has stated that the base angle of the elastic wedge in the failure mechanism is different from what was assumed by Terzaghi (1943). Thus, it can be concluded that the predefined failure wedges used in existing theoretical solutions are not capable of accurately predicting the ultimate bearing capacity of neighbouring strip footings. Consequently, considering Terzaghi's mechanism in conjunction with the presumed size of the slip lines that differs from the true mechanism in adjacent footings might be the most possible reason for overestimation made upon using Stuart's method.

2.3.4 Layered Soils

In actual practice, the soil underneath the foundation is not homogeneous and is mostly layered (Gupta et al., 2017). Layered soil profiles can be found under the footing, regardless if they are natural or man-made. A compacted (strong) soil layer is preferred under any foundation for a wide range of civil engineering work (Jahanger et al., 2010). Geotechnical engineers have to place a very strong layer of soil directly underneath the

footing at the depth of footing embedment (D_f) to sustain the applied load from the building (safe against shear failure) and transfer it safely to the underground layer, along with acceptable deformation in the soil bed (safe against settlement). The determination of the bearing capacity of the footing over homogeneous soil is considered by a number of previous studies. However, the soil encountered is non-homogeneous, especially in the case of the layered soil. The developed bearing capacity equations consider the single homogeneous soil below the footing, which does not apply to the layered soil underneath the footing (Gupta et al., 2017). Therefore, the layered profile of the soil must be considered while deriving the equation for the foundation system resting over the layered soil. The ultimate applied surface load on the layered soil system ($q_{\text{ult layered}}$) depends on individual shear strength parameters (c and ϕ) of each layer, the thickness of the upper soil layer H, the width of footing B, the shape of the footing, the depth of footing embedment D_f, and H/B (Farah, 2004).

Numerous theories have been used to simplify the failure mechanisms, together with a reduced level of shear strength mobilization on the assumed punching shear zone. Large discrepancies between the predicted and the measured values of the ultimate bearing capacities have been observed. For layered soil, therefore, the ultimate bearing capacity and settlement of footing were studied using a theoretical method, an analytical method, and an experimental method. The theory of plasticity is used in the theoretical method, and the finite element method is used for the analytical method, whereas different prototypes and small models are carried out to determine the bearing capacity in the experimental method. Numerous researchers have investigated the ultimate bearing capacity and settlement of footing resting on subsoil that consists of two layers. Button (1953) was the first to study the effects of layered clayey soil on the ultimate bearing capacity. Meyerhof and Adams (1968) investigated a number of model uplift tests and compared them to full-scale tests. They demonstrated a complex failure mechanism, as illustrated in **Figure 2.6**. In dense sand at a shallow depth, a distinct slip surface occurs, which extends in a shallow arc from the anchor edge to the ground surface (**Figure 2.6a**). At greater depths, the slip surface is less distinct, and is initially curved (**Figure 2.6b**). However, because of the complex form of the slip surfaces, the actual slip surface was simplified, and therefore a general theory was produced.

At the ultimate uplift load Q_u, a soil mass having an approximately truncated pyramidal shape is lifted up. The failure (slip) surface extends to the ground surface, according to **Figure 2.6a**. Accordingly, a state of general shear failure exists along the failure surface,

on which a cohesive force C_F and a friction force F are mobilized based on a unit shearing resistance:

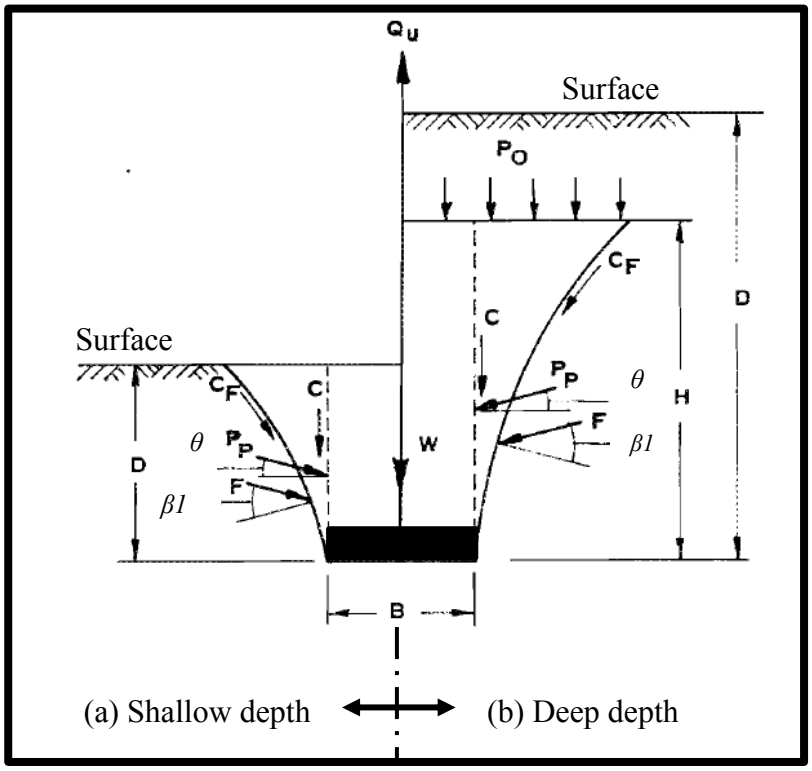

Figure 2.6 Failure of soil above a footing under uplift load (Meyerhof and Adams, 1968)

$$\tau = c + \sigma \tan \phi \tag{2.5}$$

Where

τ = Shear stress (kPa),

c = Cohesion, apparent cohesion of the soil (kPa),

σ = Normal stress (mean) on failure surface (kPa), and

ϕ = Angle of internal friction of the soil (degree).

The ultimate load per unit length of the footing may then be expressed as:

$$Q_u = 2C_F \cos \alpha 1 + 2F \cos \beta 1 + W \tag{2.6}$$

Where

W = Weight of the lifted soil mass and weight of the footing (kg),

α1 = Average inclination with vertical of forces C_f (degree), and

$\beta 1$ = Average inclination with vertical of forces F (degree).

In the absence of a rigorous solution for the stresses on the failure surface, it may be assumed that Q_u is approximately given by:

$$Q_u = 2C + 2P_p \sin\theta + W \quad (2.7)$$

Where

C = $c \times D$= Total cohesion along vertical plane through footing edge (kPa),

Pp = Total passive earth pressure (kN/m), and

θ = Mobilized angle of shear resistance on the assumed failure zones (degree) (**Figure 2.6**).

Likewise, Meyerhof (1974) assumed that the same failure mechanism for the layered soil system of the sand layer overlays the clay layer. They assumed a plane of failure instead of the actual arc form plane of failure, i.e. vertical side block, as illustrated in **Figure 2.7.** Meyerhof (1974) was the first to study the ultimate bearing capacity of footing on the sand layer overlying the clay soil layer, and the loose sand layer on the stiff clay layer, using both theoretical and experimental methodology, as illustrated in **Figure 2.7**.

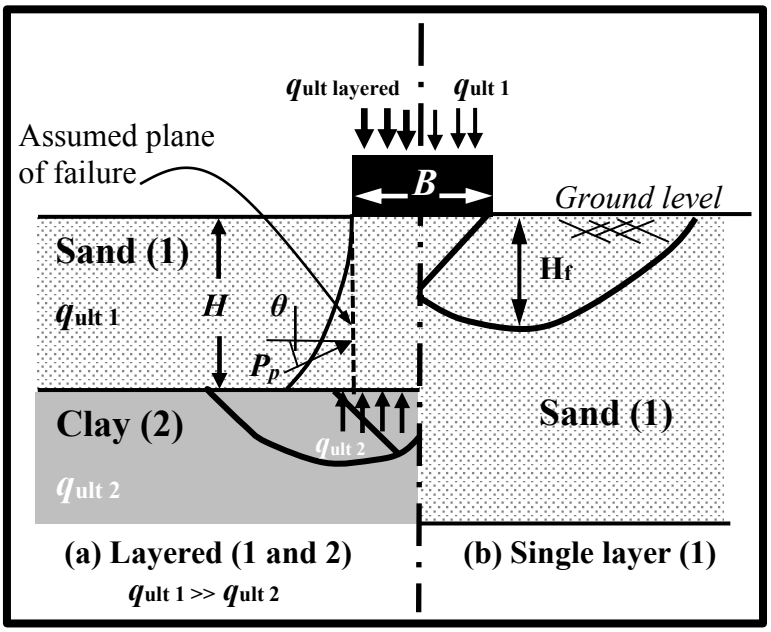

Figure 2.7 Failure of soil below footing on a dense sand above a soft clay

The forces on the failure surface (truncated pyramidal shape) in the sand layer has been taken as an equivalent to the total passive earth pressure P_p inclined at an average angle θ acting upwards on the vertical plane through the edge of the footing. Therefore, for surface footing on the layered sand of c=0 and using the theoretical equation of Meyerhof (1974), the ultimate bearing capacity of the layered dense sand overlying loose sand is approximated as below.

$$q_{ult\ layered} = q_{ult\ 2} + \frac{2P_p \sin\theta}{B} \tag{2.8}$$

$$P_p = \frac{0.5\gamma_1 H^2 K_p}{\cos\theta} \tag{2.9}$$

$$K_s \tan\phi = K_p \tan\theta \tag{2.10}$$

The ultimate soil bearing capacity for the surface strip footing (D_f = 0) resting on the homogeneous granular soil (c=0) and loaded by an axial, vertical load, can be expressed in the below form (Terzaghi's equation) neglecting the smaller N_q contribution to the bearing capacity for the current case of the surface footing (Dijkstra et al., 2013):

$$q_{ult} = 0.5\ \gamma\ B\ N_\gamma \tag{2.11}$$

Therefore, $q_{ult\ 2}$, the ultimate bearing capacity of the loose sand (bottom layer) is written as:

$$q_{ult\ 2} = 0.5\ \gamma_2 B\ N_{\gamma 2} \tag{2.12}$$

Substituting Equations (2.9), (2.10) and (2.12) into (2.8); to generate the equation for the layered dense sand on loose sand as:

$$q_{ult\ layered} = 0.5\ \gamma_2\ B\ N_{\gamma 2} + \frac{\gamma_1 H^2 K_s \tan\phi_1}{B} \leq q_{ult\ 1} \tag{2.13}$$

Where

$q_{ult\ layered}$ = Ultimate bearing capacity for footing on layered soil as a whole (kPa),

$q_{ult\ 1}$ = Ultimate bearing capacity of the top soil layer ((kPa),

$q_{ult\ 2}$ = Ultimate bearing capacity of the underlying soil (kPa),

H = Thickness of the top layer (mm),

K_p = Coefficient of passive earth pressure of the top soil,

K_s = Coefficient of punching shearing resistance,

N_γ = Bearing capacity factor due to unit weight of soil,

N_q = Bearing capacity factor due to surcharge stress,

ϕ_1 = Angle of internal friction of the top soil (degree),

ϕ_2 = Angle of internal friction of the bottom soil (degree),

γ_1 = Unit weight of the top soil layer (kN/m^3), and

γ_2 = Unit weight of the bottom soil layer (kN/m^3).

The coefficients of punching shear resistance were expressed in the case of the sand layers overlaying clay. On the other hand, in the case of the loose sand on stiff clay, modified bearing capacity coefficients were expressed to calculate the ultimate bearing capacity. Meyerhof (1974) stated that the optimum thickness of the top sand layer depends on the strength ratio of the clay to sand, the angle of internal friction of the sand (ϕ), the shape of the footing and the depth of footing embedment (D_f). Generally, the soil layer was considered a strong layer over a weak deposit, and vice versa.

Meyerhof and Hanna (1978) extended the study of the ultimate bearing capacity of footing over layered soil to cover an inclined load, using the assumed plane of failure that is used by Meyerhof (1974). These were dense sand overlaid with loose sand, loose sand overlaid with dense sand, dense sand overlying clay, and a stiff clay on soft clay, by using model-loading tests. They stated that the theoretical and experiment results show the important role of the upper layer in the whole layered system, and that the inclination of the load affects the shear strength and the ultimate bearing capacity.

Oda and Win (1990) studied interstratified layers of the soil bed deposit. Experimental tests were conducted on the sand bed with the interstratified clay layer. Oda and Win (1990) reported that the thin clay layer at 5B deep below the footing still has a significant effect on the ultimate bearing capacity of the soil.

Farah (2004) studied dense sand overlaid with weak cohesive or cohesionless soil deposits subjected to axial vertical loads using an analytical approach. A stress analysis was implemented on the observed actual failure planes in the experiments. A new bearing capacity equation was derived and compared with the experiments from the literature.

Lee et al. (2013a) derived a new conceptual model to predict the ultimate load of a circular footing on sand, overlying the soft clay based on visualisation experiments and FEM. The failure mechanism of a block of sand being pushed into the underlying clay, with an

exterior angle reflecting the dilation in the sand, was assumed. They claimed significant improvements over existing punching shear and load spread models, since the result incorporated the strength properties of the sand in a consistent manner.

2.3.5 Cyclic Loadings

Cyclic loading in geotechnical structures can be caused by machine vibration and wind force, or other sources that usually apply variable forces on the soil layer. Therefore, the cyclic behaviour of granular materials has become a critical issue in numerous civil engineering applications relating to the footing structure, especially in seismic hazard areas. These structures would undergo a significant settlement as a result of an accumulation of irreversible soil deformations due to monotonic (static) loadings and cyclic loading. The design of building foundations being located near seismic activity, offshore zones, pavements, storage tank foundations with numerous filling and discharging activities and railway ballast, has become essential due to cyclic loading (Sabbar et al., 2016).

Cyclic loading is defined as a system of repeated loads that displays a constancy rate in both frequency and amplitude. The frequency of cyclic loading is given as a load frequency between 0-1Hz and the frequency of dynamic loading is greater than 10Hz, as shown in **Table 2.1** (Peralta, 2010; Sabbar et al., 2016). Cyclic or dynamic loading can be produced from environmental origins, such as seasons, waves, tides, the wind, and earthquakes. Cyclic loading can also occur from traffic construction, blasting operations and rotating machinery (Shajarati et al., 2012). This form of loading has an effect on the soil properties, such as modulus of elasticity (E), shear stress (τ), and the void ratio (e). Therefore, it is significant that not only the static ultimate bearing capacity (q_{ult}) is investigated, but also the cyclic ultimate bearing capacity ($q_{ult\ cyc}$). However, in general, the method of determination of the ultimate bearing capacity of the footing under cyclic loading has not been standardised yet. The ultimate bearing capacity refers to the ability of the soil to sustain the load on the footing before the shear failure occurs.

Table 2.1 Classification of repeating loading of soils (Peralta, 2010)

Repeated loading of soils	Cyclic	Cyclic-dynamic	Dynamic
Frequency	0 to 1 Hz	1 to 10 Hz	>10 Hz
Strain accumulation	Mostly plastic	Plastic and elastic	Mostly elastic

Many studies into the effects of cyclic load on granular materials in geotechnical applications has been conducted by many researchers. These studies mostly consists of laboratory tests done using different test devices, such as cyclic triaxial tests and cyclic simple shear tests (Shajarati et al., 2012; Lombardi et al., 2014; Sabbar et al., 2016). They generally report that there is a significant connection between the D_r and the cyclic resistance of the sandy soil. In addition, the displacement of the soil increases with an increase of the number of loading cycles. Furthermore, drainage conditions, sample preparation methods, confining pressure, relative density, frequency, the type of loading, and stress levels, all have a considerable effect on the cyclic behaviour of granular materials.

Experimental research into the responses of granular materials under cyclic loading using different testing methods has been considered using different cyclic loading types. These studies compared the behaviour of sandy soil under monotonic and cyclic loadings at various conditions and factors, which affect the cyclic behaviour of cohesionless soils. Therefore, numerous theoretical and experimental model-scale studies have considered the factors that affect the sandy soil under cyclic loading, by using different materials and techniques (Raymond and Komos, 1978; Tafreshi et al., 2011; El Sawwaf and Nazir, 2012; Shajarati et al. 2012; Asakereh et al., 2013).

Tafreshi et al. (2011) numerically and experimentally evaluated the response of footing under incremental cyclic loads, which is similar to cyclic plate load test (PLT) loading pattern. The expected load on the footing was achieved in five incremental cycles of loading and unloading, using stress controlled loading (SCL) at a rate of 1 kg/s, as illustrated in **Figure 2.8**. Their investigations were conducted on three circular footing areas of 25 cm^2, 50 cm^2 and 100 cm^2 on sand beds at three relative densities: 42%, 62% and 72 %. The results evaluated the properties of the elastic rebound of the soil, in addition to the effects of the area of the footing and the packing density on the coefficient of elastic uniform compression of sand (CEUC). The value of the CUEC of the soil is significantly affected by the area of the footing, as CUEC value increases with a decrease

in the area of the footing, irrespective of the packing density. The value of the elastic rebound settlement for the dense sand increases with the decrease in the area of the footing, irrespective of sand packing, as illustrated in **Figure 2.9**. The contours of the vertical stress bulb, the displacement, and the shear strain below the footing of 100cm^2 at the last loading cycle for (D_r=72 %) are derived from the numerical analysis, as shown in **Figure 2.10**.

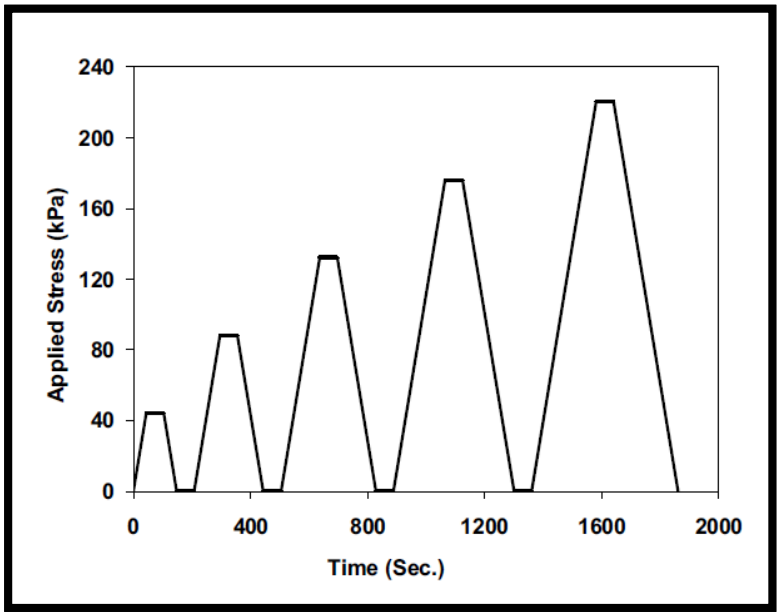

Figure 2.8 Incremental cyclic loads on footing (Tafreshi et al., 2011)

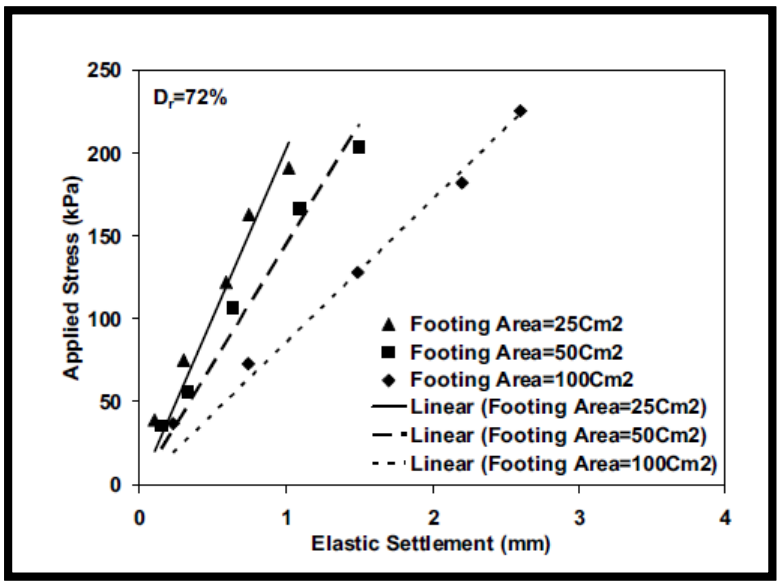

Figure 2.9 Applied stress vs. elastic rebound settlement (Tafreshi et al., 2011)

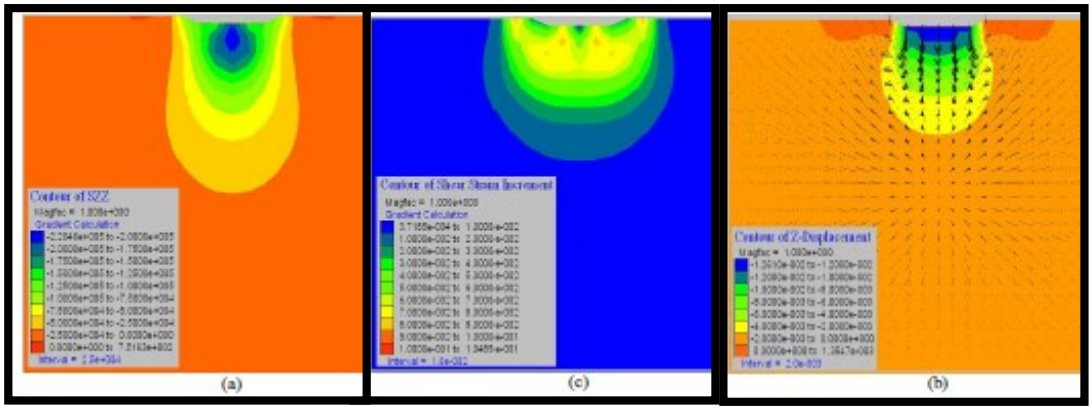

Figure 2.10 Contours at the last loading cycle of the cyclic PLT (Tafreshi et al., 2011)

El Sawwaf and Nazir (2012) studied the relationships between the initial monotonic and the cyclic settlements of the cyclically loaded laboratory model of the strip footings, supported by unreinforced and reinforced loose sandy slopes. The initial monotonic load level, along with the amplitude and frequency of the cyclic load were investigated. The researchers adapted different values of the frequency of the cyclic load, as shown in the **Figure 2.11** to simulate different types of the machines' cyclic loads. They stated that the total settlement (S) and the cyclic settlement ($S_{cyc.}$) increase with an increase in the number of cycles. Also, the total settlement (S/B) significantly decreased with E, using replaced dense sand or the inclusion of soil reinforcement. Soil reinforcement acted more efficiently than soil replacement in improving the behaviour of cyclically loaded footing on loose slopes, as illustrated in **Figure 2.12**.

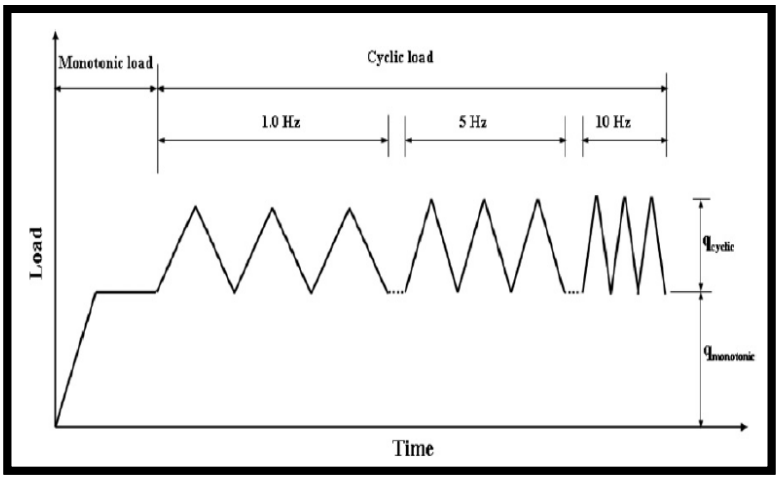

Figure 2.11 Loading sequence on the model footing (El Sawwaf and Nazir, 2012)

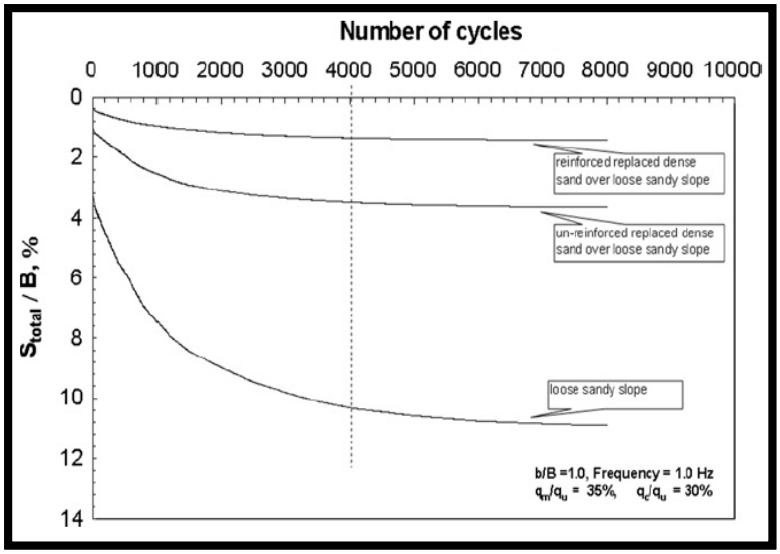

Figure 2.12 Variation of settlement ratio with number of load cycles (El Sawwaf and Nazir, 2012)

Shajarati et al. (2012) reviewed the existing research, considering the behaviour of cohesionless soils when subjected to cyclic loading in triaxial test. They concluded that the behaviour of a soil subjected to cyclic loading is found to be dependent on - the relative density, the mean effective stresses prior to cyclic loading, the average shear stresses, and the drainage conditions.

Asakereh et al. (2013) measured the settlement of the strip footing constructed on unreinforced dense sand (D_r=73 %) and geogrid-reinforced sand, with a circular tunnel void subjected to a combination of the static and the repeated loads, as illustrated in **Figure 2.13**. In this static test, the load was applied using SCL at a rate of 1 kPa/s, until failure occurred, after which the repeated loading was superimposed to the static load. The researcher has examined the effects of the number of load cycles and the amplitude value. The unreinforced sand results show that the values of footing settlement increase rapidly during the initial loading cycles; thereafter the rate of settlement is reduced significantly, as the number of loading cycle increases (as illustrated in **Figure 2.14**). In addition, it can be seen that the footing settlement increases with an increase in the ratio of repeated load to static load. The amplitude of the repeated load has a significant effect on the value of the maximum footing settlement and the number of the load cycles required to develop the stable response condition. The footing settlement increases considerably by increasing the amplitude of the cyclic load.

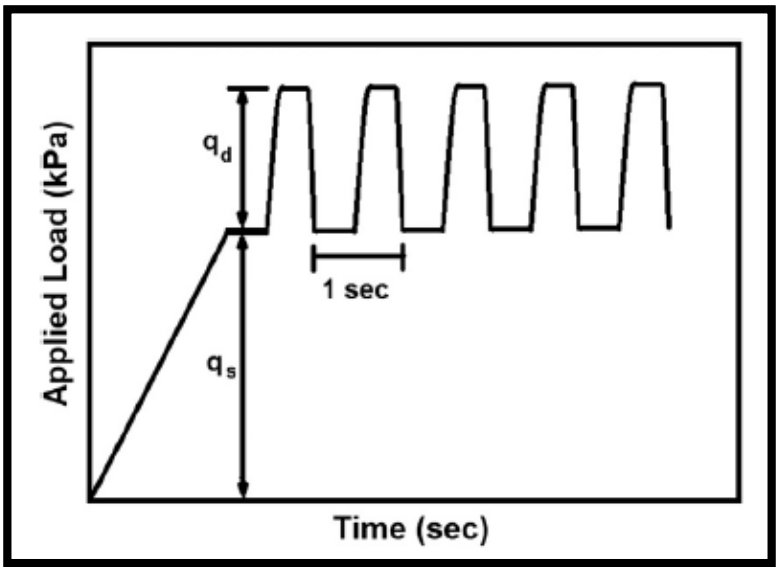

Figure 2.13 Initial static and repeated loading (Asakereh et al., 2013)

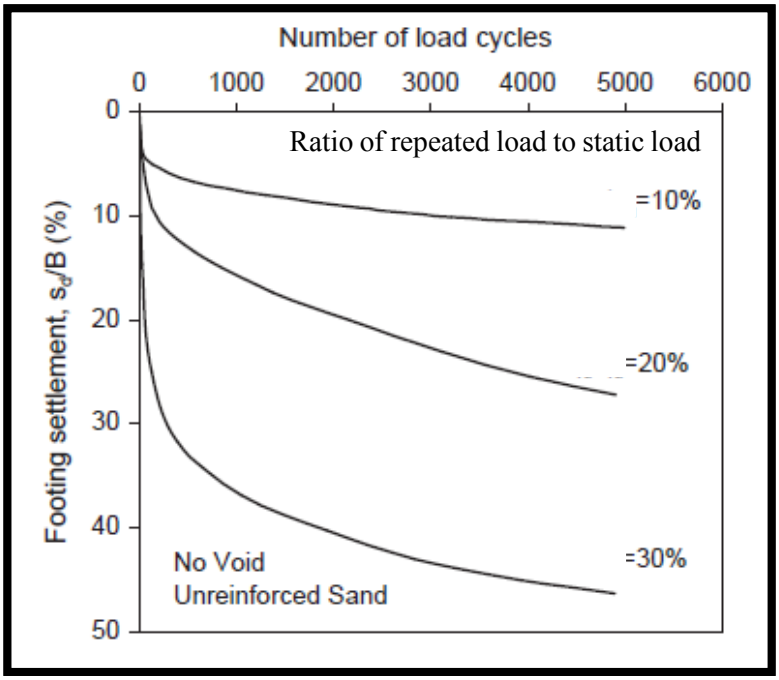

Figure 2.14 Variation of settlement of strip footing with repeated load for footing on dense sand (Asakereh et al., 2013)

An increasing number and wider distribution of seismic activities in central and southern parts of Iraq have been recorded at its northern and eastern boundaries. In addition to

blasting incidents due to terrorist action and wars have considerably increased. Thus, there is evidence of an increasing risk of seismic waves and earthquakes that will likely happen and could cause considerable effects on the soil layers beneath the foundations, such as unacceptable deformations and the liquefaction of sedimentary soil (Jassim and Goff, 2006). Consequently, it is very important to study the effect of cyclic loading on the strip footing that would be used to obtain seismic parameters in the future design of building foundations in Iraq. However, few studies have concentrated on the behaviour of shallow strip footing that is subjected to cyclic loading and resting on single sand layers at a micro and localised level, in which pattern deformation and failure mechanisms are considered thoroughly.

All the previous studies have reported that cyclic loading (i.e. the number of cycles and the magnitude of the cyclic load) had a significant effect on the strength of the sand soil, rather than under monotonic loading with the same stress amplitude. Excessive deformations in soil media and its strains accumulated with an increase in the number of cycles, causing differential settlement to foundations due to soil deformation (Shajarati et al., 2012; Nguyen et al., 2014, Sabbar et al., 2016). However, the deformation of sandy soil under cyclic loading was much more rapid than for clay soil. Furthermore, there has been no particular attention placed on the responses of the strip footing under cyclic loading and the failure mechanism, which is known as an important parameter in the derivation of the ultimate bearing capacity equation used in designing a foundation under a cyclic load. In order to develop a better understanding of the behaviour of footings supported on single sand layer under incremental cyclic loads, a series of laboratory tests, model scale tests, and simulations were implemented. The influences of the three different cyclic loading patterns were investigated; these are type 1-3. Type 1 cyclic load has selected which the loading history consists of stepwise increasing load cycles. Type 2 cyclic load selected based on the cyclic plate loading test (PLT). Type 3 of cyclic loading having staggered pattern that the amplitude of the same magnitude was used for two steps.

2.4 Introduction to PIV

The high-resolution measurement of soil deformation is essential in the solution of geotechnical engineering problems and the success of geotechnical modelling. The bulk responses received from conventional measurements carried out at the boundary of the tested sample might not be capable of revealing the internal variation of the deformation

process in granulates media, which is progressive (Das, 2009). Optical measuring techniques such as PIV have been developed recently to precisely measure deformation at a high level of accuracy. PIV is a non-invasive technique providing direct velocity vector measurements in a cross-section of a flow. This technique is often used in the field of fluid mechanics to track the motion of fluid flow (Adrian, 1991; 2005). The implementation of image-based deformation measurement using modern digital cameras and dedicated computing hardware results in real-time velocity fields. Therefore, the PIV technique has been employed to overcome the discrepancies in conventional experimental measurements to investigate the deformation patterns in granular materials at different loading levels, at a high spatial resolution. It has also been used to study the displacement and/or strain distribution in the case of some granular materials (Hamm, 2011; Murthy et al., 2012). Recently, DPIV has been applied to obtain the measurements of soil deformation in geotechnical engineering problems (O'Loughlin and Lehane, 2010; Dijkstra et al., 2013; Stanier et al., 2016; Ng et al., 2017).

In the present research, DPIV measurements will be used in the analysis of the four areas of interest to evaluate its performance in processing successive digital images containing flowing grains. This includes the model footing compression test on a single layer of different packings - loose, medium-dense and dense sand as presented in Chapter 5. The interference effects on the ultimate bearing capacity and displacement fields as presented in Chapter 6. Footing compression tests on layered systems of dense sand on loose sand will be shown in Chapter 7, and a model footing cyclic compression test on a single layer of dense sand in Chapter 8. This section begins with an introduction to DPIV, including a discussion on the DPIV principle, DPIV software and adaptive DPIV image evaluation method, which is then followed by a literature review.

2.4.1 The Principle of PIV

Digital PIV pertains to the digital platform of Particle Image Velocimetry (PIV), is often used in the field of fluid mechanics to track the motion of fluid flow using tracer particles (Adrian, 1991; 2005). The Dynamic Studio Software Platform (DSSP) helps to display the large amounts of DPIV-based experimental data in pictorial forms (DantecDynamics, 2013). A typical DPIV system used for deformation measurements under footing models is used in this research, as shown in **Figure 2.15** and consists of illumination lights, the

footing model and particulate system, a loading machine, an image recording system (camera) and a computer for image processing.

In the DPIV analysis, the velocity vectors are derived from sub-sections of the target area by measuring the movement of particles between two successive images, as shown in **Figure 2.16**. The velocity is given as:

$$V = \frac{\Delta x}{\Delta t} \tag{2.14}$$

Where

V = Velocity between successive images (mm/s),

Δx = Movement in x direction between successive images (mm), and

Δt = Time between successive images (s).

The Dynamic Studio Software Platform (DSSP) provides a range of techniques for characterising particle motions, making it the most convenient for making advanced scientific imaging-based measurements (DantecDynamics, 2013). Further, the algorithms provided within DSSP are used to analyse the DPIV measurements. This functionality built into the DSSP was used to analyse the digital frames of the grains, and to calculate two velocity components vectors of the grains and their evolution during load application within the sand layer, between two successive images.

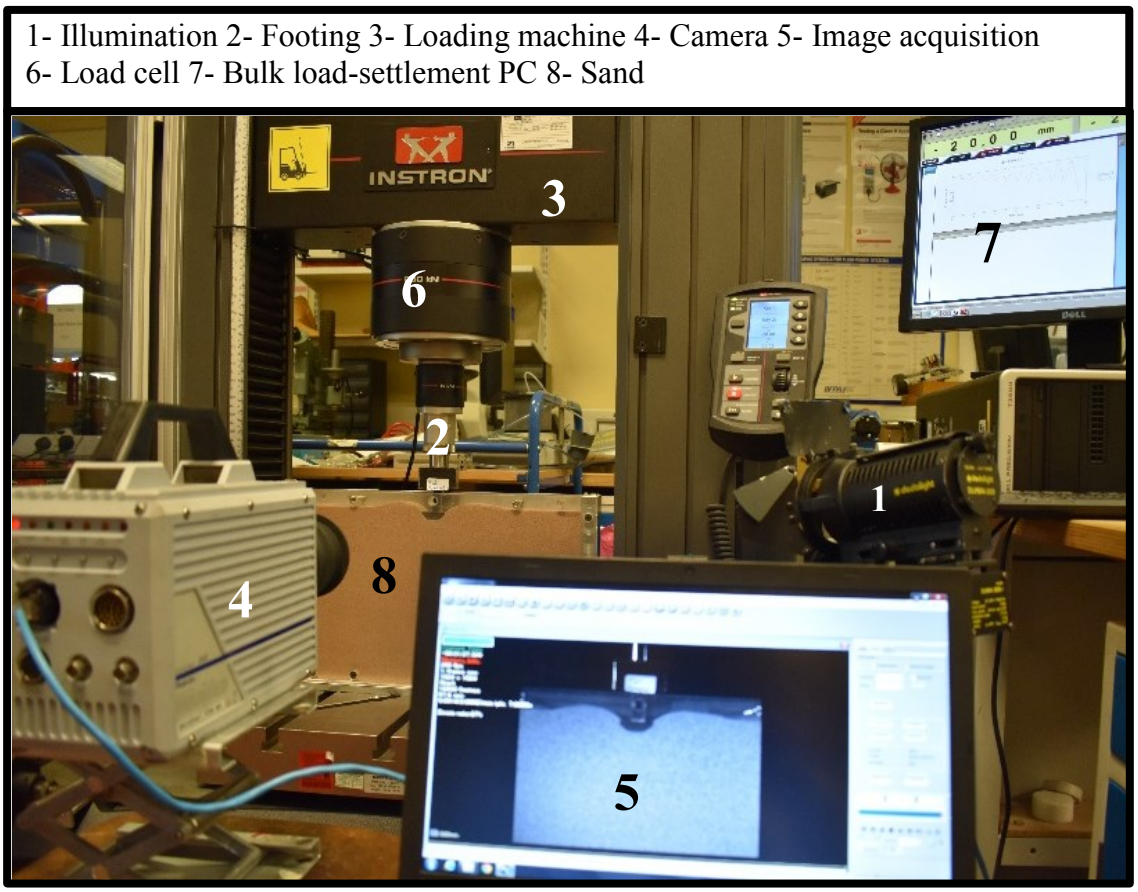

Figure 2.15 Experimental setup using DPIV with a live image of footing in contact

The 2D-DPIV system deduces differences in light intensity as a grey-scale pattern, which ranges numerically between zero (black) and 255 (pure white), recorded at each pixel on the camera. In this thesis, the area of interest (AoI), or the target area (full image), was specified before being divided into sub-sections called interrogation area (IA), each covering a zone of tested soil. Each of these IAs were tracked using an adaptive PIV method (DantecDynamics, 2013; Albaraki and Antony, 2014) to identify the movement of soil based on particle images (up to 250 frame per second depending on the type of the test) obtained from the front of the Perspex test rig captured by the camera. The interrogation areas (IAs) from each successive image are cross-correlated with each other, pixel by pixel (DantecDynamics, 2013). This correlation produces a peak signal detection, identifying the common grains movement and thus the velocity vector output is achieved with sub-pixel interpolation. A velocity vector plot over a field of view (target area) is acquired by repeating the cross-correlation for each IA over the two images captured by the camera (DantecDynamics, 2013)

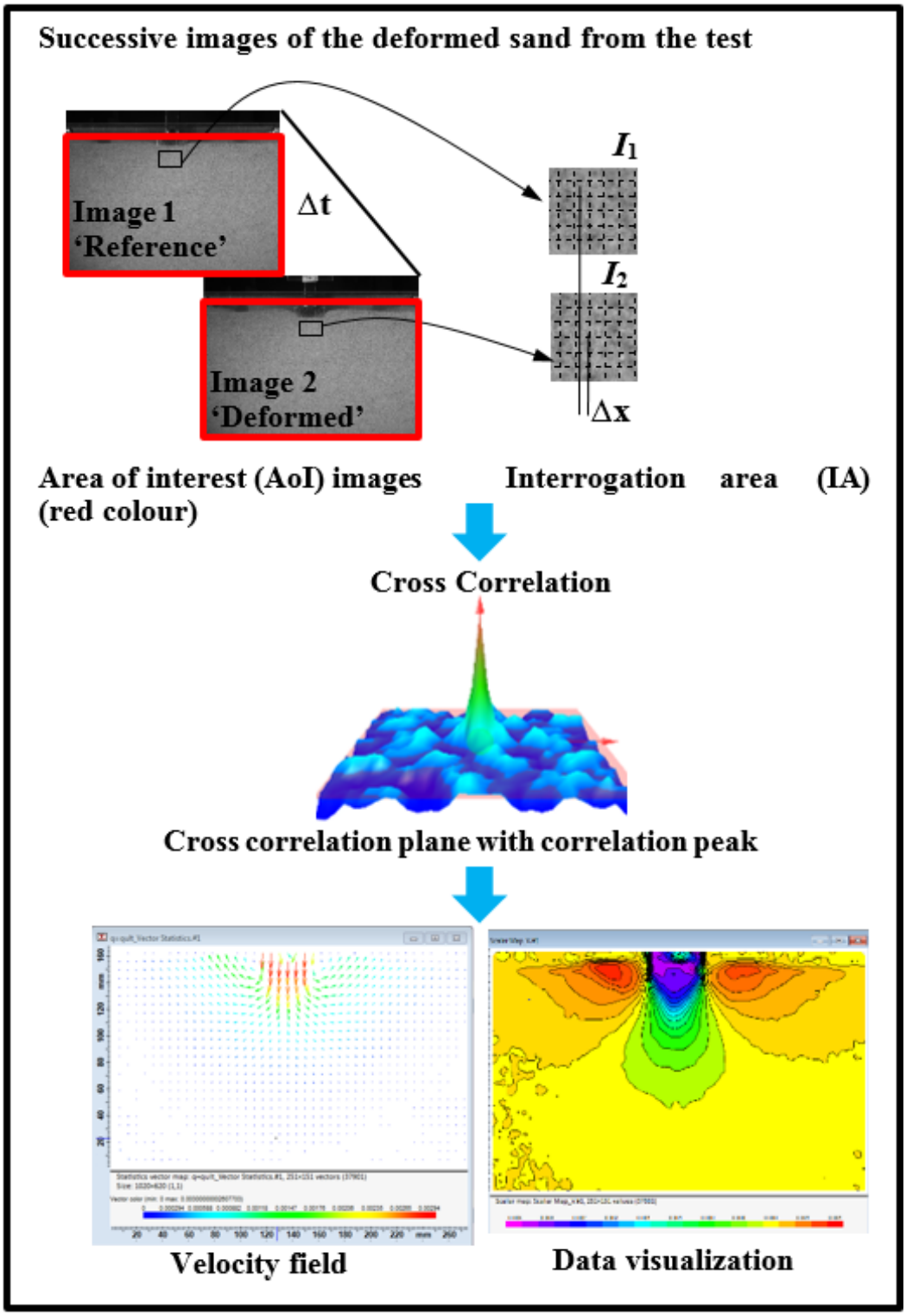

Figure 2.16 The principle of 2D DPIV system used in this thesis

2.4.2 PIV Analysis

PIV application is rapidly growing in both academic research and industrial practice, due to its ease of use and accurate data representation (DantecDynamics, 2013). Thus, a

number of commercial packages (e.g., DynamicStudio (DantecDynamics, 2013), and LaVision (LaVision, 2018)), along with freely available software used for geotechnical analysis (e.g., GeoPIV (White et al., 2003), and MAGICgeo (MAGICGEO, 2018)) have been developed. DSSP is the main software package used for image acquisition, final data processing and presentation (DantecDynamics, 2013). It offers tools such PIV for configuration, acquisition, analysis, and post-processing of acquired data. Further, DynamicStudio provides flow derivative calculations to derive new quantities from velocity data. Traditional image processing, such as in a standard PIV, uses a constant interrogation window size with a sufficient number of particles, typically 3-10 (Wieneke and Pfeiffer, 2010), which are selected to correlate and have enough stability in their window overlap factor to avoid spurious results. Therefore, the adaptive PIV method available in DSSP employs high order IA shape function, which allows IA to deform, thus allowing velocity gradient across the IA. This would improve the measurement of deformation for small and large deformations (Stanier et al., 2016). Therefore, the Dynamic Studio Software Platform (DSSP) was chosen for use in the current PIV analysis. The following sections deal with a discussion on those aspects that are important to the numerical implementation of DSSP, such as the image evaluation method, data processing and visualisation.

2.4.2.1 Adaptive PIV

The Adaptive PIV method is an automatic and adaptive method for calculating velocity vectors based on granular media images. This method iteratively adjusts the size and shape of the individual IA in order to adapt to local flow gradient and seeding densities (DantecDynamics, 2013). Adaptive PIV, with variable IA shapes and sizes will balance the robustness of calculated displacement at high velocity gradients. **Figure 2.17** shows the recipe dialogue for the adaptive PIV method in DSSP.

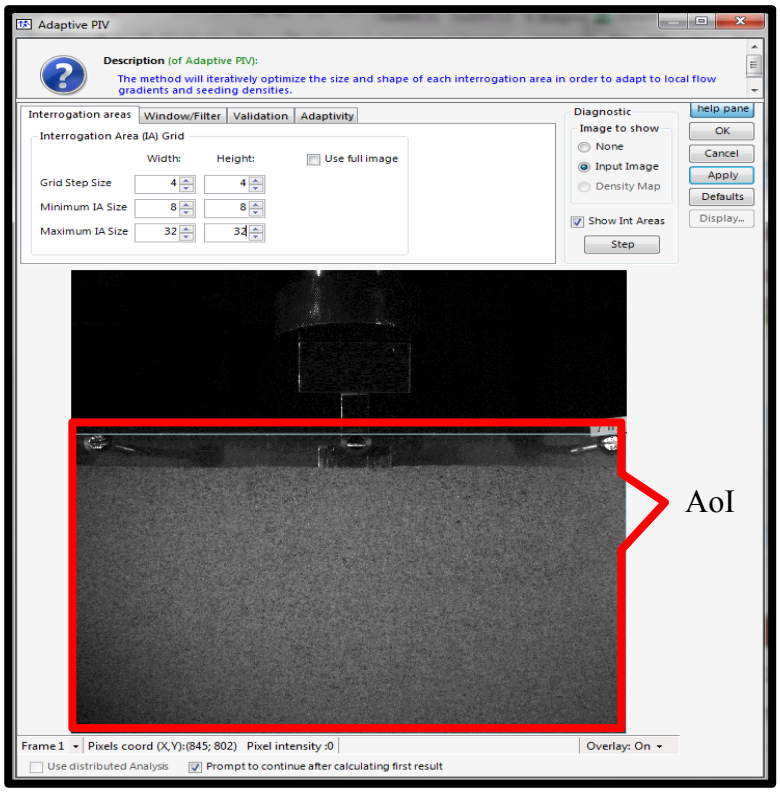

Figure 2.17 The recipe dialogue for the Adaptive PIV method with area of interest (AoI) in red colour (DantecDynamics, 2013)

Traditional image processing involves the selection of appropriate image processing parameters, particularly the interrogation area (IA) size and the window overlap factor. Settings are typically found by trial and error, wherein the optimal spatial resolution and robustness are calculated. On the one hand, windows must be large enough to capture sufficient particle image pairs yielding reliable correlation peaks (robustness), whereas velocity gradients demand small correlation windows to negate bias errors and maximise spatial resolution (i.e. reduce the smallest detectable flow feature). Contrary to the spatially varied granular density and velocity gradients, the user-defined IA parameters remain constant throughout the image and are therefore rarely optimal. The new adaptive PIV processing method decouples the above effect of granular density and velocity gradients on correlation quality.

Interrogation areas (IAs) sizes and shapes are automatically adjusted to combine information on the local amount of signal and flow topology. The former criterion imposes a minimum number of tracer images within each correlation window, in order to ensure a reliable and robust correlation peak detection, and consequently, velocity estimate; IAs are automatically enlarged in image regions with few tracer particles

present, while densely seeded regions adopt reduced correlation window sizes. Correlation windows are simultaneously sized in an iterative fashion based on velocity gradients; flow fields with low spatial variation (e.g. uniform flows) are estimated by implementing large window sizes, and vice versa. Next, a brief description of the mathematical concepts behind each method is presented.

2.4.2.2 Interrogation Area (IA)

The number of IA and the spacing between their centre positions (i.e. the distance between neighbouring IA) is determined by grid step size (i.e. the width and the height). This is specified by the number of IA that should be analysed, wherein one displacement component (velocity arrow) will be shown for each grid step size. The minimum grid step size is 4×4 pixels, and the maximum is 40×40 pixels. In addition, the minimum and the maximum IA sizes can be initially selected depending on the displacements and the image size. However, the Adaptive PIV method will automatically determine an appropriate IA size to use, as illustrated in **Figure 2.17**.

2.4.2.3 Cross-correlation Algorithm

Correlations are performed using cross-correlation. The usual method for the evaluation of two images separated by a small finite time is cross-correlation. This algorithm is the most conventional method used to calculate displacement vectors. The local patterns of displacements in an image were measured by calculating the (local) similarities (or minimal differences) between two successive images. The formula for the two-dimensional cross correlation of two images I_1 and I_2 can be defined as:

$$C_{I_1 I_2}(\Delta x, \Delta y) = \sum_{i=0, j=0}^{i<N. j<N} I_1(i, j) \times I_2(i + \Delta x, j + \Delta y) \qquad (2.15)$$

Where

$C_{I_1 I_2}$ = Cross-correlation function,

$I_1(i, j)$ = Intensity distribution value of the reference image,

$I_2(i + \Delta x, j + \Delta y)$ = Intensity distribution value of the deformed image,

Δx = Movement in x direction between successive images (mm), and

Δy = Movement in y direction between successive images (mm).

N = Total number of interrogation area.

The correlation between the two interrogation areas, I_1 and I_2, result in the particle displacement Δx, represented by a signal peak in the correlation $C_{I_1 I_2}(\Delta x, \Delta y)$, which is shown in **Figure 2.18**.

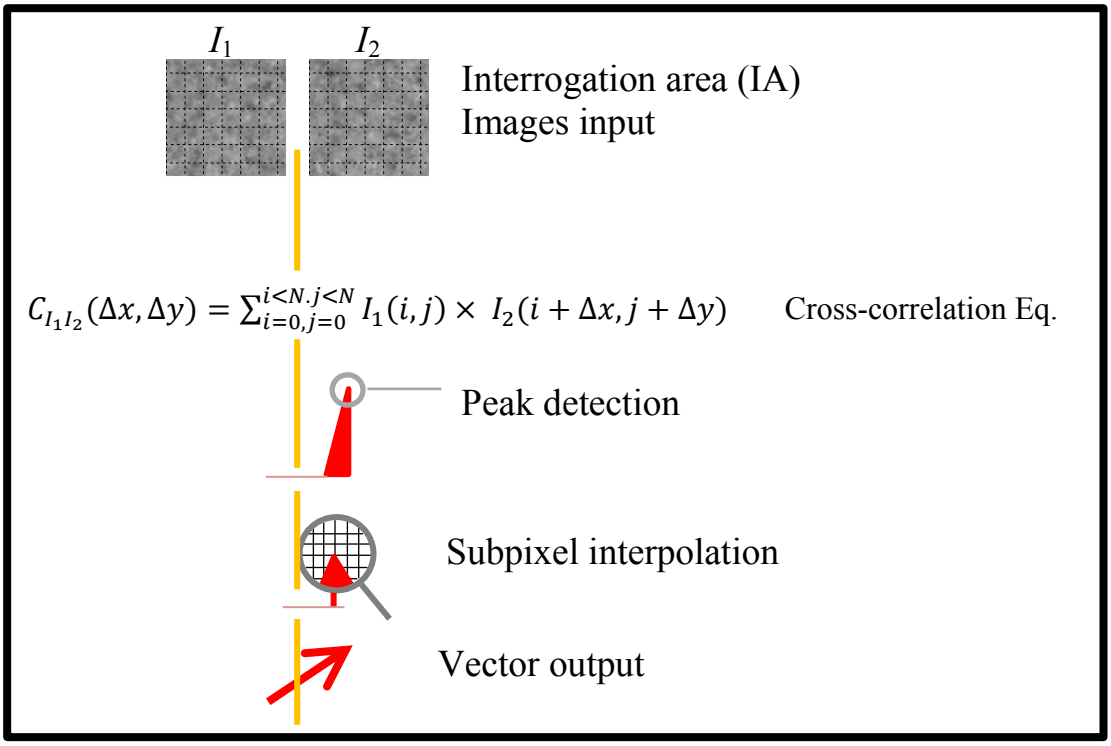

Figure 2.18 The correlation of the two interrogation areas, I_1 and I_2

2.4.2.4 Validation

Validation parameters in the adaptive PIV method are various and can be used in combination with smoothing the processing and removing spurious vectors. After, spurious vectors are identified and eliminated directly from the correlation data whilst performing the image cross-correlation as a correlation-based technique. A certain amount of invalid velocity vectors can be observed simply via visual inspection of the visualised data, as these vectors deviate significantly in direction and/or magnitude from the adjacent valid vectors. However, the velocity field should be smooth, in general; the noisy vectors within the velocity field should be presented and therefore be eliminated. Therefore, validation (post-interrogation techniques) is used prior to the flow gradient estimation to avoid outliers that disturb the calculations. This tool in Dynamic Studio Software Platform (DSSP) prevents outliers from disturbing the iterations, and thus, the velocity measurements. A peak validation of the image cross-correlation can help identify

invalid vectors. A universal outlier detection algorithm will substitute spurious vectors by comparing each vector to its neighbours. In granular materials, the deformation could sometimes be characterised by localised areas with a high strain gradient (Zhou, 2011). Therefore, the rejected vector for either peak invalidation will be replaced later with the median of the neighbouring vectors (5×5 vectors).

2.4.2.5 Adaptivity

The adaptivity setting will affect the adaptive adjustment, which is iteratively applied to each interrogation area (IA) to adapt its size, particle density, and/or its shape to velocity gradients, thus allowing velocity gradient across the IA. The adaptivity of IA size to particle density is employed using a particle detected limit, where a greyscale peak must rise a set number of times above the noise floor in order to qualify as a particle. The adaptivity of the IA shape to velocity gradient is performed using four velocity gradients. These comprise of derivatives of the velocity components, horizontal displacement component (S_h) and vertical displacement component (S_v) both in the x and in y-directions respectively. By utilising a combined algorithm of adaptive deforming windows and high accuracy sub-pixel interpolation, there is improved signal strength, hence opening the possibility to decrease the interrogation spots. Decreasing the interrogation spot whilst having high accuracy allows for small particle displacements, which when combined will result in increased spatial resolution.

2.4.2.6 Visualization Methods

Velocity vector maps are the major output of adaptive PIV analysis, which display in blue colour and the length of the arrow represents its magnitude by default. Single colour vectors of small magnitude are shown as dots and a large amount of overlap with neighbouring vectors can result in unreadable displays. Therefore, in the current research, map display options available in Dynamic Studio Software Platform (DSSP) allow both colour coding and scaling the visual appearance of the vector map. The view of any map can be controlled through the context menu in the map display options. This tool has several display options, such as the ability to colour vectors with a colour representing the length of the vector and scale. Scaling is necessary to display vectors from the selected variables. A background scalar map can be enabled and embedded in the vector map. A well-chosen colour map with embedded features therefore can be easily visualised and

analysed. In this case, a colour bar is provided to indicate the mapping of data values with axis labels. Rainbow colour coded vectors with scaling have mostly been adapted to display velocity vector maps in this study, where small magnitudes will be shown as blue small arrows and large magnitudes, shown as a large red arrow that can be displayed as illustrated in **Figure 2.19**. In this case, a colour coded bar is provided to show the data value.

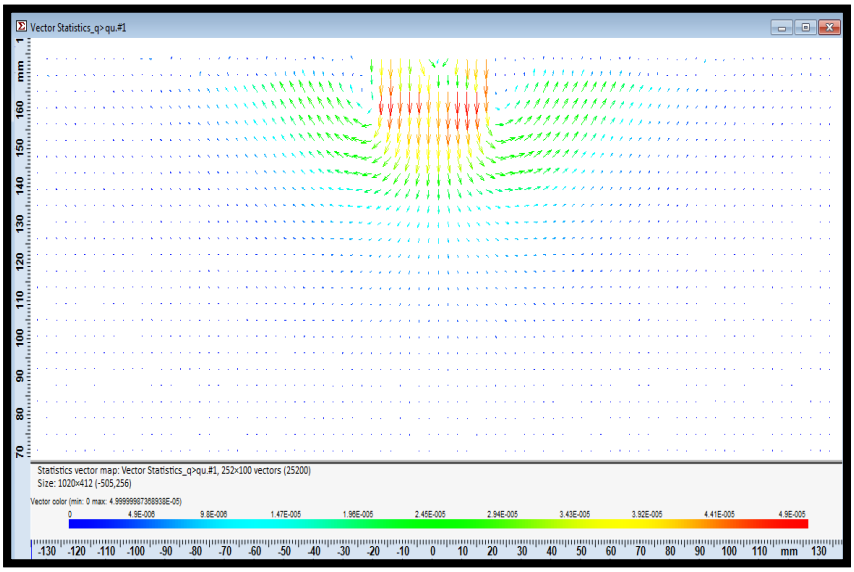

Figure 2.19 Vector plotting using both colour and scaling vectors (red is largest magnitude; blue is smallest)

2.4.3 PIV in Geotechnical Application

In this section, a review of the literature that deals with the developments of PIV in the past decades illustrates improvements in both digital image recording and numerical evaluation techniques. PIV is now applied with more confidence in many disciplines, yielding data that was not possible before. In geotechnical engineering, the use of PIV has been adapted to measure the deformation fields in soil. Deformations due to displacement and strain shear bands (etc) could be captured depending on the images from outside the soil mass (White et al., 2003). Although relatively new, PIV has recently been introduced and used to measure the dynamics of granular solids (Zhou, 2011). In this section, the application of PIV in particulate systems is briefly reviewed.

Recently, numerous researchers have aimed to study deformation, velocities, strain rate, strains in granular sand (e.g. Taib et al., 2013; Murthy et al., 2012; Liu and Iskander,

2004; White et al., 2001a), and interaction zones adjacent to the pile shaft (White and Bolton, 2004; White et al., 2001b). Others have focused on the temporal evolution or vortex rings (Willert and Gharib, 1991), bulk solid flow in silos, and flow structure evolution (Albaraki and Antony, 2014, Albaraki; 2015) using the digital particle image velocimetry (DPIV) technique. This technique uses digital recorded video images, and the analysis is conducted computationally. DPIV is the digital copy of a conventional laser speckle velocimetry (LSV) and PIV (Willert and Gharib, 1991). In these methods (LSV and PIV), photographically recorded transparency images are patched into many interrogated locations with a leaser (Adrian, 1991; Willert and Gharib, 1991). It has been demonstrated that the real advantage and strength of the digital particle image velocimetry (DPIV) is in using digital recorded video related technology to enhance images, which can be taken at real time, viewed, and then processed immediately. This helps minimise any optical errors and saves large quantities of information from the test data for post-processing analysis. The development of cameras and computers increases spatial resolution, with the use of digital DPIV. It should be noted that low speed flows need a high resolution digital video system, such as 512 by 512 pixels and greater (Willert and Gharib, 1991). Several experiments have been carried out to analysis deformation using DPIV, in which different patterns of formations were observed.

Cheng et al. (2001) adapted PIV for use in observations of the microstructure behaviour of granular soil under uniaxial compression loads, within an element test of one dimensional compression test to examine a breakage progression during compression. The plastic response of granular soil that relates to grain crushing depends mainly on both the magnitude of shear strain and the stress level. The minimum crushing stress was about 630 kPa and was consistent with the PIV measured cracks of the elastic settlement of the sand. Hence, Lambe and Whitman (1979, p.135) stated that crushing is important for stresses greater than 3.5 MPa. Therefore, in this research, the applied maximum stresses were less than 630 kPa.

White and Bolton (2004) considered the application of PIV in studying the mechanism of soil displacement and strain path under a tip of a driven pile in Dog's bay carbonate sand and Leighton Buzzard silica sand. They used a 72.8mm thick Perspex for the front window of the model box, whereas Hamm et al. (2011) used 3mm glass to sandwich their cell test. The displacement fields and strain paths were found to be relatively independent of the sand type. The macro scale result of the base resistance increases with the initial relative density. The shape of the strain path exposes a high vertical compression below

the pile tip, followed by horizontal compression as the soil element flows around the pile shoulder. The measured strain paths were similar to the analytical solutions made by the strain path method.

Liu and Iskander (2004) have used a similar technique called digital image correlation (DIC) to study the deformation and strain of dry loose sand (D_r=21%) below a rectangular strip footing subjected to a vertical downward loading. It was reported that the soil deforms under footing that is not completely symmetrical, as the soil is heterogeneity in formation. In granular materials, the load transmission occurs via inter-particle contacts in a non-homogeneous manner (Radjai et al., 1998). It also demonstrated that the maximum settlement of the footing was measured under the centre of the footing, which then decreases gradually towards the footing edge.

Hamm et al. (2011) evaluated the performance of PIV in the study of the flow field, in order to identify the shear bands of a rigid finger, who enter the granular mass vertically from the free surface. The macro scale result is similar to the California bearing ratio (CBR) test in a soil mechanics laboratory. By using PIV, the development of shear bands and its discontinuous evolution on both sides of the finger were characterised. The angles of the shear band evolve depending on the initial density of the granular medium. The vortex and maximum rate of shear strain are highly localised at the shear slip surfaces. It is well known that yielding is accompanied by dilation in the shear zones in dense sand.

Murthy et al. (2012) used similar combined techniques of PIV and PTV towards improving spatial resolutions at the micro level. They examined flow parameters such as velocity, velocity gradient and strain rate of the quasi-static indentation of a granular ensemble, by a flat punch under plane strain conditions. It was reported that the sand grains are moving and rolling. According to Radjai et al. (1998) the transmission of forces is only achieved through the inter particle contacts, which form a pattern. The contact patterns are heterogeneous, because the behaviour of granular materials is neither 100% fluid nor 100% solid when transmitting the force uniformly among the grains contact. It seems that granular materials are heterogeneous and consist of elements that are not of the same kind or nature, or the quality of being diverse and not comparable in kind. The analysis of images of the sand under the load have shown a dead zone, which is attached to the indenter face. It seems that this dead zone is similar to the wedge shaped soil zone beneath the foundation in the general and local bearing capacity surfaces, according to Terzaghi's theory of theoretical soil mechanics. High changes in velocity have been indicated to change the stress types from an active to a passive pressure, and the

interconnected faces are the slip surface. A vortex region near the corner has been produced during the penetration of the indenter to the sand, as a result of high velocity gradients.

Taib et al. (2013) studied the application of PIV using MatPIV software to measure and visualize of the deformation's pattern under different type of loadings rods, sizes and shapes of the foundation plate. They successfully pointed out that the dimension of the footing plate has a significant effect on soil displacement behaviour under centric structural loading.

Teng et al. (2017) analysed the deformation behaviour of silica and carbonate sands under a strip foundation under vertical load. Two soil deformations, failure mechanisms and load-settlement responses were observed in different sands. Their study improves our understanding of the different responses in silica sand and carbonate sands beneath a shallow footing that is subjected to uniaxial vertical load.

The use of the PIV technique to evaluate the failure mechanism and soil deformation pattern under two adjacent footings has received very little attention. Differences in load-settlement response of shallow foundations compared to two adjacent footing on sands have been reported on based on a theoretical approach (Stuart, 1962; Yadav et al., 2017), and also reported on based on numerical methodology (Griffiths et al., 2006; Kumar and Kouzer, 2008; Javid et al., 2015). Other researchers have used small-scale model tests to study the interference effects on differences in load-settlement response (Kumar and Bhoi, 2009; Lavasan and Ghazavi, 2012; Naderi et al., 2014). All these studies reveal that at close spacing, the ultimate bearing capacity, on account of soil density, increases substantially when compared to that of a single footing.

The available studies in the literature that have dealt with the effect of interference between neighbouring footings on deformation patterns remain scarce. Different soil deformation or failure mechanisms in sands may result in very different footing load-settlement response. In the current investigation, therefore, further experimental evidence for the changing deformation mechanisms at different levels of interference effects were provided, where the salient aim is to better connect the observed deformation mechanisms with the footing settlement. The current study uses DPIV, which contributes data to reduce this knowledge gap.

The use of the DPIV technique to evaluate the ultimate bearing capacity and failure mechanism modes of footing interacting with layered soil has received little attention in

the literature. Numerous researchers have investigated the ultimate bearing capacity and settlement of footing interacting with layered soil using theoretical, analytical and experimental approaches. Differences in the ultimate bearing capacity have been reported based on a theoretical approach for a sand layer overlying a clay layer (Meyerhof, 1974; Meyerhof and Hanna, 1978; Lee et al., 2013a; 2013b; Ramadan and Hussien, 2015). Other reports based on numerical methods have also been applied to two layered granular soils (Farah, 2004; Ghazavi and Eghbali, 2008) and furthermore, researchers have used small-scale model tests (Hanna, 1982). Most of the aforementioned studies have used the simplified failure mechanisms together with a reduction in the mobilized shear strength (Cohesion c and angle of internal friction ϕ) of the sand in their corresponding limit analysis and finite element method. Large discrepancies between the measured and predicted values of the ultimate bearing capacities were observed in the above studies.

Furthermore, there has been no particular attention placed on the responses of the strip footing under cyclic loading and the failure mechanism, which is known as an important parameter in the derivation of the ultimate bearing capacity equation used in designing a foundation under a cyclic load. In order to compute the ultimate bearing capacity and the settlement of a single strip footing under cyclic loading, a number of theoretical and experimental studies have been conducted (Kempfert et al., 2010; Tafreshi et al., 2011; El Sawwaf and Nazir, 2012; Asakereh et al., 2013). Therefore, very little information is available in the literature for performing an analysis of the failure mechanisms and deformation properties of foundation structures dense granular soil. In this thesis, micromechanical study of foundation structures granular soil interactions under cyclic loading have been performed to analyse the significant effects that different types of cyclic loading have on dense granular soil-foundation-structures.

2.5 Finite Element Modelling of the Sand as a Granular Material

The FEM is a robust technique for the analysis of many problems in several engineering disciplines. This method is widely used in the analysis of a wide range of linear and non-linear geotechnical problems. FEM can handle simple and complex constitutive soil models, and solve problems with complicated geometries and boundary conditions, with reasonably accurate results (Potts and Zdravkovic, 2001). A material model is a formation conducted to be representative of the actual circumstances. A mesh distortion and an entanglement of the elements that can occur in failure zones with high stress/strain

concentration (such as around footing corners) are the main drawbacks of the common FEM analysis. To overcome these difficulties, the Arbitrary Lagrangian-Eulerian (ALE) approach is a very effective alternative for simulating large deformation problems (ANSYS, 2016). In this method, in its most basic sense, the ALE method defines the mesh motion as independent of the motion of the material being analysed. Therefore, the movement of the element nodes and the material points is decoupled, which enables the constraint of the excessive mesh distortion. The greatest advantage of the ALE method is that it allows the smoothing of a distorted mesh without performing a complete re-mesh. In addition, the efficient application of the method requires experience, skills and a certain amount of trial and error, particularly when choosing an optimal time and spatial discretisation (Kardani, 2012).

2.5.1 Introduction to Finite Element Method

The finite element method is a widely used technique for the analysis of many problems in engineering disciplines. Numerous researchers over the past decades have been interested by FEM and its aspects and many publications are available in the literature. To use FEM for solving physical problems, the problem needs to be generated as a mathematical model. This can be governed by differential equations assumptions on loading, geometry, material law, and boundary conditions. Then the mathematical model is solved by a finite element analysis. The finite element solution hence will be based on the selected mathematical model with all its specific differential equations assumptions. Therefore, the choice of an appropriate mathematical model of the material has significant effects on FEM in engineering analysis.

The successful modelling of a geotechnical problem needs an appropriate soil constitutive model. Choosing an adequate material model is essential for the prediction of real soil behaviour (Schanz et al., 1999). However, currently there is no a single constitutive model that reproduces all real soil behaviour. Accordingly, choosing a soil constitutive model is a problem interest dependent based on stiffness and deformation (Potts and Zadravkovic, 2001). In geotechnical problems, the nonlinearity of the simulation may occur for numerous reasons - material nonlinearity, geometrical nonlinearity, changes in boundary conditions, and time dependency. Material nonlinearity occurs when the stress-strain relationship is not linear. Geometrical nonlinearity is showed when large deformations are affecting the analysis. In other words, the volume of body changes due to large

deformations and it cannot be considered as a constant. In some problems, the boundary conditions are not constant during the analysis, such as contact mechanics. Some dependant problems may also represent nonlinear behaviour, such as when the external forces change with time, as with a dynamic analysis and the consolidation of soils.

Traditionally, deformations and stress distributions in soil are calculated theoretically and numerically using different techniques (Cicek et al., 2014; 2018). In geomechanics, researchers have used different constitutive relations (material models) to study structure-ground interactions using FEM, such as Mohr-Coulomb (MC) and Drucker-Prager (DP) models (Díaz and Tomás, 2016; Davoudi et al., 2008). Others have used the Tresca failure mechanism, which is an elastic perfectly plastic model for clayey soil (Griffiths et al., 2006). Nainegali et al. (2013) used linearly elastic finite and infinite nonhomogeneous soil beds, with modulus of elasticity linearly varying with the depth. In FEM analyses, the accuracy of the results is more dependent on the constitutive material models used, which can replicate an expected behaviour that the soil would produce.

2.5.2 Constitutive Material Models

The structure of soil is complex and diverges across the whole soil medium. This presents a challenge in understanding and studying the behaviour of the soil medium. The reliability of the numerical results depends significantly on the suitability of the constitutive model for the soil materials and proper modelling of the foundation structures-soil interactions. Thus, various models have been proposed to model sand, such as the linear isotropic elastic material model, ISO, MC and DP. Mathematical models of granular materials, known as constitutive models, are the mathematical representation of a material's response to an applied load. The key control of FEM analysis of granular material is to select the material model, which can accurately capture the material's mechanical behaviour. It seems likely that the plasticity constitutive models in ANSYS are applicable in both small and large deformation analyses (ANSYS, 2016).

For small deformation, the formulation uses engineering stress and strain, while for large deformation; the constitutive models are formulated with the Cauchy stress and logarithmic strain. The loading conditions in geomechanics often cause large deformations of the soil mass, which has to be considered in the choice of the appropriate calculation tool. Likitlersuang et al. (2013) characterised three regions where the shear stiffness (G) is different. These are a very small strain level, where the stiffness is constant

with a linear stress-strain relationship and a small strain level, where the stiffness modulus varies non-linearly with the strain and the large strain level, where the soil is close to failure and the soil stiffness is relatively small, as illustrated in **Figure 2.20**.

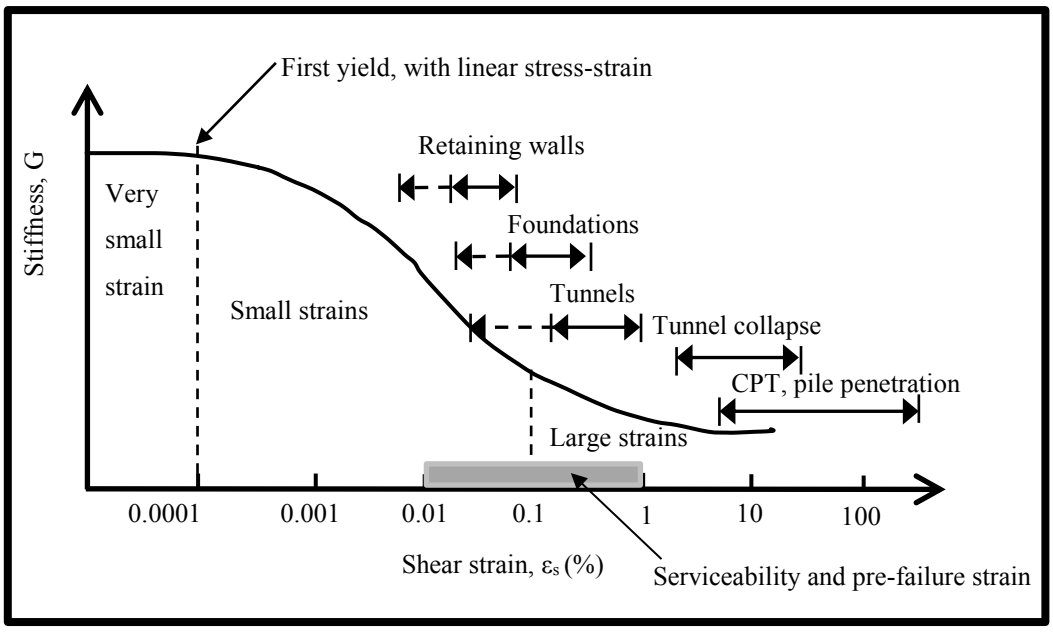

Figure 2.20 Typical strain ranges experienced in geotechnical engineering (Likitlersuang et al., 2013)

The characteristics of soil stiffness across three distinct regions show the structure strain range and measurements as highlighted in **Figure 2.20**. Generally, soil behaves significantly different in loading, unloading and reloading. However, a validation approach to the analytical abilities of the model used in a given condition is a comparison of the output of the model, where real structures are measured values under similar conditions (Potts and Zadravkovic, 2001).

2.5.2.1 Isotropic Linear Model (ISO)

The linear model (ISO) response is the basic material model that the stresses are directly proportional to the strains given by the generalised form of Hooke's law. Elastic models could be linear or nonlinear, as illustrated in **Figure 2.21**. In terms of the principal stresses and strains in axial symmetry condition where the intermediate and minor principal stresses are equal, the equations can be written as given by **Equations** (2.16) and (2.17).

$$\delta\varepsilon_s = \left(\frac{1}{3\mathrm{G}}\right)\delta q \tag{2.16}$$

$$\delta\varepsilon_v = \left(\frac{1}{\mathrm{K}}\right)\delta p' \tag{2.17}$$

Where

$\delta\varepsilon_s$ = Increment of shear strain (mm/mm),

$\delta\varepsilon_v$ = Increment of volumetric strain (mm/mm),

$\delta p'$ = Increment in mean stress (kPa),

δq = Increment of deviator stress (kPa),

K = (1/3) E / (1-2v) = the Bulk modulus (MPa),

G = (1/2) E / (1+v) = the shear modulus (MPa), and

ν = Poisson's ratio.

Under static loading conditions, true elasticity in the soil behaviour is unlikely to occur, unlike under dynamic loading conditions, which can be observed, especially in cohesive soil (Efretuei, 2013). However, calculations from elastic soil models with cautiously selected elastic parameters may be used in the prediction of soil behaviour with a reasonable degree of accuracy (Powrie, 2014). Therefore, a linear isotropic elastic material (ISO) was used to simulate the sand in the box test model, which allows comparisons with the theoretical response (Jha and Kumar, 2015). As this is an elastic model, there is no plastic strain produced by the loading. The input parameters are unit weight of the soil (γ), modulus of elasticity (E) and Poisson's ratio (v) in the model. These isotropic elasticity parameters will be used in other models as well. Sands only display linear-elastic properties in the early stages of loading, where only a small strain is generated. Consequently, the linear elastic analysis does not build up failure and idealizes the stress-strain relationship linearly.

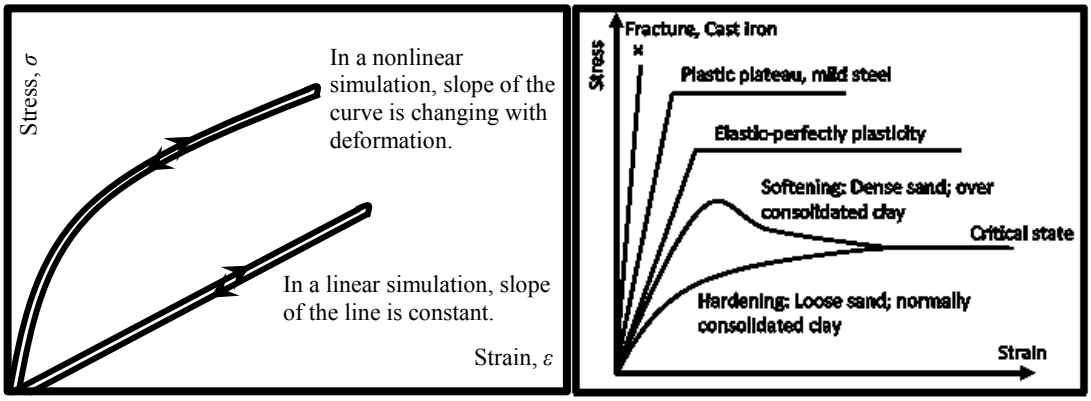

Figure 2.21 Typical elastic stress-strain relationship (Lee, 2015)

2.5.2.2 Mohr-Coulomb Model (MC)

The Mohr-Coulomb (MC) nonlinear model is contained in geomechanical materials and linear Hooke's law cannot be used (ANSYS, 2016). The MC theory is a mathematical model for a failure theory. MC soil starts to deform plastically when the shear stress exceeds the internal friction resistance between the material inter-particles. The model defines yielding as when the combination of pressure and shear stress reaches the cohesion of the soil particles. The MC model yield criterion form, as in **Equation** (2.18):

$$\tau = c + \sigma \, tan \, \phi \tag{2.18}$$

Where

τ = Shear stress (kPa),

c, ϕ = Cohesion (kPa) and angle of internal friction of the soil (degree), and

σ = Mean normal stress (kPa).

Cohesion (c) is independent of the inner friction angle. Cohesion is the shear stress that causes yielding when the mean normal stress is zero and the friction angle defines the increase in the yield condition as the mean stress increases, according to **Figure 2.22**. The MC model assumes elastic rigid-plastic behaviour of the soil, wherein the strength parameters of soil c and ϕ remain constant during the analysis (Díaz and Tomás, 2016). The MC yield function is not a smooth surface in 3D space but has corners (sharp hexagonally shaped yield surface around the hydrostatic pressure axis) that may cause singularities and numerical difficulties along each edge in the application of this model into the finite element method, as illustrated in **Figure 2.22**. The MC yield surface can be

defined in terms of three limit functions that plot as a non-uniform hexagonal cone in the principal stress space (σ_1, σ_2, and σ_3 = major, intermediate minor principal stresses, respectively) as shown in **Figure 2.22b**.

Mohr-Coulomb model (MC) in ANSYS platform involves five input parameters. *E* and *v* are used for soil elasticity, where the following strength parameters of the soil are used to define the yield surface for soil plasticity, measured using the triaxial compression test: peak angle of friction (ϕ_{peak}), cohesion (*c*), dilatancy angle (ψ), residual friction angle (ϕ_{cr}) and residual cohesion c_{cr}= 0.8*c* (ANSYS, 2016; Diaz and Tomàs, 2016). Dilatancy angle is the parameter that represents the effects of both the stress state and the soil relative density, which causes increases in volume during the loading (Cinicioglu et al., 2014). Materials such as loose sand, where the particles can easily move past one another, have relatively low friction angles. Soils that undergo plastic strains vary in dilatancy, and also experience a small strain at low load and at stress reverse. These general behaviours are involved in the simple elastic-perfectly plastic Mohr-Coulomb model, though it does offer advantages (Ti et al., 2009). MC is mostly appropriate in modelling an approximate and general behaviour of a soil under loading.

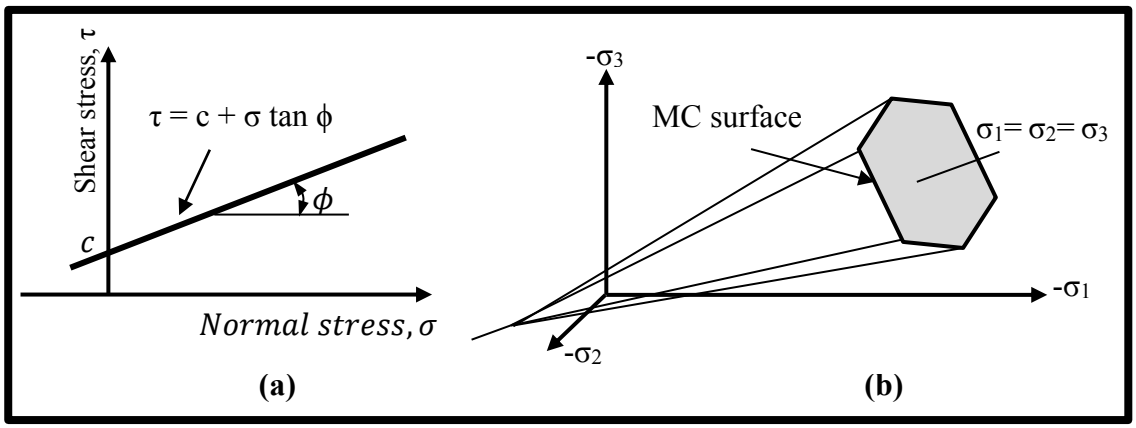

Figure 2.22 (a) MC yield surface (b) MC yield surfaces in 3D space of principal stresses (deviatoric) six-face yield surface (ANSYS 2016)

2.5.2.3 Drucker-Prager Model (DP)

Soils exhibit some elastic and/or plastic properties at different levels of loading. The DP yield surface has a smooth and cylindrical cone surface in the principal stress 3D space around the hydrostatic axis, which is much more suitable, as illustrated in **Figure 2.23**. The DP and MC yield surfaces do not change with progressive yielding, as the

material is elastic-perfectly plastic and lacks hardening. Hence, an Extended Drucker-Prager (EDP) yield surface with hardening can be changed with progressive yielding, when combined with the multi-isotropic hardening plasticity material, using MISO (ANSYS, 2016). The EDP model is an isotropic elastic perfect-plastic continuum model with either an associated or non-associated flow rule (Davoudi et al., 2008; Armin et al., 2014; Ahmed, 2014).

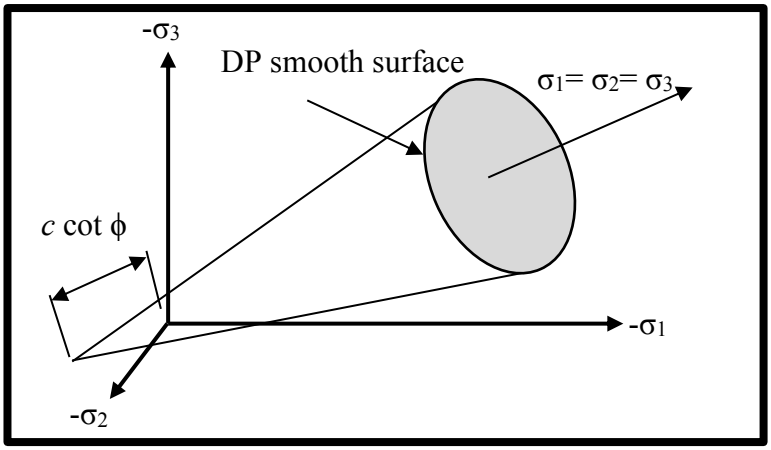

Figure 2.23 Drucker-Prager yield surfaces in 3D space (ANSYS, 2016)

The EDP material model comprises three yield criteria and corresponding flow potentials in ANSYS17.2. These offer different yield surfaces in the meridional plane (i.e. *p'–q* plane): a linear, hyperbolic and general exponent form (ANSYS, 2016). The linear form model was selected for this simulation that intended primarily for applications where the stresses are for the most part compressive. The EDP linear yield criterion form *F* is:

$$F = q + \alpha p' - \sigma_y(\varepsilon_{pl}) = 0 \tag{2.19}$$

Where

q = The deviatoric Cauchy stress tensor (kPa)= $[\frac{3}{2}\{s\}^T[M]\{s\}]^{0.5}$,

α = Material parameter referred to as pressure sensitive parameter and calculated using ϕ,

$\{s\}$ = Deviatoric stress (kPa),

p' = Mean effective stress (kPa)= $\frac{1}{3}(\sigma_1' + \sigma_2' + \sigma_3')$,

σ_y = Yield stress of material (kPa) which input as σ_y calculated using c, ϕ or can be fed as multi-yield via MISO, and

ε_{pl} = Plastic strain in DP model (mm/mm).

This model allows for the evolution of the strength parameters cohesion (c) and angle of internal friction (ϕ) as a function of the equivalent deviatoric plastic strain. The flow rule is associative if the $\psi = \phi$, and there is increase in material volume when yielding. The flow rule is non-associated if $\psi = 0$ or $\psi < \phi$. For sand, the linear model is normally used with non-associated flow, where the dilation angle is smaller than the friction angle. The linear plastic flow potential Q function in ANSYS is defined as:

$$Q = q + \alpha_1 p' - \sigma_y(\epsilon_{pl}) = 0 \tag{2.20}$$

Where

α_1 = The flow potential referred to the dilation angle (degree).

q, $\sigma_y(\epsilon_{pl})$ and p' have been defined previously. In this study, the parameters for the DP model were taken from the experimental results. Three particular parameters were used for the EDP model in ANSYS in order to simulate the material plastic behaviour: cohesion (c), angle of internal friction (ϕ) and dilation angle (ψ). As no cohesion exists in granular materials, c was set to 1 kPa to avoid simulation difficulties. It is worth mentioning that the elastic and plastic properties are combined in soil models that are considered suitable in modelling the appropriate soil characteristics.

2.5.2.4 Multilinear Isotropic Hardening Model (MISO)

The multilinear isotropic hardening (MISO) model for the soil describes the nonlinear plasticity behaviour, which is a multilinear stress versus plastic strain curve, and depends on the user-defined experimental results being implemented in the current ANSYS simulations. The multilinear hardening behaviour is described by a piece-wise linear stress-total strain curve, starting at the origin and defined by sets of positive stress and strain values, as illustrated in **Figure 2.24**. The first stress-strain point corresponds to the yield stress. Subsequent points define the elastic plastic response of the material. To achieve this, the experimentally characterised bulk stress-strain relationship corresponding to the load-displacement curves of different packing densities presented in **Figure 2.24** were discretised into a large number of linear segments (<1000) and fed as

user-defined digital input (Mulungye et al., 2007; Mohsenimanesh et al., 2009; Gordan et al., 2014). Furthermore, the experimentally characterised sand properties were used i.e., the dry density (γ), modulus of elasticity (E), cohesion (c), angle of internal friction (ϕ) and dilation angle (ψ).

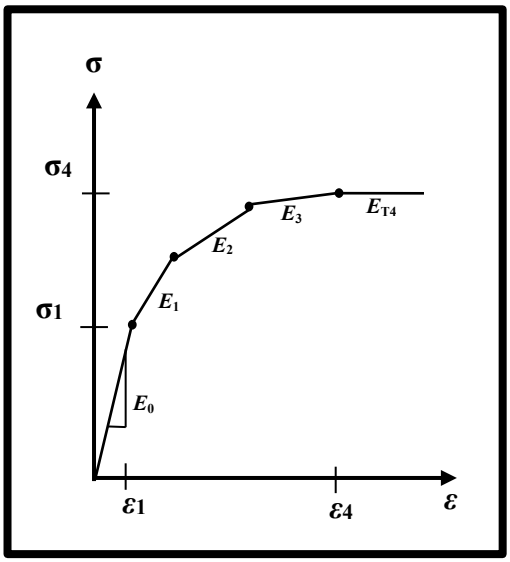

Figure 2.24 Uniaxial stress-strain curve for MISO (ANSYS, 2016)

2.6 Scale Effects and Limitations of the Current Experiments

It is acknowledged that the scale effects of the footing model could affect the estimations of their strength characteristics (Das, 2009). Though the small-scale models are widely used to investigate the behaviour of the full-scale foundation, there could be some differences between the results of the experiments using laboratory models and the prototype (Vesic, 1973). The bearing capacity factor due to unit weight of the soil (N_γ) is only dependent on the angle of internal friction of the soil (Terzaghi, 1943), and therefore the bearing capacity increases linearly with the width of the footing. In addition, it should be noted that the experimental results were obtained for only one size of the width of the footing. Though, the settlement of footings could depend on their width for a given soil (Das, 2011), the ultimate bearing capacity of sand is less dependent on the width of footing (B) when B is less than 1 m as reported by Terzaghi and Peck (1967). It means that the scale effects are minimised beyond certain sizes of the footing. Even though that

scaling effects cannot be ignored in small-scale test and the test results are of limited use in predicting the behaviour of a particular prototype, by minimising the side effects.

To minimize the scaling effect, it was suggested that the packing density of the tested sample should not pertain too close to its maximum void ratio (e_{max}) and minimum void ratio (e_{min}) (Altaee and Fellenius, 1994). These suggestions were accounted for in the current study to minimise the scale effects. However, the absolute value of maximum vertical displacement in sand (S_v) increases for an increase in the width of the footing (Bjerrum and Eggestad, 1963; Terzaghi et al., 1996). The footing with the largest width produces the smallest (S_v) under the same relative loading level in agreement with some other conventional studies (Lutenegger and DeGroot, 1995; Ismael and Ahmad, 1990). It is recognised that the scale effects of the footing model could influence the estimations of their strength characteristics as it is related to the critical state line (Cerato and Lutenegger, 2007). Cerato and Lutenegger (2007) have stated that the void ratio (e) and stress level to the critical state line affect the footing behaviour. For example, a footing with relatively small width would require a relatively low stress level, and hence, it is distant away from the critical state line, as if it was on a denser "state" soil. However, it can be seen that large discrepancies between the measured and the theoretical values were observed in the literature. Therefore, further studies are required to examine this approach for wider strip footing widths. Also, centrifuge tests are commonly conducted to simulate the full scale stress field. However, this approach is not an option given in the available laboratory facilities. Sands in the FEM are less accuracy than clay, which is not surprising considering that N_γ problem is much than N_c problem. There is an extreme concentration of deformation at corner at edge of the footing, and thus the corner leads to a singularity. Note that the value of q_{ult} reported here is helpful in quantifying the influence of packing density, and there is no intention to directly relate these experimental results to the field tests.

2.7 Summary

The literature review provides background information on strip footing-granular soil interactions, both single and multiple footings, under the quasi-static and cyclic loading conditions. The foundation system, the problems that exist in design of footing system to elaborate both ultimate bearing capacity and allowable settlement are defined. The ultimate bearing capacity refers to the ability of the soil to sustain the maximum load on

the footing before the soil collapses. Experimental and/or theoretical analyses are used to determine the ultimate bearing capacity. However, settlement often controls the design for larger foundation widths (Das, 1999). In many cases, sand settlement controls the design of footing (Bowles, 1996). Layered soil profiles could be found under footing structure, but footing cannot be designed anymore using conventional Terzaghi theory. Therefore, the available approaches for determining the ultimate applied surface load (q_{ult}) depends on individual such as cohesion (c), angle of internal friction (ϕ) of each layers, thickness of the top layer (H), The width of footing (B), the shape of the footing, the depth of footing embedment (D_f) and H/B. In the city of Najaf and Karbala, granular soil (sand) usually is found along the west of the city. Granular thickness can reach 15 m in thickness. Due to the increase demanding to construction projects especially houses, the majority of future planned construction developments projects are located on these sand soils.

The principle to PIV was then introduced starting with a description of the optical measuring technique such as PIV that is developed recently to precisely measure deformation at high level of accuracy. The limitations and potential sources of errors of the PIV experiments were discussed in the validation and adaptivity sections. In summary, the new adaptive image processing methodology adaptive PIV can be considered truly adaptive. Correlation window sizes are locally optimised in an automated, recursive structure, to yield reliable velocity estimates with the highest resolution while minimising user dependent input. A literature review was also given in this chapter. The DPIV-based experiment can measure not only the large displacement close to the footing base, but also the very small displacement in the far field.

Finally, finite element modelling of sandy soil was discussed. Modelling of geotechnical problem successfully needs an appropriate soil constitutive model. Choosing an adequate material model is essential for the prediction of the real soil behaviour (Schanz et al., 1999). Numerous researchers over the past decades have interested by FEM and its aspects and many publications are available in the literature. Research on the ultimate bearing capacity (The ultimate bearing capacity refers to the ability of the soil to sustain the maximum load on the footing before the soil collapses) and settlement problems can be conducted using either analytical solutions or experimental investigations. The former could be considered through theory of plasticity or finite element analysis, while the latter is carried out through conducting prototype, model and full-scale tests. An adequate

solution is established only when theoretical results agree with those achieved experimentally.

The research focus on understanding the local and global geomechanical properties of key structure-soil interaction problems under quasi-static and cyclic loading condition, using DPIV and FEM simulations coherently. The methodologies complement each often used in the investigations. Experimentally based user-defined constitutive relations got from the footing compression test during the run of DPIV experiment are applied in the FEM analysis. The localised subsoil deformations from FEM are validated experimentally using DPIV outputs. The results from the DPIV cannot provide stress measurements, therefore by validated the suitability of using the user-defined constitutive relations got from simulate the footing compression test in FEM helps to overcome this by validated the FEM with DPIV measurement of displacement. Then, this could be applied in the real geotechnical site by doing plate load test (PLT) on the surface of the soil and thus fed the stress-strain curve of PLT test to the FEM simulation as MISO to get more information from the outputs of the FEM regarding for example stress and strain along any section horizontal and vertical subsoil.

Chapter 3 Experimental Characterisations of Sand and Setup of Footing-Sand Interactions

3.1 General

This chapter includes the materials used in this research, their properties and steps followed in the preparation of the specimens. It also includes the procedures of the tests in addition to the testing program. The test program includes footing compression experiments on homogeneous sand bed. The sand packings are prepared in different relative densities such as loose, medium-dense and dense. Hence, before probing the displacement features of the sand bed in detail (presented in the next Chapters), it was made sure that the macroscopic characteristics of the samples are consistent and robust.

3.2 Material Characterisations

It is important to distinguish between the grain and the bulk properties, whether referring to a physical or mechanical property. Prior to the footing compression experiments, both the particle (local/micro) and bulk (macro) sand samples were quantitatively characterised. The physical tests were performed using laboratory tests on the characterisation of the sand included a particle size distribution, minimum dry density properties, maximum dry density, direct shear test and triaxial compression tests.

3.2.1 Soil

Three types of distributed samples were selected as preliminary samples. The first sample is disturbed dry sand sample (Kiln dry sand) obtained in the UK. The other two sand samples (Sand 1 and 2) are disturbed dry samples obtained in Kerbala-Iraq. The sand properties were measured according to the American Society for Testing and Materials (ASTM, 1989; Head, 2006). However, the Iraqi sand 1 compares well using particle size distribution with the UK sand; therefore, the UK sand that similar to the Iraqi sand was adopted. Three different relative densities loose (L), medium-dense (M) and dense (D) packings were used.

3.2.2 Particle Size Distribution (PSD) Analysis

Particle size distribution also is called sieve analysis test is a commonly used test in civil engineering to assess the particle size distribution (gradation) of the soil such as clay, silt, sand, gravel and boulder. The physical (mechanical) and the chemical weathering processes of the rock masses decay into granular particles, ranging from boulders, gravels, sands and silts; whereas into clays, as a result of the chemical action that produces a new mineral other than the original rock. The PSD test is based upon dividing into discrete classes of particle size. It can be determined by sieving and hydrometer test (sedimentation process). For soils with more than 10% of fines (particle size less than 0.075 mm) can be analysed by a combination of both the sieving and the hydrometer test, whereas for soils with less than 10% of fines, the distribution of the particle sizes in soils is determined only by sieving. In PSD, the soil sample was shaken through a stack of sieves that have progressively smaller openings (Das, 2016). The PSD curve is often of critical importance to the way the material performs in use.

Grain size distribution was carried out on the sand used in this research according to the American Society for Testing and Materials (ASTM standard D421-2002). Particle size distribution of the sand sample was obtained using sieving analysis method. Around 1 kg of the prepared dry sand were sieved using series of standard sieves ranging in sieve opening from 9.5 mm to 0.063 mm. The sieve sets used are 9.5, 4, 2, 1, 0.5, 0.25, 0.125 and 0.063 mm. The test was conducted using a sieve shaker (Haver and Boecker EML 200 Digital plus T) for 5 minutes using 10 mm horizontal intervals and 0.3 mm amplitude. The fractions retained on each sieve have weighted and the percentages retained were obtained as shown in **Figure 3.1**. This procedure was repeated three times.

The grain size distribution was performed on the two Iraqi sands 1 and 2 and compared to one UK sand. Both groups of sand are classified as a poorly graded sand (SP) according to the Unified Soil Classification System (USCS) (ASTM standard D2487). **Figure 3.1b** shows the PSD curve for the UK sand that will be used in this study.

The definition of particle shape in terms of roundness and sphericity is widely accepted. Roundness (R) is defined as the ratio of the average radius of the corners of a particle image to the maximum radius of the inscribed circle (Wadell, 1932). Sphericity (S_{sph}) is defined as the ratio of particle width (L_2~ sieve size that the particle retained on) to particle length (L_1). Sphericity is used to describe the overall form of the particle

irrespective of the sharpness of edges and corners as shown in **Figure 3.2** (Krumbein and Sloss, 1951; Hryciw et al., 2016).

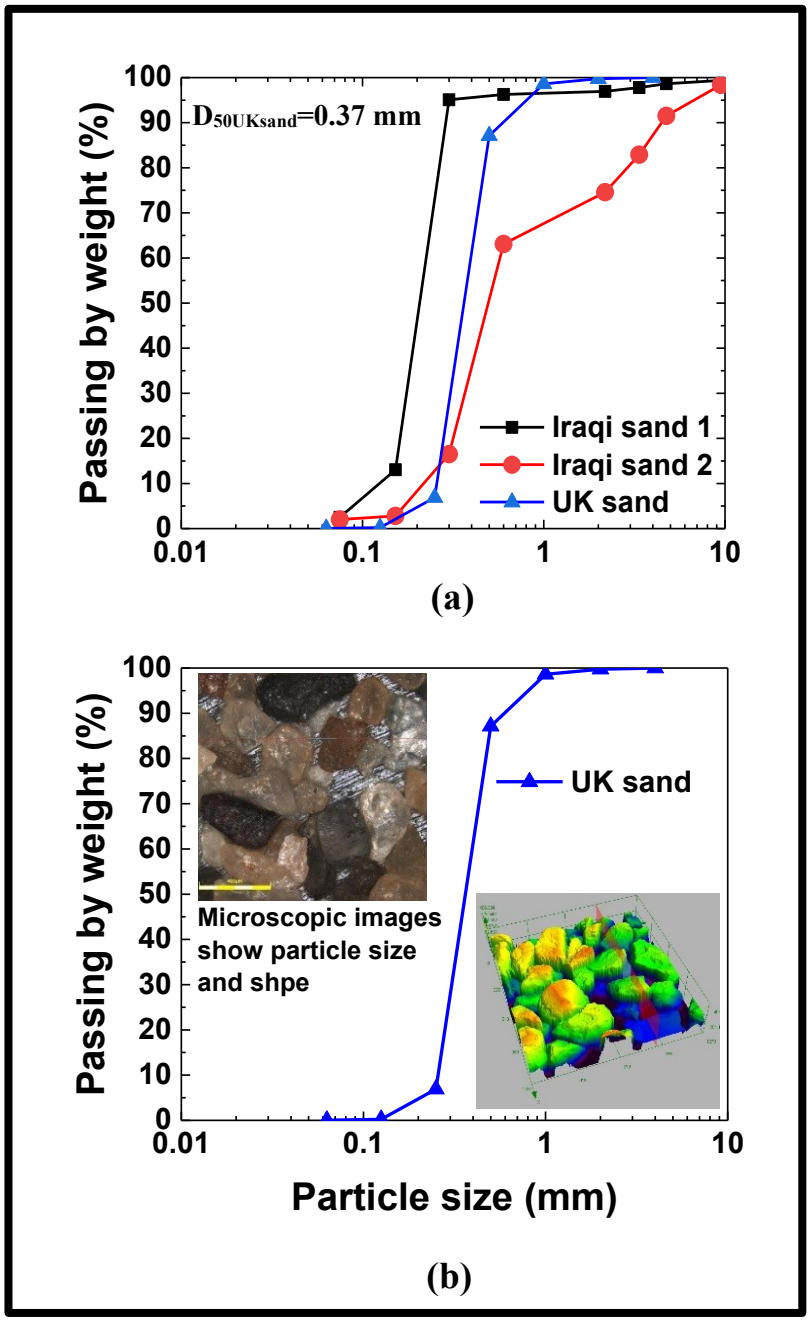

Figure 3.1 (a) Particle size distribution curve of the sands (b) particle size distribution curve of the selected sand for this research (fine to medium-grained) using sieve analysis and high magnificent image

A 3D Microscopy (Olympus machine) have used to get 3D surface imaging and micro-profile measurement with Laser confocal techniques (White et al., 2003). For this, digital microscopy images of the grain samples were used as shown in **Figure 3.1** and **Figure**

3.2. The roundness of the grain was mostly spherical to sub-prismoidal (R=0.3-0.5) and the angularity of the grains are characterised as angular and sub-angular. Their material properties and size distribution are summarised and tabulated in **Table 3.1** at the end of **Section 3.2**.

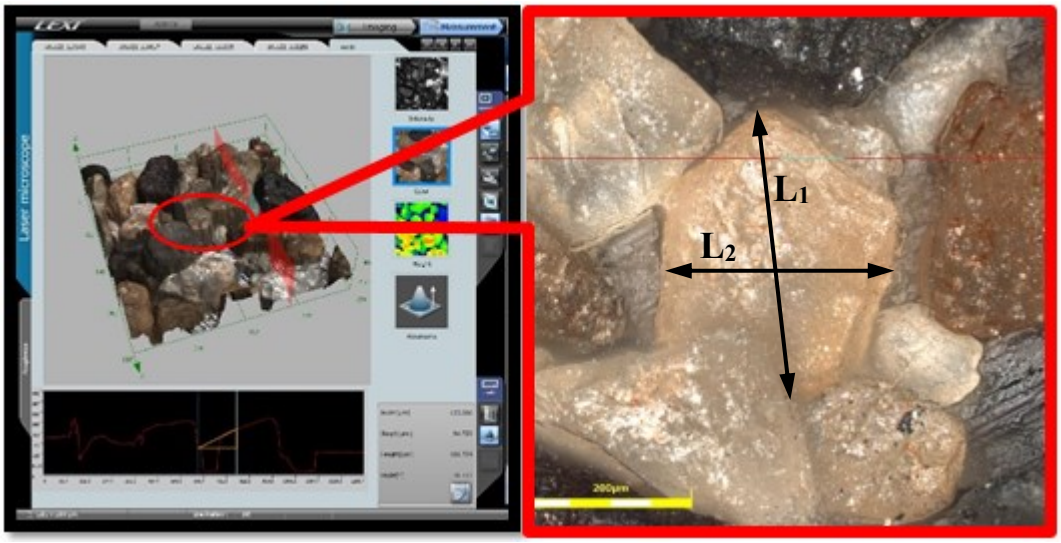

Figure 3.2 3D Microscopy Olympus platform with zoomed image of UK sand

3.2.3 Minimum Index Density (MID)

This test is used to determine the value of minimum index density for clean sand and free draining soils in which 100 % passing a 9.5 mm (3/8-inch) sieve. However, less 10% by dry mass of soil particles retained on a No. 10 (2.00 mm) sieve. This test is used to measure the void ratio of the soil in its loosest state (e_{max}). A representative specimen of soil was selected; the specimen should have a mass of ~1.5 kg. This test was carried out according to ASTM D 4254 method C. This is done in a measuring cylinder (2000 cm^3) in which 1000 g of sand shaking by inverting it a few times (5 times), to loosen thoroughly the sand. Then the sand was allowed to rest. The procedure was repeated 10 times until three consistent values of the minimum dry density are obtained. Finally, the density was then taken as the mass of the tested dry sand (M_s) to highest volume reading of the tested dry sand (V cm^3) and measuring the minimum dry density $\gamma_{d\ min.}$ as:

$$\gamma_{d\ min.} = \frac{M_s}{V} \tag{3.1}$$

Then the maximum void ratio ($e_{max.}$) is calculated as:

$$e_{max.} = \frac{G_S \gamma_w}{\gamma_{d\ min.}} - 1 \quad (3.2)$$

Where

G_s = Specific gravity of the solids = 2.65 (Das, 2016),

γ_w = Density of water at 20°C (1.0 g/cm^3).

Void ratio (*e*) is the ratio of the volume of voids in the soil to the volume of soils in a given volume of materials (Bowles, 1996).

3.2.4 Maximum Dry Density (MDD)

Standard Proctor test was used to calculate the maximum dry density of the sand of size that is smaller than 20 mm according to the standard Proctor test, ASTM D 698. In this test, a 2.49 kg rammer with a 305 mm drop and a mould (940 cm^3) were used as illustrated in **Figure 3.3**. The soil compacted into the 101.6 mm diameter mould in three layers applying 25 blows per each layer.

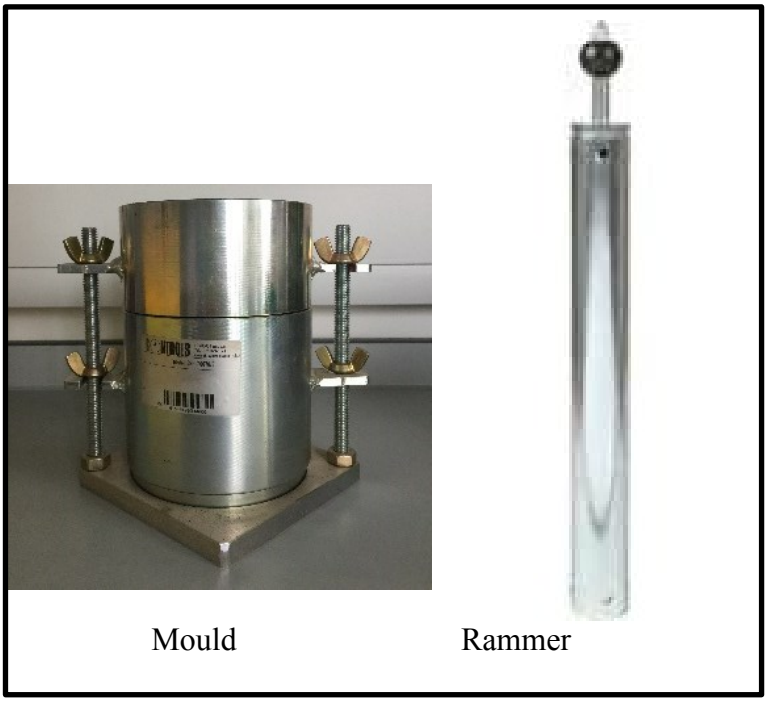

Figure 3.3 Standard proctor test apparatus

A bulk density is defined as the mass of grains divided by the total volume they occupy, which considers the total solid space as well as pore space (usually air). The wet density (γ_{wet}), dry density (γ_d) and water content (w_c) are calculated for each test trail as:

$$\gamma_{wet} = \frac{W_{(soil+water)}}{V_{mould}} \tag{3.3}$$

$$\gamma_d = \frac{\gamma_{wet}}{1+w_c} \tag{3.4}$$

Where

W = Weight of compacted soil (kg),

V_{mould} = Volume of compaction mould (mm^3),

γ_d = Dry density (kN/m^3), and

w_c = Water content= weight of water/weight of solid.

This test was repeated at least five times until a peak point appears in the drawing curve between the moisture content and the dry density as shown in **Figure 3.4**.

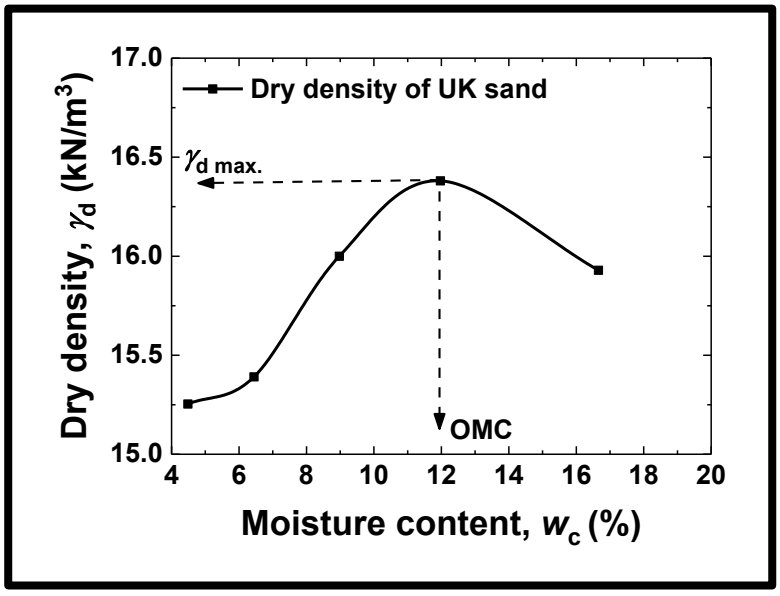

Figure 3.4 Compaction test: dry density-moisture content curve for UK sand

The test is average of three attempts with ± 5%. The peak point of this curve is the maximum dry density (MDD) and the corresponding optimum moisture content (OMC). These results are 16.5 kN/m^3 and 15 % for MDD and OMC respectively.

3.2.5 Static Angle of Repose (AoR)

Angle of repose (AoR) is the angle of friction of the sand in its loosest state. This has been applied in many areas of science and engineering, such as sediment transport and chemical engineering. To confirm this, angle of repose of the sand was measured as per ASTM C1444 (ASTM, 1998). In this method, the dry sand was carefully poured through a glass funnel filled with its tip held at a specific height (3 cm) to form a sand apex until the funnel is in contact with the inverted conical pile. This method was used for measuring the angle of repose of sands (Vangla and latha, 2015). After the heap was made, high definition images were captured, and the average angle of repose was estimated. The mean diameter of the base for the sand cone was measured in mm and the tangent for the angle of repose in degree is given as:

$$\tan(AoR) = \frac{Height}{0.5\ base} \tag{3.5}$$

The average value of five readings of the slope of the heap for different directions is (34°) identical to the residual (critical) friction angle (ϕ_{cr}) and the results is shown in **Table 3.1**.

3.2.6 Direct Shear Test (DST)

The shear strength properties of the soil can be conveniently measured by direct shear test (DST). The DST has been widely used to determine the bulk material strength properties such as cohesion (c) and the angle of internal friction (ϕ) of the soil required for the design of geotechnical structures. These parameters c and ϕ are usually measured by DST. The DST for each sand packing was performed on three specimens from the same sand and the same initial condition by varying the normal load.

A compacted sample was placed in a shear box in three layers of equal height. The sand samples were contained in the shear box split at mid height. The packing density of the sand specimens was maintained as 24%, 53% and 72% ± 3. All specimens were prepared with a size of (60 × 60 × 40) mm as illustrated in **Figure 3.5**. This has two halves (top and bottom). Weight of the sand required for each specimen was calculated. Then the sand poured into the shear box was compacted to the top level of the of the shear box, as illustrated in **Figure 3.5**. The compaction was carried out by placing a metal of plan area of 25 mm × 25 mm and 100 mm height on the sand surface on which light hammer blows were applied. A uniform specimen prepared by gradually increasing number of blows

from bottom layer to top layer. A normal confining stress (σ_n) was applied vertically to the specimen through the upper load pad (**Figure 3.5**) by a lever arm mechanism and the upper half is pushed laterally until the sample fails along a predefined spilt surface. The tested sample in the split box was sheared laterally by moving the top half of the box relative to the bottom half under constant normal load that applied first to the specimen. The normal (σ) and shear stresses (τ) at failure were measured from the applied force divided by the area of the failure plane in the soil that is the cross-sectional area of the shear box. A series of shear tests were carried out using the direct shear apparatus (**Figure 3.5**) according to the procedure was proposed by ASTM D3080. A calibrated proving ring of (2 kN) capacity (proving ring constant=2.1 N/division) and (0.01) gauges for horizontal and vertical deformation were used. The rate of strain was (1 mm/min).

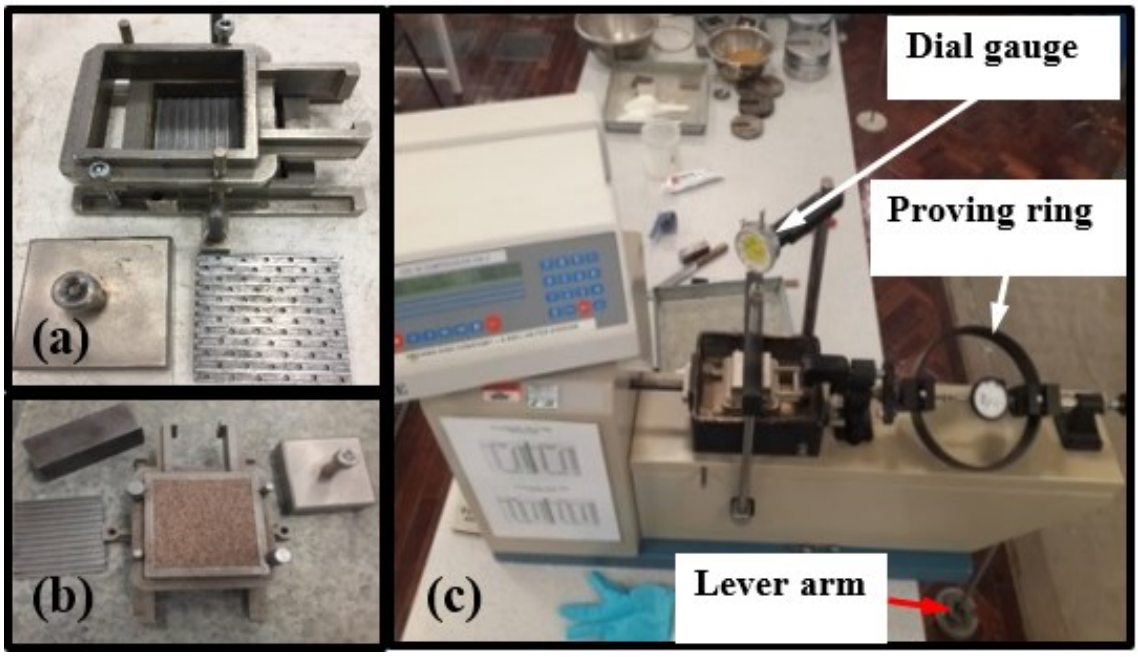

Figure 3.5 (a) DST box setup (b) specimen (c) test device image

The tests were performed on three specimens from same sand and same initial condition, at three normal stresses (σ_n) of 42 kPa, 84 kPa and 104 kPa for loose sand (**Figure 3.6 a and b**) and 51 kPa, 102 kPa and 204 kPa for medium-dense and dense sand respectively (**Figure 3.6 d and f**). The shear load (τ) and the strain for both horizontal and vertical induced are recorded at frequent intervals up to greater than 10 % shear displacement (6 mm) to plot the graph of stress–strain for each specimen. As the sand was forced to fail along the predefined plane, the vertical load and the shear load divided by the cross-

sectional area of the sample (60 mm × 60 mm) are the normal stress (σ) and the shear stresses (τ) respectively. As the sand was tested dry, therefore; the effective stress equals the total stress.

It is well known that the failure of the sand bed can usually be adequately described by the Mohr-Coulomb failure (failure envelope) criterion as (Das, 2016):

$$\tau = c + \sigma \tan \phi \tag{3.6}$$

Where τ, c, σ, and ϕ are previously defined. Hence, Mohr-Coulomb (MC) envelope should go through the origin and therefore $c \sim 0$ and ϕ depends on the soil density, particle shape and size, confining pressure etc. (Atkinson, 2007).

Furthermore, corresponding volume change (ΔV) responses are presented in **Figure 3.6**. This shows DST results for loose (**Figure 3.6 a-b**), medium-dense (**Figure 3.6 c-d**) and dense sand (**Figure 3.6 e-f**) where the shear stress versus the horizontal shear strain on a right-hand side (RHS) and the vertical strain versus the horizontal shear strain on a left-hand side (LHS). Because of the different relative densities employed herein, both loose and medium-dense sand exhibited a volume decrease and dilatant behaviour, as illustrated in **Figure 3.6**, but not in dense sand, which displays dilatant behaviour during shear. **Figure 3.6** shows that the stress–strain responses of the sand prior to the peak are not the same for all three sands, irrespective of the large variations in their relative density.

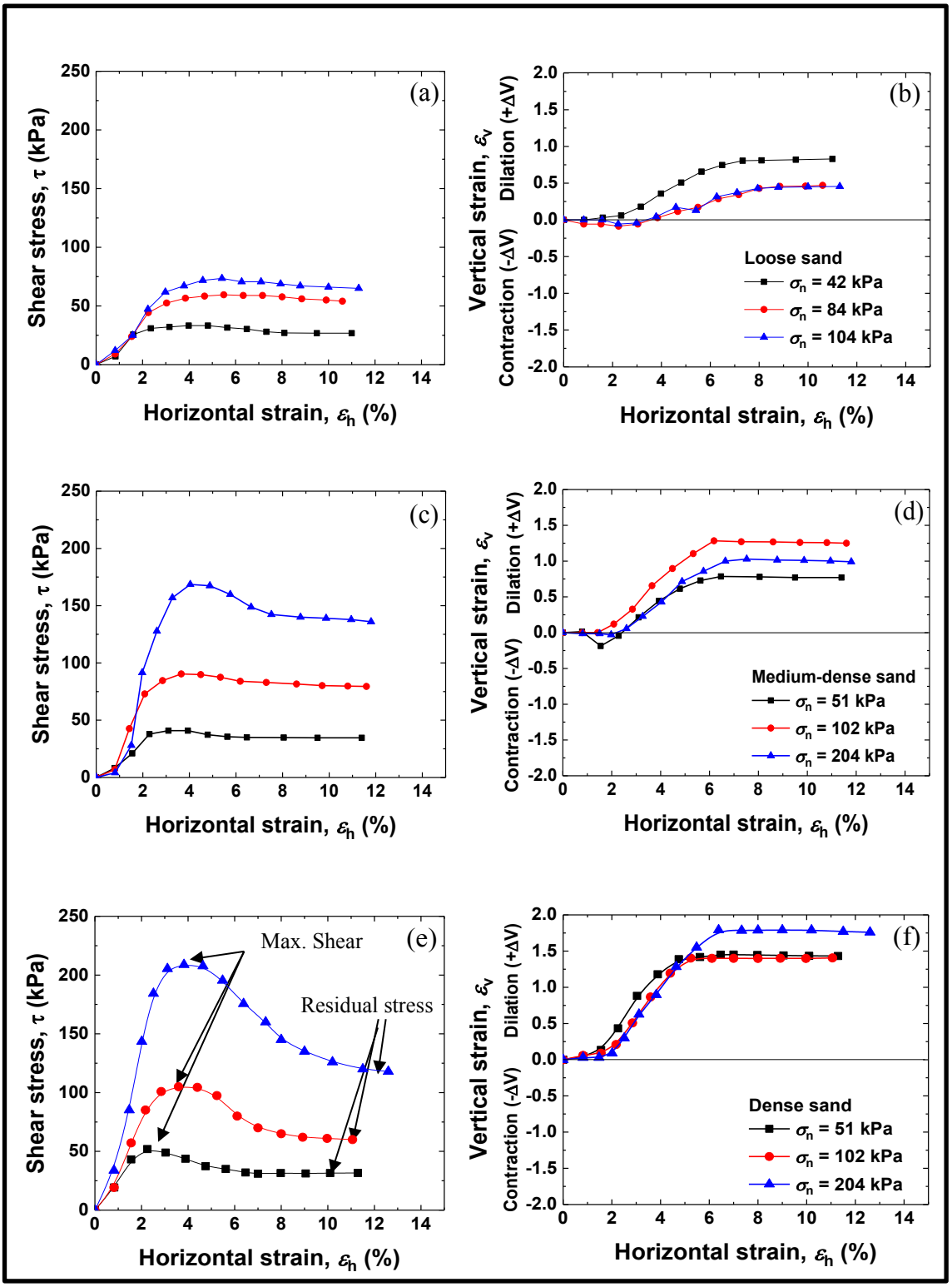

Figure 3.6 DST results for loose, medium-dense and dense sand (left) shear stress versus horizontal shear strain (right) vertical strain versus horizontal shear strain. (a-b) loose sand (c-d) medium-dense sand and (e-f) dense sand

The results of the tests on each specimen are plotted on a graph with the peak shear stress on the y-axis and the normal confining stress on the x-axis, as shown in **Figure 3.7**. In

Figure 3.7, the maximum shear stresses (**Figure 3.6 e**) versus the normal stresses were presented with linear fit regression, as it was the best fit using the regression analysis. The y-intercept of the curve that fits the test results is *c* and the slope of the fit line is ϕ_{peak}. The angle of internal friction of the sand can be determined by plotting the graph of σ against τ, as shown in **Figure 3.7**, or is given as:

$$\phi_{\text{peak)ds}} = tan^{-1}\left(\frac{\tau}{\sigma}\right) \tag{3.7}$$

Where

τ = Shear stress (kPa), and

σ = Normal stress (kPa).

Atkinson (2007) has showed that the residual (critical) friction angle (ϕ_{cr}) that determined from the direct shear tests is equal to the angle of repose (AoR). **Table 3.1** gives the measured values of the peak angle of internal friction, residual friction angle and angle of repose of sands for all three sand packings used.

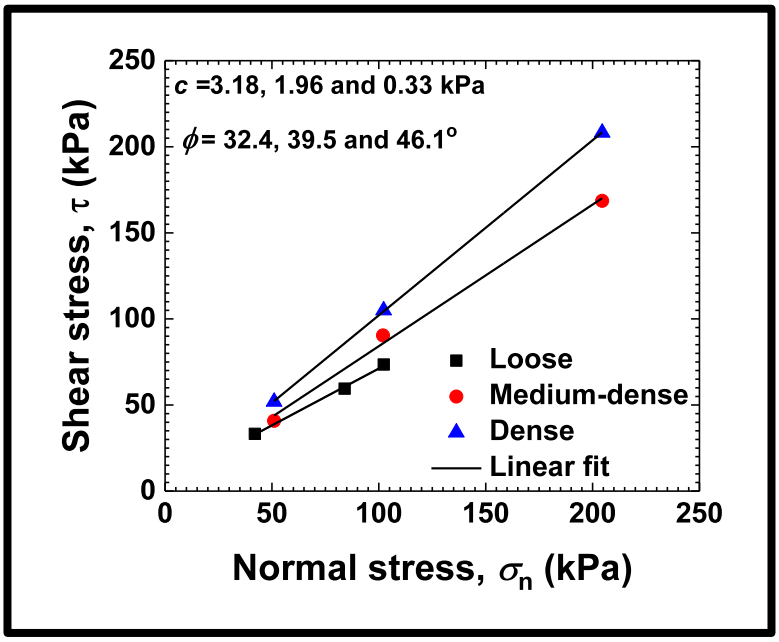

Figure 3.7 Maximum shear stress versus normal stress and the Mohr-Coulomb envelope for DST results for loose, medium-dense and dense sand

3.2.7 Triaxial Test

Triaxial compression tests can be performed on sands and clays. The triaxial compression tests were conducted on the sand of different relative densities under drained conditions, at different confining pressures (σ_3) 100 kPa, 200 kPa, 300 kPa. For sands, angle of internal friction (ϕ) ranges from 26° to 45°, increasing with an increase in the relative density (D_r) and cell pressure (σ_3). In the current study, the sand samples, with a relative density of 24% ± 3, 52% ± 3 and 72% ± 3 were prepared using a compaction technique for the loose, medium-dense and dense sand respectively. The height (h) of the sand samples was typically 76 mm and the diameter (a) was 38 mm. A calibrated proving ring of 2 kN capacity (proving ring constant=1.379 N/division) and (0.01) gauge for vertical deformation were used as illustrated in **Figure 3.8**. The axial loading rate of each sample was 0.5 mm/min (e.g., Zhu et al. (2001) have used 1 mm/min).

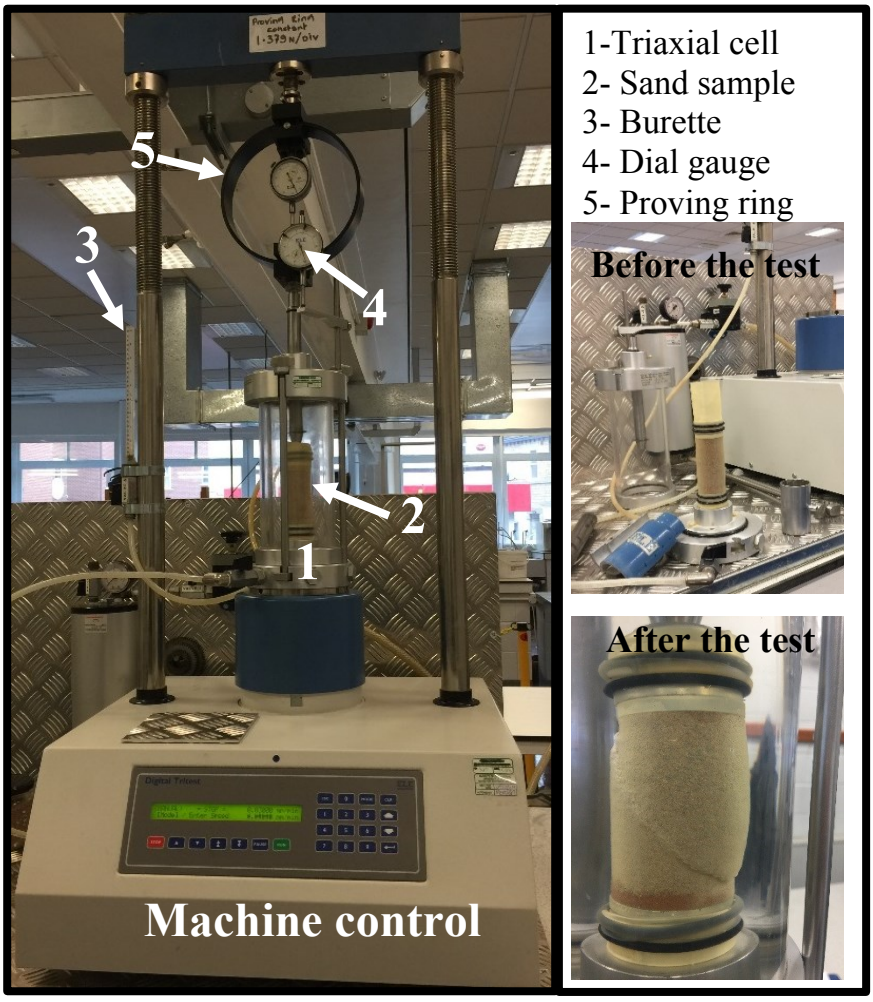

Figure 3.8 Triaxial testing machine with sand sample, sample before and after the test

It is worth mentioning that the stress–strain behaviour of the saturated and dry sand is similar (Lambe and Whitman, 1979). Similarly, Bowles (1996, p. 101) have stated that water does not provide a measurable lubrication effect, as its primary effects are surface tension and pore pressures. However, it is difficult to measure very accurate the volume changes occurring during the shearing stage within coarse soils (Lambe and Whitman, 1979). Therefore, volumetric strains are usually studied using Oedometer compression test for the sand. For drained test, the volumetric strain (ε_{vol}) could be measured from the volume of drained water, which is measured in a volume gauge or a burette that is used to measure out precise volumes of liquids or gases (Powrie, 2014). Consequently, burette was used to measure out approximately the volumes of liquids or gases during the shearing stages as shown in **Figure 3.8**. In addition, the failure envelope for a given soil is curved for larger cell pressure in the triaxial tests. The MC failure criterion is only an approximation at very large cell pressure tests. The soil tested at higher normal stress will yield a lower value of angle of internal friction. Vesic (1963) showed the variations of friction angle were obtained from triaxial tests with void ratio for Chattachoochee river sand.

For drained compression tests, the axial stress σ_a is equal to the major effective principal stress σ_1 and the cell pressure σ_r is equal to the minor effective principal stress σ_3 which is equal to the intermediate effective principal stress σ_2 (Das, 2011). For each sample, the deviator stress (principal stress difference = σ_1–σ_3) increases with axial strain (ε_a) until the peak strength is reached. After the peak value, the shear stress decreases. Further increases of shear strain leads to the critical state of the soil where the shear stress and the void ratio of soil remain constant. The peak angle of friction of the soil is obtained according to the stress state at peak strength, as illustrated in **Figure 3.9**. The effects of increasing the relative density of the sand and the confining pressure around the sand are clearly visible. The axial strain at the peaks strength increases with an increase in the pressure level for all the sand packings. Furthermore, the stress-strain behaviour depends on the confining pressure and the axial strain at the peak strengths increases with an increase in pressure level, as shown in **Figure 3.9**. In addition, it can be seen that the sand shows a softening strain behaviour. For loose sand it can be seen there are peaks in the test. There is a possibility that, during the characterisation experiment of the loose sand using the tri-axial test, the test was prone to a minor level of initial disturbance (loading) before the intended loading were applied. However, the c and ϕ values obtained were independently verified with the direct shear test, and the results were comparable. This confirms that, the potential errors occurring the triaxial test results were to a minor extent.

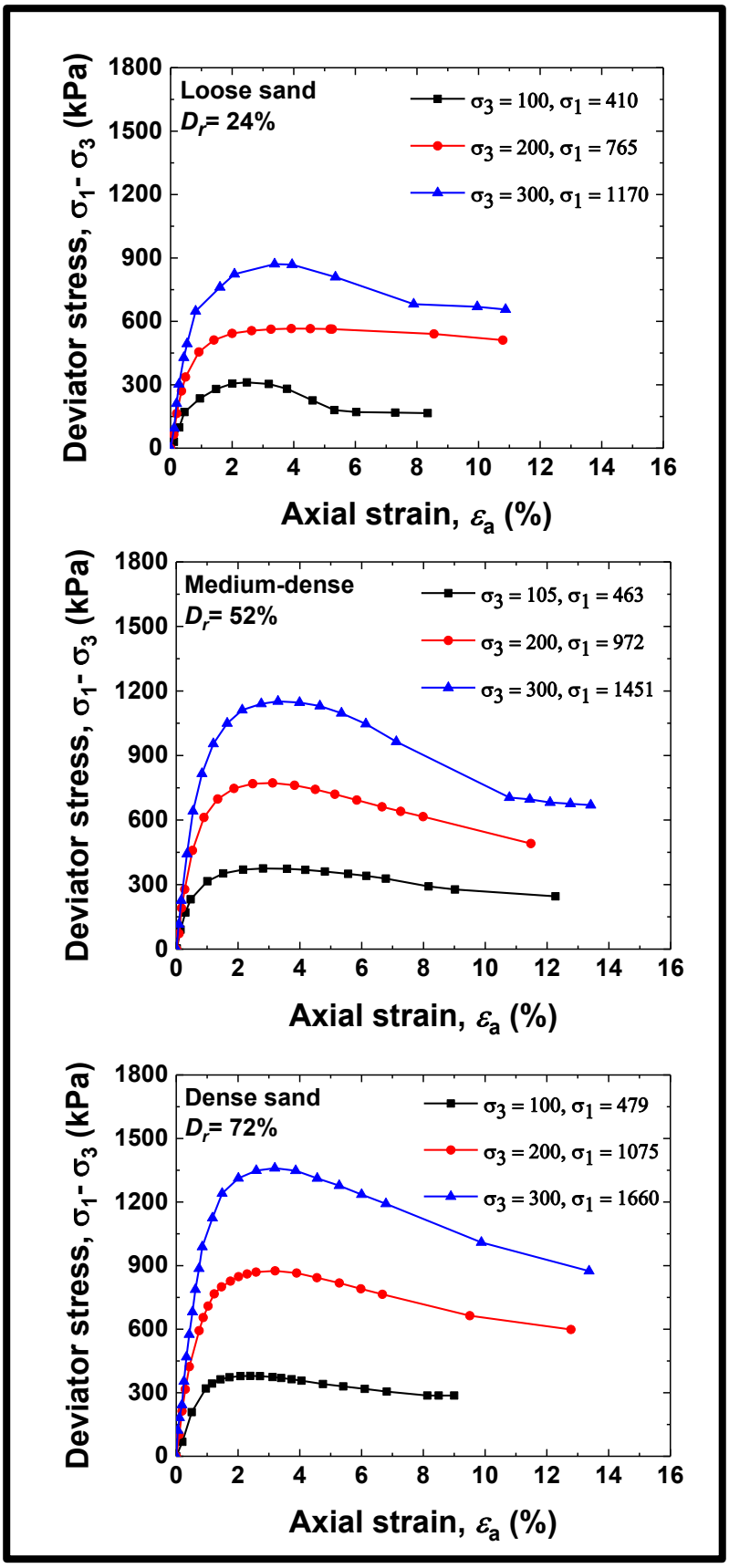

Figure 3.9 Plot of deviator stress versus axial strain–drained triaxial compression test for loose, medium-dense and dense sand

The Mohr circle along with the failure envelope for the sand is shown in **Figure 3.10**. The normal stress on the shear failure envelop is σ_f and the shear stress is τ_f. Then, the MC failure envelope is then a straight line rather than a curve, within these applied cell stresses as shown in **Figure 3.10**. Therefore, the shear strength parameters (c and ϕ) can be measured by plotting Mohr's circle at failure stresses. Using the MC failure envelope, the angle of internal friction of the sand packings are determined by the tangential value of the MC failure envelope according to the stress state at failure rather than the secant value that is as:

$$\phi_{\text{peak)tr}} = tan^{-1}\left(\frac{\tau_f}{\sigma_{nf}}\right) \tag{3.8}$$

where τ_f and σ_{nf} as defined previously.

Therefore, the residual angle of internal friction, ϕ_{cr} can also be determined as:

$$\phi_{\text{peak)cr}} = tan^{-1}\left(\frac{\tau_{f\,cr}}{\sigma_f\,cr}\right) \tag{3.9}$$

where

$\tau_{f\,cr}$ = Shear stress at residual (kPa), and

$\sigma_f\,cr$ = Normal stress at residual (kPa).

The test results indicate that when the confining pressure increases from 100 to 300 kPa, the peak angle of internal friction is not changed that much as it could be noticed in **Figure 3.10**. This minor change in the angle of internal friction at peaks is due to an increase in the cell pressure by only three folds which in turns not yet have significant effects that could be detected. However, Zhu et al. (2001) have increased the cell pressure from 25 to 2500 kPa that is 100 folds; the peak angles of internal friction decrease about 20%. Therefore, Mohr's failure envelope is then a curve rather than a straight line for too big range of all-around pressure. However, in their results, slight decreases have been recorded in the range of 100-300 kPa for peak angle results.

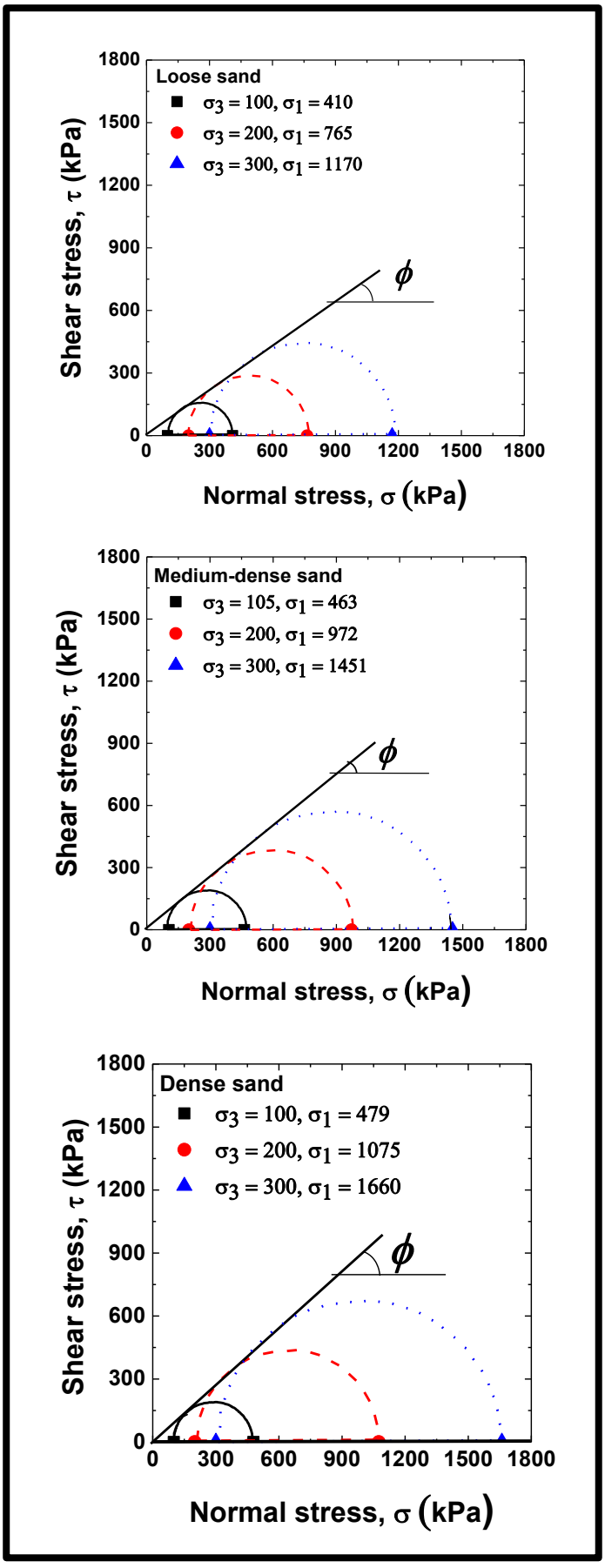

Figure 3.10 Mohr circle and failure envelope for loose, medium-dense and dense sand for triaxial test

The deviator stress ($\sigma_1 - \sigma_3$) of the test is expressed in terms of the confining pressure σ_3. Using the data in **Figure 3.11**, the deviator stress can be expressed with linear fit regression, as it was the best fit using the regression analysis as:

$$Deviator\ stress_L = 21.7 + 2.8\sigma_3 \tag{3.10}$$

$$Deviator\ stress_M = -59.3 + 4.06\sigma_3 \tag{3.11}$$

$$Deviator\ stress_D = -109.7 + 24.29\sigma_3 \tag{3.12}$$

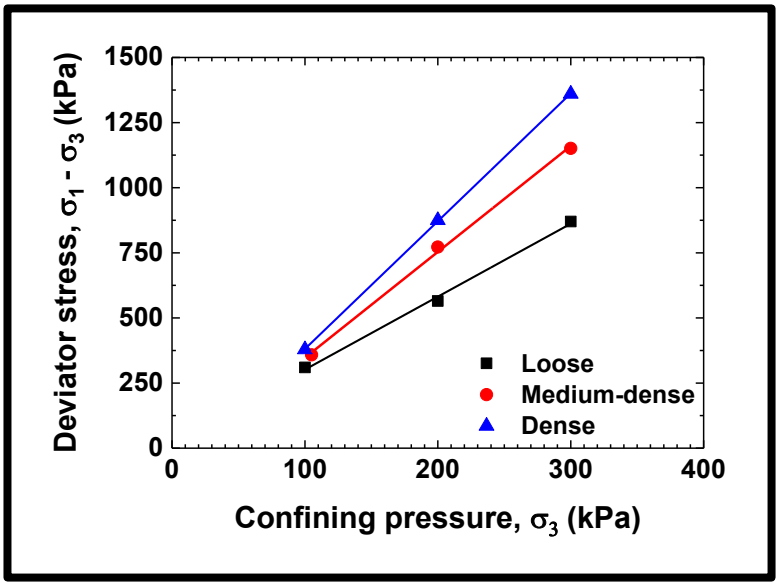

Figure 3.11 Variation of peak deviator stress versus confining pressure for different sand densities from triaxial test

Furthermore, the initial tangent modulus (E_i) was determined from the deviator stress versus the axial strain curves (**Figure 3.9**). The normalised E_i and σ_3 by atmospheric pressure (101 kPa) were drawn as illustrated in **Figure 3.12**. These fitted lines are consistent qualitatively with the results of Ismail and Ahmad, (1990).

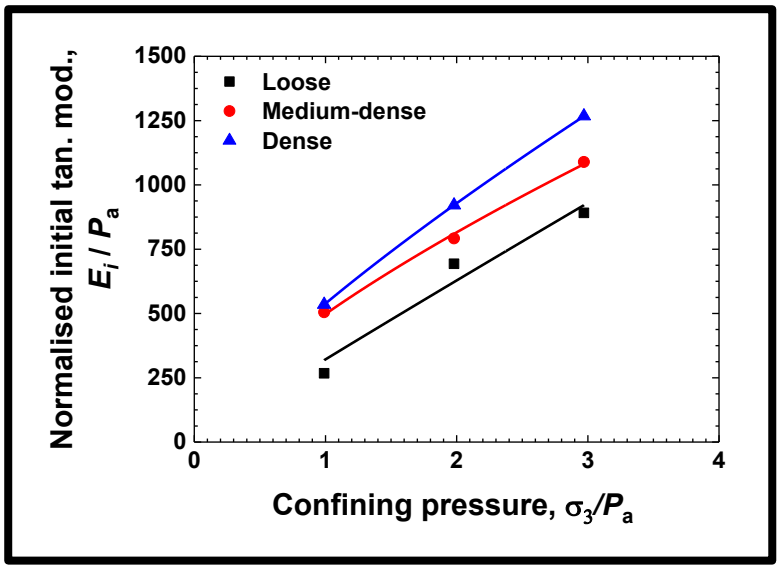

Figure 3.12 Variation of initial tangent modulus, versus confining pressure for different sand densities under experimental triaxial test

The fit lines were embedded, as it was the best fit using the regression analysis. The corresponding equations calculated in kPa are defined as:

$$E_{i\,L} = 321\,P_a + (\sigma_3/P_a)^{0.96} \tag{3.13}$$

$$E_{i\,M} = 497\,P_a + (\sigma_3/P_a)^{0.71} \tag{3.14}$$

$$E_{i\,D} = 538\,P_a + (\sigma_3/P_a)^{0.78} \tag{3.15}$$

where

$E_{i\,L}$ = Initial tangent modulus (MPa), and

P_a = Atmospheric pressure (101 kPa).

It is worth mentioning that the developing of the theoretical bearing capacity equations has assumed plane strain condition. Thus, the values of ϕ_{peak} should come from plane strain tests (Budhu, 2011). However, it has been stated that the angle of internal friction from triaxial test (ϕ_{tr}) on the same soil is from 1-5° smaller than that from the plane strain test (ϕ_{ps}) (Bowles, 1996). Therefore, the plane strain condition is what the DST supposes to generate (Bowles, 1996). In general, the DST yields a higher angle of internal friction compared to that obtained from the triaxial test.

For similar soils the angle of internal friction ϕ determined by triaxial tests is slightly lower (0–3°) than that obtained from DST (Das, 2009). However, recent studies suggest that the angle of internal friction measured from the direct shear and the plane strain for sand are generally considered the same (Bowles, 1996). The Mohr circle along with the failure envelope for the sand is shown in **Figure 3.13**. The direct shear test (DST) results are also included as illustrated in **Figure 3.13**. The peak angle of internal friction measured from direct shear test for sand is higher than that obtained from triaxial test, approving the observations in the literature (Lini Dev et al., 2016). It is worth mentioning that the peak angle of internal friction measured in this research from direct shear tests is about 1–3° higher than that obtained from triaxial compression test, for the cohesionless soils. The difference ($\phi_{ds} - \phi_{tr}$) is more for the loose sand.

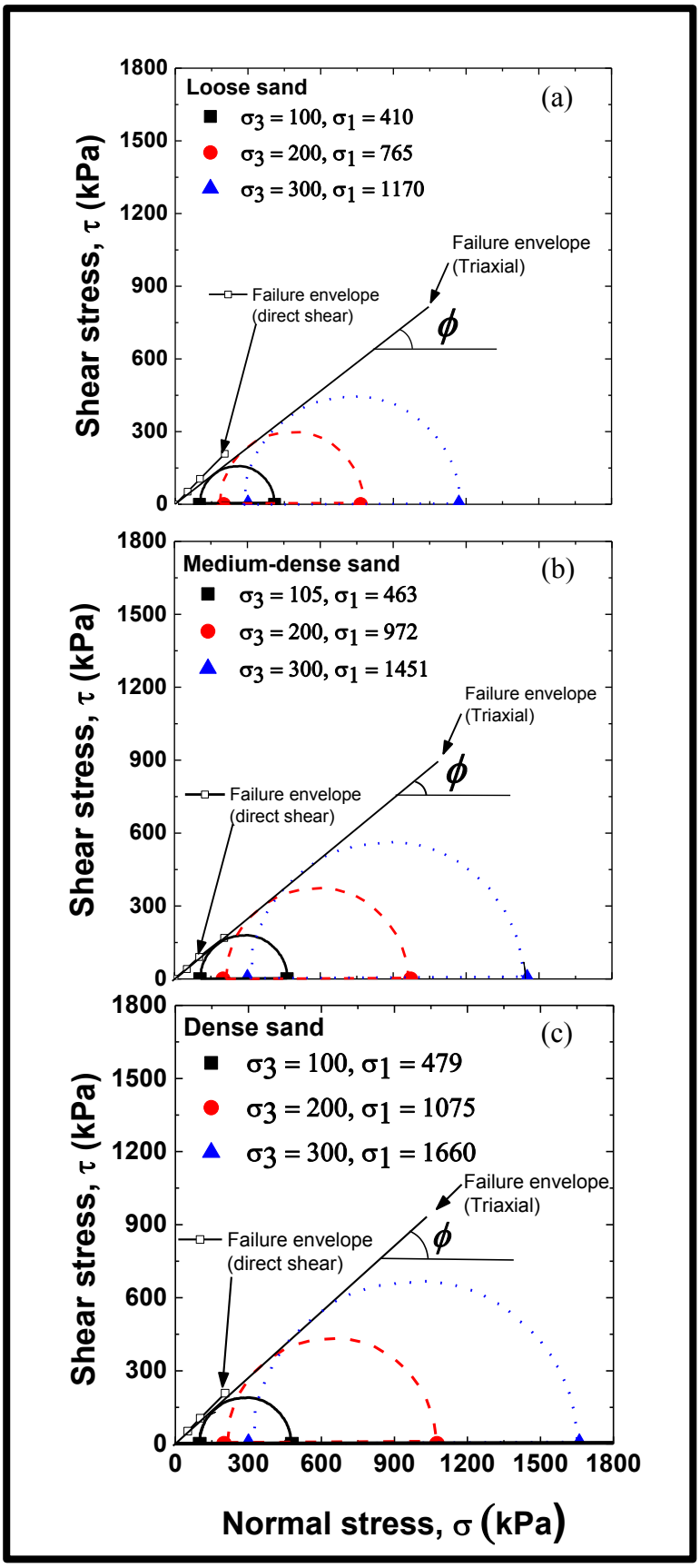

Figure 3.13 Mohr circle and failure envelope for (a) loose (b) medium-dense (c) dense sand for DST and triaxial tests

Table 3.1 Experimentally measured physical properties of the sand used

Type of sand	**Loose (L)**	**Medium-dense (M)**	**Dense (D)**	**Standards**
Dry density (γ_d): (kN/m^3)	14.70	15.30	15.80	ASTM C29/C29M
Void ratio (e_o)	0.76	0.70	0.64	
Relative density, D_r: % ± 2%	24	53	72	ASTM C128
Peak angle of internal friction, ϕ_{peak}: °	32(32.4)*	39(39.5)*	44.3(46.1)*	ASTM D3080
Residual angle of internal friction, ϕ_{cr}:	30	32	36.3	ASTM D4767
Max. dry density (γ_{dmax}): kN/m^3	16.50			ASTM D698
Min. dry density (γ_{dmin}): kN/m^3	14.23			ASTM D4254 C
Maximum void ratio (e_{max})	0.83			ASTM C29/C29M
Minimum void ratio (e_{min})	0.58			ASTM C29/C29M
D_{10}: *mm*	0.25			ASTM D421 ASTM D422
D_{30}: *mm*	0.31			
D_{50}: *mm*	0.37			
D_{60}: *mm*	0.40			
Uniformity coefficient, C_U	1.55			
Coefficient of curvature, C_C	0.93			ASTM D2487
Mineralogy	Silica			Head (2006)
Grain shape	Mostly spherical to sub-prismoidal			
Angularity of grains	Angular and sub angular			
Angle of repose of the sand: °	34°			
()* DST results				

3.3 Experimental Setup for Strip Footing-Sand Interactions

3.3.1 Planar Model

To conduct the footing compression experiments, a planar model box was designed and constructed to satisfy both the mechanical and optical requirements. The former requirement is that the granular box was able to sustain the external loading while minimising the out of plane deformation of the walls (including the front measuring side of the box) under the ultimate load. Furthermore, the dimensions of the test box were kept much greater than that of the footing to minimize the boundary effects, as illustrated in **Figure 3.14**. The latter requirement pertains to enabling the image recording of the grains at the front face of the box model. The front face of the box was made of 15 mm thick Perspex sheet (rigid). The backside of the box was made of 10 mm thick smooth aluminium sheet whereas the side of the box was made of aluminium frames having the dimension of 25 mm × 39 mm. The final planar model has an internal dimension of 460 mm×300 mm×39 mm and 950 mm×300 mm×39 mm. Hence, any boundary effects from walls of the box were practically negligible.

Figure 3.14 shows the complete setup of the footing test in the current study, which includes a high-speed camera HSC (Photron Fastcam SA5) and a digital single-lens reflex

(DSLR) camera (Nikon D5500) in front of the designed planar model that located in an Instron machine with 5kN/0.1N resolution (Instron, Norwood, Massachusetts, No. 5985L3398). HSC (1920 × 1080 pixels) and Nikon D5500 high definition camera (6000 × 4000 pixels) were used here. Typical images recorded at various penetration depths using HSC and DSLR were shown in **Figure 3.14**.

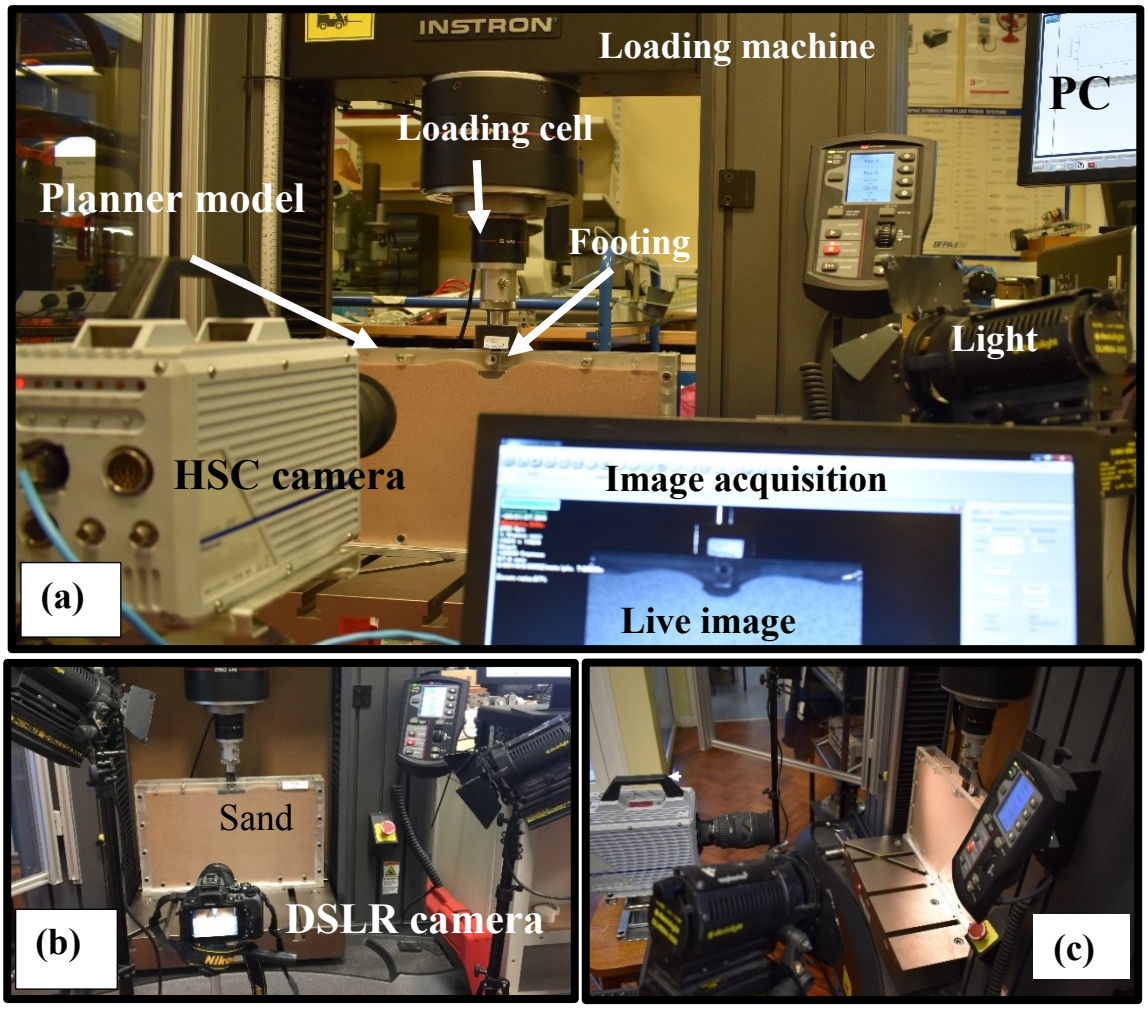

Figure 3.14 Laboratory setup of footing compression test (a) high speed camera HSC (b) DSLR camera (c) side view of the test

Footing size has constructed from aluminium in the current study. Three footings of 38, 76 and 152 mm width were used in the tests. The gap between the footing and the aluminium wall was kept small to allow no particle to pass by, and yet not too tight that resisting frictional forces would be generated, as illustrated in **Figure 3.15**. To meet these requirements aluminium with very smooth side finish, which has a relatively low friction coefficient, was selected to construct the strip footing. Therefore, the footing should remain rigid during the test, meanwhile the friction between the side of the footing and

Perspex wall can be very small and negligible. Hence, any boundary effects from the bottom rigid wall of the box was practically negligible. The roughness of the walls was characterised and evaluated in a mechanical engineering laboratory and the results were also presented in **Section 3.3.2**. A plane strain strip footing was generated in which the information along the cross section of the length of the footing are the most important to study.

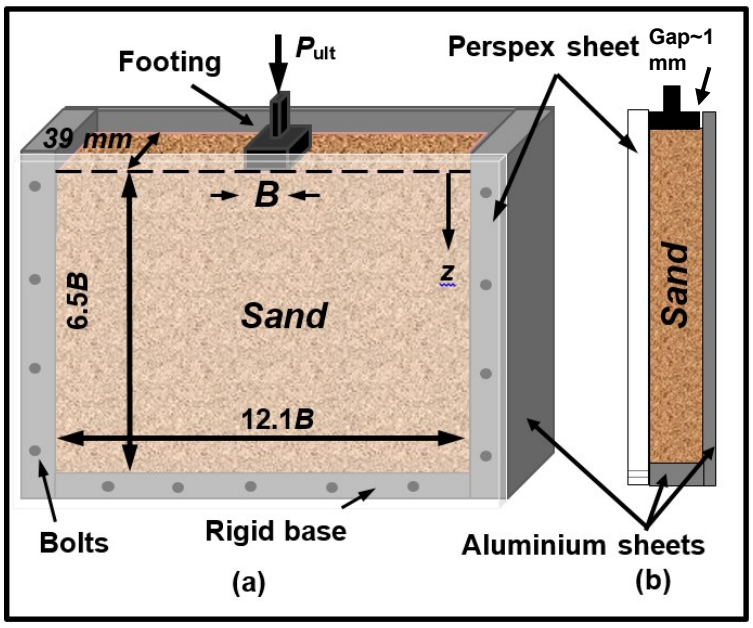

Figure 3.15 Sketch of the planar model box (a) front view (b) side view

3.3.2 Roughness Test

The footing surface roughness in contact with the sand was induced by scratched it by metal pin. The surface roughness of the base of the footing, side wall of the footing in contact with the Perspex walls, and the Perspex walls of the experimental box was measured in a metrology laboratory in school of mechanical engineering using 3D optical microscopy based on white light interferometry (Bruker, Npflex) as shown in **Figure 3.16**. Also, using contact measurement by Talysurf machine (Taylor Hobson) as shown in **Figure 3.17**. The mean roughness value R_a was obtained as 3.2, 1.2 and 0.09 µm, then at the end of the test program, the mean roughness value R_a was obtained as 4.5, 1.4 and 0.99 µm for the base of the footing, the sidewall of the footing, and the Perspex walls respectively.

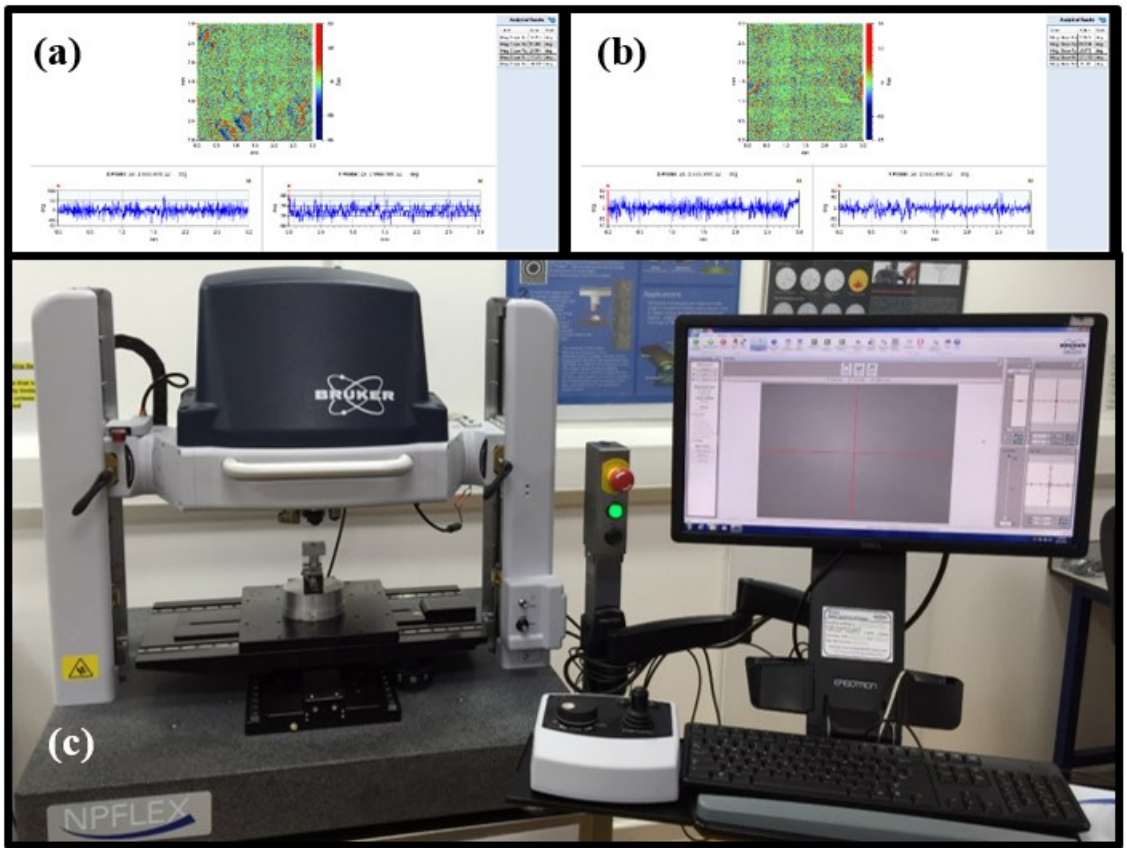

Figure 3.16 Experimental measurements of the roughness of the footing base surface (a and b) results (c) 3D optical microscopy machine

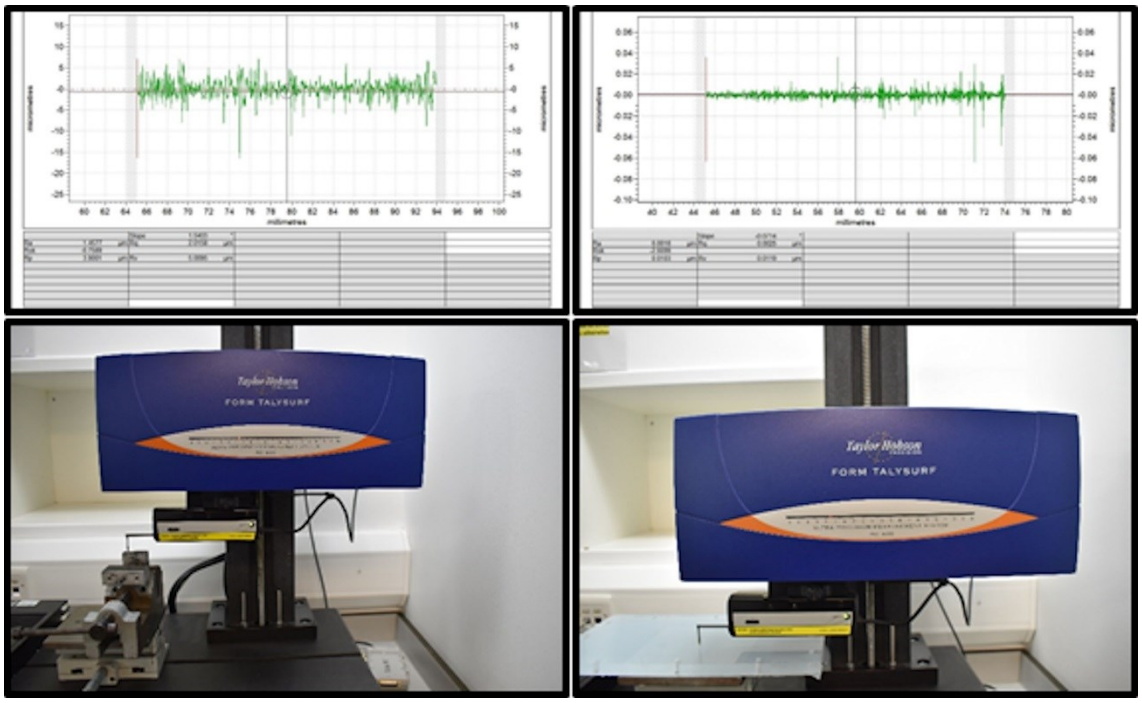

Figure 3.17 Experimental measurements of the footing side and the Perspex sheet using Taylor Hobson (left) side surface of footing results (right) Perspex sheet test

3.3.3 Sample Preparation

It is well known that the macroscopic behaviour of a particle assembly is rather sensitive to its packing structure, which can be largely controlled by the manner that the bulk sample is prepared. The engineering properties, such as shear strength parameter (c and ϕ) and compressibility of the given soil depend on its packing. A relative density (D_r) and a percent compaction are commonly used for evaluating the state of compactness of a given soil mass.

The degree of compaction of granular soil is normally characterised according to the relative density D_r, defined as (Das, 2016):

$$D_r(\%) = \frac{e_{max} - e}{e_{max} - e_{min}} \times 100 \tag{3.16}$$

Where

e_{max} = Void ratio of the soil in loosest condition,

e_{min} = Void ratio of the soil in densest condition, and

e = In-place void ratio of the tested soil (**Table 3.1**).

With the aim to explore the influence of packing structure, it is necessary to develop a robust filling method so that all the testing samples can be directly compared with each other. In the current study, a raining filling and compaction methods were employed to form different packings for the sand particles, as illustrated in **Figure 3.18**. The compaction method was used only to form a more densely packed sample than the loose sand such as the medium-dense and dense sands. Layered of the free-falling sample was prepared using pouring technique method from Kumar and Bhoi (2009), by moving the filling pipe along the width of planar model at a constant rate, such that the materials formed layers of approximately 90 mm. The mass of sand grains laid in the box to the required height pertains to the density of the sample.

For the loose sand packing: the process was repeated for three layers by tracking to one side of the model then back gain. The preparation procedure was done directly on the loading machine baseplate. The top surface of the sand layer was gently levelled off using a hand scraper. It also took care not to disturb the constructed loose sample in any way before applying the axial loading in our experiments. The mass of sand grains (~2250 g) laid in the box to the required height pertains to the density of the loose sample.

For the medium-dense sample: To achieve a uniform density over the whole bulk volume, the sample was prepared in three compacted layers of 90 mm each. After each layer of filling (~2330 g), the layer was compacted using 50 blows per layer in 0.035 m lifts each with a 16 cm^2 (cross-sectional area of the tamper) compaction tamper. This of maximum of 1.1 kg (10.3N) weight designed for this purpose, which resulted in a theoretical energy of 0.36 Nm (J) (Cerato and Lutenegger, 2007; Lavasan and Ghazavi, 2012).

For the dense sand sample: To achieve a uniform density over the whole bulk volume, the sample was prepared in five layers of ~55 mm each. After each layer of filling (1550 g), the layer was compacted using 60 blows by the hand compaction tamper.

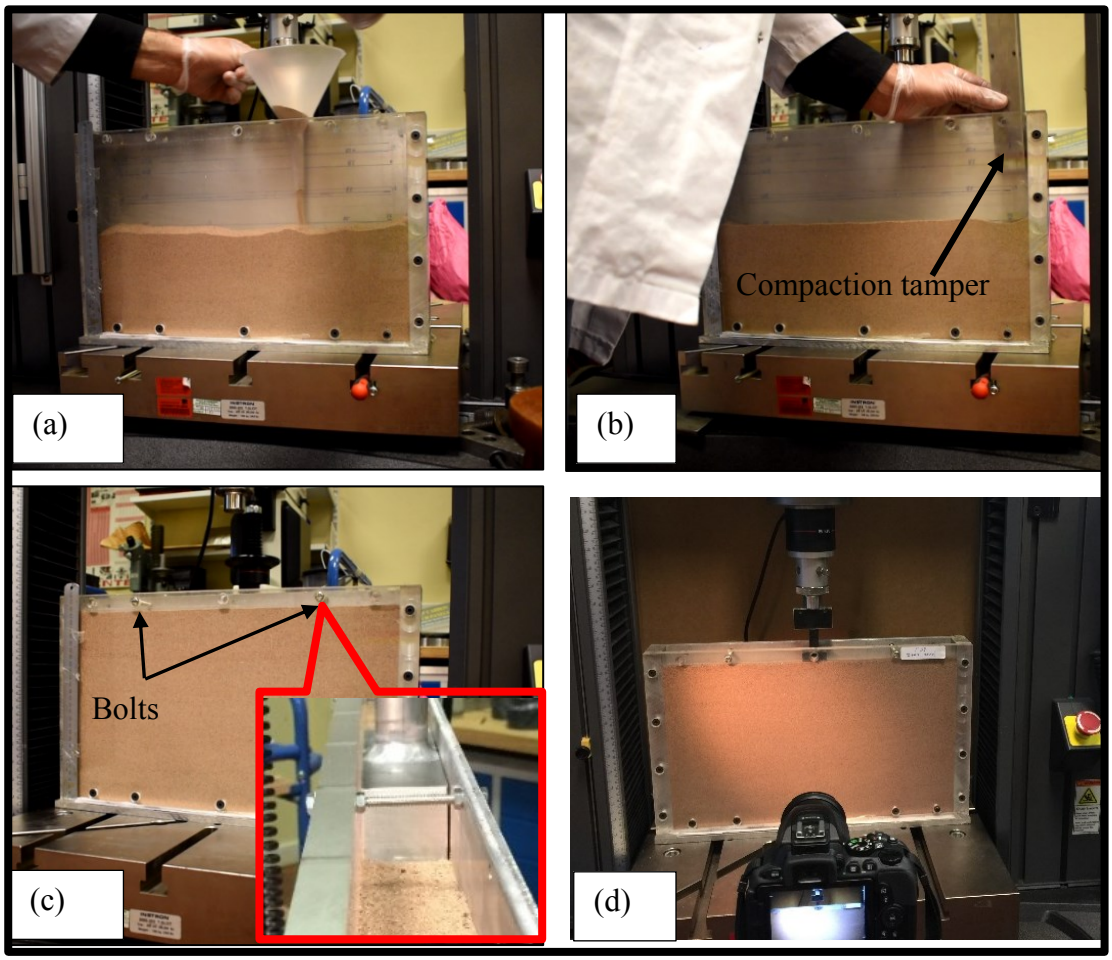

Figure 3.18 Sample of compacted sand medium under preparation (a) free falling (b) compaction (c) level off and screwed the top of the planner mode with magnified view of the bolt (d) attach the footing

The planner model was firmly screwed at two locations on the top positions to minimise any possible out-of-plane deflection during the test (**Figure 3.14** and **Figure 3.18**).

Special attentions were paid such as dim the lights and positioned the lights above the level of the top surface of the planar box to minimise the reflection on the Perspex front wall, as well as the image distortion caused by camera lens not perpendicular to the measurement plane.

3.3.4 Cone Penetration Test

The cone penetration and penetrometer test (CPT) is an in-situ test used to measure soil strength. The CPT is a simple test that is now widely used compared to the standard penetration test (SPT). This test has been practised since 1917 and standardized in 1986 by ASTM as D 3441. The test consists of pushing the standard cone (an instrumented cone), with the tip facing down, into the soil at a controlled rate between 15-25 mm/s are accepted (Das, 2011). Nowadays, the CPT is also used for the soil classification and the soil property assessment.

Many soil variables are affecting the cone resistance. These are the stress level, soil density, soil layers, soil type, soil mineralogy, and soil fabric. The CPT is quick to conduct, with fewer applied error compared to the SPT. It can provide continuous readings of soil conditions. The CPT is used particularly for soft clays, soft silts, and in fine to medium sand deposits. The test is not well adapted to gravel deposits or to stiff/hard silts and clays (Budhu, 2011).

Laboratory CPT were used by many researchers (O'Loughlin and Lehane, 2010; Dijkstra et al., 2013; Teng et al., 2017). By applying the CPT, the soil data can be obtained continuously with depth, which offers better reliability of soil data. Classification of the soil layers using the CPT results has been a great challenge in geotechnical engineering. The CPT results have been directly correlated with the packing density used in this research by comparing the results for different packing density of single layer such the loose, medium-dense and dense sand and for the layered soils of dense sand overlaid loose sand. **Figure 3.19** shows the CPT test in progress for single sand layer and layered soil. The CPT penetration resistance (q_c) profiles in MPa are drawn against either the penetration depth beneath the footing level (z) or the normalised penetration depth, defined as the penetration depth divided by the width of the footing (z/B).

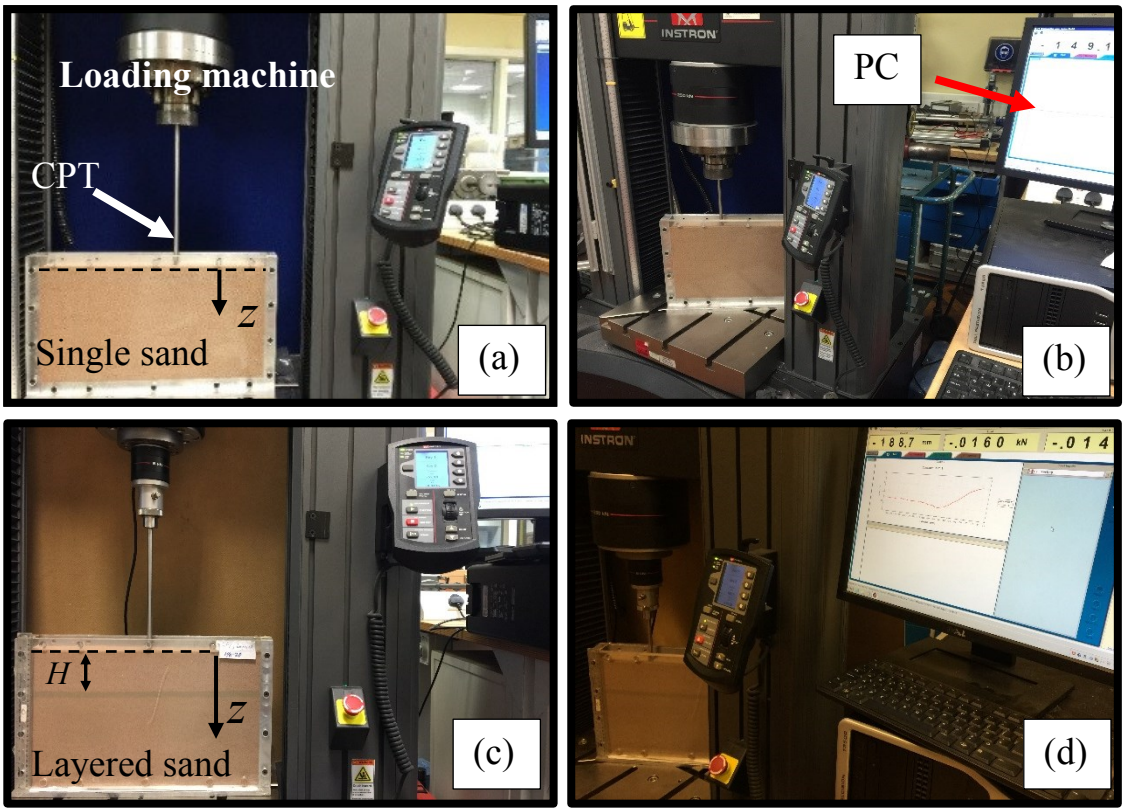

Figure 3.19 CPT photos (a)-(b) test in progress for single layer (c)-(d) test in progress for layered soil with a live image of penetration-load curve

The bulk sand layers were quantitatively characterised. The CPT was inserted using the identical filling procedure of the grains used in the footing structure–granular sand indentation experiments presented earlier using a 10 mm diameter model CPT (O'Loughlin and Lehane, 2010; Dijkstra et al., 2013; Teng et al., 2017). The CPT was inserted at a penetration rate of 1 mm/s in the current experiments. Following the footing compression tests, also two cone penetration test (CPTs) tests were also carried out for each soil density to characterise the sand layer samples. These (CPTs) tests were located either side of the footing, at an approximate 1.5*B* to 2*B* from the footing edge. The loading rate was kept constant throughout all the tests at a rate of 1 mm/s, which simulates a standard CPT loading.

Figure 3.20- Figure 3.21 shows the average CPT penetration profiles for the soil for all relative densities of sand and for layered soil respectively used in the current research. The penetration resistance (cone resistance =q_c) profiles in linear or semi-log scale type are plotted against (z) and (z/B) for more comparison with the literature.

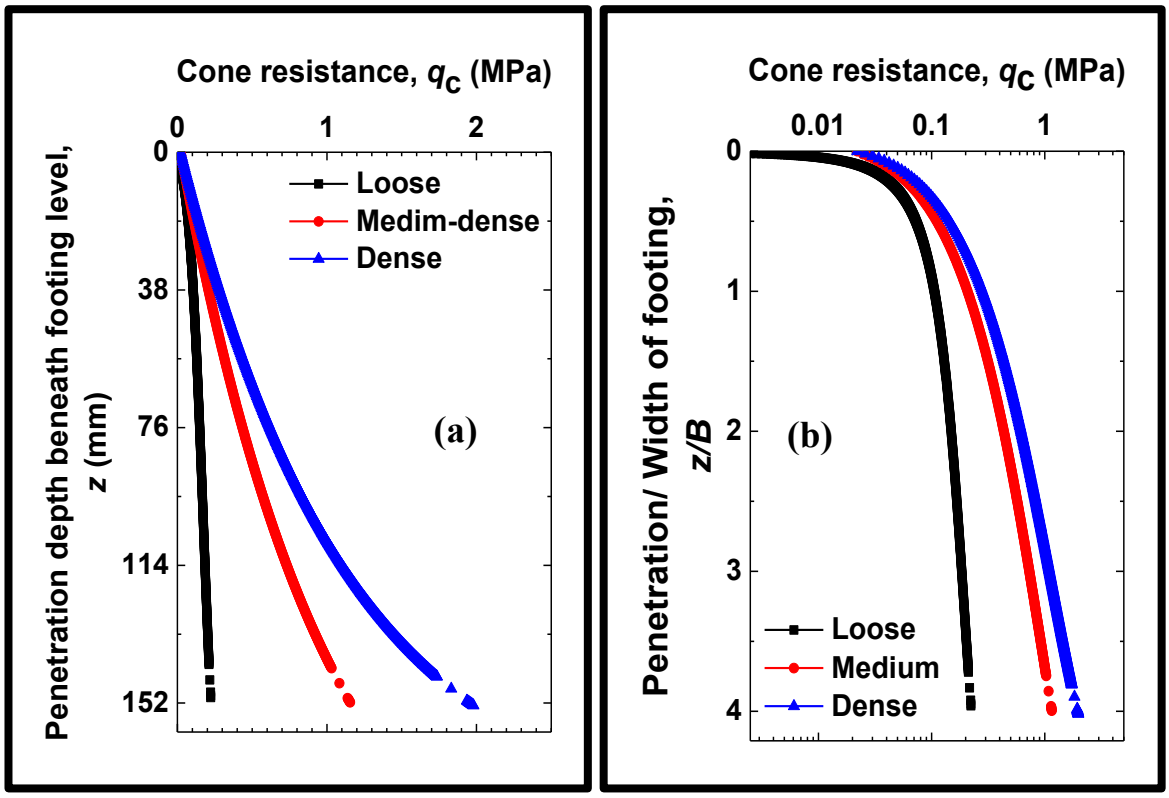

Figure 3.20 CPT data as cone resistance versus penetration (a) and cone resistance versus normalised depth (b) for the three sand densities, average readings of two tests

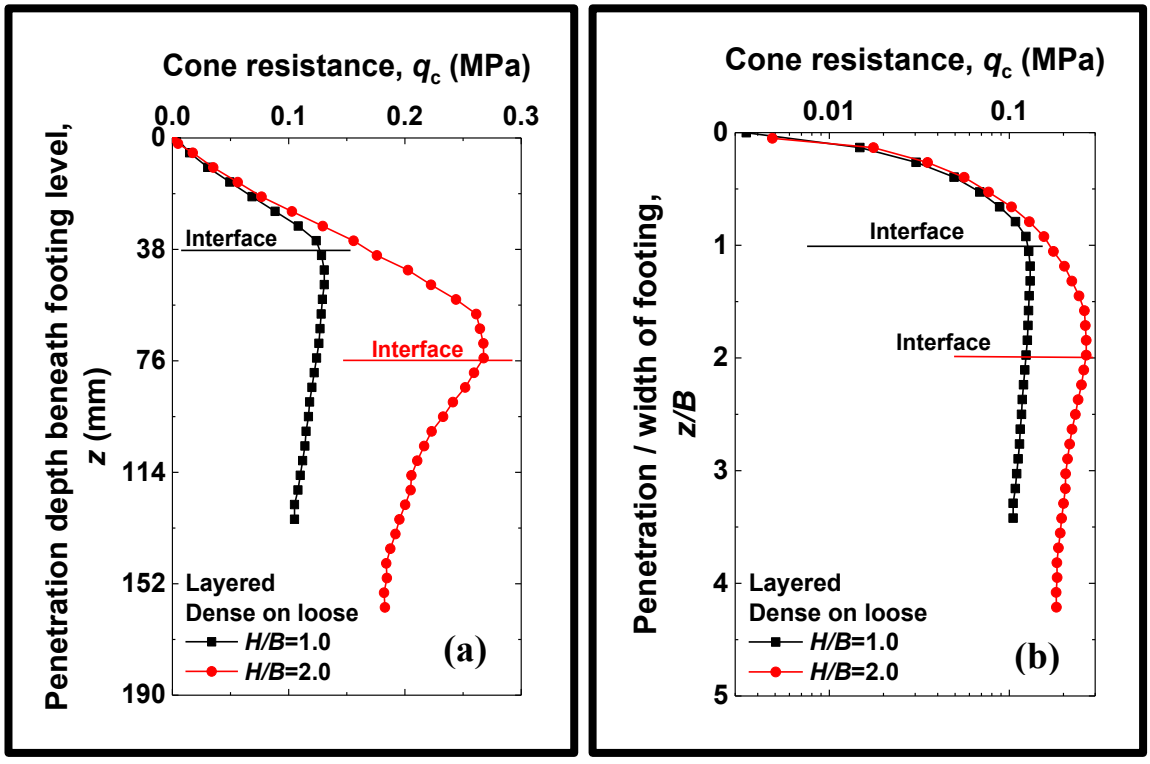

Figure 3.21 CPT data for the layered soil as cone resistance versus penetration (a) and cone resistance versus normalised depth (b), average readings of 2 tests

3.4 Summary

The experimentally measured physical properties of the sand used here were explained in detail. The principle to each single test used here was introduced starting with a description of the measuring technique.

Grain size distribution was carried out on the sand used in this research according to the American Society for Testing and Materials (ASTM standard D421-2002). Particle size distribution of the sand sample was obtained using sieving analysis method. The compaction properties of the natural soil were obtained by the standard Proctor compaction test following the procedure of ASTM D698 –78. Minimum index density test is used to measure the void ratio of the soil in its loosest state (e_{max}). In addition, the angle of repose (AoR) was the angle of friction of the sand in its loosest state was measured. In summary, the shear stress is plotted against horizontal displacement and plotted for each test, from which the shear stress versus normal stress was obtained, and the strength parameter, the cohesion intercept (c) and the angle of internal friction (ϕ) are determined. Finally, the triaxial compression tests were conducted on the sand of different relative densities under drained conditions, at different confining pressures (σ_3) 100, 200, 300 kPa. **Table 3.1** presents the experimentally measured physical properties of the sand used.

Chapter 4 Research Methodologies using DPIV and FEM and their Comparisons

4.1 General

The overall aim of this chapter is to assess the accuracy of using different constitutive models for sand in the footing-structure interaction studies, including using experimentally-derived constitutive relation (MISO) for sand in this work.

4.2 Digital Particle Image Velocimetry (DPIV)

DPIV pertains to the digital platform of PIV, is often used in the field of fluid mechanics to track the motion of particles in the fluid flow using the tracer particles (Adrian, 1991; 2005). Likewise, many researchers have used PIV to study the displacement and (/or) strain distribution in some cases of granular packing under static loading conditions (Murthy et al., 2012). Recently, DPIV has been applied to get measurements of soil deformation in geotechnical engineering problems (O'Loughlin and Lehane, 2010; Hamm et al., 2011; Jahanger et al., 2016, Jahanger et al., 2018a; 2018b).

Dynamic Studio Software Platform (DSSP) is used to analyse the digital images acquired during the test using DPIV. The DSSP provides a range of techniques for characterising particle motions, making it the most convenient for making advanced scientific imaging-based measurements (DantecDynamics, 2013). The DSSP helps to display the large amounts of DPIV-based experimental data in pictorial forms (DantecDynamics, 2013). The algorithms provided within DSSP are used to analyse the DPIV measurements further. This functionality built in the DSSP was used to analyse the digital frames of the grains, and to calculate two velocity components vectors of the grains and their evolution during load application within the sand layer between two successive images.

4.2.1 DPIV Analysis

A typical PIV system for the deformation measurements under the footing compression model used here, as shown in **Figure 4.1**, consists of the illumination lights, the footing model and the particulate system, the loading machine, the camera and computer for image processing.

In this study, the AoI was specified before being divided into sub-sections called interrogation areas IA of (i.e., 16×16 pixels) each covering a zone of soil area size depending on the spatial-temporal calibration (**Figure 2.15** and **Figure 2.17**). Each of these IAs was tracked using an adaptive PIV method (DantecDynamics, 2013; Albaraki and Antony, 2014; Jahanger et al., 2016; Jahanger and Antony, 2017a; 2017b; Jahanger et al., 2018a; 2018b) to identify the movement of soil based on particle images (here) obtained from the front of the Perspex test rig. The IA sizes from each successive image are cross-correlated with each other, pixel by pixel (DantecDynamics, 2013). The correlation produces a peak signal detection, identifying the common grains movement and thus the velocity vector output is computed with sub-pixel interpolation as illustrated in **Figure 2.18**. A velocity vector plot over AoI is acquired by repeating the cross-correlation for each interrogation area over the two images (DantecDynamics, 2013).

An axial compression loading (q) was applied on the footing using the Instron with 5kN, as illustrated in **Figure 4.1**. The tests were conducted using strain-controlled condition in which the load applied on the footing using 0.05 mm/s and 6 mm/s penetration velocity for the static load and the cyclic loads respectively. The DPIV camera (HSC) with an allowable frame speed up to 100000 frames per second (fps) was fixed in front of the box (For the experiments in **Chapter 5 and 8**). The DPIV camera (DSLR) with an allowable frame speed up to 60 frames per second (fps) was fixed in front of the box and two light sources were used to illuminate the rig (For the experiments in **Chapter 6 and 7**). However, as the loading conditions are quasi-static and some cyclic in this study, the recording at 30 – 250 fps was found to be adequate until soil failure was reached, although higher frame speeds were considered in the early stages of the experimental programme. It was verified that the recording at greater than 30 fps did not affect the result noticeably. The resolution of the images was 1920 × 1080 pixels and 6000 × 4000 pixels for the HSC and DSLR cameras respectively.

Initially, a number of trials were conducted to determine the suitable acquisition rate of the recorded DPIV images for the analysis. It was found that, for the current experiments, an acquisition of 30-250 frame/s of the recoded images is adequate in which images were captured at displacement increments of 0.0017 ((0.05mm/s)/ (30 fps)) mm/frame - 0.024 ((6 mm/s)/(250 fps)) mm/frame depending on the test condition. The adaptive PIV iteratively adjust the size of the individual IA in order to adapt to local seeding densities and flow gradients (DantecDynamics, 2013). The former needs seeding with grains to create a colour coded upon which the image processing can operate. The latter is the

algorithms allow iterative sub image deformation that avoids a gradient biasing between the slower and faster moving particles. This is suitable to study granular systems even under different flow conditions (Albaraki and Antony, 2014), bearing capacity of layered system (Jahanger et al., 2016), the scale effects in granular soil (Jahanger and Antony, 2017a; 2017b) and the local and global granular mechanical characteristics of grain–structure interactions (Jahanger et al., 2018a; 2018b). Here, the distribution of velocity vectors of the grains was examined in the image analysis using searching area of a minimum interrogation area (IA) of size and maximum IA size with a measurement resolution of sub- pixel (DantecDynamics, 2013). The space-pixel dimension of the measurement was calibrated by printing a known scale on the test box along the horizontal and vertical directions. White et al. (2003) have shown that the precision of the measurement (i.e., the random difference between multiple measurements of the same quantity) improves with larger PIV patches and it is inversely proportional to the amount of the measurement resolution. Furthermore, texture enhancement of the sand with coloured grains was adopted to increase the accuracy of the image correlation. This size of the mesh patch used here reveals a standard error better than 0.01 pixel (DantecDynamics, 2013). In the experiments, two illumination lights were positioned above the testing box to avoid reflection and glare on the measurement side of the Perspex wall. It was verified that the variation in image scale in both horizontal and vertical direction were not significantly different. The DPIV camera lens was focused normal to plane the footing-soil interface region where the measurements are most important to make. Therefore, the dimension of area of interest (AoI) was as illustrated in **Figure 4.1**. The displacement measures i.e. resultant displacement (S_R), vertical displacement (S_v) and horizontal displacement (S_h) were evaluated under a given load in total (i.e., between the reference image at zero load (q = 0) and the image at the required fractions of the ultimate load level, such as $0.34q_{ult}$ and q_{ult}. Also, **Figure 3.14** shows the complete setup of the footing test in the current study, which includes a high-speed camera HSC (Photron Fastcam SA5) and a digital single-lens reflex (DSLR) camera (Nikon D5500) Nikon D5500 high definition camera in front of the designed planar model that located in an Instron machine with 5kN/0.1N resolution. HSC (1920 × 1080 pixels) and DSLR (6000 × 4000 pixels) were used here. HSC was used in the studies of Chapter 5 and 8, whereas DLSR was used in Chapter 6 and 7.

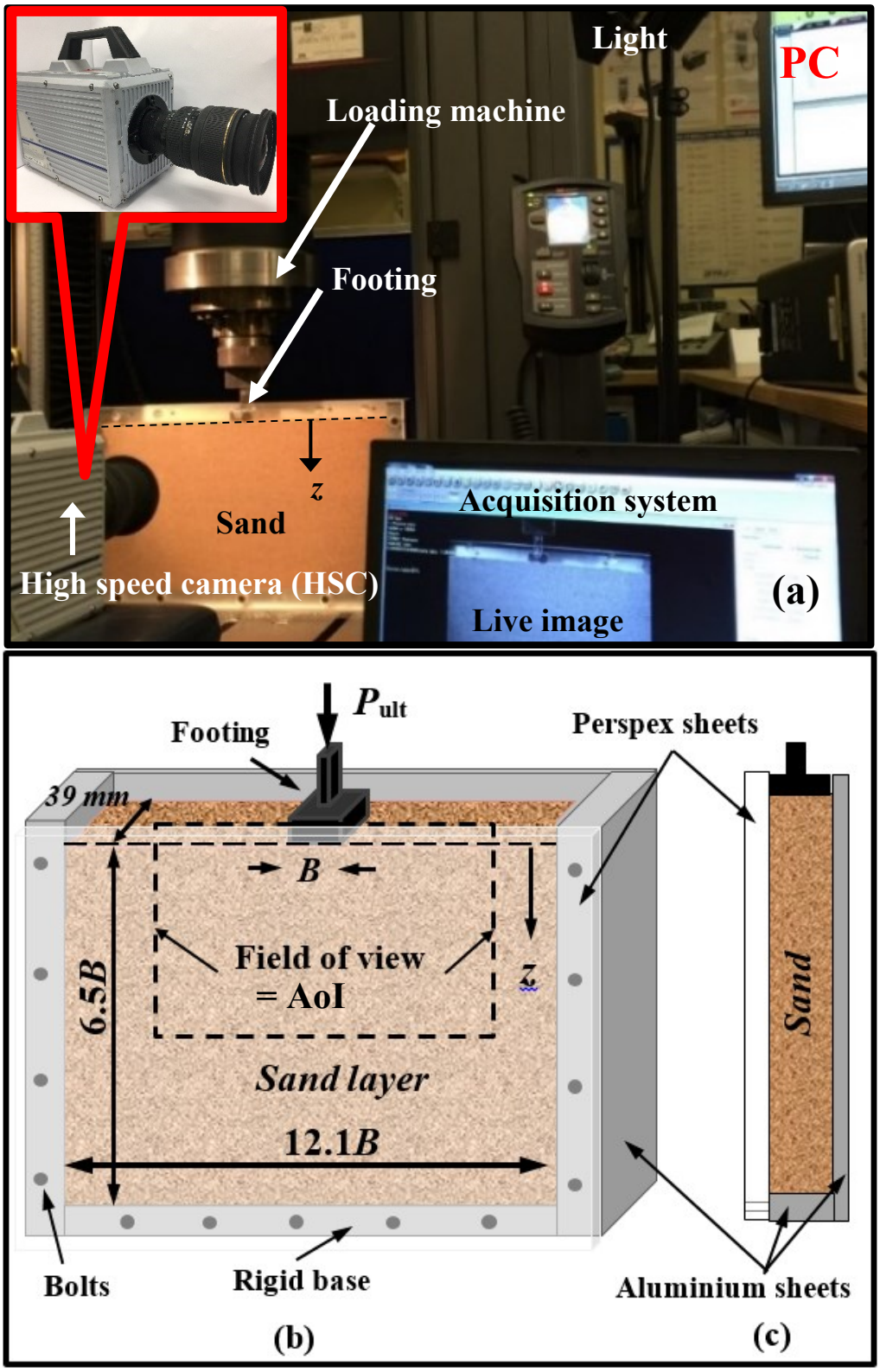

Figure 4.1 (a) Experimental setup using DPIV with a live image of footing in contact with sand (b)-(c) schematic diagram of the experimental setup (not to scale)

4.3 Finite Element Method (FEM)

The FEM is widely used in analysis of a wide range of linear and nonlinear geotechnical problems. The FEM can handle simple and complex constitutive soil models and solve problems with complicated geometries and boundary conditions (Potts and Zdravkovic, 2001).

4.3.1 FEM Simulations

Non-linear elastic finite element simulations have been made for the cases of a single footing indenting on the loose, medium-dense and dense sand packing using ANSYS workbench 17.2 version (ANSYS, 2016). The ANSYS program is a broad purpose finite element modelling (FEM) package for numerically solving a wide variety of mechanical interactions (ANSYS, 2016).

In the present study, ANSYS is used to create a two-dimensional solid geometry. The chosen domain along with applied boundary conditions is shown in **Figure 4.2**. The simulations were held under identical boundary conditions for footing indenting with different types of sand packing as in the case of physical experiments. In the simulations, the bottom most nodes were fully constrained in both the horizontal and vertical directions ($S_h = S_v = 0$). A line of symmetry is used along the footing centre line, $S_h = 0$ and $S_v \neq 0$ (Kumar and Kouzer, 2007). The far side of the assembly was fully constrained in the horizontal direction ($S_h=0$) and free to move in the vertical direction ($S_v \neq 0$) (Mosadegh and Nikraz, 2015; Jahanger et al., 2018a; 2018b). The contact regions between the rigid footing and the sand were modelled as a relatively rough surface (interface friction coefficient=0.25) corresponding to the experimental study (Armin et al., 2014; Gordan et al., 2014; Lee, 2015; Jahanger et al., 2018a; 2018b). An adaptive FE mesh was generated at the footing-soil interface where the largest stresses and strains would be expected. It should be mentioned that Skewness mesh metric (a measure of mesh quality) of less than 0.001 maximum value was obtained in all the current study for all cases except for the case in chapter 5, which is acceptable (Lee, 2015; Jahanger et al., 2018a; 2018b). The size of the elemental geometry is shown **Figure 4.2**.

Material model for sand describes the nonlinear plasticity behaviour, which depends on the engineering soil properties in the current ANSYS simulations. For this, the experimentally characterised bulk stress-strain relationship corresponding to the load-

displacement curves of different relative densities of the sand used in this study presented in **Figure 4.3** are discretised into a large number of linear segments and fed as user defined digital input MISO model (ANSYS, 2016; Lee, 2015). This was used to define the yield surface of the sand used here instead of using the inbuilt constitutive models in ANSYS. Furthermore, the experimentally characterised material physical properties were used i.e. bulk density (γ), initial modulus of elasticity (E) and typical value of Poisson's ratio (v) for sand (E = 25 MPa, 35 MPa and 50 MPa whereas v=0.2, 0.25 and 0.35 for the loose, medium-dense and dense sands respectively (Das, 2009)). In the present analysis, ANSYS used the multilinear isotropic hardening of the stress-strain relation (Lee, 2015). The initial state of stress is important in FEM modelling of geotechnical problems. Hence, standard earth gravity was applied prior to application of the external load. The width of the loading area is 0.5B. The loading is applied vertically in increments of constant displacement of 0.15B, uniformly across the width of the footing within the time step of 0.001 second (~1000 cumulative iteration). The simulation time in real was between 20 minutes to 3 hours. The evolution of different displacement components in the solid geometry (depicting the sand packing) is tracked for different loading levels and compared with corresponding DPIV measures later. More details for DPIV can be found with discussion in **Section 2.4.2, Chapter 2**.

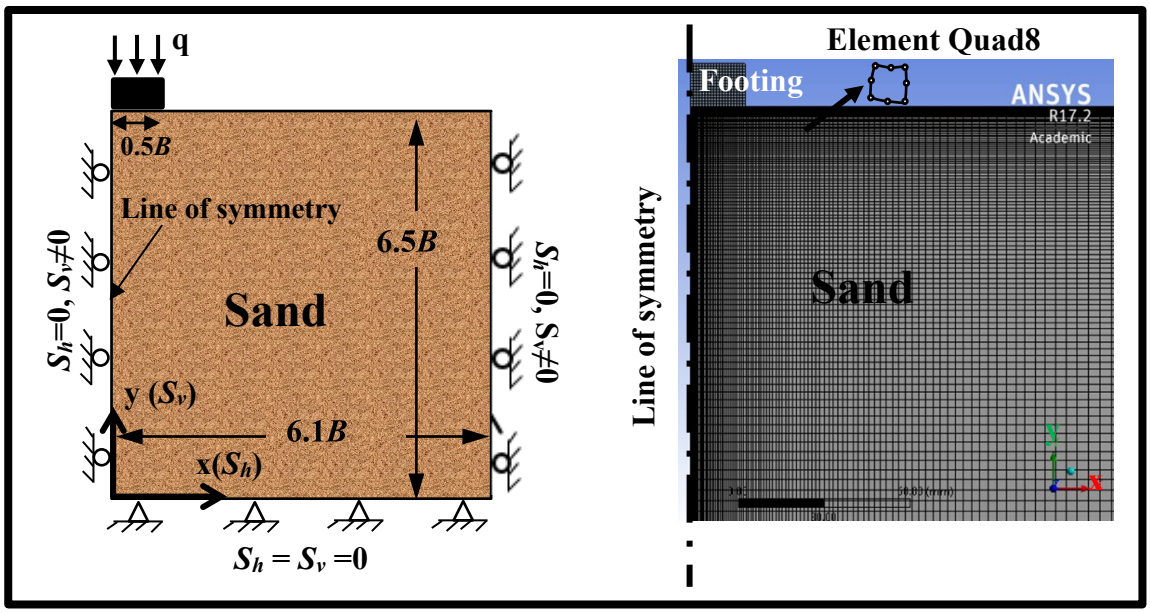

Figure 4.2 (left) Chosen domain and boundary conditions, not to scale (right) finite element mesh, and element enlarged for single homogeneous sand layer

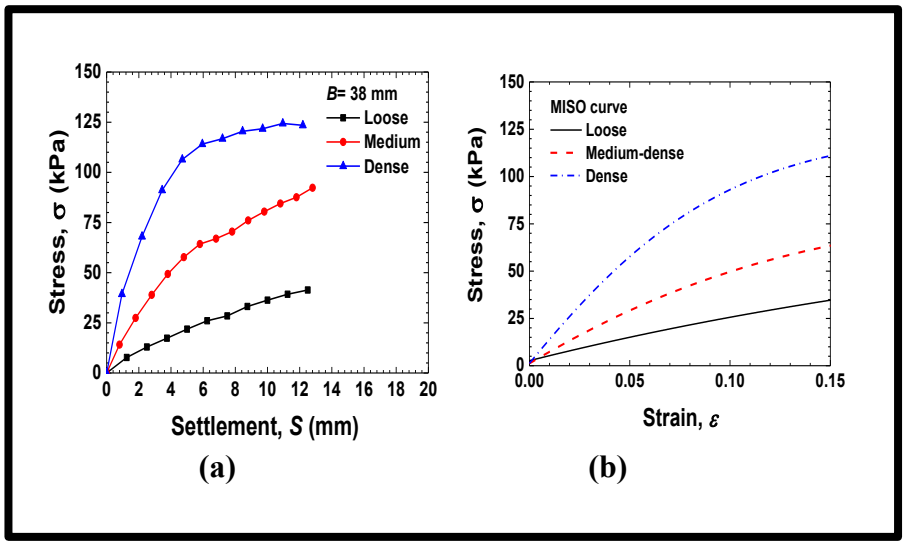

Figure 4.3 (a) Load-settlement curves for loose, medium-dense and dense sand (b) MISO input curves for loose, medium-dense and dense sand

4.3.2 Initial Validation of Using User-defined Constitutive Relation in the FEM Simulations

It is unclear on whether compute modelling, for example using FEM, could capture displacement fields more accurately at the local scale for the above said cases of footing-sand interactions. Re-evaluating the suitability of the commonly used constitutive relations in the FEM, and where required, to employ a new strategy. Therefore, the DPIV results from the footing-sand interactions of different relative densities were used to validate the appropriateness of the commonly used constitutive relations in the FEM compared to the MISO.

In the present analysis, the multilinear isotropic hardening of the stress-strain relationship offered in ANSYS17.2 software was used (Lee, 2015). The hardening rule results in an increase in yield stress upon further loading during plastic deformation, so an increase in stress is accompanied by an increase in plastic strain. This can model the behaviour of materials under monotonic loading and elastic unloading, as well as under cyclic loading (ANSYS, 2016). The evolution of different displacement components in solid geometry (depicting the sand packing) is tracked for different loading levels. This straightforward application describes nonlinear plasticity behaviour; therefore, the experimentally characterised bulk stress-strain relationships corresponding to the load-settlement curves, as illustrated in **Figure 4.3**, are discretised (MISO) and compared with corresponding DPIV measures later.

Figure 4.4 shows the load-settlement curves obtained from experimental and FEM results. The load–settlement curve for the loose and medium-dense sands obtained from the measured values from the physical test and the FEM agree very well. However, for dense sand until the ultimate settlement (S_u) of 4.0-5.0, mm, the curves agree well, whereas for larger settlements, the FEM results deviate from the measured values.

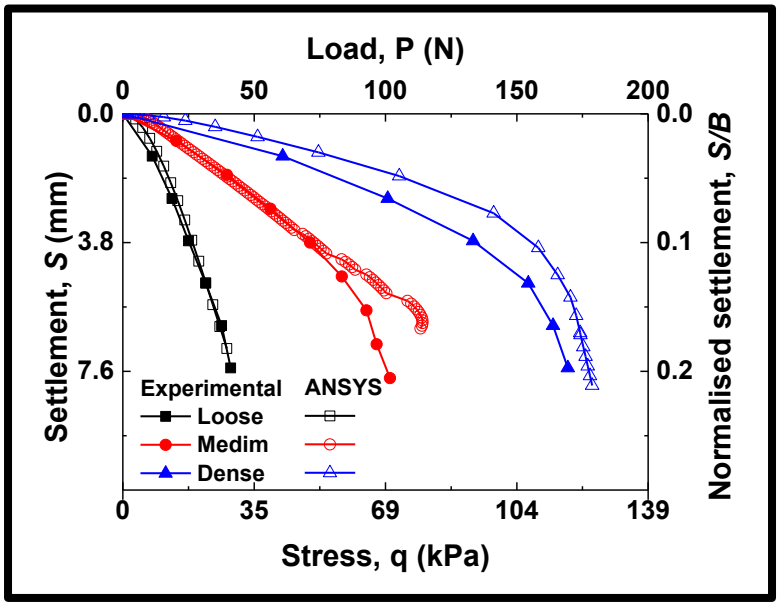

Figure 4.4 Comparison of experimentally measured and numerically calculated of load-settlement curves of strip surface footing on single loose, medium-dense and dense sand

To illustrate the disturbance in stress caused by the different constitutive models, the increase in internal stress within the soil body along the centreline is plotted non-dimensionally in **Figure 4.5**. This illustrates the comparison between normalised vertical stresses under the ultimate loading stage, which is measured at various depths along the footing centre line from the footing–dense sand interface level under the strip footing. It can be observed from **Figure 4.5** that the FEM curve trends are similar to Boussinesq's approach results (Bowles, 1996). However, changes in the vertical stress distribution using ISO model approaches the Boussinesq's theory at smaller depths when $z/B \leq 1.0$, whereas it deviates for greater depths, as illustrated in **Figure 4.5**. It can be further noticed that the measured vertical stress values using the MC and EDP models are smaller than the ISO and the MISO model, along with the theoretical solutions using Boussinesq's approach (Boussinesq, 1885). However, it can be also noted that the vertical stress values obtained below the footing from MC and EDP approaches closer to the values determined

from Boussinesq's theory at greater depths of 4.5*B*-6.0*B*. However, the calculated vertical stress values distribution using MISO approaches the Boussinesq's theory at smaller depths, when $z/B \leq 2.5$, whereas it deviates for greater depths. It seems that for the ISO and MISO approaches, the shallow depth in the dense sand is first compressed and will be behaved in a truly elastic manner. At deeper depths, the soil plasticizes and therefore again deviates from the elastic behaviour of Boussinesq's theory. Nevertheless, in cases of MC and EDP the sand soil behaves totally elastic-perfectly plastic and therefore deviates from elastic behaviour. The changes in the stresses calculated using MC and EDP remain lower than Boussinesq's for z/B <4.5. Boussinesq's distribution for homogeneous semi-infinite mass was originally applied to the problem of uniformly loaded single layers, underlain by a rough rigid rectangular base.

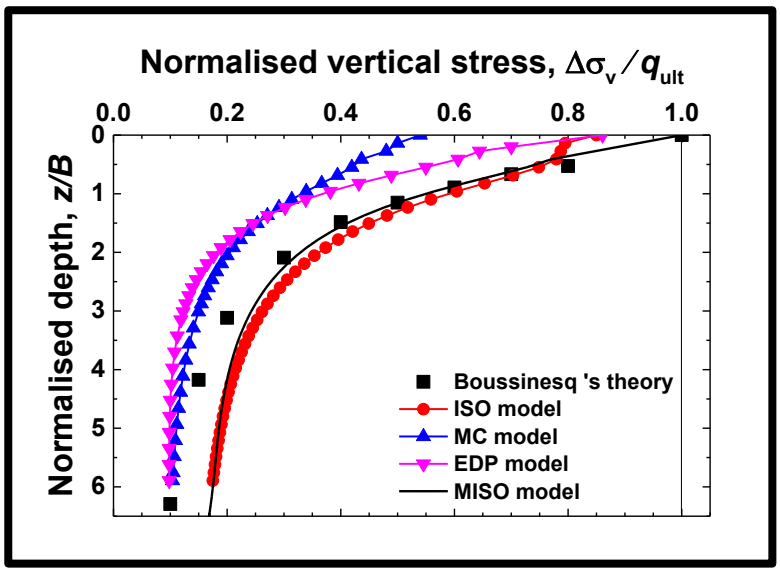

Figure 4.5 Comparison of the normalised vertical stress using different constitutive models under ultimate load and Boussinesq's results

It can be observed that the increase in vertical stresses fall below 10% of the surface value q at a depth ~ 6.5*B* for Boussinesq's, Mc and EDP methods, whereas they fall to below 10% of the surface value q at a depth ~ 7.5*B* for the ISO and MISO methods. This is a result of the distribution of the load in strip footing, where spreading can only occur in the direction perpendicular to the footing centre line (Powrie, 2014). The normalised vertical stresses ($\Delta\sigma/q_{ult}$) calculated based on input from the MISO model decrease with depth at a slower rate than those derived from an elastic analysis (Boussinesq's equation). This is consistent with the experimental results beneath a rigid foundation resting on a

sand layer, which has been reported by Selvadurai (1979). The stress percentages at deeper layers increased in MISO when compared to other models, potentially because the load compacts the soil under the footing and therefore the stress could be transferred to the deeper layers, as expected for strip footing. As can be observed from the FEM analysis using MISO, the failure zone reaches depths of z=4.0B.

Figure 4.6 and **Figure 4.7** present a comparison between the vertical displacement components along a horizontal section at a depth of 0.5B below the footing on loose and dense sand, as obtained from FEM and DPIV under the ultimate load. The sand directly under the footing centreline has the largest vertical displacement. In addition, it can be seen that from the normalised vertical displacement component responses for the MISO model soil presented in **Figure 4.6** and **Figure 4.7**, there is a softer numerical response when compared with the ISO, MC and EDP models. It can be further observed that there is an excellent agreement with the experimental results from DPIV-based tests for loose sand, as shown in **Figure 4.6**. This was expected, because sand soils are inelastic. Thus, using this finite-element MISO framework, which allows for the introduction of plasticity to the sand, presented significant advantages to more accurately capture the physical behaviour of the sand.

In ISO analysis, the soil is characterised by E and v. However, it can only approximate the variation of stiffness for sand, and only for relatively low magnitudes of applied loads. The ISO model offers relatively fast, but not very accurate estimates of the true material response. It is not suitable, as soil performs mostly none elastically under the load. It is widely used for simple analysis, such as identifying the stress distribution or concentration of the in situ ground. The results suggest an excellent response of the soil to the external load when using the MISO model, in comparison to the ISO, MC and EDP models, which in the present study show similar behaviour and stiffer responses of soil to the external load. As can be seen in **Figure 4.6-Figure 4.7 (c)**, the MISO models from smaller footing (B=38mm) for both loose and dense sand were used as an input for larger footing (B=76mm) simulation, in addition to the MISO model for 76mm, to verify the limitations of using the MISO model technique for larger footing. A very strong agreement can be seen when calculated to 1.25B away from the footing centre line when using the MISO model for larger footing, which is twice the size of the footing used to obtain the MISO model.

Therefore, comparisons between the results for vertical stress distribution below the footings were made only for settlements lower than approximately the ultimate settlement

(S_u). Hence, the researcher compared the results of the ultimate settlement (S_u) which is related to the ultimate bearing capacity at failure. Consequently, the comparison between the experimental and FEM stress distribution for larger stress values was not carried out. The results suggest a considerably stiffer response of soil to the external load when using the FEM model in dense sand, when compared with the loose and medium-dense sand, which in the below figure shows a similar behaviour to the MISO model.

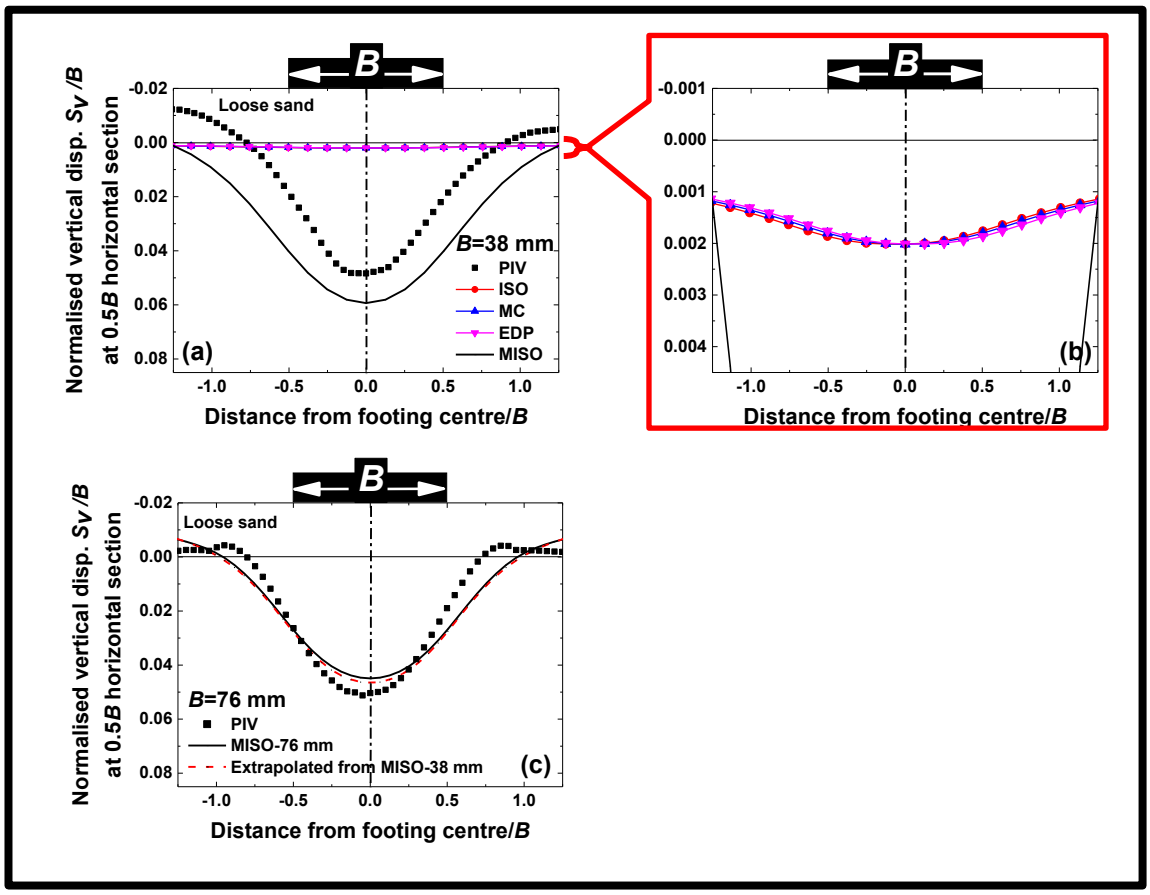

Figure 4.6 Comparison of vertical displacement component along a horizontal section at a depth of 0.5*B* below the footing on loose sand under ultimate load (a) different constitutive models and DPIV for *B*=38 mm (b) magnified view (c) *B*=76 mm

Although the planar test simulation provided an understanding of stress and strain distributions in footing-sand interactions, it is considered necessary to adopt a non-elastic system to better reproduce footing-sand interaction behaviour. Thus, using an elastic perfectly plastic model, which allows for the inclusion of plasticity in the model, would present significant improvement in more accurately visualising the sand behaviour under compression loading. Adding a pushing region in the model (with displacements) will

usually converge better than force loading. Yet, what is not mentioned here is that the results show stress and strain concentration zones near the footing bottom corners. It appears that the footing at the concentration zones suffers very high stress, which is not accounted for in the existing theory.

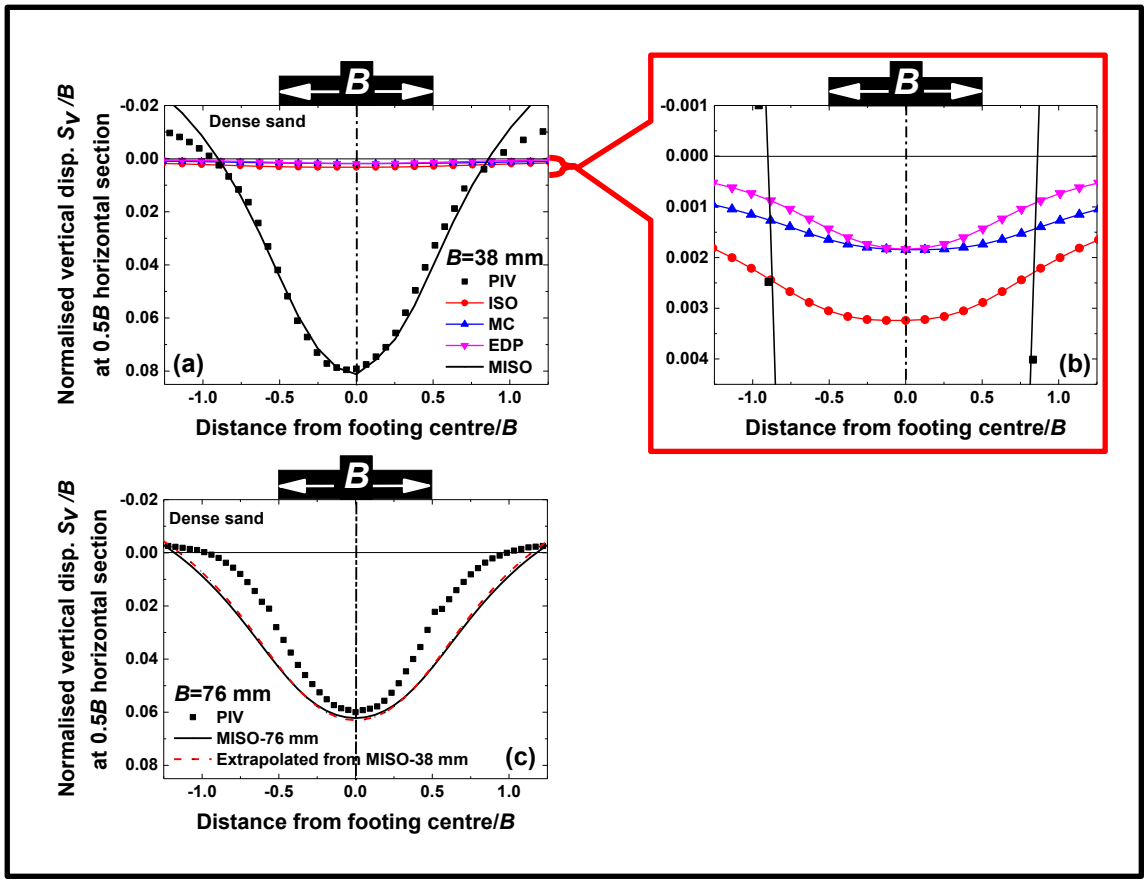

Figure 4.7 Comparison of vertical displacement component along a horizontal section at a depth of 0.5*B* below the footing on dense sand under ultimate load (a) different constitutive models and DPIV for *B*=38 mm (b) magnified view (c) *B*=76 mm

Details of the parameters used in the numerical simulations are presented in **Table 4.1**. The table divided to three sections for each relative density used in the current study loose, medium-dense and dense sand. Also, to get a better convergence to the end of the applied load, it is worth mentioning that the mesh discretization was finer at the footing- sand interface region. Also, the sizing of the mesh (bias) was chosen to maintain the same aspect ratio of the elements of the footing and the soil at the interface region. An adaptive FE mesh generation (Lee, 2015) was applied at the footing-soil interface where the largest strains and stresses would be expected. It should be mentioned that Skewness mesh metric (a measure of mesh quality) of less than 0.001 maximum value was obtained in all

the current study for all cases, which is acceptable (Lee, 2015; Jahanger et al., 2018a; 2018b). The size of the elemental geometry is shown **Figure 4.2**.

Table 4.1 Parameters used in the numerical simulations

Loose sand						
		Units	ISO	MC	EDP	MISO
	γ_d	kN/m^3	14.7	14.7	14.7	14.7
Isotropic elasticity Derive from	E	MPa	25	25	25	25
	ν		0.2	0.2	0.2	0.2
Yield surface for soil plasticity	c	kPa	1.0	1.0	1.0	Multilinear isotropic hardening of stress-strain
	ϕ_{Peak}	Degree	32.0	32.0	32.0	
	ψ	Degree	1.0	1.0	1.0	
	ϕ_{cr}	Degree	30	30	30	
	$c_{cr}= 0.8c$	kPa	0.8	0.8	0.8	
Medium-dense sand						
	γ_d	kN/m^3	15.30	15.30	15.30	15.30
Isotropic elasticity Derive from	E	MPa	38	38	38	38
	ν		0.25	0.25	0.25	0.25
Yield surface for soil plasticity	c	kPa	1.0	1.0	1.0	Multilinear isotropic hardening of stress-strain
	ϕ_{Peak}	Degree	39.0	39.0	39.0	
	ψ	Degree	5	5	5	
	ϕ_{cr}	Degree	32	32	32	
	$c_{cr}= 0.8c$	kPa	0.8	0.8	0.8	
Dense sand						
	γ_d	kN/m^3	15.80	15.80	15.80	15.80
Isotropic elasticity Derive from	E	MPa	50	50	50	50
	ν		0.35	0.35	0.35	0.35
Yield surface for soil plasticity	c	kPa	1.0	1.0	1.0	Multilinear isotropic hardening of stress-strain
	ϕ_{Peak}	Degree	44.3	44.3	44.3	
	ψ	Degree	10	10	10	
	ϕ_{cr}	Degree	36.3	36.3	36.3	
	$c_{cr}= 0.8c$	kPa	0.8	0.8	0.8	
Temperature =22 ± 1 °C						

To conclude, the simulation schemes including the elemental discretisation and the user-defined constitutive relation of sand (MISO) are validated initially for the case of strip footing interaction with sand packing of different densities. Overall, the displacement measures agree well with experiments conducted using DPIV. Hence, in the following

chapter, the FEM modelling is applied with the elemental discretisation and user-defined (experimentally based) constitutive relation for sand. Expanded details on different foundation structure interactions with sand under quasi-static and cyclic loading are presented in the following chapters.

Chapter 5 Local and Global Granular Mechanical Characteristics of a Single Strip Footing-Sand Interactions

The aim of this chapter is to explore quantitatively and qualitatively the influence of the packing densities on the ultimate bearing capacity of the strip footing under plane strain condition and the deformations of the sand at localised level using DPIV. The ultimate bearing capacity refers to the ability of the soil to sustain the maximum load on the footing before the soil collapses. The planar model of different sand packings was filled in layers as detailed in **Section 3.3.3, Chapter 3**. The focus of this work is on systematically understanding the effects of packing density of the sand grains on both the internal and bulk mechanical properties for strip footing interacting with granular soil. The studies are based on DPIV method, coupled with a high resolution-imaging camera. This provides valuable new insights on the evolution of slip planes at grain-scale under different fractions of the ultimate load. This analysis based on quantitatively measurement of the velocity vectors at a whole area of the failure under the footing. The constitutive relation of sand (MISO) are validated initially for the case of strip footing interaction with sand packing of different densities with DPIV. The reported results would serve to the practicing engineers, researchers and graduate students in unravelling the mechanics of granular soil at both local and global levels when they interact with structures. The outcomes would be beneficial not only to the geotechnical engineering community, but also to related disciplines dealing with granular materials such as materials processing, minerals and space exploration. Most of the results reported here have been published in the Indian Geotechnical Journal (Jahanger et al., 2018a).

5.1 Introduction

Cohesionless sands comprise of discrete grains of varying size and packing density. Their mechanical behaviour is different from that of conventional solid, liquid and gaseous state of matter (Jaeger et al., 1996). Numerous researchers have studied the micromechanical characteristics of granular materials using experiments, theoretical descriptions and computer simulations (Duran, 2000; 2012). From the micromechanical perspective (Desrues and Viggiani, 2004), some studies have attributed the origin of shear strength

of granular media to the anisotropy of strong force chains (Radjai et al., 1998; Thornton and Antony, 1998; Antony, 2007). Their dilation characteristics are attributed to the displacement connection network of granular media (Kruyt and Antony, 2007).

In foundation engineering, ultimate bearing capacity (q_{ult}) and allowable settlement (S_{all}) are used as key design parameters (Hansbo, 1994; Bowles, 1996; Liu and Evett, 2004). In sand, settlement controls the design criteria of footing (Fang, 1991; Das, 2009) which is independent of the loading rate (Liu and Evett, 2004). In addition, the settlement of footings could depend on their width for a given soil (Das, 2009), but ultimate bearing capacity of sand is less dependent on the width of the footing (B) when less than 1m as reported by Terzaghi and Peck (1967). In soil-structure interaction analysis (Hansbo, 1994), engineers use constant vertical displacement profiles for rigid footings interacting with sand at the level of the footing. However, the settlement in sand could vary significantly below the level of the footing-sand interface within the influence zone of depth (z) about 2-4 times B in homogeneous sand (Schmertmann et al., 1978; Powrie, 2014). The previous researches discussed above on the settlement profiles along the footing central axis do not vary linearly with depth. However, detailed information on how the displacement field evolves within the sand bed under mechanical loading is still not well established. Historically, bi-linear model (simple triangle approximation) is used to describe the variation of elastic displacement in sands (Schmertmann et al., 1978) and others use nonlinear variation (Mayne and Poulos, 1999) At the micro scale, grain displacements are non-uniform (Liu and Iskander, 2004). However, experimental results on the role of relative density of sand for all three major types, loose, medium-dense and dense sand on their geomechanical characteristics using DPIV is not yet probed systematically. This is addressed here using two-dimensional DPIV. The Dynamic Studio Software Platform (DSSP) helps to display the large amounts of DPIV-based experimental data in pictorial forms (DantecDynamics, 2013). Recently DPIV was applied to understand the flow properties of granular materials (Albaraki and Antony, 2014). Here, it is worth mentioning that focus was given on the local deformation, velocity fields and bulk strength for different relative densities of sand when a strip shallow footing interacts with sand under quasi-static axial loading (P). The aim is at first to compare the variation of displacement fields measured in sand packing using DPIV with FEM analysis. Thereafter, the variation of fundamental mechanical features at both local and global scales are studied in detail using DPIV for strip footing interacting with sand packing of different relative densities in a systematic manner.

5.2 Materials

Materials used in this chapter are the disturbed dry silica sand samples obtained in UK that described in **Section 3.2, Chapter 3**, having a particle size range of 0.1 mm- 1.0 mm. Sand properties were characterised according to the American Society for Testing and Materials (ASTM 1998; Head, 2006). Their experimentally measured material properties and size distribution using the sieve analysis as shown in **Figure 3.1**. **Table 3.1** shows the properties of sand were obtained from the soil characteristics test. These data revealed that the soil chosen is classified as poorly graded sand (SP) according to the Unified Soil Classification System (Liu and Iskander, 2004; Cerato and Lutenegger, 2007; Tafreshi et al., 2011; Cicek et al., 2014; Tehrani et al., 2017; Ziccarelli et al., 2017). The roughness of the footing base, sidewall of the footing and the Perspex wall were characterised and evaluated in the mechanical engineering laboratory as in **Section 3.3.2, Chapter 3** and the results are presented in this Chapter.

5.3 Methodologies

5.3.1 DPIV Analysis

In this study, DSSP is used to analyse the digital images acquired during test using DPIV. The DSSP platform provides a range of techniques for characterising particle motions, making it the most convenient for making advanced scientific imaging-based measurements (DantecDynamics, 2013). In this study, the AoI or the target area (full image) was specified before being divided into sub-sections called IA of 16 pixels ×16 pixels each covering a zone of soil approximately 2.2 mm^2. Each of these IA was tracked using an adaptive PIV method to identify the movement of soil based on particle images (here 30 images per second) obtained from the front of the Perspex planar test box. The IA sizes from each successive image are cross-correlated with each other, pixel by pixel (DantecDynamics, 2013). A velocity vector plot over AoI is acquired by repeating the cross-correlation for each interrogation area over the two images (DantecDynamics, 2013). More details are discussed in **Section 4.2, Chapter 4**.

5.3.2 FEM Simulations

In the present study, ANSYS is used to create a two-dimensional solid geometry. The chosen domain along with applied boundary conditions is shown in **Figure 5.1**. The simulations were held under identical boundary conditions for footing indenting with different types of sand packing as in the case of physical experiments. The contact regions between the rigid footing and the sand were modelled as a relatively rough surface (interface friction coefficient=0.25) corresponding to the experimental study (Armin et al., 2014; Gordan et al., 2014; Lee, 2015). An adaptive FE mesh was generated at the footing-soil interface where the largest stresses and strains would be expected. It should be mentioned that Skewness mesh metric (a measure of mesh quality) of 0.132 maximum value was obtained which is acceptable (Lee, 2015). The size of the elemental geometry is shown in **Figure 5.1**. The nodes and element numbers in the soil body are equal to 44000 and 14360 respectively. More details are discussed in **Section 4.3, Chapter 4**.

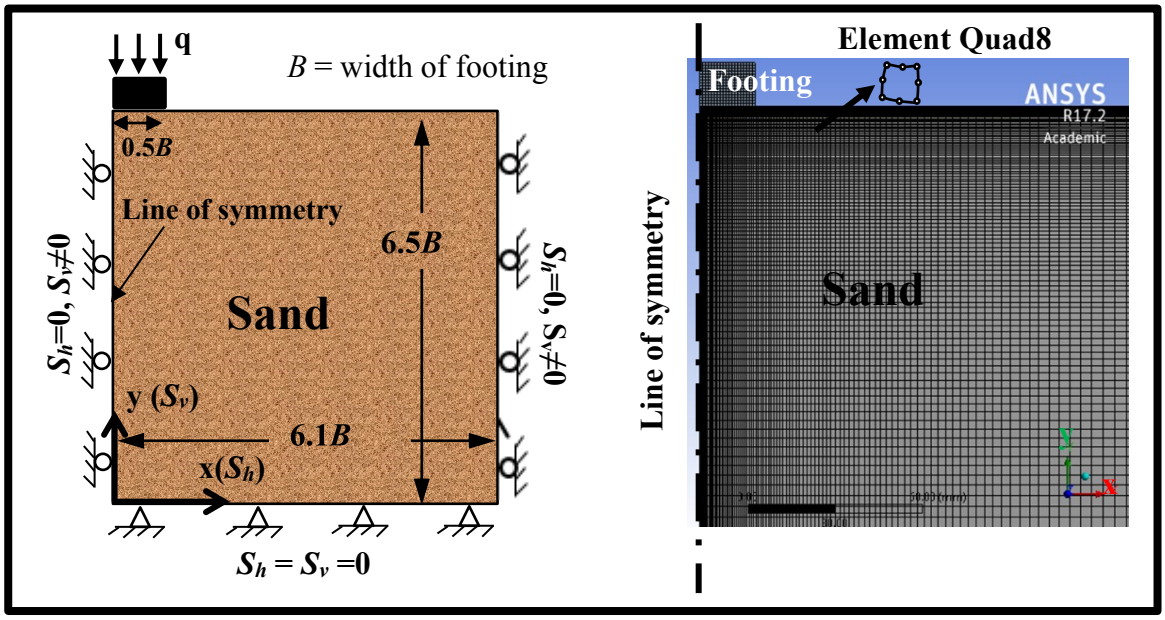

Figure 5.1 Strip footing on single homogeneous sand layer (left) chosen domain and boundary conditions, not to scale (right) finite element mesh, and element enlarged

The initial state of stress is important in FEM modelling of geotechnical problems. Hence, standard earth gravity is applied prior to the application of the external load. The width of the loading area is 0.5*B*. The loading is applied vertically in increments of constant displacement of 0.15*B*, uniformly across the width of the footing within the time step of 0.01 second (~300 cumulative iteration). The evolution of different displacement

components in the solid geometry (depicting the sand packing) is tracked for different loading levels and compared with corresponding DPIV measures later. More details can be found with discussion in **Section 2.4.2, Chapter 2**.

5.4 Experimental Work for DPIV Test

Bearing capacity of the model-scale footing was tested using the aluminium planner box of 460 mm in length, 300 mm in height and 39 mm in thickness, filled with the dry silica sand. The box had smooth and transparent Perspex walls of 15 mm thickness also to eliminate any bending effects during the test, as illustrated in **Figure 5.2**. It is worth mentioning that it is also verified during all tests that under the ultimate loads (P_{ult}) of the dense sand packing did not lead to any remarkable out of plane movement of the of the walls occurred along the thickness direction. This was checked using a dial gauge (0.01 mm resolution) mounted to the sidewall from a magnetic base (though the picture of this arrangement is not included here). The surface roughness of the footing in contact with sand, and the Perspex walls of the experimental box was measured using 3D optical microscopy based on white light interferometry (White and Bolton, 2004; Jahanger et al., 2018a; 2018b) from which the mean roughness value R_a was obtained as 3.204 μm and 0.09 μm respectively. The rigid foundation base was relatively rough (ratio between the angle of interfacial friction of the footing (δ) and angle of internal friction of the sand (ϕ), (δ / ϕ) is 0.25).

Two cases of footing width are considered in this study, i.e., smaller and larger footing width with dimensions 38 × 38 × 15 mm^3 and 76 × 38 × 15 mm^3 respectively (footing width B/D_{50} = 102 and 204 respectively to avoid any grain size effect, and height at least = 15 mm) was used here. It is recognised that the scale effects of the footing model could affect the estimations of their strength characteristics (Cerato and Lutenegger, 2007). For example, a footing with relatively small width would require a relatively low stress level in the laboratory experiments, as if it were on a denser "state" of soil than a larger footing, even if they were tested on sand with the same void ratio (Cerato and Lutenegger, 2007).

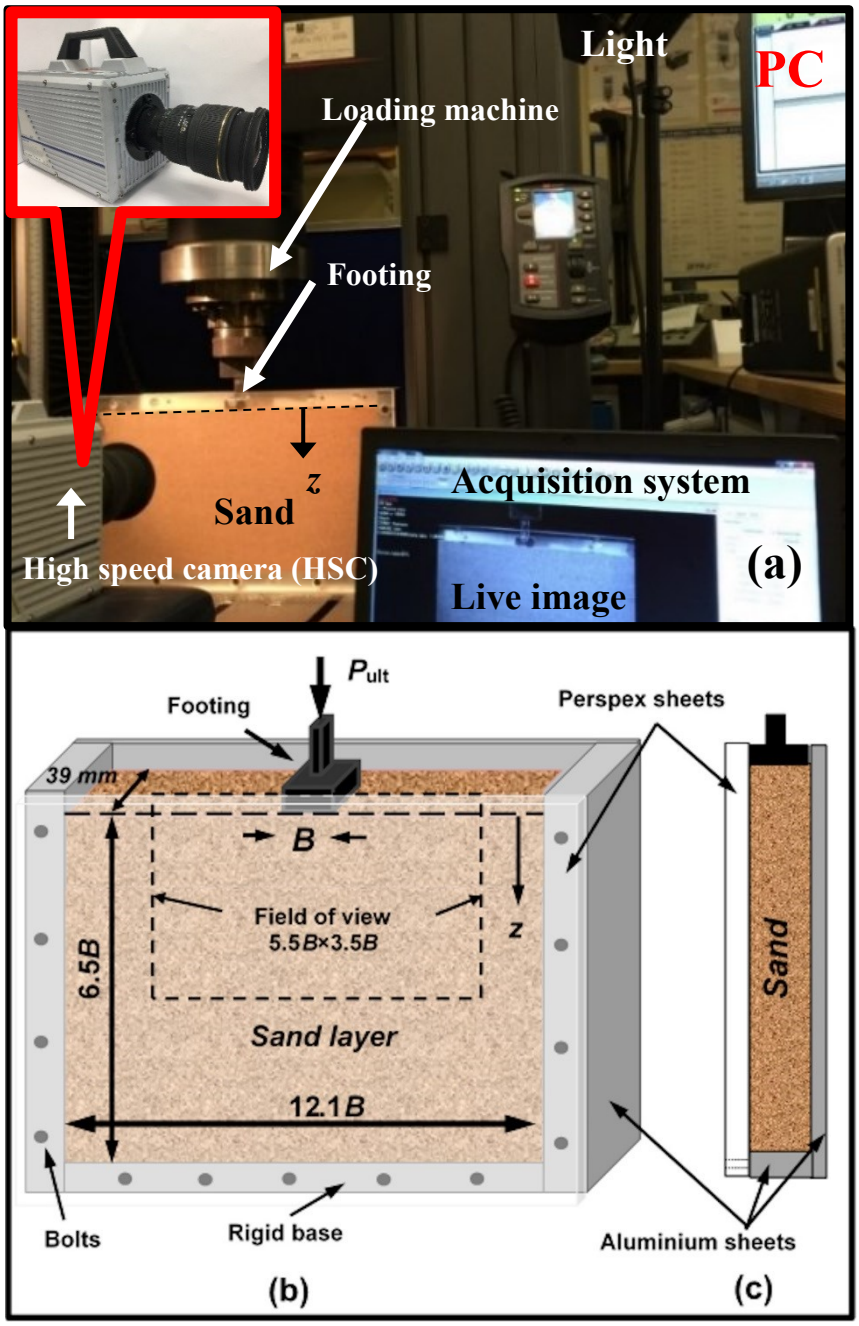

Figure 5.2 (a) Experimental setup using DPIV with a live image of footing in contact with sand (b)-(c) schematic diagram of the experimental setup (not to scale)

To minimize the scaling effect, it is suggested that the model testing for studying the effect of packing density should not be too close to the limits of void ratio (e_{max} and e_{min}, Altaee and Fellenius, 1994). Considering this in the present study, the packing densities are kept away from these limits (**Table 3.1**). The value of B/D_{50} used here is within the permissible limit of testing strip footing in the lab although footing sizes used in real practice could be higher (Lau, 1988). Such model dimensions have been used in previous experimental studies in this field (Raymond and Komos, 1978; Bowles, 1996; Raymond,

2002; Jahanger et al., 2016). To minimise any frictional effects of the footing with the wall, a small gap of 1 mm is allowed between the footing and the back wall, so that they do not affect the deformation of the soil recorded by DPIV at the front of the box. It is also worth noting that about 12.5% of particles were in the size range of 0.5-0.9 mm as shown in **Figure 3.1**, which helped to avoid any noticeable leakage of grains from behind the footing. These measures ensure that the observed movement from the images is due to the inner movement in the grains under mechanical loading (White and Bolton, 2004).

Three cases of relative densities (D_r) loose (L), medium-dense (M) and dense (D) were used in this study. The loose granular packing (γ=14.7 kN/m^3=1500 kg/ m^3, D_r =24 ±2%, e= 0.76) was prepared by pouring the grains mass uniformly across the width of the box in small layers using pluviation technique method (Kumar and Bhoi, 2009) so that any segregation of the grains was avoided during the construction process. The top surface of the sand layer was gently levelled off using a hand scraper. This researcher also took care not to disturb the constructed loose sample in any way before applying the axial loading in our experiments. The mass of sand grains laid in the box to the required height pertains to the density of the loose sample. The medium-dense packing (γ=15.30 kN/m^3, D_r =53 ±3%, e= 0.7) was hand compacted in three layers, using 50 blows per layer in 0.035 m lifts each with a 16 cm^2 compaction hammer of 1.1 kg (10.3N) weight designed for this purpose, which resulted in a theoretical energy of 0.36 Nm (J) (Cerato and Lutenegger, 2007; Jahanger et al., 2016). The dense sand (γ=15.80 kN/m^3= 1610 kg/m^3, D_r =72 ±3%, e= 0.64) was achieved in five layers, 60 blows per layer. The footing was placed symmetrically on the surface of the sand layer. More details can be found with discussion in **Section 3.3.3, Chapter 3**.

An axial compression loading (q) was applied slowly on the footing (0.05 mm/s penetration velocity) using the Instron loading machine with 5kN/0.1N resolution, as illustrated in **Figure 5.2**. The loading machine also had an inbuilt dial gauge (linear variable differential transformer, LVDT) to record the vertical displacement of the indenting footing on the sand packing. The macroscopic load and vertical displacement of the footing were also measured from the tests. The DPIV camera with an allowable frame speed up to 100000 frames per second (fps) was fixed in front of the box and two light sources were used to illuminate the rig. However, as the loading condition is quasi-static in this study, the recording at 30 fps was found to be adequate until soil failure was reached, although higher frame speeds were considered in the early stages of the experimental programme. We had verified that the recording at greater than 30 fps did

not affect the result noticeably. The resolution of the images was 1920 × 1080 pixels. Initially, a few trials were conducted to determine the suitable acquisition rate of the recorded DPIV images for the analysis. It was found that, for the current experiments, an acquisition of 1 frame/s of the recoded images is adequate in which images were captured at displacement increments of 0.0017 mm. DSSP was used to analyse the images using an adaptive PIV (DantecDynamics, 2013). Here, the distribution of velocity vectors of the grains was examined in the image analysis using searching area of a minimum interrogation area (IA) of size 16× 16 pixels and maximum IA size of 64 × 64 pixels with a measurement resolution of sub-pixel (DantecDynamics, 2013). The space-pixel dimension of the measurement was calibrated by printing a known scale on the test box along the horizontal and vertical directions. White et al. (2003) have shown that the precision of the measurement (i.e., the random difference between multiple measurements of the same quantity) improves with larger PIV patches and it is inversely proportional to the amount of the measurement resolution. This size of the mesh patch used here reveals a standard error better than 0.01 pixel (DantecDynamics, 2013; White et al., 2003). In the experiments, two illumination lights were positioned above the testing box to avoid reflection and glare on the measurement side of the Perspex wall. It was verified that the variation in image scale in both horizontal and vertical direction were not significantly different by printing black dots on the Perspex sheet to validate the spatial-temporal scale. The DPIV camera lens was focused normal to plane the footing-soil interface region where the measurements are most important to make. Therefore, the dimension of area of interest (AoI) was ~ 5.5B× 3.5B (**Figure 5.2**). A typical mean size of sand grain (D_{50} = 0.37 mm) was represented by about 3×3 pixels. Hence, the DPIV experimental measurements made here are at the local-scale.

Following the footing tests, two standard cone penetration (CPTs) tests were also conducted for each soil density to characterise the samples medium using a 10 mm diameter model CPT (O'Loughlin and Lehane, 2010; Dijkstra et al., 2013; Jahanger and Antony, 2017a; 2017b; Jahanger et al., 2018a; 2018b). These were located either side of the footing, at an approximate 2B-3B from the footing centre. The CPT was inserted at a penetration rate of 1 mm/s in the current experiments as shown in **Figure 5.3**, but using the identical filling procedure of the grains used in the footing–sand indentation experiments presented earlier. **Figure 5.3** shows the average CPT penetration profiles for the soil for all sand packings. The cone penetration resistance (q_c) profiles in linear or semi-log scale type are plotted against the penetration depth from the bottom level of the

footing (z) and against the normalised penetration depth (z/B). These results are compared to the results from O'Loughlin and Lehane (2010) and Dijkstra et al. (2013).

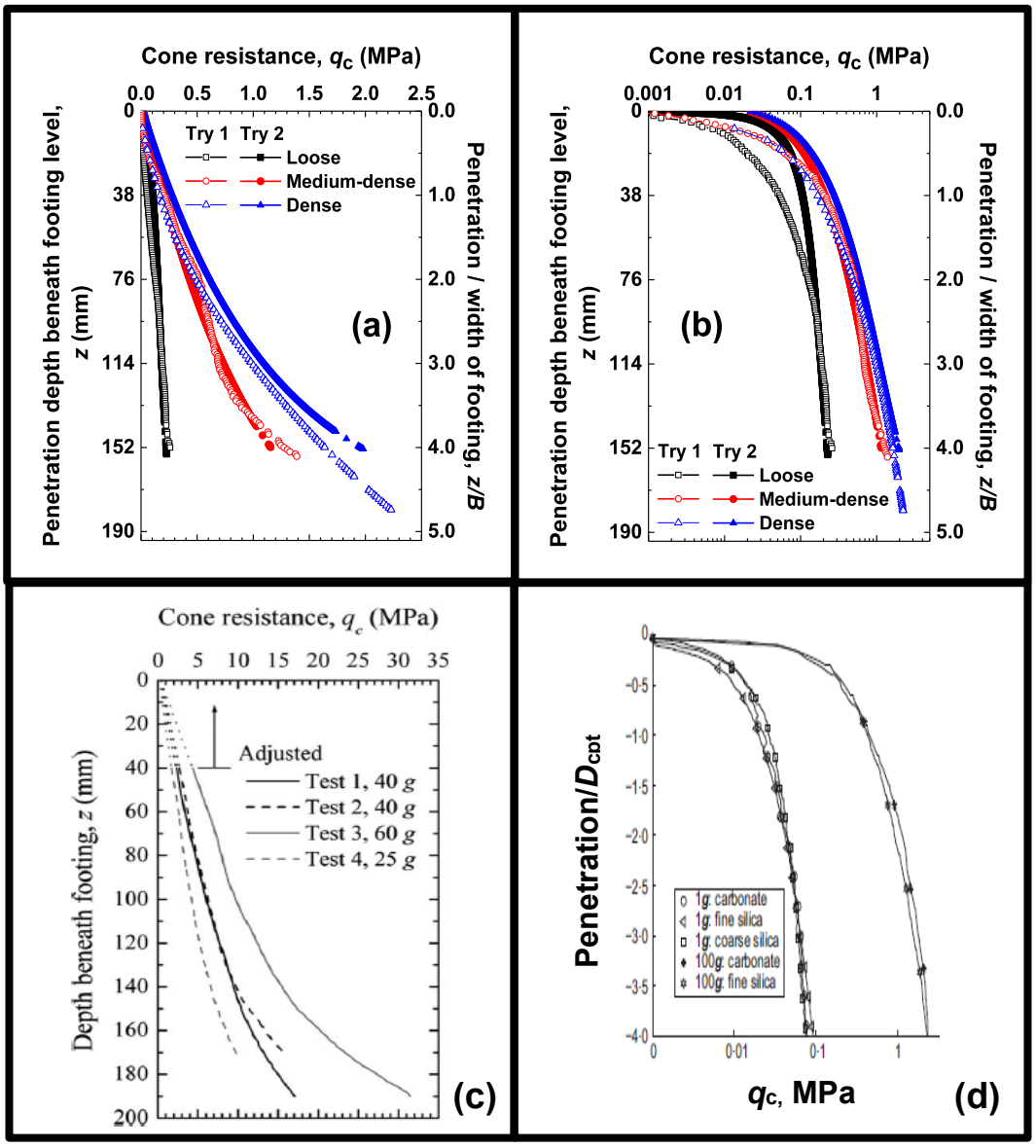

Figure 5.3 CPT data for the three sand packing (a) cone resistance versus penetration (b) log cone resistance versus normalised depth (c) O'Loughlin and Lehane, 2010 (d) Dijkstra et al., 2013

As expected, the penetration resistance (q_c) of dense sand is higher than medium-dense and loose sand. The penetration resistance (q_c) of loose sand remains almost constant with depth after z/B =2.5, but penetration resistance for medium-dense and dense sand increase with depth at an increasing rate. The rate of the penetration resistance (MPa/mm) of dense sand is larger than that of the medium-dense. Again, the differences in the penetration

resistance (q_c) for different relative densities are primarily accounted for the relatively larger volumetric compressibility in loose, medium-dense sand than the dense sand. The CPTs results for all the densities show the average response of the two results (error within 5%).

5.5 Results and Discussions

5.5.1 Macroscopic Analysis

The load–settlement relationship for a typical footing (B=38mm) interacting with sand is presented in **Figure 5.4**. The loading rate was kept constant throughout all the tests at the rate of 0.05 mm/s, which was slow to simulate the quasi-static loading scenario. It is worth mentioning that the DPIV curves loads are simultaneously measured using the corresponding load outputs from the Instron. The settlements obtained using the DPIV and LVDT gauge agree well. This justifies applying DPIV to examine the displacement measures in sand layer later.

Lutenegger and Adams (1998) compared few ways in the literature to measure the ultimate bearing capacity from loading curves. The ultimate bearing capacity refers to the ability of the soil to sustain the maximum load on the footing before the soil collapses. These are a tangent intersection method, a log-log method and a 0.1B method. They found that the value of predicted q_{ult} increases according to the log-log method, the tangent intersection method then the maximum from the 0.1B method. Vesic (1973) reported that very large displacement of the order of 50% of the footing size is required to get the ultimate bearing capacity. The tangent method was used to determine the ultimate bearing capacity in order to consistently and equally compare each loading response. Using the load-settlement data, the tangent intersection method (Akbas and Kulhawy, 2009) was applied to obtain the value of the ultimate bearing capacity, as illustrated in **Figure 5.4**. This involves linear curve fittings for the initial loading and hardening phases of the load–settlement relations. The intersection point of these two lines thus corresponds to the q_{ult}. The ratio of ultimate vertical settlement under ultimate load (S_u) to footing breadth (B), S_u/B is ~ 5.0, 7.1 and 11.7 % for the loose, medium-dense and dense sand respectively. These measures and the nature of bulk load-settlement curves are consistent (Das, 2009) with punching (without a well-defined peak), local shear failure (moderate peak) and

general shear failure (well-defined peak) for sand described by Liu and Iskander (2004), Dijkstra et al. (2013), Vesic (1973).

It is worth mentioning that a good level of comparison with De Beer's study (1965) for the variation of N_γ (Bearing capacity factor) with γB for different sand packing were obtained. Both the bearing pressure and the failure strain increase with the packing density of sand.

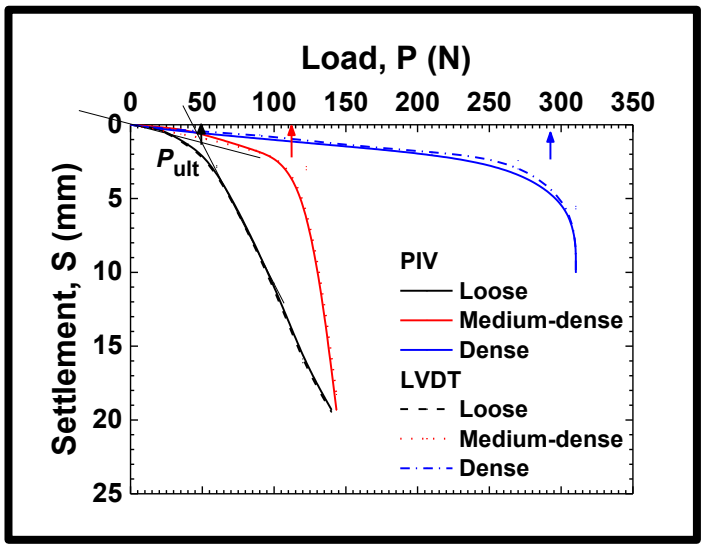

Figure 5.4 Load-settlement curves of footing (B=38mm) interacting with loose, medium-dense and dense sand. The guide arrows show the ultimate load level (P_{ult})

Figure 5.5 shows the measured values of N_γ embedded and compared qualitatively with previous research for the circular, squares and rectangular footings (De Beer, 1965; Cerato and Lutenegger, 2007). It can be seen that the test results are within the range of the computed values presented by other researchers. N_γ decreases with a decrease in the sand packings and width of the footing (De Beer, 1965; Ismael and Ahmad, 1990; Cerato and Lutenegger, 2007; Kumar and Bhoi, 2009; Jahanger and Antony, 2017a; 2017b). The results also indicate that sand packings may have a more pronounced influence on N_γ than footing size that the rate of decreasing of N_γ is larger in dense sand than medium-dense and loose sand and that is consistent with Cerato and Lutenegger (2007). It is worth pointing out that, in the case of strip footings used in practice, 3D condition could exist around the ends of the strip footings even if the footing is long. However, for most parts of long strip footings, plane-strain condition could exist (White and Bolton, 2004;

O'Loughlin and Lehane, 2010) as assumed in the current 2D plane-strain experiments (Raymond, 2002; Lemmen et al., 2017).

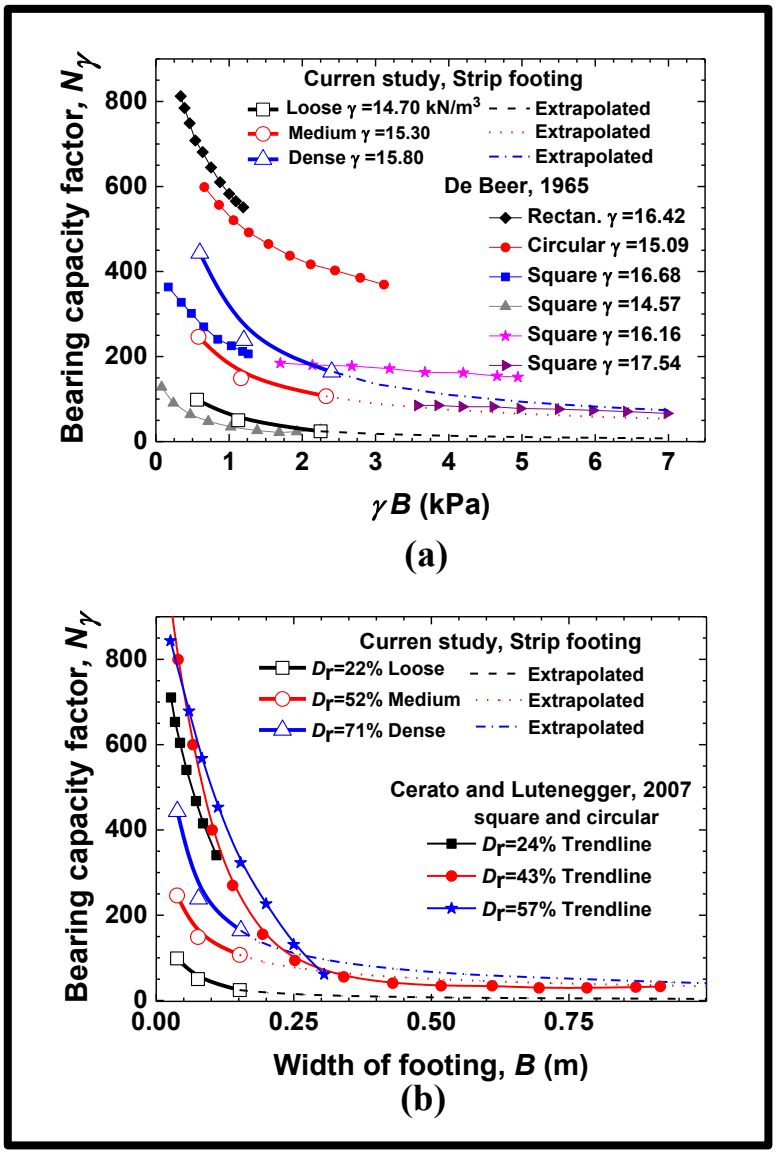

Figure 5.5 Comparison of the variation of $N\gamma$ with γB and B

The peak angle of internal resistance (ϕ_{peak}) for all cases of the packing density was also determined from triaxial compression test at different confining pressures 100, 200, and 300 kPa. For sands, the angle of internal friction typically ranges from 26° to 45°, increasing with the relative density. Three cases of relative densities were used as that in the experiment tests: loose, medium-dense and dense. Subsequently, the plots of deviator stress (σ_d) against axial strain (ε_a) were made. The peak angle of friction of the soil is obtained according to the stress state at peak strength. The measured angles of internal

friction are 32°, 39°, and 44.3° for loose, medium-dense and dense sand respectively. Using these, the peak angle of shearing resistance of the samples was evaluated and plotted against the relative density (D_r) as illustrated in **Figure 5.6**. This variation is described as:

$$\phi_{\text{peak)tr}} = 24.7 + 0.267\, D_r \tag{5.1}$$

Where angle of internal friction measures in degree. In addition, the (ϕ_{peak}) determined from the standard direct shear test (DST) (ASTM D3080) under three different normal stresses 50, 100 and 200 kPa. The measured angles of internal friction are 32.4°, 39.5° and 46.1° for loose, medium-dense and dense sand respectively. The peak angle of shearing resistance of the samples was evaluated and plotted against the relative density as well in **Figure 5.6**. This variation is described in a mathematical form in **Equation 4.2** as follows:

$$\phi_{\text{peak)ds}} = 25.2 + 0.277\, D_r \tag{5.2}$$

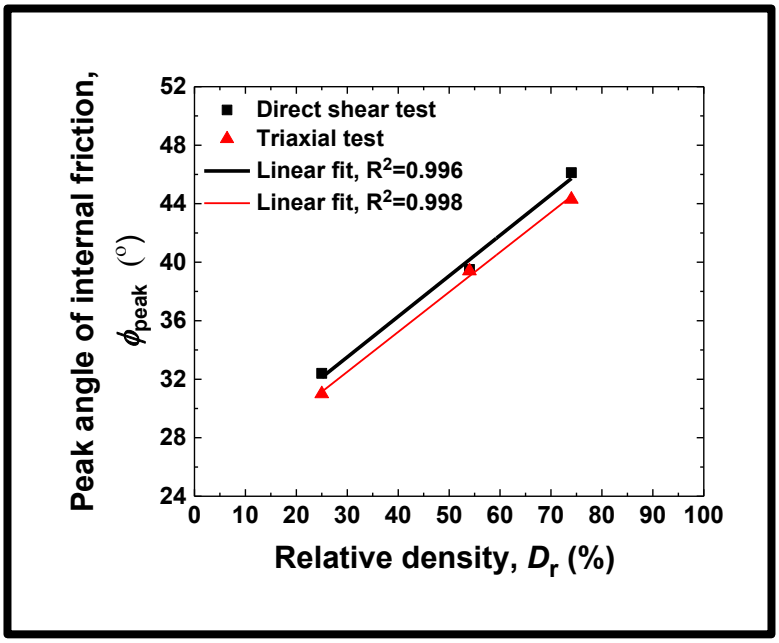

Figure 5.6 Peak angle of internal friction versus relative density of sand obtained from DST and triaxial tests

These macroscopic relations obtained from the characterisation experiments agree with other literature (Bowles, 1996). It is worth mentioning that, some literature suggest that the shear friction angle measured using DST may not pertain to that of sand under the plane strain experiments (Kumar and Bhoi, 2009). Jewell (1989) suggested that symmetrical DST could provide a more reliable measure of the plane strain angle of friction and the angle of dilation for sand than conventional direct shear test. In some studies, the angle of internal friction of sand obtained from the conventional DST also correlated well with the experimental results of plane strain condition (Leshchinsky and Marcozzi, 1990). However, in analysing the footing-soil interactions using theoretical and computational methods by idealising soil as an elastic media (Selvadurai, 1979); friction angle does not form as a direct input in the analysis. Therefore, before probing the microscopic displacement features of the granular media in more detail (presented below), it is made sure enough that the macroscopic characteristics of the used samples are consistent and robust.

5.5.2 Comparison of the DPIV Measurements with FEM Analysis

To validate the use of the user-defined constitutive relation of sand (MISO) in FEM analysis with DPIV measurements, here the typical results are presented below for the case of single footing interacting with the dense sand packing. **Figure 5.7 (a,b)** shows the variation of DPIV-based vertical displacement component and horizontal displacement component (S_h) profiles in the dense sand at ultimate load and compared with the FEM (ANSYS) analysis. It is evident that a good level of agreement between the DPIV and FEM approaches are obtained both qualitatively and quantitatively up to 2.5B from the footing edges. As the far-field displacements (>2.5B) are generally considered as unimportant in the foundation engineering designs of footing-sand interactions. Furthermore, quantitative comparison of variation of the normalised vertical displacement component (S_v/B) and the normalised horizontal displacement component (S_h/B) along a horizontal section at a depth of 0.5B below the level of footing under the ultimate load is provided for different packing conditions of sand, as illustrated in **Figure 5.8**. A good level of agreement is obtained between them. **Figure 5.7 (c, d)** shows the variation of normal and shear elastic strain contours at ultimate load for the case of dense sand using FEM. It can be seen from the normal and shear elastic strain map that there is a strain concentration around the corner of the footing. It can be noticed from the contours of shear strain in the dense media that the soil is sheared in the area below the edge of the

footing. Though not presented here, similar observations were made for the loose and medium-dense sand packing used in this study.

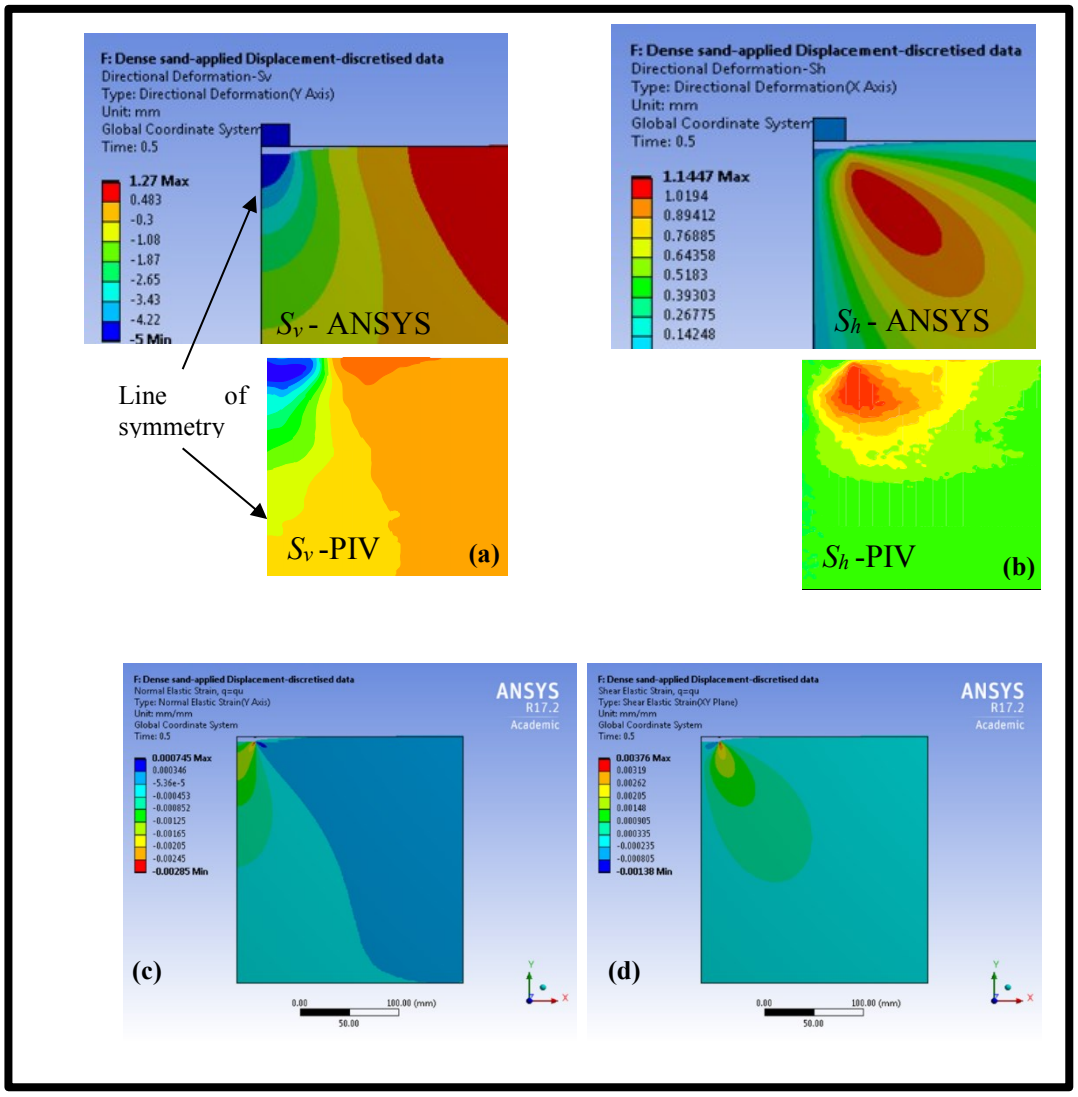

Figure 5.7 Comparison of DPIV-based vertical displacement profile in dense sand at ultimate load below the footing with FEM analysis (identical colour codes are used): (a) vertical displacement component (b) horizontal displacement component below the footing. Taking advantage of FEM, the strain distributions are presented: (c) normal and (d) shear elastic strain

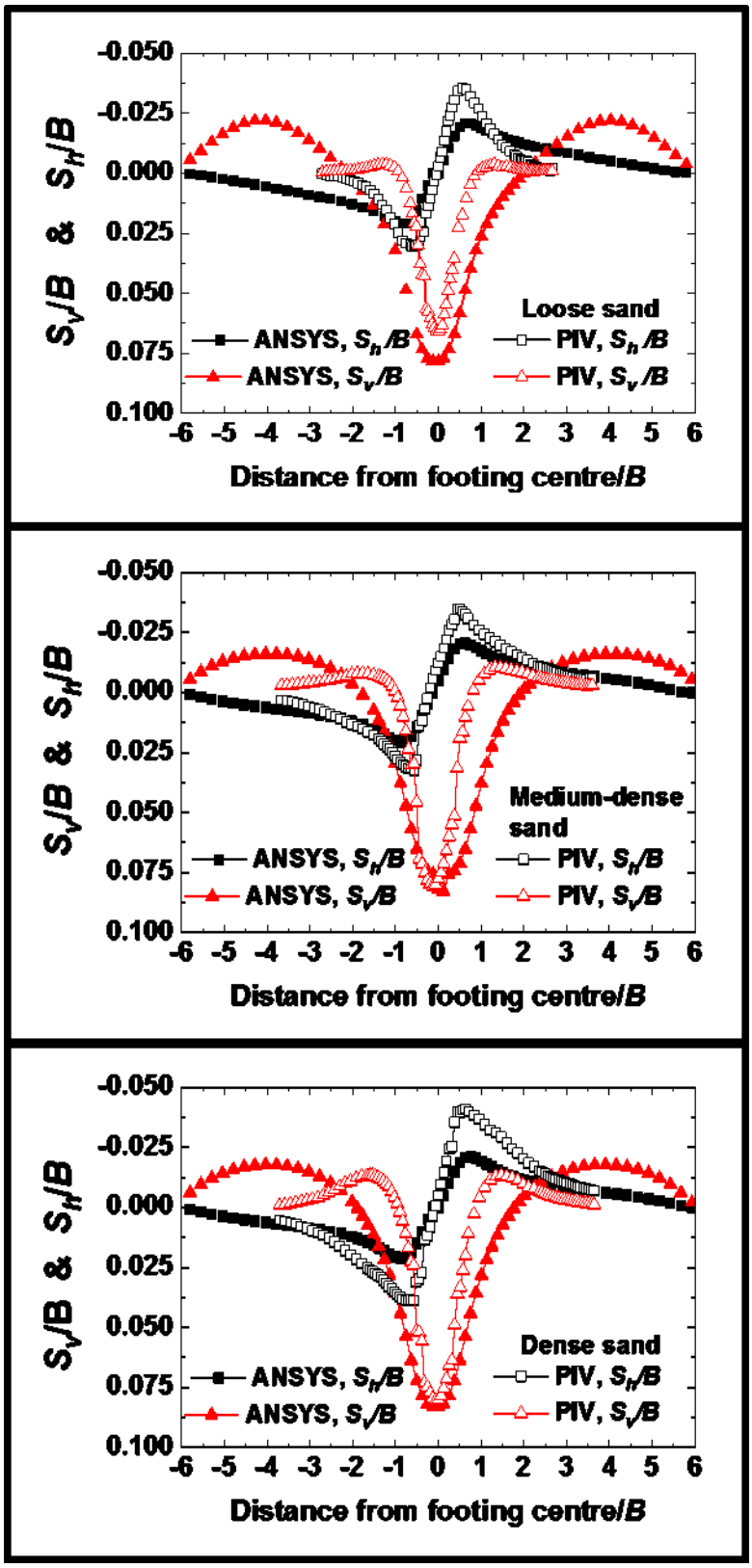

Figure 5.8 Comparison of DPIV and FEM based results on the vertical displacement component (S_v/B) and horizontal displacement component (S_h/B) along a horizontal section at a depth of 0.5B below the footing on different sand packing

5.5.3 Analysis of Footing-Sand Interactions

5.5.3.1 The Mechanism of Failure

Figure 5.9-Figure 5.11 present a detailed evolution of the resultant velocity (S_R) vectors in the sand packing under four stages of loading of q = 0.34q_{ult}, q = 0.68q_{ult}, q =q_{ult} and q>q_{ult} (typically for B= 38mm). Also, the corresponding evolution of vertical and horizontal strain rate ($\dot{\varepsilon_v}$ and $\dot{\varepsilon_h}$ respectively) in the sand packing are provided which help to identify the difference regions of granular flow in the sand packing such as dead, active and passive zones as discussed below. It is worth mentioning that had verified that these generic observations were similar in the case of the larger footing width (B=76 mm). In this plot, the contours of the vertical velocity are also obtained from the DSSP and superimposed for information. It is worth mentioning that the resultant velocity S_R is given as:

$$S_R = \sqrt{(S_h)^2 + (S_v)^2} \tag{5.3}$$

At the early stages of the loading (c.a. q<0.5q_{ult}), approximately a triangular wedge of dead zone (region 1 in **Figure 5.9-Figure 5.11** with a constant amount of resultant velocity of the grains but has the highest vertical velocity) is formed beneath the footing in all cases of packing densities (Terzaghi, 1943). It is worth mentioning that the dead zone does not mean that the grains are not moving at all but move as a block of grains with almost the same velocity. In granular mechanics, the dead-zone is characterised by the block of materials beneath the indenting objects with the granular materials and moving as if they are continuous extension of the indenter, i.e., no slip at the indenter-granular interface (Murthy et al., 2012). Noticeably, outside this zone the particles tended to move downward and sideward symmetrically until the ultimate bearing capacity is reached in the sand packing. Similar trends were noticed in other studies, for example in sand (Murthy et al., 2012), different soil types (Terzaghi, 1943) and soft metal (Prandtl, 1920).

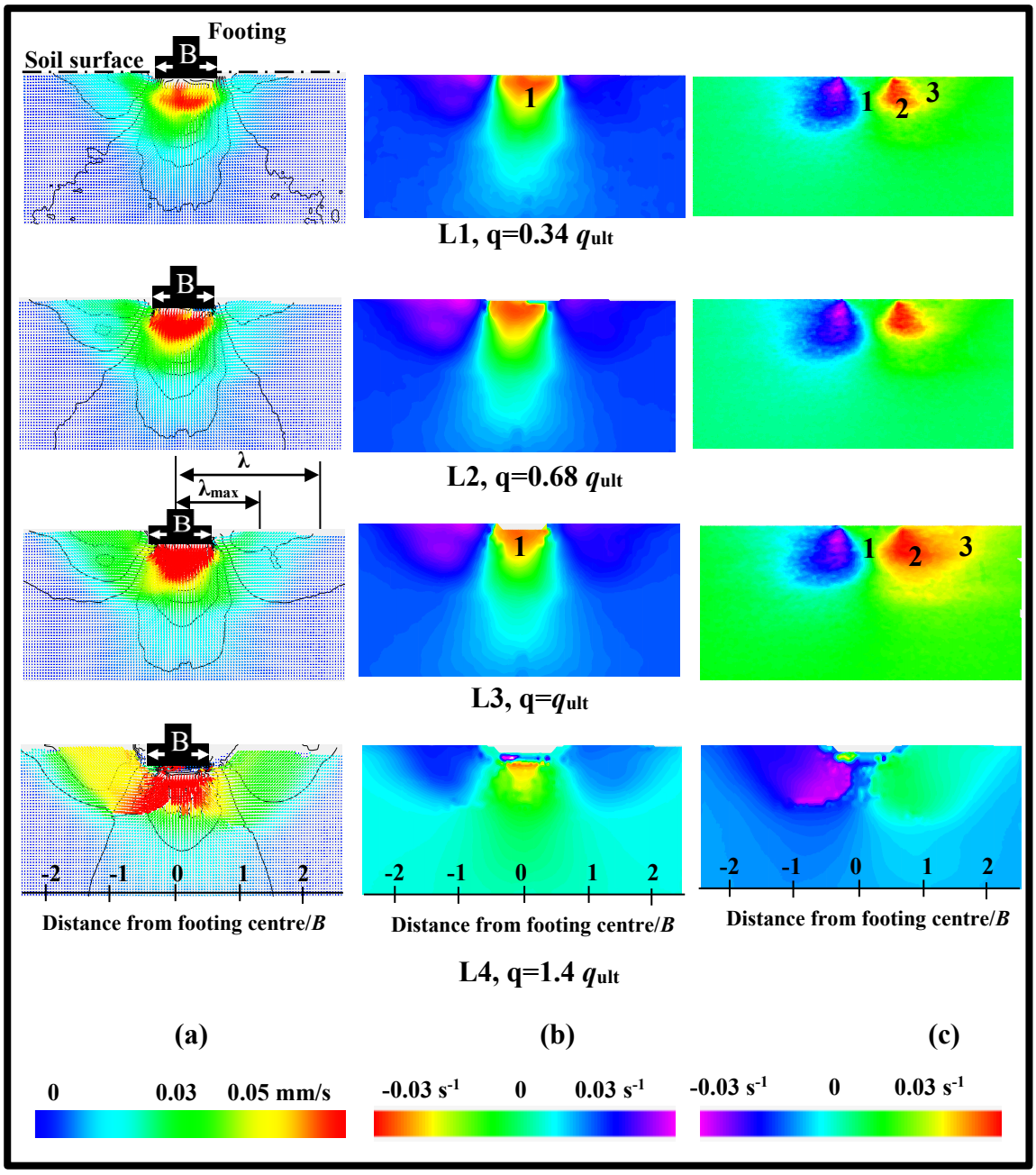

Figure 5.9 (a) Evolution of the resultant velocity vectors at a typical loads in loose sand and the scalar contours of the vertical velocity using DPIV (b) vertical strain rate $\dot{\varepsilon}_v$ (c) horizontal strain rate $\dot{\varepsilon}_h$. Zones: 1- dead zone, 2-active zone, 3- passive zone. B= 38 mm

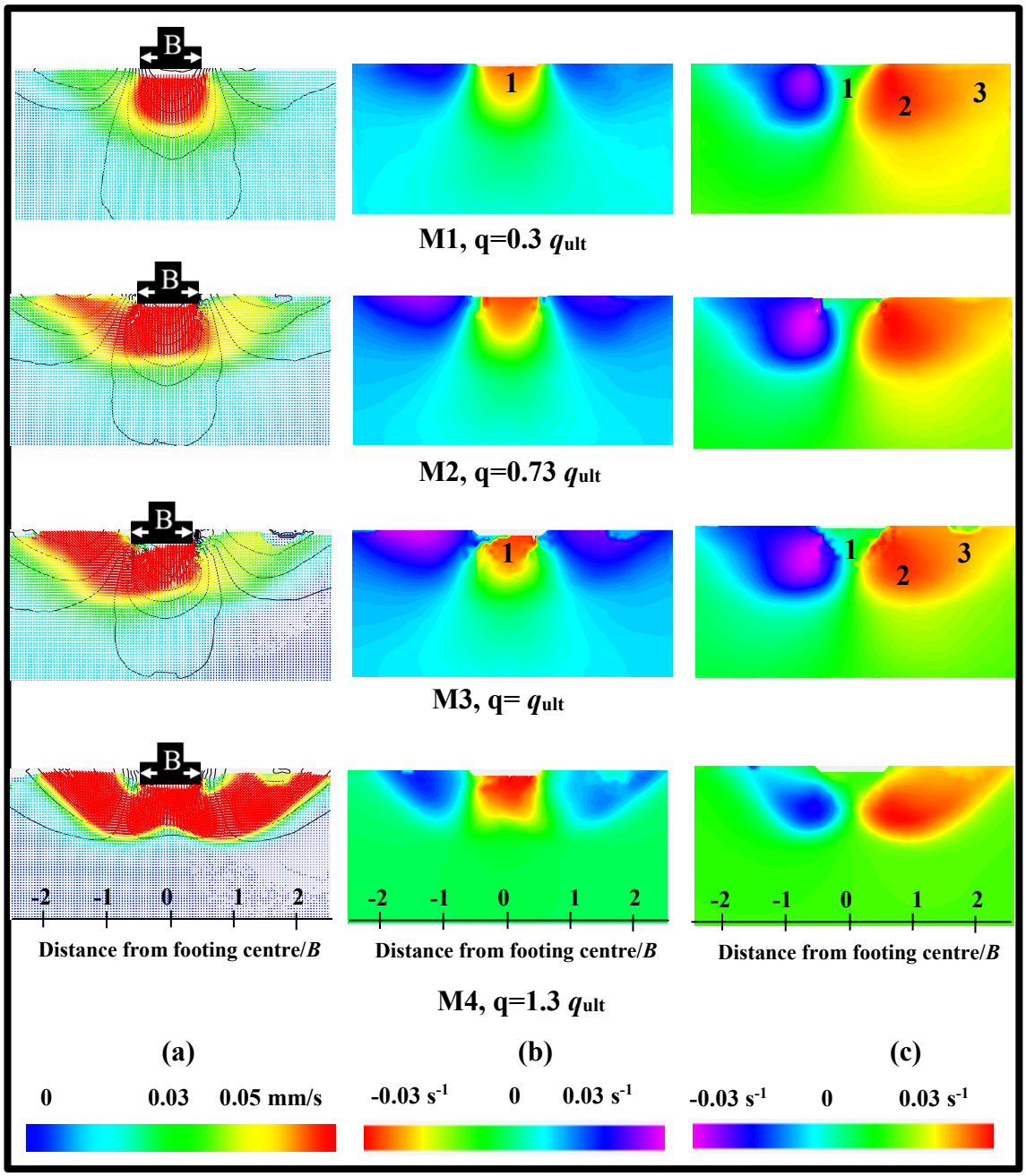

Figure 5.10 (a) Evolution of the resultant velocity vectors at a typical loads in medium-dense sand and the scalar contours of the vertical velocity using DPIV (b) vertical strain rate $\dot{\varepsilon_v}$ (c) horizontal strain rate $\dot{\varepsilon_h}$. Zones: 1- dead zone, 2-active zone, 3- passive zone. B= 38 mm

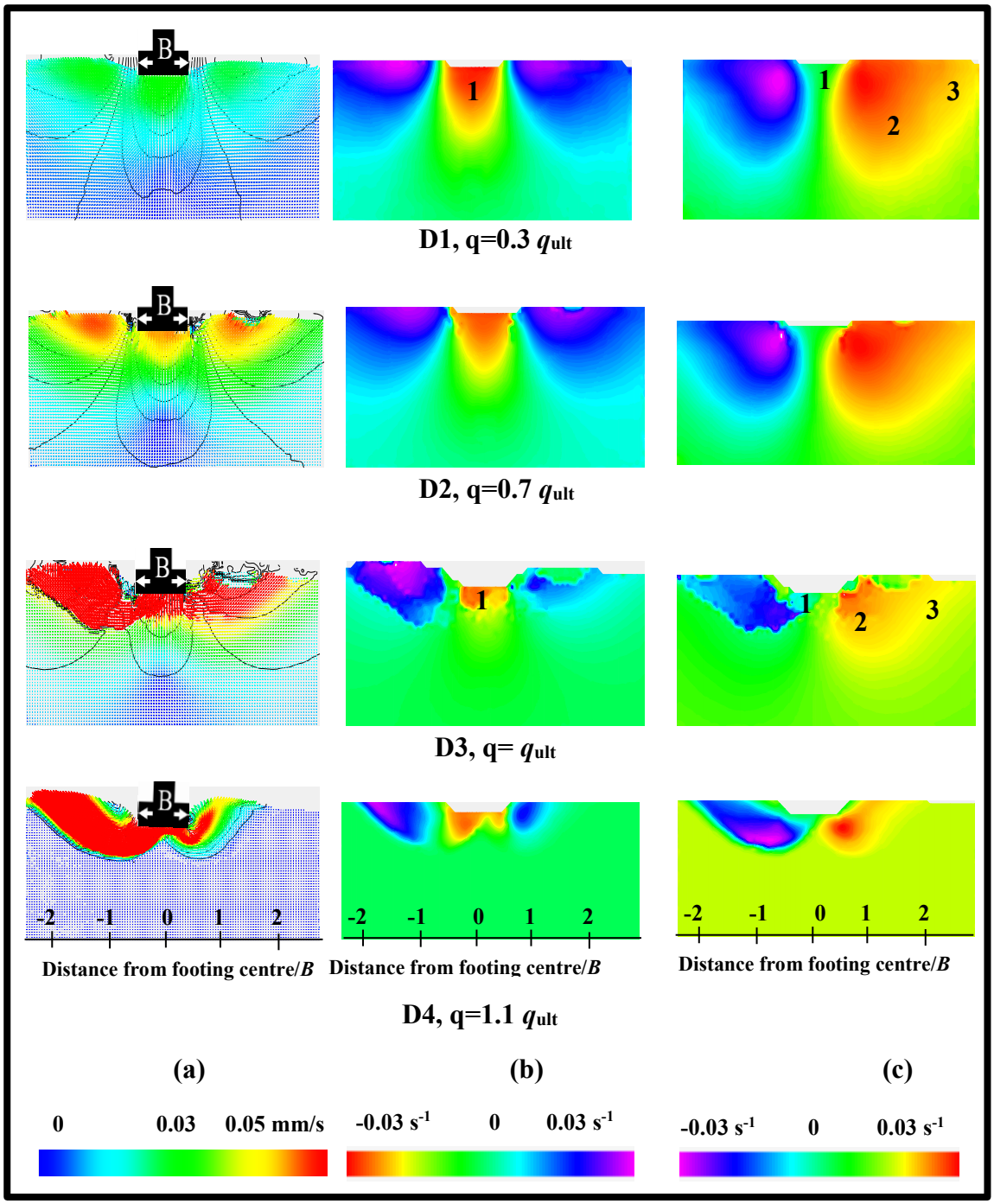

Figure 5.11 (a) Evolution of the resultant velocity vectors at a typical loads in dense sand and the scalar contours of the vertical velocity using DPIV (b) vertical strain rate $\dot{\varepsilon_v}$ (c) horizontal strain rate $\dot{\varepsilon_h}$. Zones: 1- dead zone, 2-active zone, 3- passive zone. B= 38 mm

The depth of this wedge at the ultimate bearing load is equal to about B, whose vertices (slip planes) intersect the horizontal at an angle (α = Angle of dead zone wedge/active zone 1) of about 62◦ ±2°. These are consistent with Prandtl's assumption (Prandtl, 1920) for smooth footing (α = 45+ ϕ/2), which have not been confirmed using microscopic experiments, but using DPIV here. Furthermore, Kumar and Kouzer (2007) have reported

similar measures for smooth footing using plasticity limit analysis with the help of finite element method (FEM). For a further increase in the load, the grains in the dead zone tend to punch the neighbouring grains in zone 2 radially outwards, as illustrated in **Figure 5.9-Figure 5.11**. A failure pattern consistent with Vesic (1973) at the ultimate failure load is visualised (**Figure 5.9-Figure 5.11**) for all cases of sand considered here. By and large, the grains flow symmetrically with respect to the central axis of the footing until reaching the ultimate load ($q=q_{ult}$) then, unsymmetrical flows occur beyond the ultimate load. This is consistent with the classical literature, e.g. Vesic (1973) for medium and dense sand, but the current study observes that this could happen in the case of loose sand as well. At ultimate load, the dense soil failed suddenly corresponding to the pronounced peak in the bulk strength curve as presented in **Figure 5.4**, and the unsymmetrically strong velocity distribution presented in **Figure 5.11** at the localised level. Therefore, in the higher relative density tests, the horizontal displacement (**Figure 5.11c**) seems to be highly non-symmetric under ultimate load. In reality, local structural non-homogeneities could exist, and this triggers the non-symmetrical flow of grain (post-failure) even under the symmetric loading conditions. Otherwise, the fixed footing may be loosened under ultimate load, leads to tilt a bit that may trigger the non-symmetrical behaviour. At this stage, the grains flow like a fluid. The grains beneath this flow region are solid-like and almost stagnant. The shear failure occurs progressively from the dead zone and extending radially outwards.

The sand surface forms a heap spreading up to about 2.7B, 2.6B and 2.4B away from the footing centre (λ= Distance of sand heap from the centre of the footing, as illustrated in **Figure 5.9**) for the loose, medium-dense and dense sand packing respectively, as illustrated in **Figure 5.9-Figure 5.11**. The height of the heap attains maximum at distances of about 1.7B, 1.55B and 1.31B for loose, medium-dense and dense sand respectively (λ_{max}= Location of sand heap attaining maximum height from the centre of the footing). The slope of sand heap at the ultimate load is 31°, 33° and 38 ° for the loose, medium-dense and dense sand respectively. The average value of the slop of the heap for the different sand packing is (34°) identical to the angle of repose of the sand. These angles are close to the residual angle of internal friction of the sand (ϕ_{cr}) about 31°, 33°, 37° for the loose, medium-dense and dense sand respectively. These residual angles are consistent with the previous literature (Bolton, 1986).

5.5.3.2 Schematic Failure Mechanism of a Plastic Equilibrium Wedge

The effect of sand packings at ultimate load on the failure mechanism are summarised both qualitatively and systematically as illustrated in **Figure 5.12** for a typical case of footing (B=38 mm). This shows the resultant velocity vectors of soil movement at ultimate bearing capacity and the schematic diagram of the failure mechanism underneath the footing of different packing densities. It is evident that the footing load test in the loose packing corresponds to a punching failure and local shear mechanism, consistent with the literature (Dijkstra et al., 2013). On the other hand, tests in the medium-dense and dense packings exhibit a general failure mode with relatively larger horizontal displacement and soil heap next to the footing edges, typical of a conventional rigid plastic bearing capacity, and Prandtl's wedge-shaped zone mechanism (Terzaghi, 1943). Hence, the formations of velocity discontinuities are linked to the density of the sand packing.

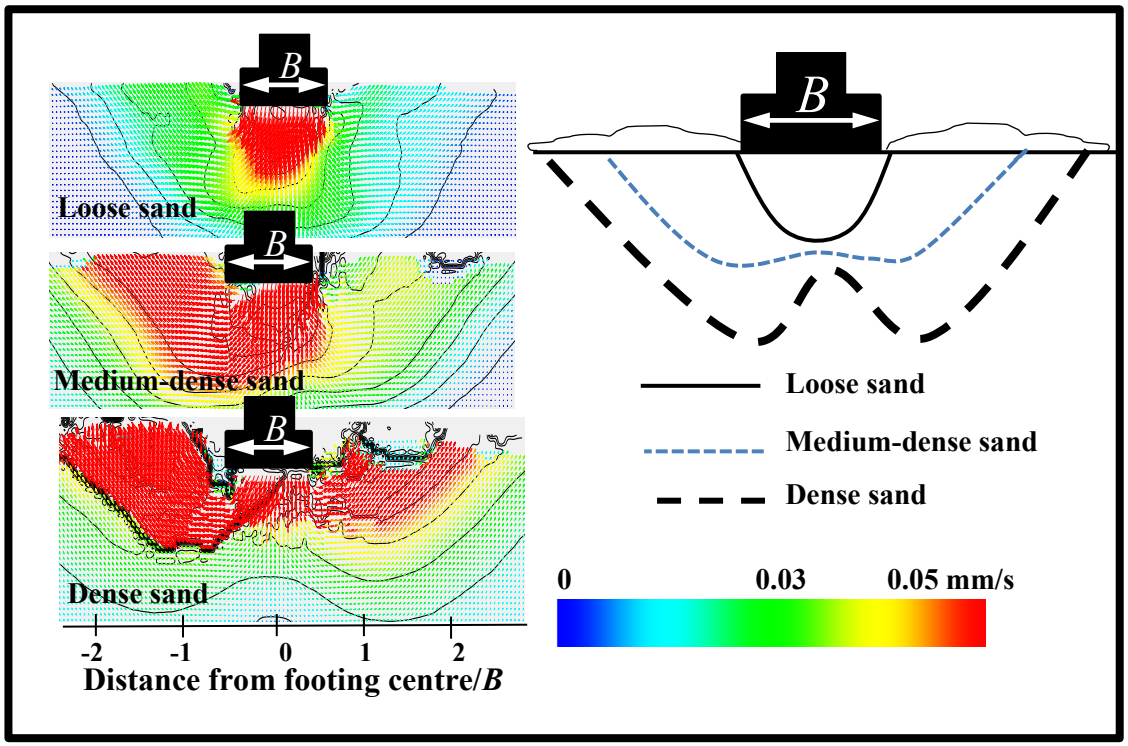

Figure 5.12 (left) Resultant velocity vectors of soil movement under ultimate bearing capacity, B=38 mm (right) sketch of general schematic failure mechanism underneath footing of different packing densities

Interestingly, the boundaries of the zone of plastic flow in sand at failure load sketched using DPIV here (in terms of the resultant velocity vector, and the components of strain rate presented in **Figure 5.9**-**Figure 5.11**) are remarkably similar to such intuitive diagrams suggested by Fröhlich in the 1930's (Terzaghi, 1943). However, at or beyond the ultimate load, the DPIV experiments have shown non-symmetric flow of grains even under the symmetric loading conditions on the footing. They could be attributed to the potential existence of (even minor level) non-symmetrical structural arrangements of the grains at local scale in reality. These could amplify the non-symmetrical velocity patterns under the above said condition that is consistent with experiments reported by Vesic (1973).

5.5.3.3 Vertical Deformation at Different Horizontal Sections

Figure 5.13 shows the typical normalised vertical displacement component in loose, medium-dense and dense sand at different horizontal sections below the footing-soil interface under q_{ult}. It is evident that at a depth of z/B=2.5 the vertical displacement is practically negligible in all cases of footing width and packing densities. Furthermore, for a given packing density, the normalised vertical displacement in the soil at a given depth (e.g. z/B= 0.1) decreases for an increase in the width of the footing under the ultimate load. However, here it is found that the absolute value of the vertical displacement in the soil for a given depth increases for increase in the width of the footing as also referred in other studies (Lutenegger and DeGroot, 1995). The heap close to the free surface (secondary peaks) increases with increasing relative density but decreases with z/B. Also, the heap height decreases with footing width as shown in **Figure 5.13**. This is related to potentially particles interlocking and rolling over of the grains. This has a significant effect in the development of the vortex map adjoining the footing sides (Murthy et al., 2012). The discontinuities in the velocity measures directly beneath the footing and the edges of the footing could result some error in the measurement (O'Loughlin and Lehane, 2010). However, these measurements are taken at and beyond a depth z/B= 0.1 after the ultimate loading is applied. Therefore, any such potential errors are expected to be minimal here.

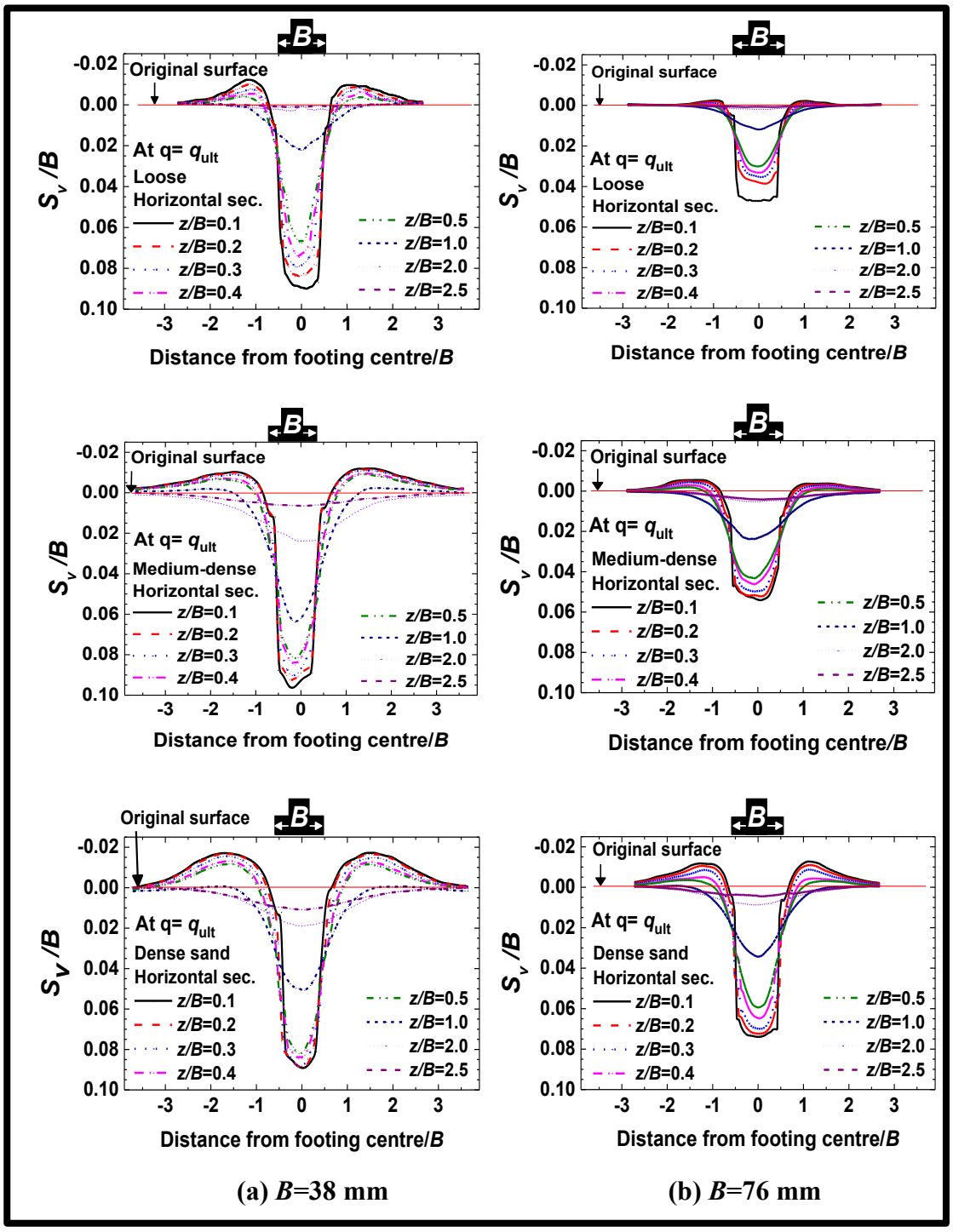

Figure 5.13 DPIV-based normalised vertical displacement component profiles in different sand packings under the ultimate load (q=q_{ult}) along different horizontal sections at different depths (z/B) from the footing-soil interface

5.5.3.4 Vorticity and Stagnant Zones

The images of flow of grains near the corner of the footing (B=38 mm) for loose, medium-dense and dense sand are superimposed on their resultant velocity distribution plots and presented in **Figure 5.14** for the pre-failure and post-failure stages for a typical case of

B=38 mm. The grains flow radially outwards and non-uniformly in all cases of the sand packing. The grains resting beyond the influence zone of deformation (or velocity) do not move in the post-failure stage, which is beyond about 1.25B, 1.2B, and 1.1B for loose, medium-dense and dense sand respectively for both cases of footing width. This trend agrees with Liu and Iskander (2004) who stated that this influence zone is limited within a depth of about 1B of the footing at post-failure stage in the case of loose sand (D_r is limited to 21% in their experiments). From the DPIV results, it is worth mentioning that it is observed that the depth of this influence zone is lower than that of pre-failure stages possibly due to relatively radially outwards movement from the edge of footing as a block, which is consistent with conventional Terzaghi's bearing capacity analysis, as illustrated in **Figure 5.14** (Terzaghi, 1943). The vortex in the total velocity distribution profiles is clearly seen nearer the corner side of the footing for all sand densities. It started when the vertical displacement (S_v) ratio $S_v/B \sim 0.1$. This is a result of gravitational movement of sand from the surface heap while the subsurface grains move upward with loading. Eventually the grains fall back from the passive zone toward the edge of the footing and form a loop-like resultant velocity profile. The spatial nature of the vortex is consistent with Murthy et al. (2012) where the sand medium was dense. The present study confirms the presence of such vortex maps in loose and medium-dense sand as well.

Computational studies based on FEM, for example Griffiths et al. (2006) and Kumar and Kouzer (2007) have reported velocity discontinuities near the footing edge, but the current study has shown their evolution in the sand packing using DPIV experiments. The presence of such vortices around the corner at $q > q_{ult}$ is likely to be related to the local density at the corner rather than the bulk density underneath the footing. Hence, even in a loose sand under compression loading, once the materials close to the footing corner compact to a certain density that is close to the maximum density of the tested soil then vortex will be observed around the edge of the footing. Since features like this are really local features and not bulk features, so it is the density in the local zone around the corner that would be important than the whole soil density for characterise of the vortex formation.

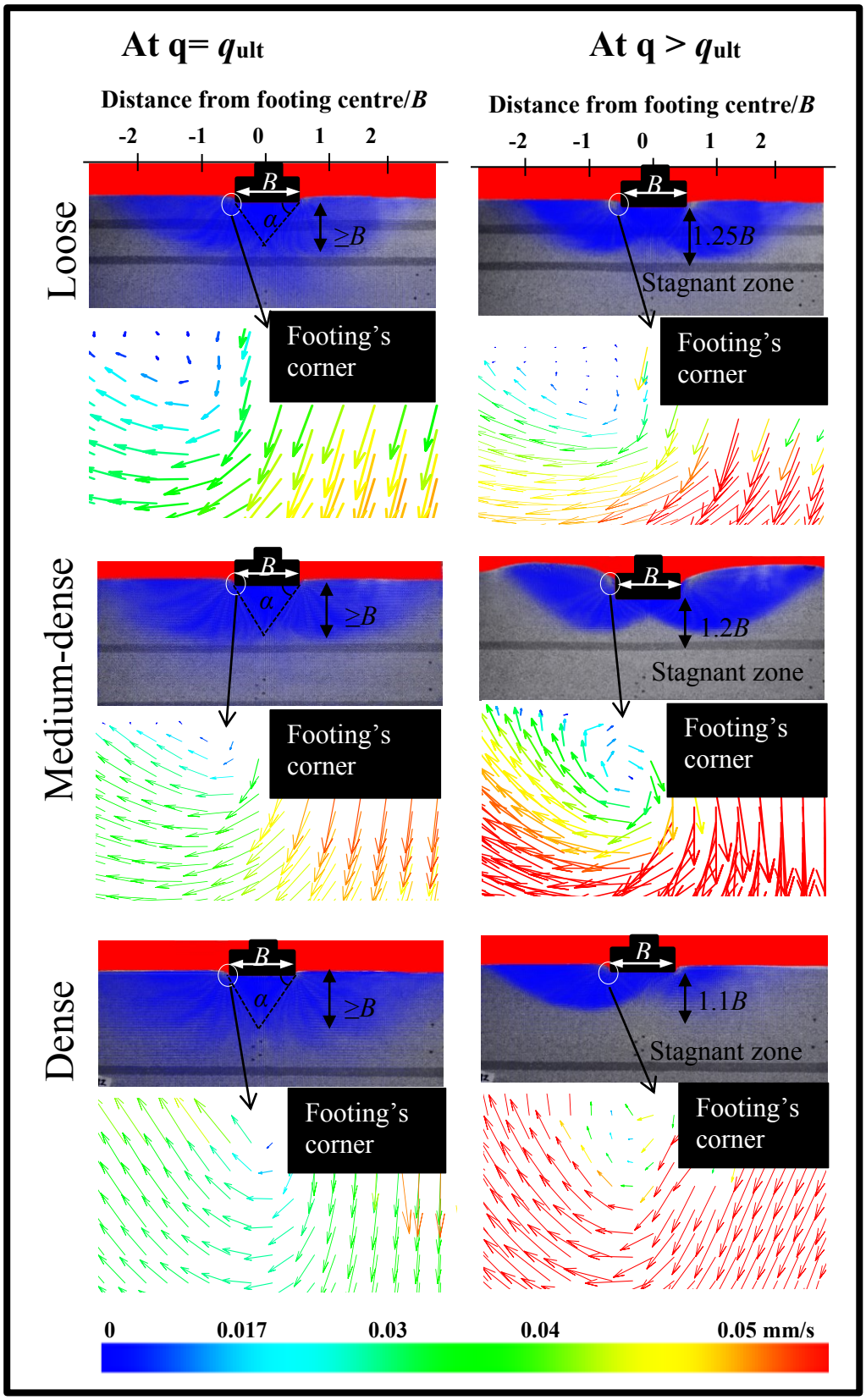

Figure 5.14 Vortex formation of resultant velocity vectors for footing (B=38) interacting with sand of different relative densities. Enlarged view of the corner of the footing is also presented here

5.5.3.5 Vertical and Horizontal Displacements at 0.5*B* Horizontal Section

Figure 5.15 quantifies the normalised vertical displacement component S_v/B and horizontal displacement component S_h/B of loose, medium-dense and dense sand (for a typical case of B= 38mm) at 0.5B horizontal section under different loading levels ($q \leq q_{ult}$). S_v presents an inverted triangle-like profile that becomes deeper and narrower with increasing load level. The maximum value of S_v occurs along the footing centre, and then decreases gradually towards the footing edge (Liu and Iskander, 2004). S_v decreases to zero within a distance of 0.25B from the footing edge. This behaviour is due to the lack of confinement in the soil (Das, 2009). The secondary peaks in the distribution of S_v diminish with decrease in the density of sand. Such patterns, at times non-symmetric, are seen mostly at or beyond the ultimate load even under the symmetric loading conditions on the footing as discussed earlier. The secondary peaks increase with increasing density as shown in **Figure 5.15**. This could be due to the particles interlocking, jamming and dilation that increase with the relative density of sand.

The profile of S_h component presents S-like shape with a neutral point (zero value) occurring along the axis of symmetry of the footing. The soil along the vertical axis of symmetry is confined by the maximum vertical displacement and therefore $S_h \sim 0$. It is worth mentioning that, though not presented here, the variation of resultant displacement at the footing-soil interface was uniform along the footing width.

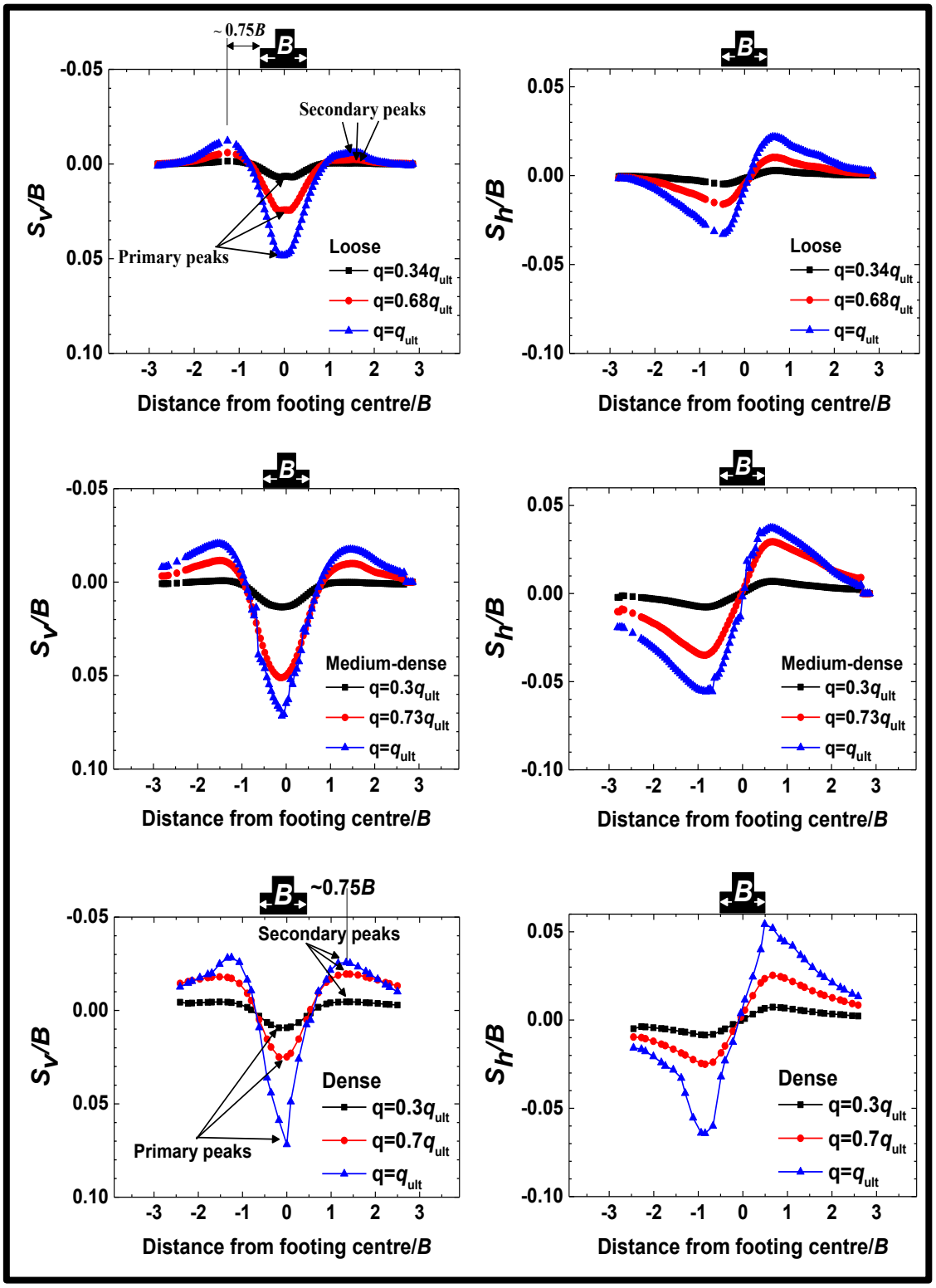

Figure 5.15 (left) Normalised vertical displacement component S_v/B (right) normalised horizontal displacement S_h/B at a horizontal cross section $0.5B$ below footing using DPIV at different loading levels in different sand packings. Signs: vertical displacement (positive down, negative up), horizontal displacement (Negative toward left, positive toward right from the central axis). B = 38 mm

5.5.3.6 Vertical and Horizontal Displacements at Vertical Sections

Previous classical approaches have estimated the elastic settlement of footings using influence factors, which could vary along the depth of sand (Bowles, 1996; Lee et al., 2008). Such variations are also observed from numerical solutions, for example using finite element method (Lee et al., 2008), elastic theory (Mayne and Poulos, 1999) and simple triangular profile using in situ cone penetration tests (Schmertmann et al., 1978). However, they show different types of profiles. Using DPIV here, the variation of S_v/B along the centre line of the footing is examined, and S_h/B along edges of the footing with depth for loose, medium-dense and dense sand (for a typical case of B=38 mm) is presented in **Figure 5.16**. They show a nonlinear response for all cases of sand packing. They gradually decrease to a negligible value beyond ~ z/B= 1.5-2.0, similar results have been reported for loose sand by Liu and Iskander (2004), however this distance decreases for an increase in the relative density of sand. The normalised vertical displacement (S_v/B) attains the peak at a depth of about 0.1B for all cases of sand packing and footing widths, which are almost independent of the loading stages, as illustrated in **Figure 5.16**.

Similarly, the normalised horizontal displacement component (S_h/B) attains maximum at a depth of about 0.25B-0.35B from the surface of the footing. At q ≤ q_{ult}, the maximum value of normalised vertical displacement for smaller width (B=38mm) is $S_{v\,max}/B$ =0.070, 0.086 and 0.0.096 and $S_{h\,max}/B$= 0.02, 0.03 and 0.07 for loose, medium-dense and dense sand respectively. These values increase with the relative density and load level. However, these values for the larger width of footing (B=76 mm) is $S_{v\,max}/B$ =0.045, 0.052 and 0.074 for loose, medium-dense and dense sand respectively. It is worth mentioning that it observed that the values of $S_{v\,max}/B$ at ultimate load are close to the measured values of S_u/B presented earlier. Interestingly, the values of $S_{v\,max}/B$ agree with the common assumption of using S/B between 0.05B - 0.1B for estimating q_{ult} from the load-settlement plots in foundation engineering designs (Lee et al., 2008; Kumar and Bhoi, 2009; O'Loughlin and Lehane, 2010). Overall, the displacement measures reported here could be used to derive more realistic description of displacement profiles in soil media in the future.

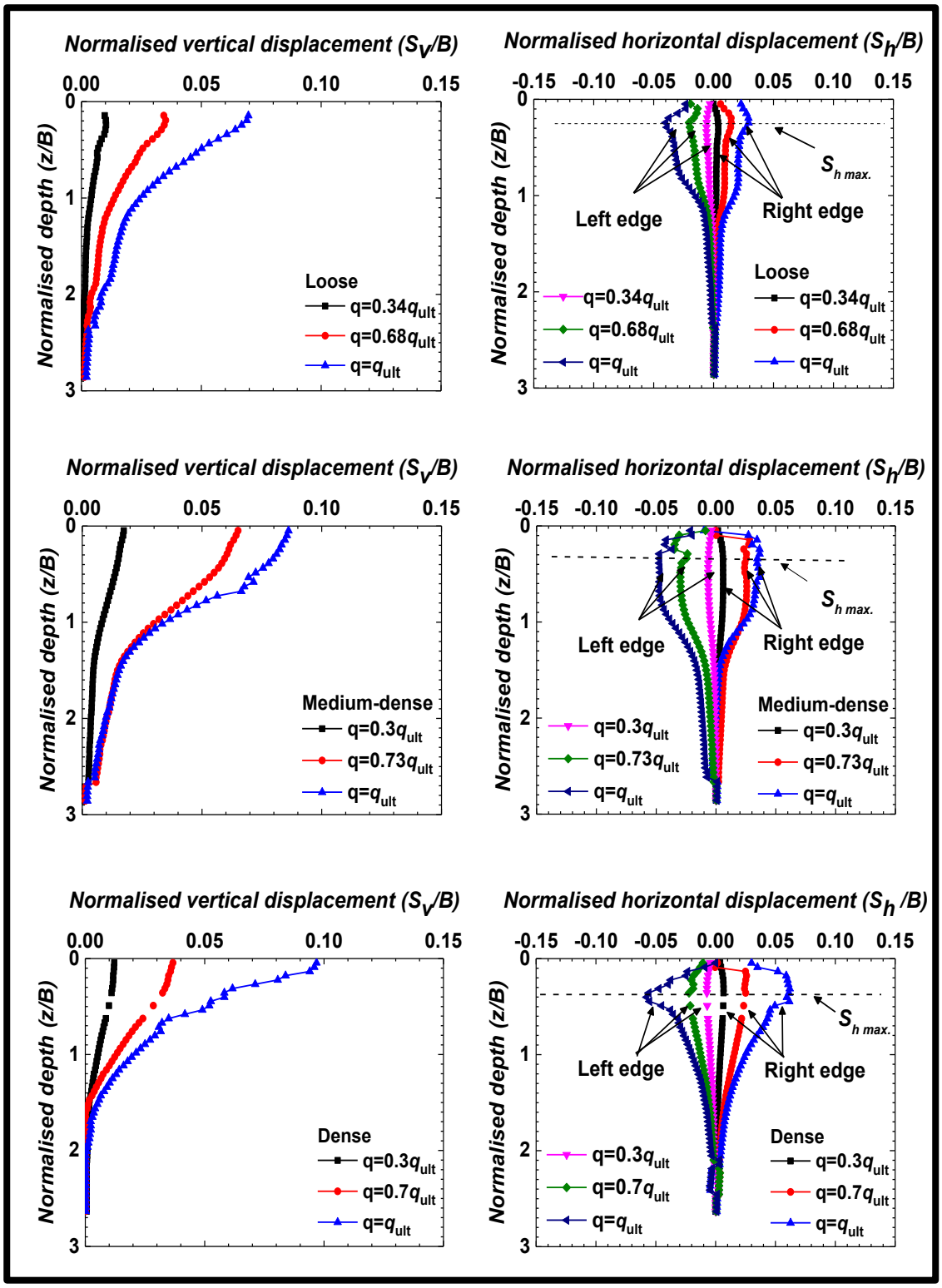

Figure 5.16 Settlement profiles with depth *z* from the bottom surface of the footing at different loading levels: (left) normalised vertical displacement component, (right) normalised horizontal displacement for the sand packing. *B*= 38 mm

5.6 Summary

DPIV is shown to be effective and promising in understanding the local and global geomechanical characteristics of footing interacting with sand media of different relative densities in a coherent manner. Where possible, the displacement measures and generic characteristics of velocity fields in the sand are compared with existing literature and FEM analysis and a good level of agreement is obtained.

DPIV clearly shows detailed descriptions of the stages of velocity discontinuities for the sand media. The velocity profiles of the medium-dense and dense sand are consistent with Vesic (1973) but the advanced measurements reported here detect their evolutions more precisely. For the loose sand, the velocity discontinuities could reach the free surface. Significant vortex zones are existent near the footing corner at and beyond the ultimate bearing capacity of sand of all relative densities studied here. The ultimate bearing capacity refers to the ability of the soil to sustain the maximum load on the footing before the soil collapses. The boundaries of the zone of plastic flow in sand at failure load profiled using the advanced DPIV here are remarkably similar to such intuitive diagrams suggested by the forefathers of soil mechanics, for example Fröhlich in the 1930's and Terzaghi's in 1940's (1943). The depth at which the settlement vanishes in the sand decreases for increase in the relative density of sand. The present study provides both the spatial and temporal distribution of displacements in soils of different packing densities under key stages of loading elegantly. DPIV could be applied in future to develop robust failure surfaces for more complex soil profiles and foundation types encountered in geotechnical engineering applications. Further analysis is required for evaluating the scaling and size effects of footing-sand interactions in a detailed manner with a better resolution of the digital measurements (e.g. using multiple grids per grain).

In addition, simulations using DEM could be more suitable to model the grain-scale movements of granular assemblies under mechanical loading, but they would require extensive level of computing resources to study the cases considered in this work. However, as shown in the current study, FEM-based displacement fields can match to the level of local-scale grain displacements of corresponding experimental systems based on DPIV. In particular, experiments-based, user-defined constitutive relation was used as input in the FEM simulations here, which is found to be useful. The research contributes new advancements on both the experimental and computational fronts in the field of soil-structure interactions in which the DPIV- based experiment is used to measure the grain-

scale (local scale) displacement fields, and they are used to characterise the failure envelopes of key footing-granular soil interaction problems. For the first time, such outcomes are generated in terms of the packing density of the sand. In the finite element analysis (FEA), It is worth mentioning that, using an inbuilt(/existing) model of constitutive relation of sand does not produce the displacement fields of sand grains that are comparable with FEM outputs. Hence, a new approach of using experimentally-derived constitutive relations are represented as an input in the FEM simulations. Also, it is shown that, such an approach results an excellent level of agreements between the above said experimental and finite element analysis approaches. These contributions are entirely original in my thesis.

Chapter 6 Interference Effects on Displacement Fields in Strip Footings-Sand Interactions

In this Chapter, the ultimate bearing capacity and local deformation patterns of sand beneath two neighbouring footings under the plane-strain condition have been systematically studied as a function of separation distance between the footing and different packing densities of sand using DPIV-based experiments and FEM simulations. The ultimate bearing capacity refers to the ability of the soil to sustain the maximum load on the footing before the soil collapses. In the FEM, experimentally characterised single grain-scale properties and the constitutive relation of the sand grains were fed as an input. The deformation pattern and failure mechanism of the zone of plastic flow (active and passive zones) in sand at failure load are studied. The experimental analyses have shown a significant influence of interference effects on the deformation pattern, failure mechanism and the ultimate bearing capacity of the soil. At a close spacing between the two footings, non-symmetrical triangular wedges were sensed below the base of each footing. In addition, an invert arch can form beneath the footings, leading to an increase in the bearing capacity with spacing of $0.25B$ and $0.5B$ distance in the case of loose and medium-dense sand packing; however, such an increase was not evident in the case of dense sand packing. The obtained interference failure mechanisms could be employed to improve numerical solutions. Hence, a journal manuscript has been prepared.

6.1 Introduction

Engineers come across the instance of foundations interfering with each other due to intentional design requirements of space restrictions. The mechanical behaviour of foundation interference could be different from that of a single isolated footing. The use of the conventional ultimate bearing capacity equation of a single foundation (Terzaghi, 1943), which was developed by Terzaghi (1943) does not consider the effect of interfering with each other. To understand the interference effects of the footings, an extensive level of theoretical and numerical approaches have been reported in the literature to calculate the interference effect in terms of the edge to edge spacing (S) between the adjacent footing. However, detailed experimental investigation on to effects of the interference of footing on the local–scale displacement field, failure envelope and subsequent the ultimate bearing capacity characteristics are still scare in the literature.

Furthermore, all these studies reveal that at close spacing the ultimate bearing capacity increases substantially when compared to that of a single footing. The results of these studies demonstrate that the interference effects obtained from theoretical analysis is considerably greater than in the experiment studies. Das (1999) has stated that the base angle of the elastic wedge in the failure mechanism is different from what was assumed by Terzaghi (1943). Thus, it can be concluded that the predefined failure wedges used in existing theoretical solutions are not capable of accurately predicting the ultimate bearing capacity of neighbouring strip footings. It is worth mentioning that no work has been carried out that considers the failure mechanism pattern under adjacent footings located in sand using PIV. In the current study is aimed at providing a more rigorous understanding of the deformation fields and failure mechanisms of sand due to the interference effects of the rough footings ($\delta/\phi = 0.25$) for different packings densities of sand. In this, DPIV is used to track the displacements of sand at local scale and corresponding failure envelopes.

6.2 Review of the Literature

Stuart (1962) was the first to study the effect of interference on the ultimate bearing capacity of neighbouring rough and smooth strip footings as schematically. Stuart (1962) used a theoretical approach by considering the limit equilibrium method (based on a predefined Terzaghi's failure mechanism) to calculate the interference effects between two foundations on ultimate load. Stuart (1962) presented the efficiency factors of footings with interference in terms of the unit weight of the soil (ξ_γ) and for the surcharge load (ξ_q). The efficiency factors (ξ_γ, ξ_q) are the ratio of the ultimate load (due to coefficients of the bearing capacity N_γ and N_q according to Terzaghi, 1943) of interfering footing of width B to that of single footing having the same value of B for a given unit weight of soil and the surcharge load respectively. Stuart (1962), unlike previous studies of a single rough base strip foundation (roughness angle of the footing base (δ) is equal to the angle of internal friction of the soil (ϕ) ($\delta=\phi$)), a condition of interpenetrate of the passive zones was considered below the base of the footings with interference in the cohesionless soil. For a smooth footing ($\delta=0$), the ultimate bearing capacity increases to its maximum value with a decrease in interference spacing to zero when the two footing touch each other, rather than before they touch, as with the rough base footing (i.e. ($\delta=\phi$)). In the case of footings on cohesive soils where $\phi=0$ as in reported by Stuart (1962), the

footings with interference did not exhibit any change in bearing capacity as they approached each other because the blocking (interpenetrate of passive zones) does not occur underneath the footings. The development of the failure surfaces as two foundations approach each other on the cohesive and the cohesionless soils have been explained (Stuart, 1962). Later, by using a failure mechanism similar to that used by Stuart (1962), many researchers have employed the method of stress characteristics to obtain a solution for the bearing capacity, accounting for the interference of two strip footings.

Kumar and Ghosh (2007) have studied the effects of the spacing of two closely spaced rough strip footings on bearing capacity by using the method of stress characteristics. A quadrilateral non-plastic (mechanism 1) and non-symmetrical triangular non-plastic (mechanism 2) trapped wedges were chosen below the footing base, as illustrated in **Figure 6.1**. Using mechanism 1, Kumar and Ghosh (2007) noted that the value of ξ_γ decreases continuously with an increase in spacing. Whereas, using mechanism 2, a maximum value of ξ_γ has been noticed at optimum space S_{opt} ($S/B = S_{opt}/B$ at which $\xi\gamma$ becomes maximum); then the value of ξ_γ decreases to 1.0 with an increase in the spacing between the two footings at $S=S_{max}$. Kumar and Ghosh (2007) argued that mechanism 1 provides more conservative results than mechanism 2, when compared to the theory of Stuart (1962).

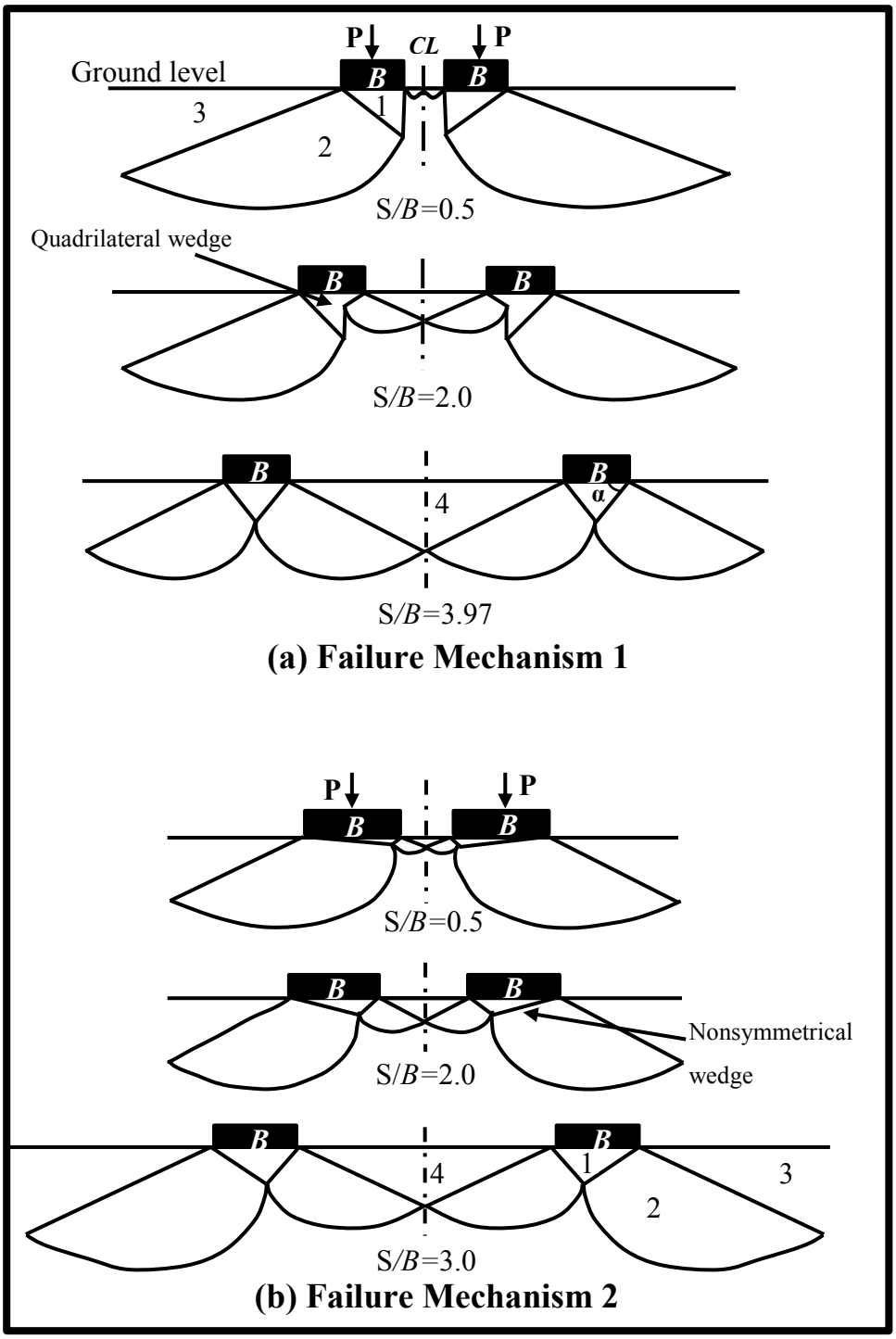

Figure 6.1 Interaction of the failure surfaces in sand soil beneath adjacent rough strip foundation using numerical analysis for sand (a) Mechanism 1 (b) Mechanism 2. Zones: 1 trapped zone, 2 active zone, 3 passive zone, 4 blocking zone (Reproduced from Kumar and Ghosh, 2007)

Lavasan and Ghazavi (2014) studied computationally the failure mechanism and deformation pattern of granular soil (ϕ = 34°) beneath two closely spaced square footings using FLAC^{3D} by assuming the constitutive behaviour of soil based on the Mohr-Coulomb failure criterion with non-associated flow rule. It stated that although the system

of failure mechanism is symmetric, the failure and deformation patterns were non-symmetric under the base of each footing. The blocking was observed at ~S=0.3*B*.

Recently, Lavasan et al. (2018) have analysed the ultimate bearing capacity of adjacent rigid rough strip footings on granular soil based on enhanced limit equilibrium (**Figure 6.2** right), plastic limit load (**Figure 6.2** left), and finite-difference solution using FLAC software. These are developed based on the different failure mechanisms, as illustrated in **Figure 6.2**. The results are compared with those reported from existing experimental (Das and Larbi-Cherif, 1983; Kumar and Saran, 2003), theoretical (Stuart, 1962), and numerical studies (Kumar and Kouzer, 2008). Furthermore, the results showed that an invert arch could form beneath the footings at close spacings between the footings. This leads to an increase in the bearing capacity, with spacing up to a certain value of S/*B*; however, this does not occur for granular soil of low angle of internal friction.

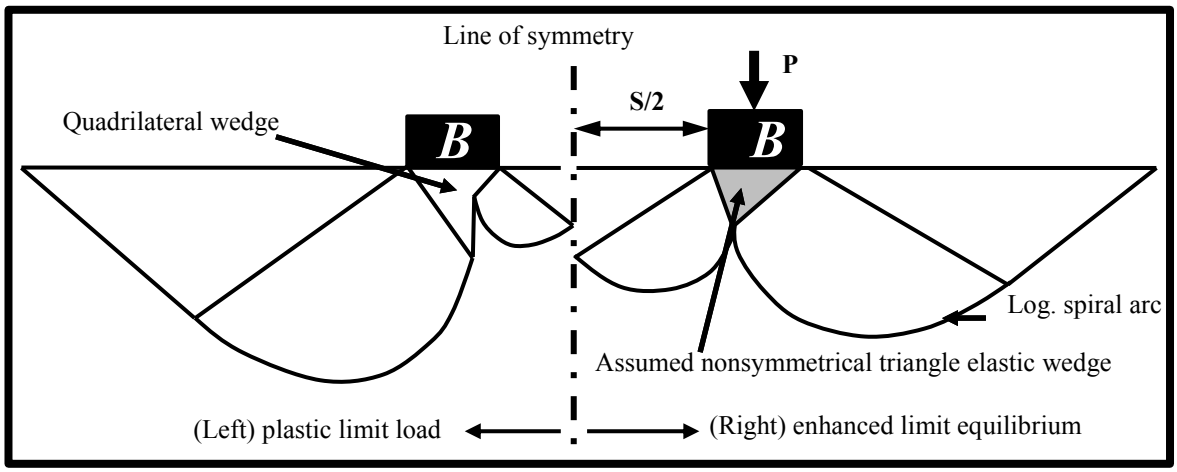

Figure 6.2 Schematic geometry and shape of the failure wedges (Reproduced from Lavasan et al., 2018)

In addition, in order to study the effect of the interference of two closely spaced footings on unreinforced, reinforced cohesionless and cohesive soils, a number of studies were carried out by researchers (Das and Larbi-Cherif, 1983; Al-Ashou et al., 1994; Kumar and Saran, 2003; Lavasan and Ghazavi, 2012). A number of numerical studies have also been conducted by different researchers (Griffiths et al., 2006; Ghazavi and Lavasan, 2008; 2014; Kumar and Kouzer, 2008; Lee et al., 2008). Other researchers have used small-scale model tests (Das and Larbi-Cherif, 1983; Kumar and Saran, 2003; Kumar and Bhoi, 2009; Lavasan and Ghazavi, 2012). They reported that the ξ_γ and ξ_q obtained from

the experiments is underestimated compared to the theoretical solutions. All these studies reveal that, at close spacing of about $0.5B$ the ultimate bearing capacity increases substantially when compared to that of a single footing.

These results, however, indicate a certain S_{opt} for footings with a rough base ($\delta = \phi$). However, for smooth footings ($\delta = 0$), as seen in the work of Stuart (1962), the ultimate bearing capacity increases with a decrease in interference spacing. The results of these studies demonstrate that the interference effect obtained from theoretical analysis is considerably greater than from the footing model experimental studies. Das (1999) has stated that the base angle of the elastic wedge (α) as illustrated in **Figure 6.1** in the failure mechanism of the footing is different in the magnitude of the base angle from what was assumed by Terzaghi (1943). Thus, it can be concluded that the predefined failure wedges used in existing theoretical solutions do not predict adequately the ultimate bearing capacity of neighbouring strip footings. To the best of my knowledge, no experimental work has been carried out that considers the failure mechanism pattern under adjacent footings located at a local scale using an advanced measurement method such as DPIV. In the current study is aimed at providing a more rigorous understanding of the deformation fields and failure mechanisms of sand due to the interference effects of the rough footings ($\delta/\phi = 0.25$) for different packings densities of sand using DPIV and FEM.

6.3 Materials

Soils used in this **chapter** are the disturbed dry silica sand samples obtained in UK that presented in **Section 5.2, Chapter 5**.

6.4 Methodologies

6.4.1 DPIV Analysis

Appling of DPIV technique to interference effects of adjacent footing on a single sand layer, image capturing, and experimental setup are identical to those reported in detail in **Section 4.2, Chapter 4**. However, DSLR camera (Nikon D5500) in front of the designed planar model that located in the Instron machine was used. Typical images recorded at

various penetration depths using DSLR camera were shown later in this Chapter. The adjacent footing compression test was performed under the same ambient laboratory conditions.

6.4.2 FEM Simulations

In the current study, ANSYS is used to create a two-dimensional solid geometry. The chosen domain along with applied boundary conditions is shown in **Figure 6.3**. The simulations were held under identical boundary conditions for footing indenting with different types of sand packing as in the case of physical experiments. The size of the elemental geometry is shown in **Figure 6.3**. The nodes and element numbers in the soil body are equal to 48478 and 15920 respectively. The width of the loading area was *B* (half of the adjacent footings). The loading is applied vertically in increments of constant displacement of 0.25*B*, uniformly across the width of the footing within the time step of 0.001 second (~1000 cumulative iteration). FEM setup are identical to those reported in detail in **Section 4.3, Chapter 4**.

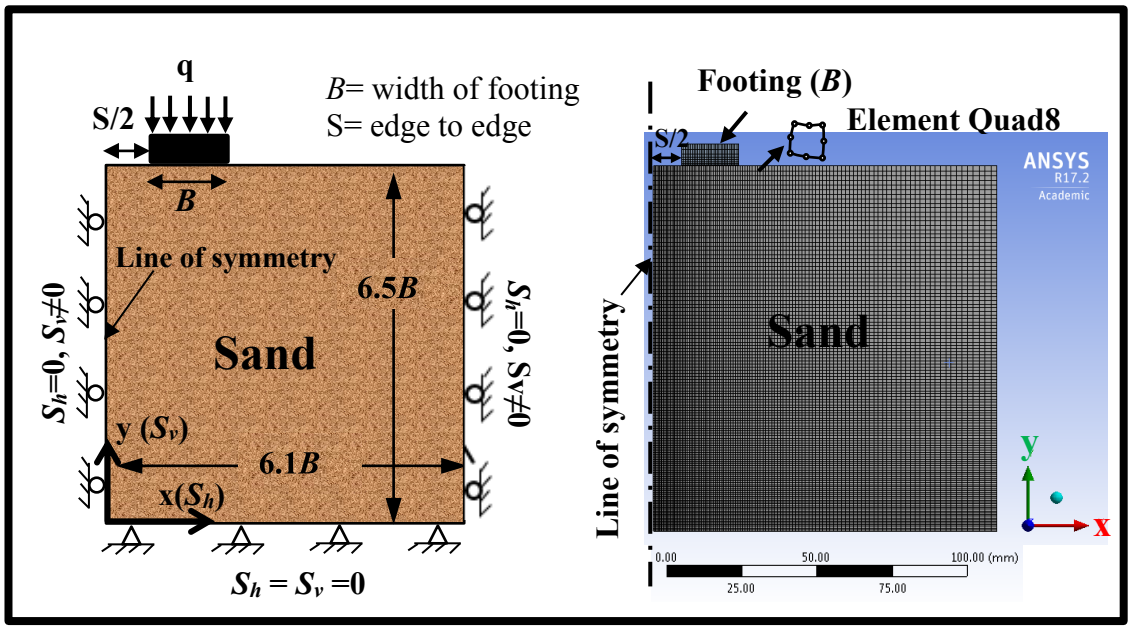

Figure 6.3 (left) Chosen domain and boundary conditions, not to scale (right) finite element mesh, and element enlarged

6.5 Experimental Work for DPIV Test

The DPIV tests were conducted on two aluminium model footings, each 38 mm wide, 38 mm long and 15 mm thick. A steel square shaft (column) having a length 15 mm was rigidly fastened to each model footing at its centre (**Figure 6.4**). During the load test of a single footing, the load was directly applied to steel square column as illustrated in **Figure 5.2**. For the bearing capacity tests on adjacent footings, the two shafts of the footings were rigidly connected to an aluminium beam having a cross-section of 21 mm × 34 mm and 300 mm length (**Figure 6.4**). Therefore, no tilting of the footing was allowed in the experiments. The tests were conducted in the planar box of 460 mm in length, 250 mm in height and 39 mm in thickness, filled with sand as illustrated in **Figure 6.4**. The planner model was firmly screwed at two locations on the top positions to minimise any possible out-of-plane deflection during the test. Further discussions regarding the boundary condition and frictions between the base surface of the footing and the sand grains were detailed in **Section 5.4, Chapter 4**.

Three cases of relative densities of the sand packing were considered in this study. The loose granular packing (γ=14.7 kN/m^3=1500 kg/ m^3, D_r=24 ± 2%, e = 0.76), the medium-dense packing (γ=15.30 kN/m^3, D_r=53 ±2%, e= 0.7) and the dense sand (γ=15.80 kN/m^3= 1610 kg/m^3, D_r =72 ±2%, e= 0.64) was achieved in the same procedure detailed previously in **Section 3.3.3, Chapter 3** and **Section 5.4, Chapter 5**. To study the interference effects of the footings, both the identical were placed symmetrically on the surface of the sand bed for all test using S/B (S= edge-to-edge) =0, 0.25, 0.5, 1.0, 2.0, 3.0 and 5.0. However, due to some practical constrains of the Instron machine and the dimensions of the test box, the experimental tests are conducted for values of S/B ≤5.0. The loose sand samples were tested for S/B =0, 0.25, 0.5, 1.0 and 2.0 in which the interference effects diminished at S/B=2.0. The medium-dense sand samples were tested for S/B =0, 0.25, 0.5, 1.0, 2.0, 4.0 and 5.0. The dense sand samples were tested for S/B =0, 0.25, 0.5, 1.0, 3.0 and 4.0.

A quasi-static axial compression loading was applied slowly on the beam centre (0.05 mm/s penetration velocity) using the Instron loading machine with 5 kN loading capacity and 0.1N resolution. Nikon D5500 camera that offers high definition (24 Mega Pixels) for more accurate kinematic measurements was fixed in front of the box and two light sources were used to illuminate the rig, as illustrated in **Figure 6.4**. However, as the

loading condition is quasi-static in this study, an image at every second (1 fps) was found to be adequate until the failure of the sand.

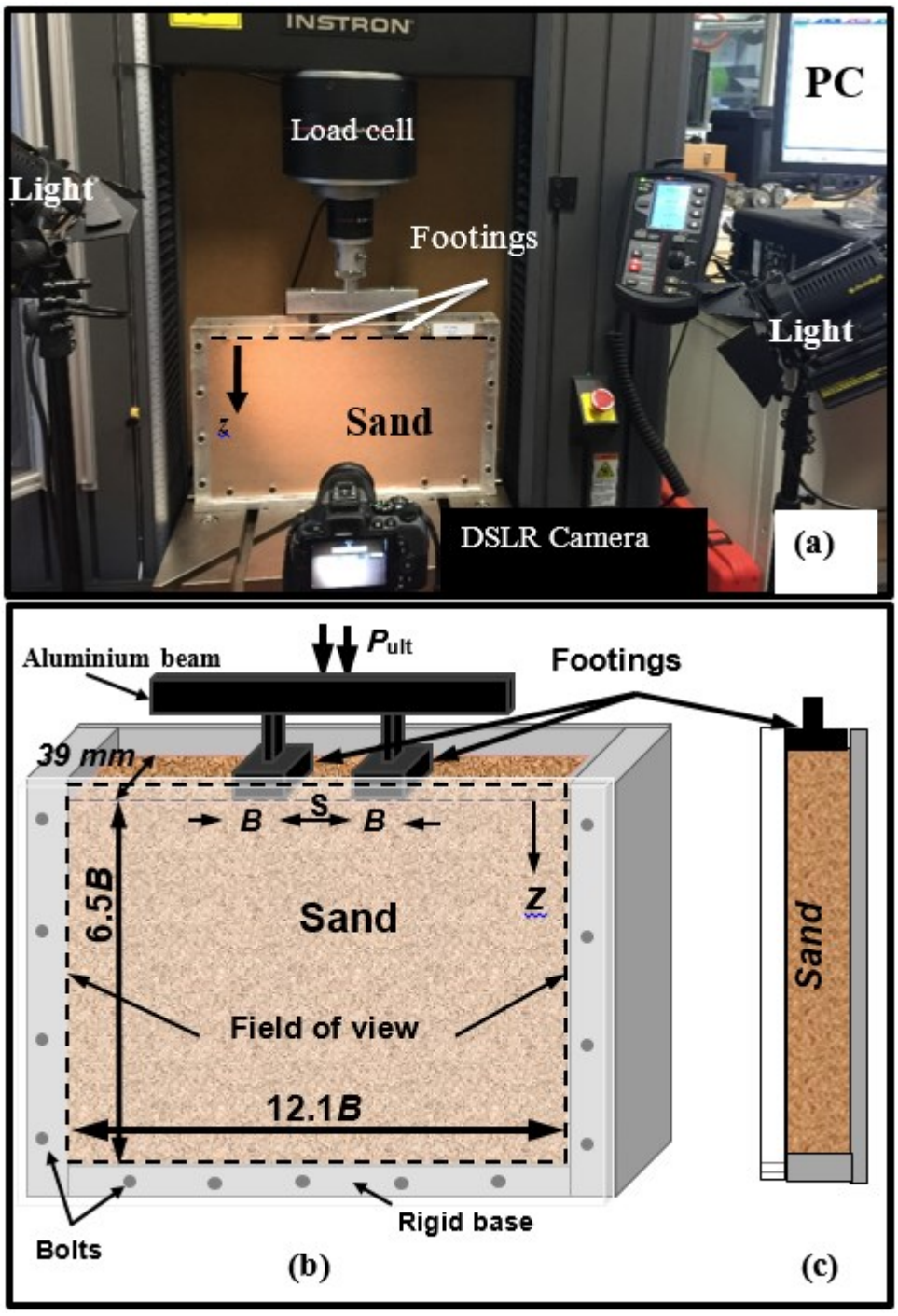

Figure 6.4 Experimental setup of adjacent footings with definition of the problem, not to scale

DSSP was used to analyse the images using an adaptive PIV to identify the movement of soil between consecutive images obtained from the front of the Perspex test rig (Albaraki

and Antony, 2014; Jahanger et al., 2016; Jahanger and Antony, 2017a; 2017b; Jahanger et al., 2018a; 2018b). The DPIV camera lens was focused normal to plane the footing-soil interface region was 460 mm × 310 mm where the measurements are most important to make. The full image was specified as area of interest (AoI) by dividing into 81000 sub-interrogation areas of 16×16 pixels (mesh of PIV patches) each covering a zone of soil approximately 1.25 mm × 1.25 mm windows. Nikon D5500 camera (6000×4000 pixels) was used here. This corresponds to a scale of ~ 0.08 mm per pixel ((460 mm)/ (6000 pixel)) in this study. The distribution of velocity vectors of the grains was examined for which the DPIV imaging, a single grid size was covered ~10 grains. A typical mean size of sand grain (D_{50} = 0.37 mm) was represented by about 5×5 pixels. It is worth noting that the settlement profile is measured from velocity vectors of the granular soil interacting with the footing (Hamm et al., 2011; Jahanger et al., 2018a; 2018b). The displacement measures i.e. resultant displacement (S_R), vertical displacement (S_v) and horizontal displacement (S_h) were evaluated under a given load in total (i.e., between the reference image at zero load (q = 0) and the image at the required fractions of the ultimate load level, such as 0.34q_{ult} and q_{ult}. Hence, the DPIV experimental measurements made here are at the local-scale rather than a continuum measure. The current studies provided herein are based on small-scale 1g model test and plane-strain condition. The tests were repeated at least twice to verify the repeatability of the test data and the differences in them within ±10% and acceptable for practical purposes.

6.6 Results and Discussion

6.6.1 Average Footing Stress versus Settlement

The load–settlement relationship for a typical footing (B=38mm) interacting with sand for different spacing distances is presented in **Figure 6.5**. Using the load-settlement data, the tangent intersection method (Akbas and Kulhawy, 2009) was applied to obtain q_{ult}. The ratios of ultimate vertical settlement of footing (S_u) to footing breadth (B), S_u/B for single footing (B=38mm) and for adjacent footings of S/B=0, (B=76 mm) is 8% and 16% respectively. These ratios increase with an increase in sand packings that the value S_u/B in dense sand is larger than in medium-dense and loose sand but decrease with the increase of the width of the footing. These measures and the nature of bulk load-settlement curves are consistent (Das, 2009) with punching (without a well-defined

peak), local shear failure (moderate peak) and general shear failure (well-defined peak) for sand described by Vesic (1973).

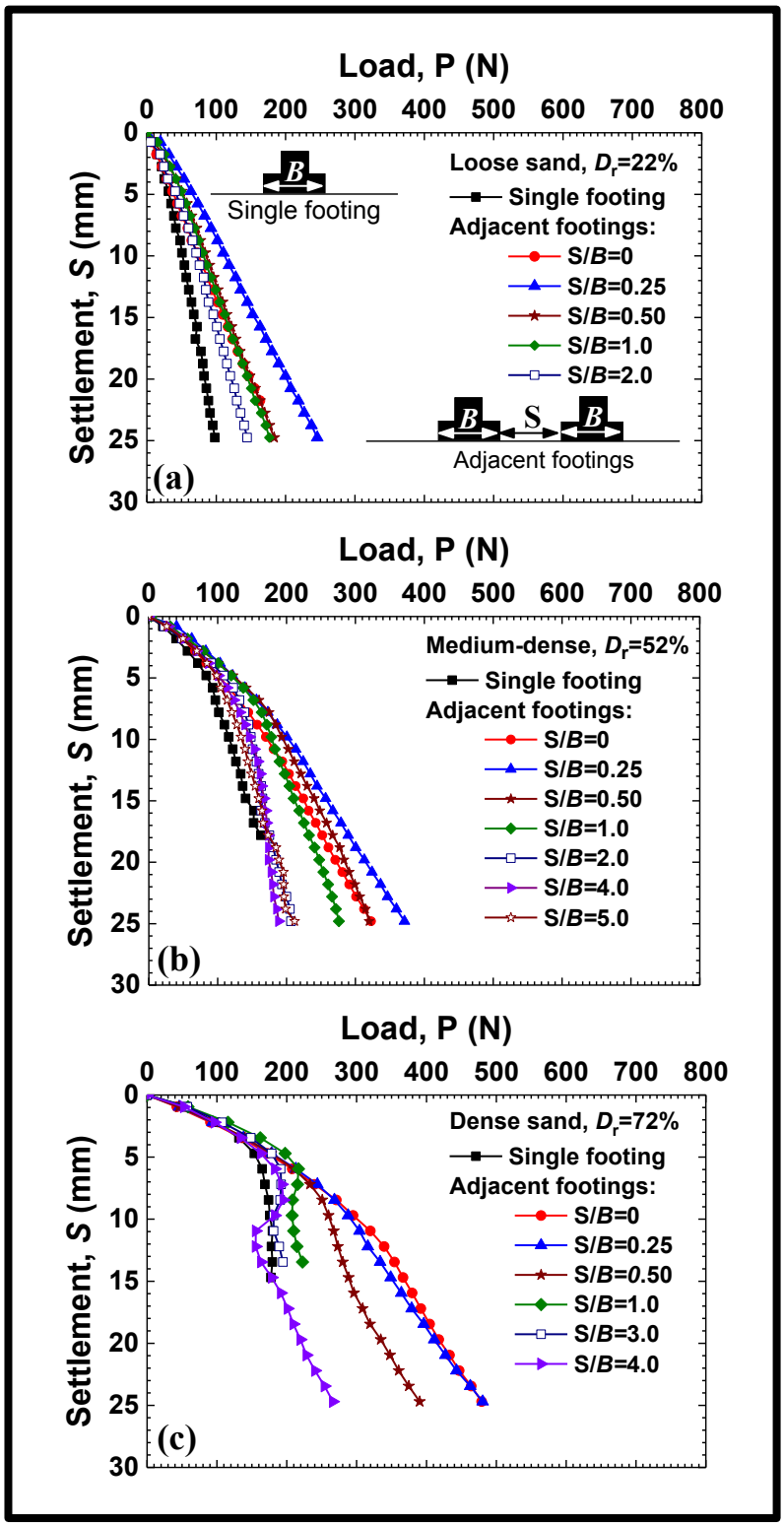

Figure 6.5 Load-settlement curves for different spacing of adjacent footings interacting with loose, medium-dense and dense sand

6.6.2 Development of the Failure Surfaces Vs Spacing under Ultimate Load

Figure 6.6-Figure 6.8 present typically the evolution of the total resultant velocity vectors in the sand packing for a typical case of adjacent footings (B=38 mm, and S/B=0-2, 0-4 and 0-3 for loose, medium-dense and dense sand respectively) interacting with them under the ultimate load. In this plot, the contours of the total resultant displacement (S_R) are embedded as well. The scalar contour is used to display resultant displacement in the vector map using numerical method to extract a scalar quantity from a dataset with multiple values of the same values (DantecDynamics, 2013).

For different sand densities, at S/B=0, the deformation patterns are similar to an isolated footing under the ultimate load. The pairs of the footing acts as a single footing with the width=2B, and the total load on the one of the pairs is $1.0 < \xi\gamma < 1.6$ the load taken by single footing. The value of S_{opt}/B corresponding to which the value of ξ_γ becomes maximum $\xi_{\gamma\,max}$ is called as S_{opt}/B. As the spacing increases up to S_{opt}/B, they act as a single footing in which the breadth of the pairs of the footings (breadth=2B +S_{opt}) and $\xi_{\gamma\,max}$~1.4 and 1.75 for the loose and medium-dense respectively. It means that $\xi_{\gamma\,max}$ due to blocking (superposition of the displacement field) occurs in the loose and medium-dense sand between the footings of breadth =2B +S_{opt} (**Figure 6.6**, S/B=0.25, **Figure 6.7**, S/B=0.5). However, the blocking occurs at S_{opt}/B =0 for footing pairs on the dense sand when the footings touch each other, as illustrated in **Figure 6.8**. These results were consistent with the literature (Stuart, 1962; Kumar and Saran, 2003; Lavasan and Ghazavi, 2012; Lavasan et al., 2018). These blocking patterns in all sand densities are disappeared while the interference effect slightly diminish with an increase in the spacing until they behave as an isolated footing for clear spacing greater that (S_{max}/B). These failure mechanism observations, yet, qualitatively have not been reported in the literature; however, results for the efficiency factor ξ_γ quantitatively were reported in the literature for different sand packings.

It can be clearly seen that approximately a triangular trapped wedge of 'dead zone" (with constant amount of resultant velocity of the grains beneath the two footings) is formed for all cases of spacings. However, the influence depth of this zone is greater in the blocking pattern, which reaches ~ 2.2B, 1.93B and 1.7B for the loose, medium-dense and dense sand respectively, as illustrated in **Figure 6.6-Figure 6.8**. It seems that the soil in dead zones is rigidly resist against the downward moving of footings for $S \leq S_{opt}$. The soils freely move in this zone due to the decrease of passive force on the interfering zone.

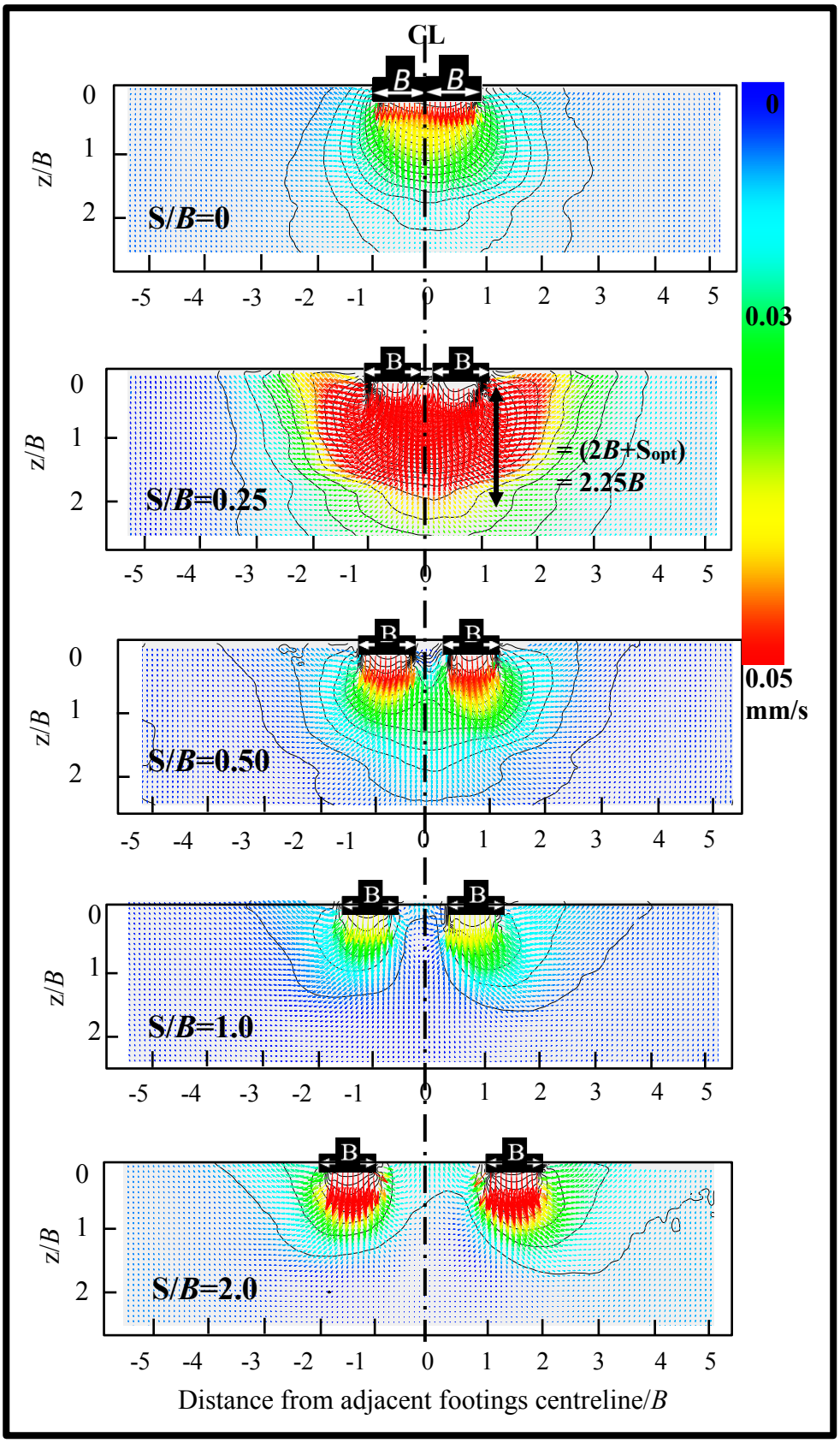

Figure 6.6 Evolution of accumulative resultant velocity vectors with contour lines of resultant velocity S_R in loose sand using DPIV for interfering strip under q=q_{ult}

A well-defined failure pattern beneath the adjacent footings under q_{ult} consistent with the work of Stuart (1962) is visualised as shown in **Figure 6.6- Figure 6.8** for all cases of sand densities. Mostly, the grains flow symmetrically with respect to plane of symmetry (CL) until reaching the ultimate load ($q=q_{ult}$). A non- symmetrical triangle (scalene triangle has all three angles are different) is formed under each pairs of footings which is consistent well with the work of Stuart (1962), Kumar and Ghosh (2007) and Lavasan and Ghazavi (2014). These trapped wedges of dead zones from the plastic failure surface are changed to isosceles triangle, which has two base angles α and two sides the same, beyond the S_{opt}/B until it reached the space S_{max}/B where the two footings behave as two isolated footings.

For the medium-dense and dense sand, the failure profiles are similar to the loose sand, but the velocities are smaller than the loading velocity. Hence, the velocity of the grains is the least in the dense sand packing. These reductions in velocities are due to the confinement condition in the higher relative density that reduces the movement of the soil. The deformation pattern in sand at the optimum spacing comprises of the soil in the effective width ($2B+S_{opt}$). In such conditions, the shear bands could not be developed due to the highly confined pressure in the soil between the two footings that works as an elastic rigid block. The interference has less effect on the failure mechanism when the spacing exceeds $0.25B$, $0.5B$ and $0B$ under the ultimate bearing capacity for loose, medium-dense and dense respectively. At wider spacing, the size of failure mechanism becomes symmetric about the plane of symmetry. As seen **Figure 6.6-Figure 6.8**, the formed heaps beyond the footings edges are piled about $2B$, $2.5B$ and $3B$ for loose, medium-dense and dense respectively.

The DPIV-based results show a slightly wide and deep failure fields at S_{opt} because of the blocking mechanism. At close spacing between the footings, a wedge form beneath the two footings, leading to an increase in the bearing capacity of the soil with increase in spacing up to S_{opt}; however, such mechanism takes place at zero spacing for high friction angles such as in dense sand. This justifies and confirms the agreement between the $\xi_{\gamma\,max}$ and the larger failure envelope at closer spacing. Consequently, it can be concluded that the DPIV-based tests in conjunction with the packing densities used in the current study to address the failure fields are robust enough to capture the phenomenological aspects of interference such as blocking, bearing capacity at optimum spacing, critical spacings, and realistic shear strength envelopes.

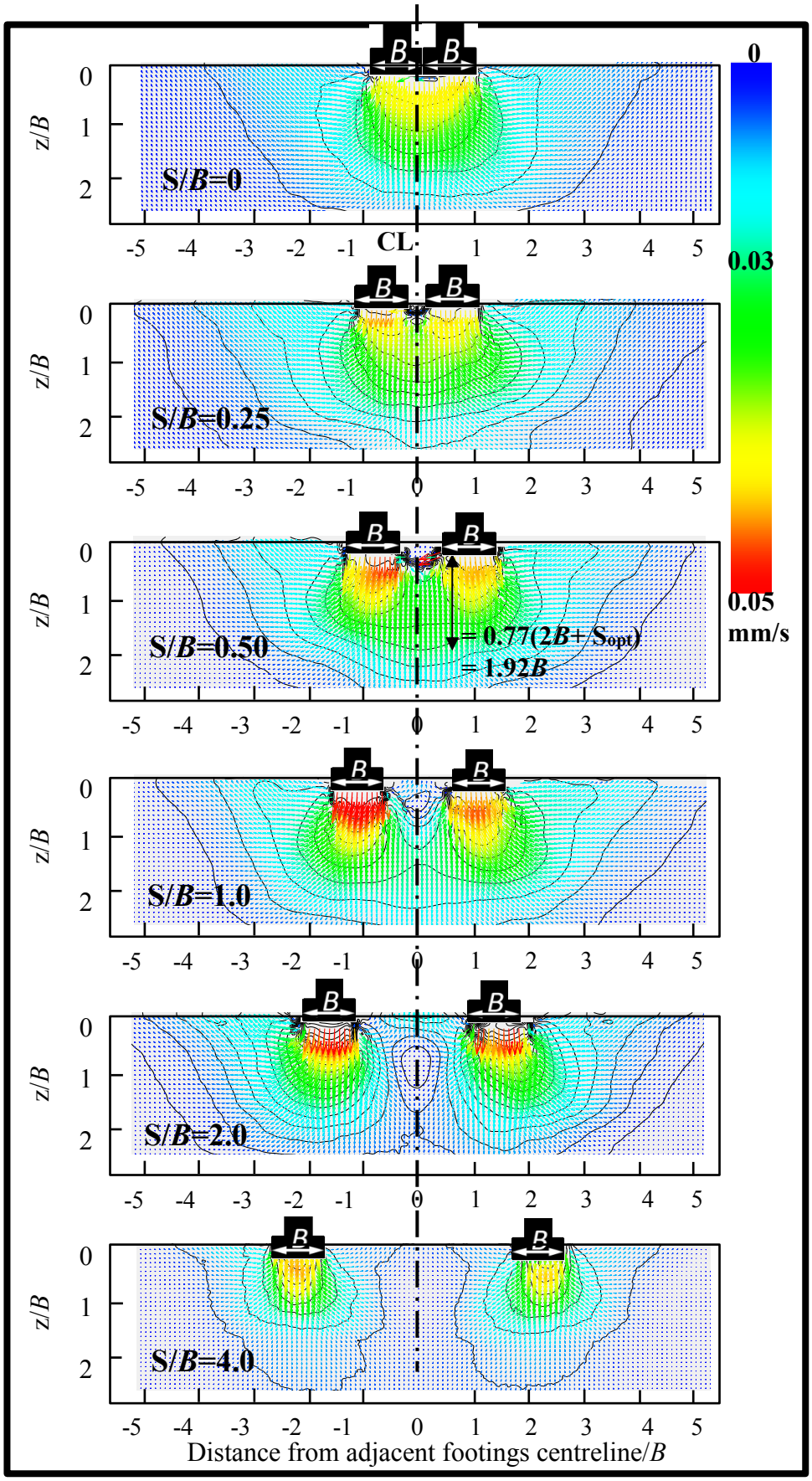

Figure 6.7 Evolution of accumulative resultant velocity vectors with contour lines of resultant velocity S_R in medium-dense sand using DPIV for interfering strip under q=q_{ult}

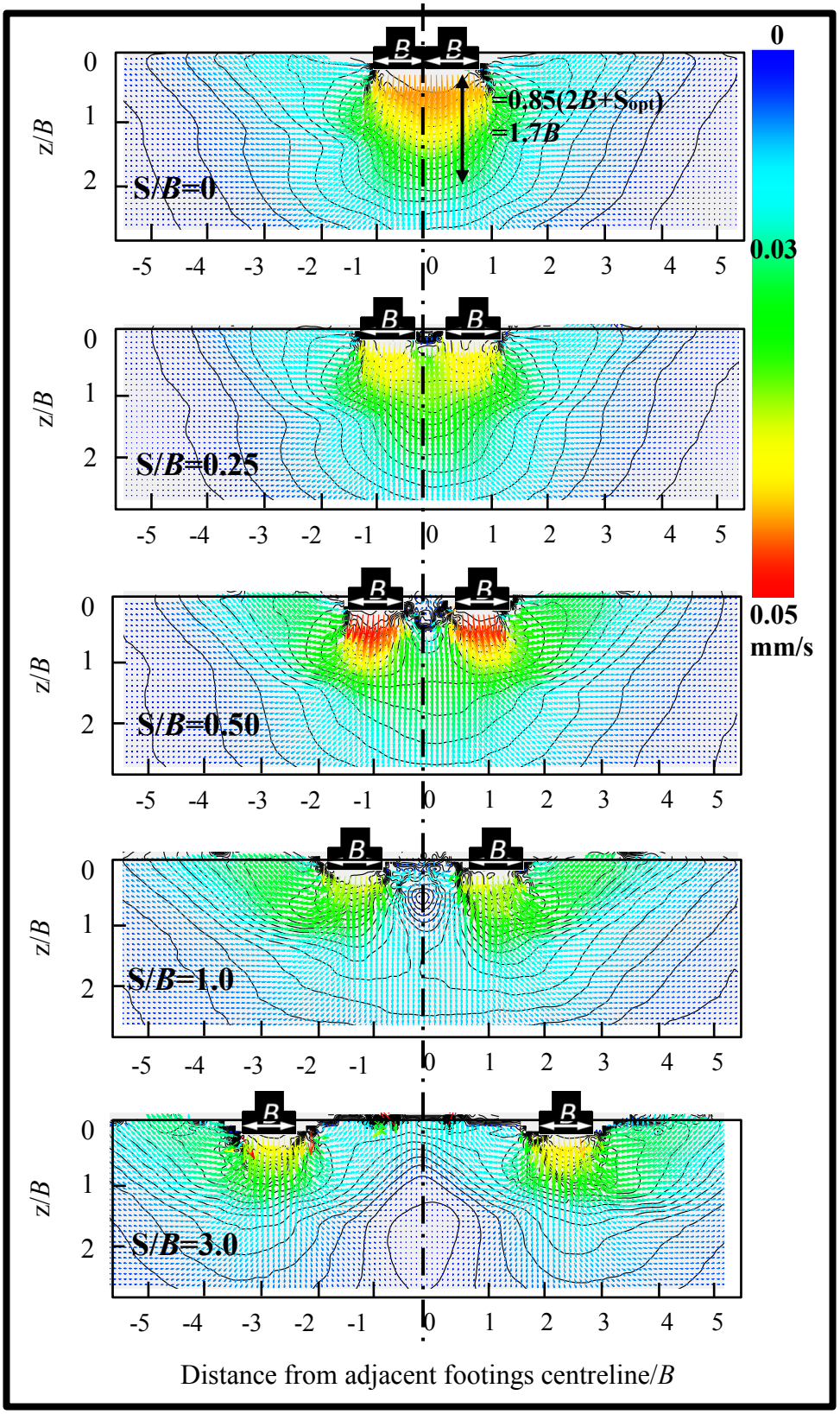

Figure 6.8 Evolution of accumulative resultant velocity vectors with contour lines of resultant velocity S_R in dense sand using DPIV for interfering strip under q=q_{ult}

6.6.3 Influence of Spacing Distance S on the Local Settlement Components (S_v and S_h versus S/B) at Different Stress Levels (q/q_{ult})

Figure 6.9-**Figure 6.11** quantify the normalised vertical displacement component S_v and horizontal displacement component S_h in loose, medium-dense and dense sand respectively. These are profiled at 0.5B horizontal section below the footing–soil interface under different loading levels ($q \leq q_{ult}$).

For the single footing and for the adjacent footings with S/B=0, the S_v presents an inverted triangle-like profile that becomes deeper and narrower with increasing load level. The maximum value of S_v occurs along the footing centre, and then decreases gradually towards the footing edge (Jahanger et al., 2018a). S_v decreases to zero within a distance of 0.25B from the footing edge. This behaviour is due to the lack of confinement in the soil (Das, 2016). The secondary peaks in the distribution of S_v diminish with decrease in the density of sand.

For the adjacent footings at S/B= S_{opt}/B=0.25, 0.5 and 0 for loose, medium-dense and dense sand respectively, the maximum value of S_v occurs along the adjacent footings centre line like the single footing behaviour. Then for S/B > S_{opt}/B, the maximum value of S_v occurs along the individual footing centre line. Again, this justifies the agreement between the $\xi_{\gamma\,max}$ and the larger failure envelope at close spacing. Such patterns, at times non-symmetric, are seen mostly at or beyond the ultimate load q_{ult} even under the symmetric loading conditions on the footing as discussed earlier. The results along the line of symmetry (distance from adjacent footings centre line/B=0) as illustrated in **Figure 6.9**-**Figure 6.11**, showed that there are horizontal displacements S_h along the plane of symmetry of about 20% of the maximum S_{hmax} (i.e., **Figure 6.11**, S/B=0) along the edge of the footing under the $q_{ult.}$ This contradicts the zero-shear stress and the horizontal displacement along the line of symmetry in the literature (Sloan, 1988; Lyamin and Sloan, 2002; Kumar and Kouzer, 2007).

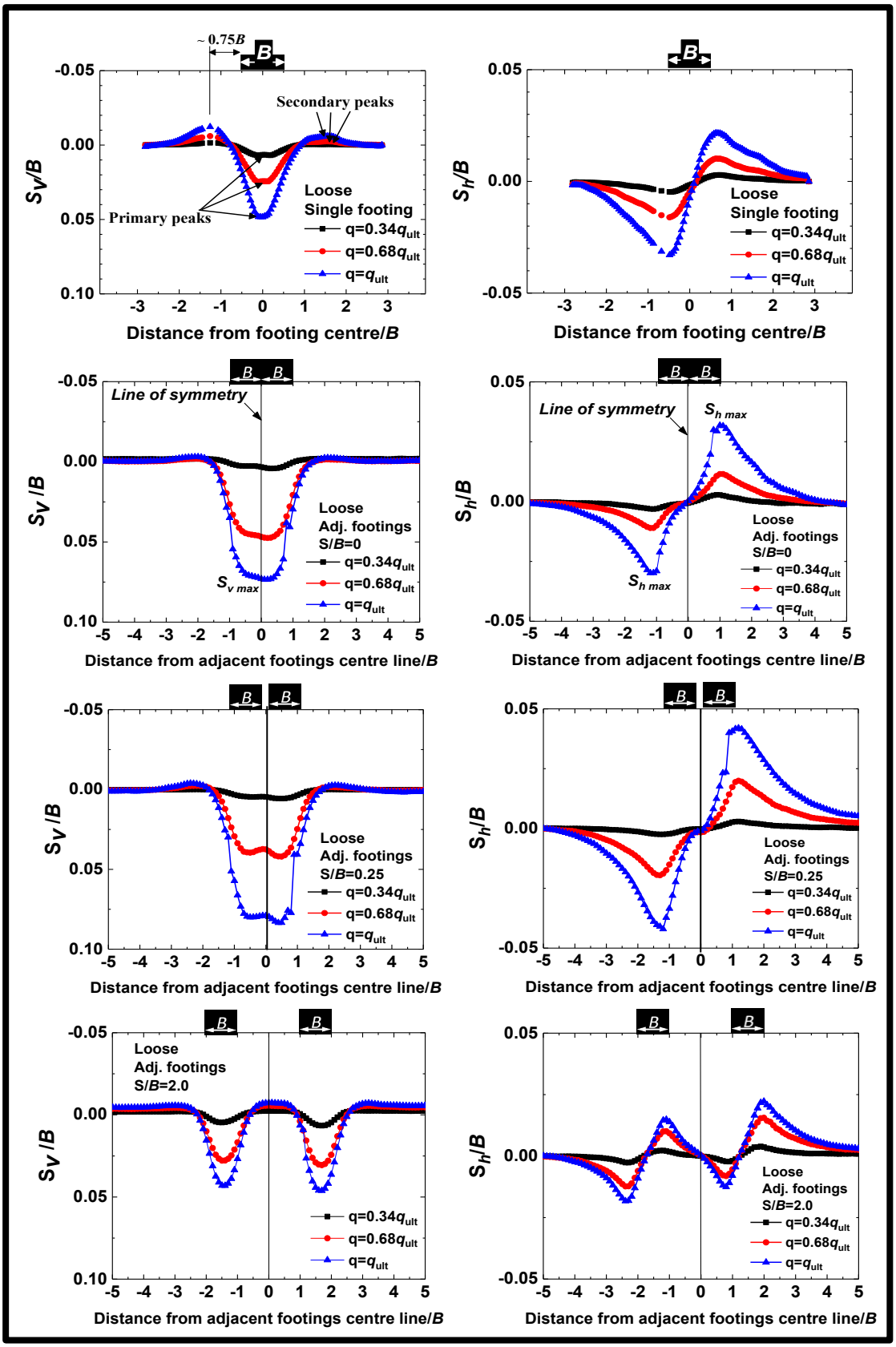

Figure 6.9 (left) Normalised vertical displacement (right) normalised horizontal displacement at horizontal cross section 0.5*B* below footing on loose sand

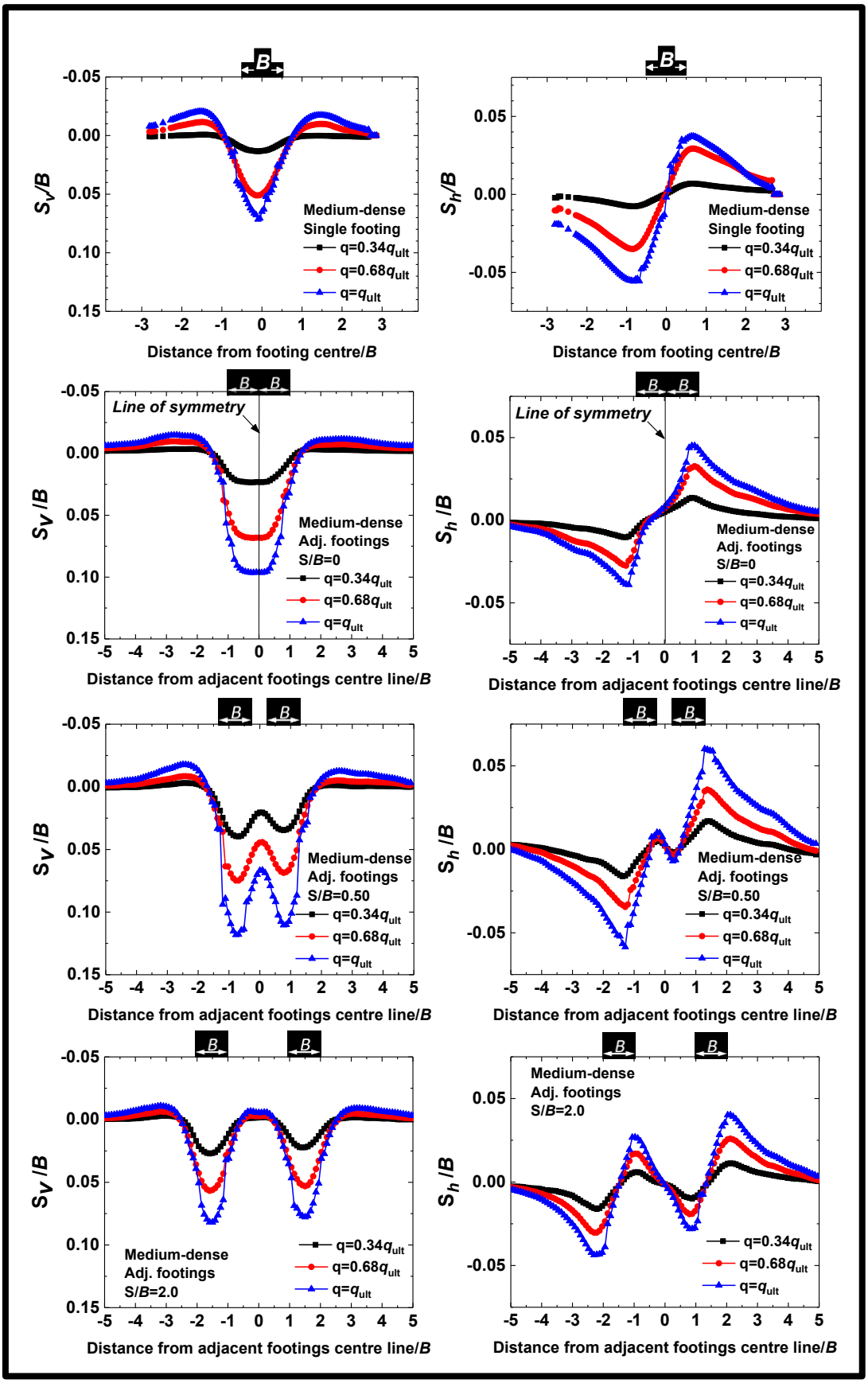

Figure 6.10 (left) Normalised vertical displacement (right) normalised horizontal displacement at horizontal cross section 0.5*B* below footing on medium-dense sand

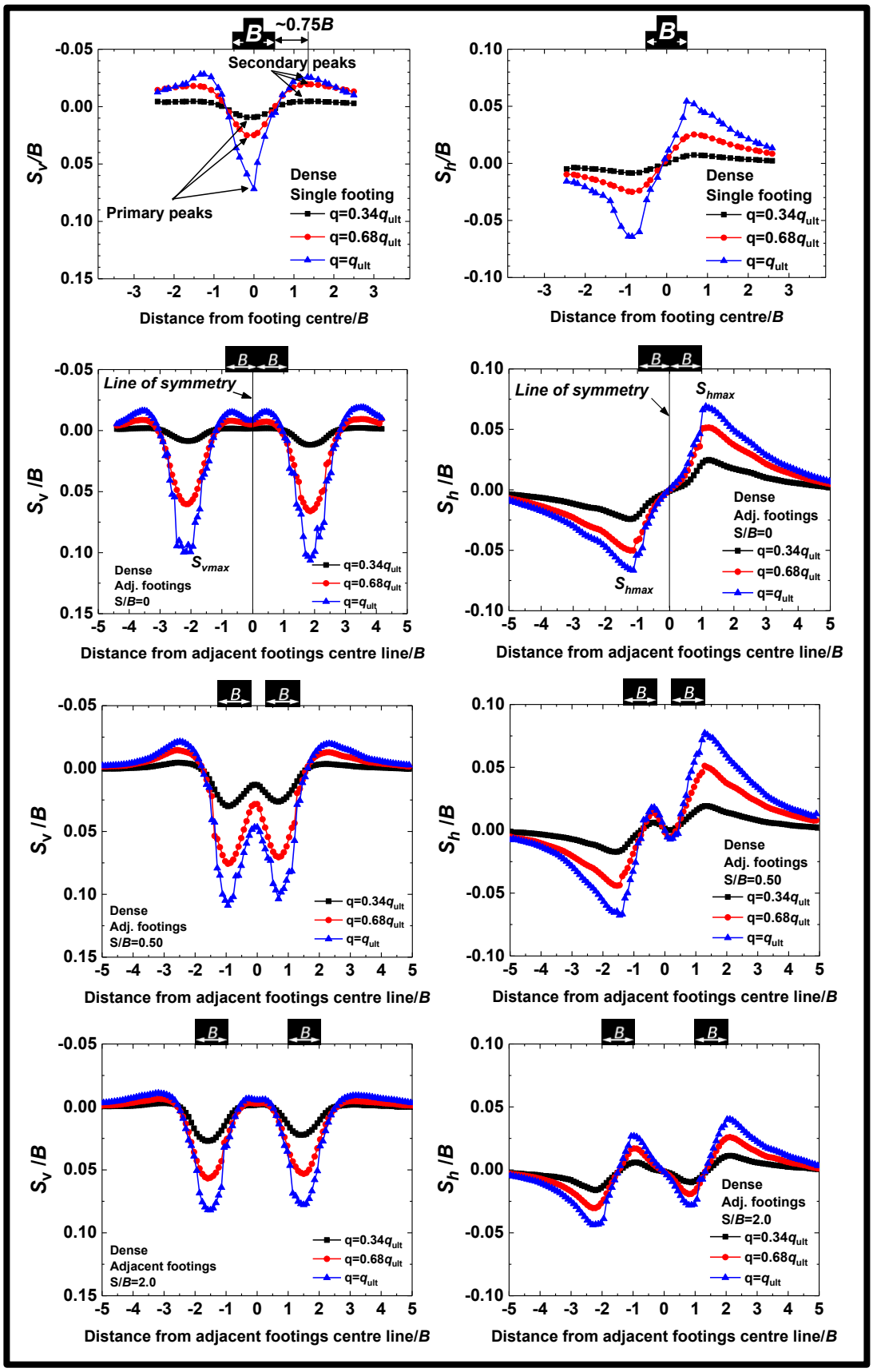

Figure 6.11 (left) Normalised vertical displacement (right) normalised horizontal displacement at horizontal cross section 0.5*B* below footing on dense sand

6.6.4 Vertical Displacements Component along Vertical Sections

Using DPIV here, the variation of normalised vertical displacement component (S_v/B) along the line of symmetry (CL_Adj.) is examined, and S_v/B along the centre line of the right footing (CL_RF) with depth for the loose and medium-dense and dense sand under different loading levels ($q \leq q_{ult}$) is presented in **Figure 6.12**. These results are for the cases at optimum spacing S_{opt}/B=0.25, 0.5 and 0 for loose, medium-dense and dense sand respectively and post the optimum spacing that has not yet presented in the literature.

They show a nonlinear response for all cases of sand packing. They gradually decrease to a negligible value beyond ~ z/B= 2.5, similar results have been reported for single footing resting on loose sand by Liu and Iskander (2004). However, this distance (~ z/B) increases for an increase in the relative density of sand in contrast to the case of single footing on sand that have been reported earlier in **Chapter 5** (Jahanger et al., 2018a). The S_v/B along the line of symmetry attains the peak at a depth of about ~ 0.2B- 0.75B for all cases of sand packing, which are almost independent of the loading stages (**Figure 6.12**). But, the ($S_{v\ max}/B$) along the line of symmetry values increase at post optimum spacing (S_{opt}) for all cases of sand packing, which are independent of the loading stages.

It is observed that the values of S_{vmax}/B at ultimate load are close to the measured values of S_u/B presented earlier. Interestingly, the values of S_{vmax}/B agree with the common assumption of using S/B between 0.05B -0.1B for estimating q_{ult} from the load-settlement plots in foundation engineering designs (Lee et al., 2008; O'Loughlin and Lehane, 2010; Kumar and Bhoi, 2009). Overall, the displacement measures reported here could be used to derive more realistic displacement profiles.

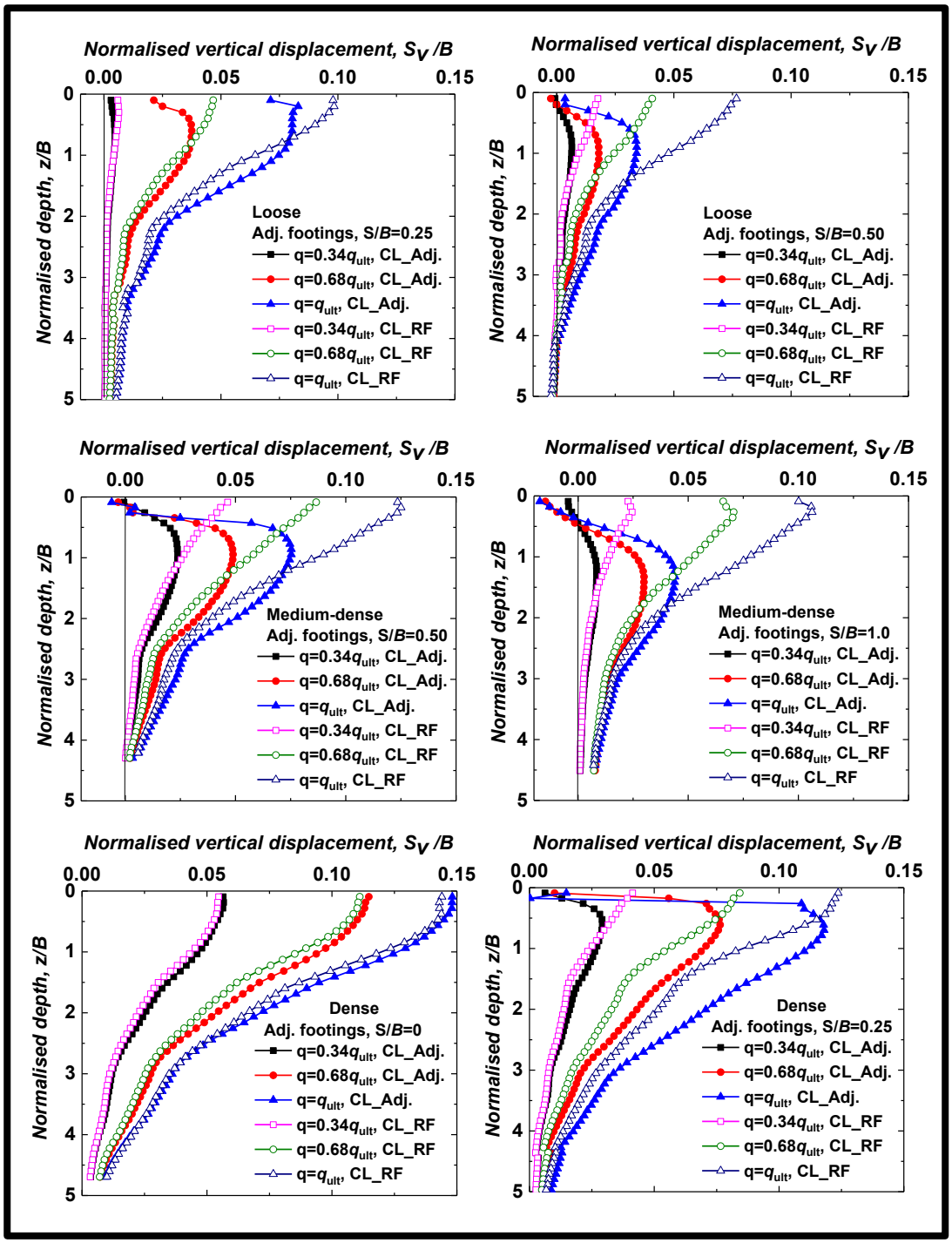

Figure 6.12 Normalised vertical displacement with depth at S_{opt} and post S_{opt} of adjacent footings on loose, medium-dense and dense sand for different stress levels: Signs: vertical displacement (positive down, negative up), CL_Adj.= centre line of the group, CL_RF= centre line of the right hand side footing

6.6.5 Comparison of Measured Efficiency Factor ξγ with Available Theoretical and Experimental Work

The computed values of ξγ for strip footing under the ultimate bearing capacity for loose, medium-dense and dense sand packing were compared with other theoretical and experimental results, as illustrated in **Figure 6.13**. Stuart (1962), Kumar and Ghosh (2007), Kumar and Kouzer (2008), Lavasan and Ghazavi (2014) and Lavasan et al. (2018) have presented theoretically the variation of ξγ with S/*B* between footings for different values of ϕ= 30°, 35°, and 40° as illustrated on LHS in **Figure 6.13 a, c, and e**. The theoretical results reported by Lavasan and Ghazavi (2014) for square footings were also presented in **Figure 6.13a** for qualitatively purpose only. Furthermore, the results of experimental studies conducted by Das and Larbi-Cherif (1983), Kumar and Saran (2003), Kumar and Bhoi (2009) and Lavasan and Ghazavi, 2012 on sands with friction angles of 37°, 38°, 42° and 46° are presented in **Figure 6.13 b, d and f**. The experimental results reported by Lavasan and Ghazavi (2012) for square and circular footings were also presented in **Figure 6.13 b** for qualitatively purpose only. The plate load test result reported by Lee et al. (2008) for circular footings were also presented in **Figure 6.13d** for qualitatively purpose only. In general, the theoretical studies show relatively low differences compared to the experimental investigations.

As seen, ξγ from the current study presented for the loose, medium-dense and dense sand results are found to be less than the theoretically calculated values of ξγ. In addition, the results of the loose and medium-dense sand results are in a good agreement qualitatively and quantitatively with experimental data in the literature; however, for dense sand (higher friction angle) a significant difference observed qualitatively and quantitatively compared to the experimental data is shown in **Figure 6.13e and f**. However, the results from current study showed that the loose sand results are very well consistent with the results of Lavasan and Ghazavi (2014) which is shown in **Figure 6.13 a, b**.

Unlike the experimental data from the literature for (ϕ=46°) as seen in **Figure 6.13 e, f** the tests conducted in the current study for dense sand does not show any clear peak corresponding to the S_{opt}/B. Because the blocking does not happen, and the peak bearing capacity occurs when the footings are in contact of S/*B*=0. This is not proved yet for the dense sand. This observation, yet, qualitatively compared to that reported in the literature. For example, Stuart (1962) and Lavasan et al. (2018) have presented that for loose sand (ϕ=32°), while Stuart (1962) and Kumar and Saran (2003) reported that for medium-dense sand (ϕ=32°, D_r=60%). However, same trend was observed in **Figure 6.13** for circular

footing on loose sand (Lavasan and Ghazavi, 2012). Furthermore, very rare results obtained from PLT using circular plate of 30 cm diameter by Lee et al. (2008) is shown in **Figure 6.13d**.

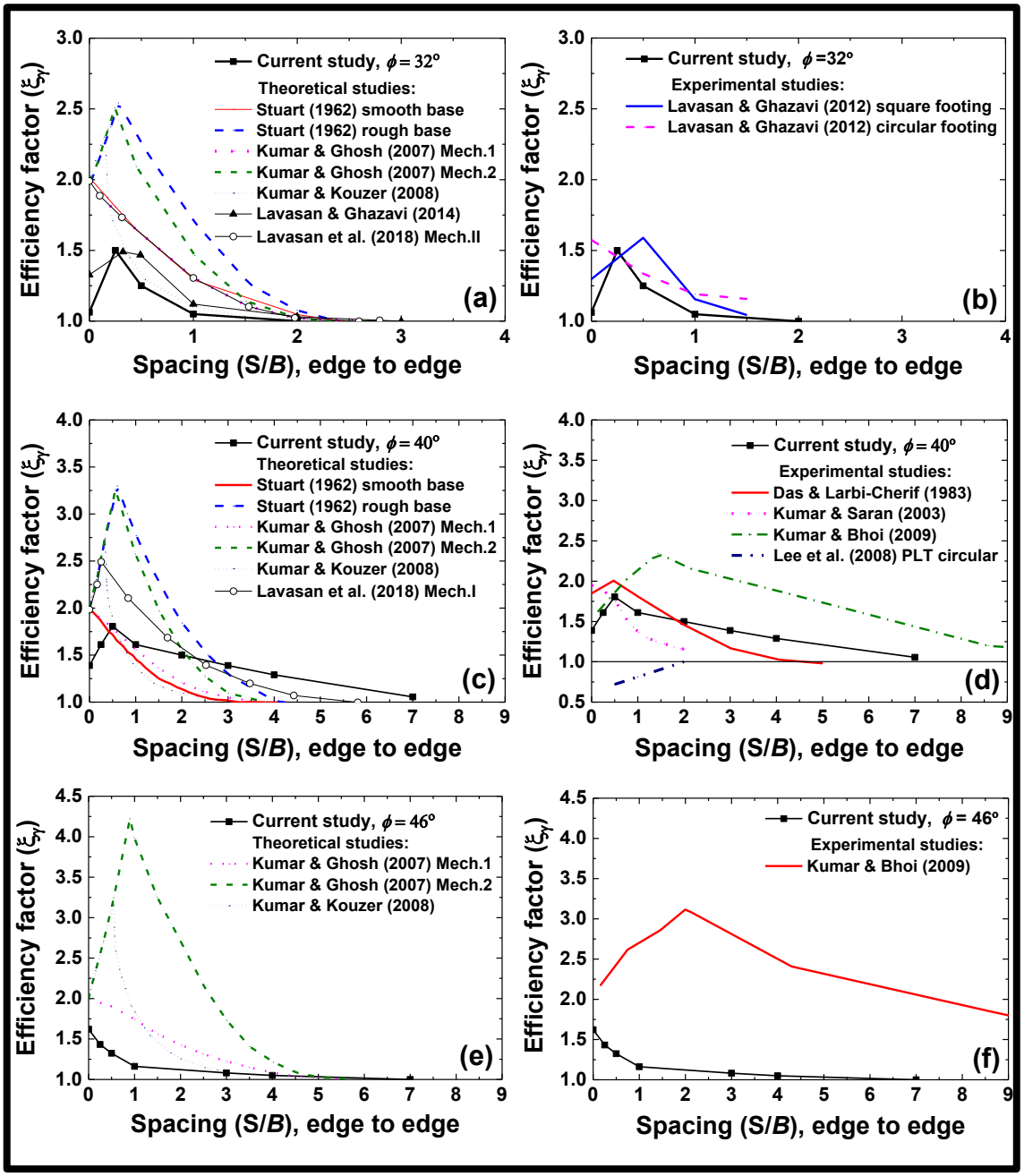

Figure 6.13 Comparison of current experimental ξ_γ for loose, medium-dense and dense sand packing to ϕ =32°, 40°, 46 with existing theoretical curves° (a, c, e) and experimental (b, d, f) results

The current experimental data presented a certain S_{opt}/B at which ξ_γ becomes maximum. The peak values of ξ_γ, hence, are seen to be significantly less than the theories, however;

peak values of ξ_γ are slightly less than those experimentally reported values in literature. At S/*B*=0, all the theories provide the value of ξ_γ for strip footing exactly equals to ~2.0 except that from Lavasan and Ghazavi (2104) which is for square footing. Based on results from the theories and experiments, it can be concluded that the effects of neighbouring footings on the ultimate bearing load is diminished at S/*B*=2.0 for loose sand and 7.0 for medium-dense and dense sand. While, it may be generally scattered results plots in the literature, they follow a general trend. According to **Figure 6.13**, there are lack of experimental studies related to loose sand (D_r < 30%, ϕ=32°) and dense sand (D_r >75%, ϕ=46°). Discrepancies between the theoretical and experimental results need to be checked in which fundamental aspects such as the blocking underneath the footings (interpenetrate of passive zones) and degradation of the ξ_γ with spacing is systematically determined.

6.6.6 Efficiency Factor versus Footing Spacing (ξ_γ versus S/*B*)

The plot of the efficiency factor (ξ_γ) versus clear spacing between footings (S/*B*) is presented in **Figure 6.14** for different packings underneath relatively rough footing under plane strain condition. It can be seen that the efficiency factor ξ_γ increases as the clear space (S) increases from S=0 (footings in touch) up to maximum value $\xi_{\gamma\ max}$ when S/*B*=S_{opt}/B, for loose and medium-dense soils then decreases to minimum $\xi_{\gamma\ min}$ value of ~1.0 again at S/*B*= S_{max}/B. S_{opt} and S_{max} are spacings for maximum ($\xi_{\gamma\ max}$) and minimum ($\xi_{\gamma\ min}$) efficiency factors respectively. However, in the case of dense sand, ξ_γ reaches higher value as the footings get touched S/*B*=0 and then decreases for an increase in S. The value of S/*B*= S_{max}/B beyond which ξ_γ becomes equal to ~1.0 and the adjacent footings behave as two single footings was found to be about 2*B* for loose sand and 7*B* as extrapolated from the trend of the results for medium-dense and dense sand. At this space S_{max}/B, no interaction in the area between the two footings occurs and the system reverts to two single footing. The blocking, which described previously in **Section 6.2** and **Figure 6.1**, in the medium-dense and loose sand occurs when S ≤ 0.5*B* which agrees well with the results of the theoretical and experimental studies in the literature (Stuart, 1962; Das and Larbi-Cherif, 1983; Kumar and Ghosh, 2007; Kumar and Kuozer, 2008).

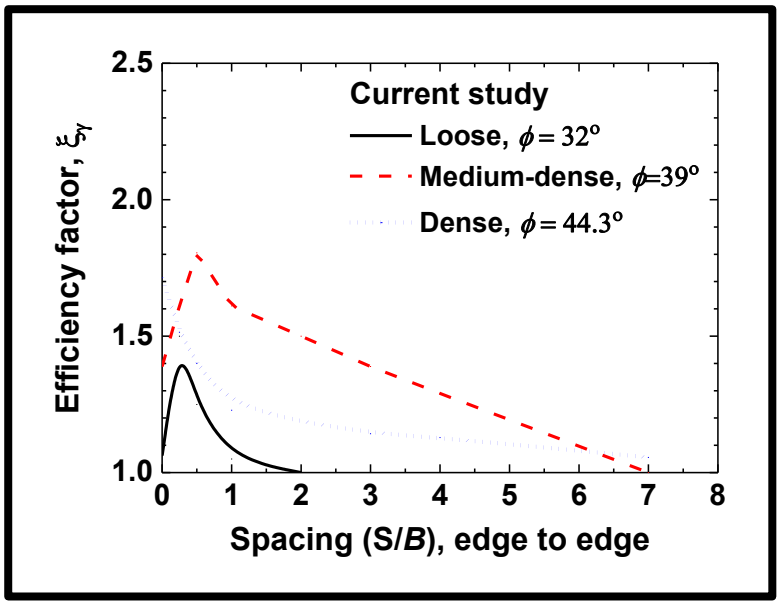

Figure 6.14 Variation of efficiency factor (ξ_γ) with (S/*B*) for different packing densities (relative roughness of the footing, δ/ϕ=0.25

6.7 FEM Analysis

6.7.1 Comparison of the DPIV Measurements with FEM Analysis

The FEM approach used here is validated with the DPIV results. For this, the ultimate load q_{ult} obtained from current experiments are compared with the FEM simulations (**Table 6.1**) and presented in **Figure 6.15**. The obtained from the current FEM analysis is seen to be close to the values measured from the experiments. As seen, the results of q_{ult} obtained here from the current FEM analysis are qualitatively in an excellent agreement with those obtained from experiments analysis for different cases of S/*B*. However, quantitatively some FEM results are not comparable to the experiments, due to the assumed line of symmetry along the footing centre line, S_h= 0 and $S_v \neq 0$. The results that are along the line of symmetry as presented in **Figure 6.9-Figure 6.11**, showed that there could be some horizontal displacements (~20% of the maximum S_{hmax}) under the q_{ult} in the experiments. This does not mean that the load was not applied symmetrically, nor the samples are not prepared uniformly. In addition, it is well known that the theoretical (numerical) methods usually show higher calculated values of ultimate load than the experiments as shown in **Figure 6.13** (Kumar and Kouzer, 2008), and Lavasan et al., 2018). In the case of dense sand, for S/*B*>3.0 the domain in x-direction is not verified experimentally in the range of 6*B*, and this could be affected the calculated

results. **Figure 6.15** shows the variation of the efficiency factor (ξ_γ) versus S/*B* determined from FEM analysis and the current experiments. According to **Figure 6.15**, FEM results have slightly over-predicted the values of efficiency factor (ξ_γ). However, the FEM-based values for the efficiency factor (ξ_γ) are in excellent agreement qualitatively with experimental data for all the cases of sand packings. The reasonable configuration of numerical and experimental ultimate bearing capacity of interfering footings confirm that the procedure used here in the numerical analyses are reasonable though further analyses are desired for verifying that there is zero horizontal displacement along the line of symmetry between the adjacent footing-sand interactions.

Table 6.1 Comparison of ultimate load results obtained from current study with FEM

Sand	S	S/*B*	Ultimate load q_{ult} (kN/m^2)		
			Current experiments*	FEM	Error %**
Loose ($\phi_{tr} = 32°$)	0	0	29.1	38	+30
	9	0.25	41.9	44.6	+6.4
	18	0.50	34.6	31.8	-8.0
	38	1.0	28.9	26.3	-8.9
	76	2.0	27	22	-18.5
Medium-dense ($\phi_{tr} = 39°$)	0	0	87	92.7	+6.6
	9	0.25	101	114	+12.8
	18	0.50	112.5	132	+16.8
	38	1.0	101	111	+10.1
	76	2.0	94	84	-10.6
	152	4.0	97	87	-10.3
Dense ($\phi_{tr} = 44.3°$)	0	0	200.8	227	+13
	9	0.25	183.5	216	+17.4
	18	0.50	169.6	185	+8.9
	38	1.0	148.9	150	+1.0
	114	3.0	138.5	120.8	-12.8
	152	4.0	136.8	105	-23.6
	420***	11	118	127	+7.6
* Results are for one side of the assembly					
**$Error(\%) = ((FEM - Exp.)/Exp.) \times 100$; (+) overestimated, (-) underestimated					

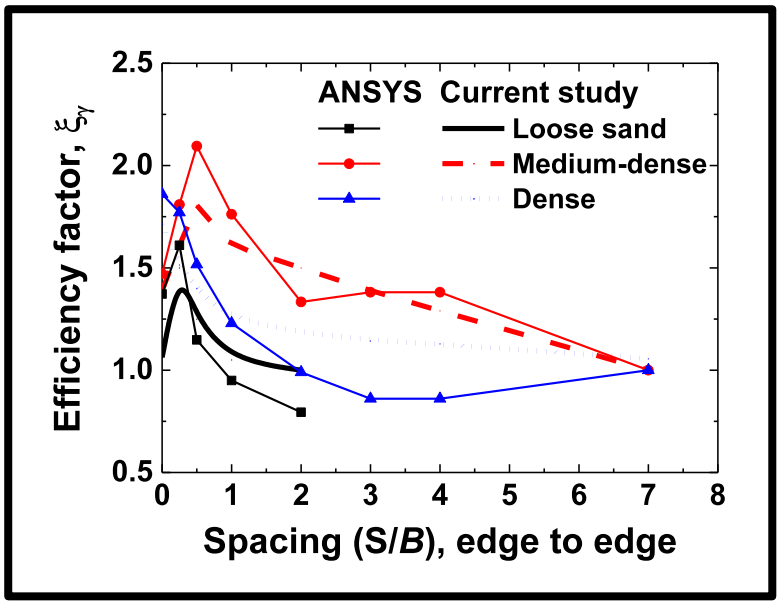

Figure 6.15 Comparison of efficiency factor from experiments and FEM ANSYS

6.7.2 Analysis of Failure Mechanism (FEM)

Here the typical FEM acquired failure mechanism results are presented below for the case of adjacent footing at their optimum spacing (S_{opt}/B) interacting with the single soil of loose, medium-dense and dense sand under the ultimate load, as illustrated in **Figure 6.16**. This reports the comparison of resultant displacement profile and vertical stress contour bands. The observed mechanisms are interpreted in conjunction with load-settlement response and displacement fields obtained from the DPIV-based experiments. As seen, the non-symmetrical triangular elastic active wedge (mostly red colour) is developed under each of the adjacent footings (**Figure 6.16 left**) which differs from Terzaghi's mechanism for single footings. This might be the most reason for enhancing the ultimate bearing capacity upon using adjacent footings at their optimum spacings.

Furthermore, though the figures are not presented here, it is worth mentioning that the FEM analysis for the other spacings contained in this study had performed, and a good level of agreement of the displacement fields with DPIV was obtained. A single failure mechanism is developed when two neighbouring strip footings are placed touch each other. The same single failure mechanisms underneath pairs of footings are observed for S_{max}/B=2.0, 4, and 6 for the loose, medium-dense and dense sand under the ultimate load. It means that for S/B values between adjacent strip footings less than S_{max}/B, the two footings and the soil between them act as a single footing. Therefore, a unique failure zone is formed in a larger dimension beneath the two footings. The ultimate bearing

capacity of interfering strip footing increases significantly due to the blocking zone. For spacing greater than S_{max}/B, the sizes of deformation pattern and failure mechanism begin to shrink.

Further, to explore the difference in displacement fields, strain fields are plotted in **Figure 6.17**. Normal strain fields are shown on LHS of the figure with corresponding shear strain fields for the same region mirrored on RHS for the loose, medium-dense and dense sand at S_{opt}/B. In all sands, a highly concentrated zone of the normal shearing is seen around the corners of the adjacent footings. However, the inside corner in between the interfering footings shows a maximum value but more diffuse and of generally lower magnitude than other outer corner of the adjacent footings. It is worth mentioning that in the dense sand case, there appears to be a dilating zone close to the free surface, however there is significantly more volumetric compression beneath the footing in the loose sand test than the medium-dense and dense sands, which agrees well with the difference in displacement fields were seen in **Figure 6.6-Figure 6.8**. The heap close to the free surface increases with increasing relative density (Jahanger et al., 2018a). The results presented improve understanding of the different responses in sand beneath adjacent footings under vertical load.

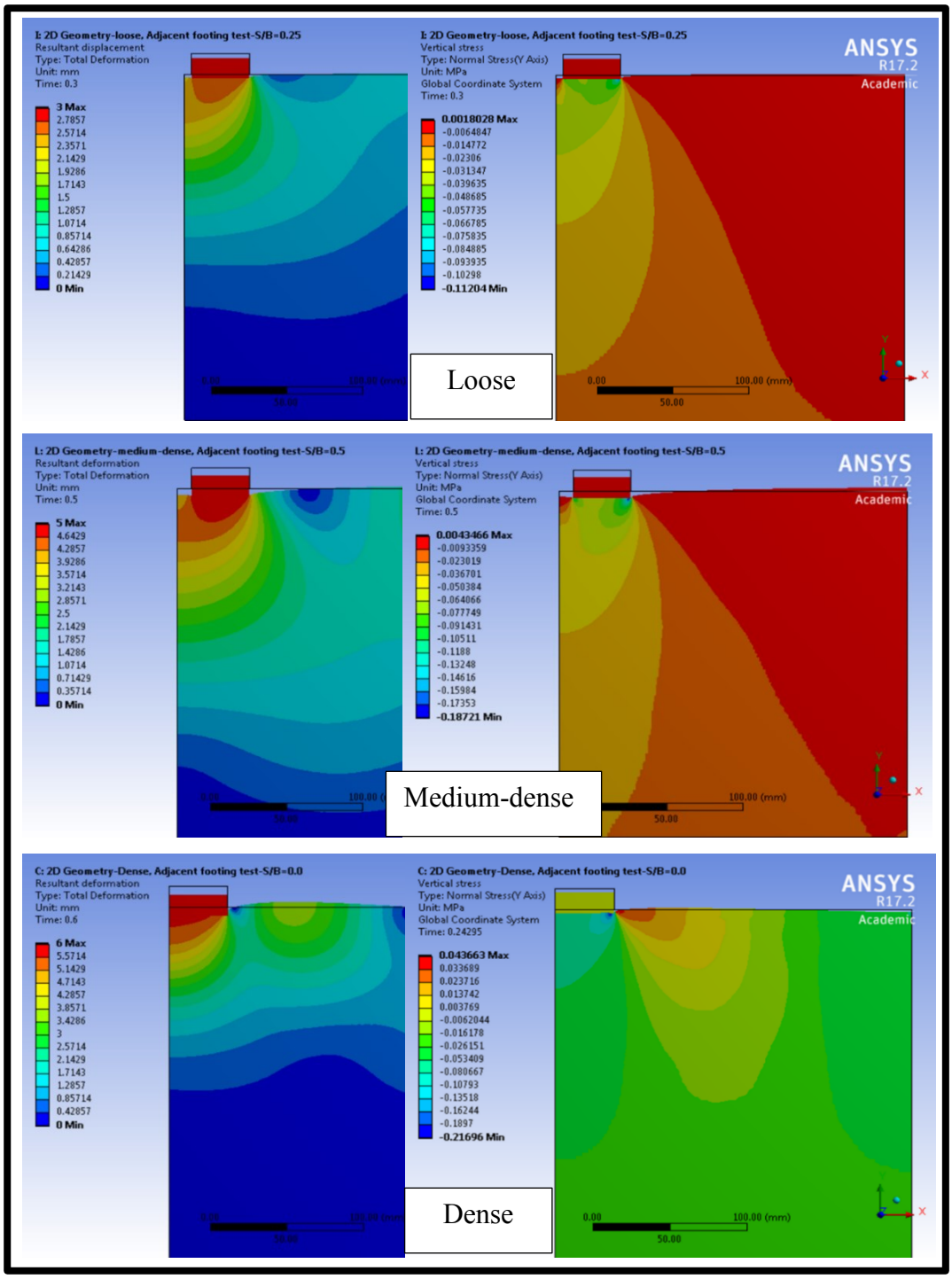

Figure 6.16 FEM results for adjacent footing on loose, medium-dense and dense sand at their optimum spacing (S_{opt}/B) (left) resultant deformation (right) vertical stress

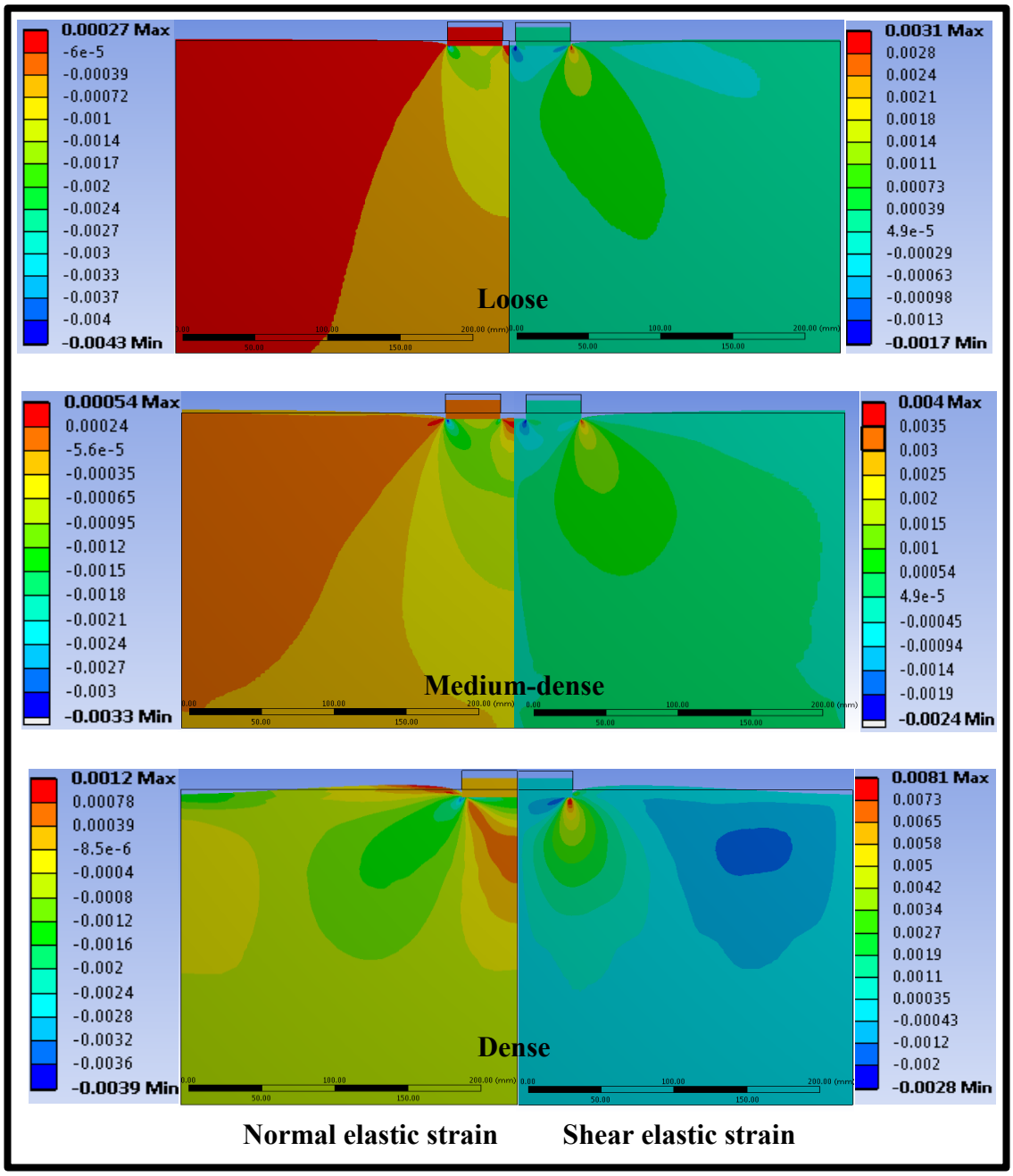

Figure 6.17 Normal elastic strain field (left) and mirrored corresponding shear elastic strain field (right for adjacent footing on loose, medium-dense and dense sand at their optimum spacing (S_{opt}/B)

6.8 Summary

The effects of interference on the bearing capacity of two adjacent strip footings placed on sand packings have been evaluated. A set of laboratory model tests have been performed to study the deformation fields of two adjacent footings under monotonic vertical load. The system of interfering footings is analysed using DPIV-experiments. Where possible, the displacement measures and generic characteristics of velocity fields

and displacements in the sand are compared with existing literature and FEM analysis and a good level of agreement is obtained.

Results of this research presented that at a close spacing between the two footings, non-symmetrical triangular wedge was observed below the base of each footing. Also, an inverted arch form beneath the footings, leading to an increase in the bearing capacity with spacing up to 0.25*B*, 0.5*B* and 0*B* for loose, medium-dense and dense sand respectively; however, such an incident does take place for dense sand case when they touch each other. Theoretical methods have over-predicted the efficiency factor (ξ_γ) and need more experimental studies related to loose sand (D_r < 30%, ϕ=32°) and dense sand (D_r >75%, ϕ=46°). Discrepancies between the theoretical and experiments results need to be checked in which fundamental aspects such as blocking underneath the adjacent and reduction of the ξ_γ with spacing are systematically determined. For different sand densities, at S/*B*=0, the deformation patterns are similar to that of an isolated footing (width =2*B*). The pairs of footing acts as single footing (width=2*B*), and the total load on one of the pairs is simply $1.0 < \xi\gamma < 1.6$ the load taken by one footing only. As the spacing increases up to optimum spacing S_{opt}/B, they will act as a single footing (breadth= $2B + S_{opt}$) and ξ_γ equals ~1.4 and 1.75 for loose and medium-dense respectively. This means that blocking (superposition of the displacement field) occurs in loose and medium-dense sand between the two footings. However, for dense sand packing, which does not show any optimum value of ξ_γ, $\xi\gamma$ reaches higher value as the footings get touched (at S/*B*=0). The results here showed that there could be some level of horizontal displacements S_h along the plane of symmetry (~20% of the S_{hmax} under the ultimate load) in practice due to nonuniformity of the sand grains (heterogeneity). This contradicts the zero-shear stress and the horizontal displacements along the line of symmetry in the literature. DPIV clearly shows detailed descriptions of the stages of velocity discontinuities for the sand media under loading. The boundaries of the zone of plastic flow in sand at failure load profiled using the advanced DPIV here are remarkably similar to such intuitive diagrams suggested by Stuart (1962) for interference effects. The present study provides both the spatial and temporal distribution of displacements in soils of different packing densities and spacings under key stages of loading elegantly.

Chapter 7 Strip Footing-Layered Soil Interactions

The aim of this chapter is to report about research on the application of digital particle image velocimetry (DPIV) as a non- invasive visualising technique and finite element method (FEM) simulations to measure the ultimate bearing capacity and failure mechanism pattern. The ultimate bearing capacity refers to the ability of the soil to sustain the maximum load on the footing before the soil collapses. Here, the bearing capacity of as relatively rough strip footing under the plane strain condition resting on dense sand layer on loose sand. The investigation emphasises the influence of thicknesses of the top dense layer H (H/B=0, 0.5, 1.0, 2.0, 3.0, 4.0, and 6.5 on the evolution of grain-scale velocity fields and slip surfaces angle β in the sand for different loading levels. In this, H/B = 0 means a single layer of homogeneous loose sand packing and H/B = 6.5 pertains to practically a single layer of homogeneous dense sand packing. In the FEM, experimentally characterised constitutive behaviour of the sand grains is fed as an input. From the DPIV experiments, a correlation between the slip surface angle and the thickness of the dense sand layer H/B has been determined. A new approach is proposed to calculate theoretically the ultimate bearing capacity of layered sand based on a well-defined failure pattern beneath footing under ultimate loading in which the top layer acted as a raft. The new approach has shown quantitatively a good comparison with the literature. Significant improvements over existing method are shown. Some of the results reported here published as proceedings in ISTVS 2016 (Jahanger et al., 2016). However, most of the results reported here have been published in the Journal of Terramechanics (Jahanger et al., 2018b).

7.1 Introduction

In the terramechanical engineering applications, we often come across the foundation structures and rigid structural elements interacting with non-homogeneous soil profiles of complex nature. In actual practice, the soil underneath the foundation is non-homogeneous and is mostly layered (Gupta et al., 2017). Layered soil profiles are often found either naturally or man-made. Due to the demands of the scarcity of the construction spaces, there is an increasing demand to construct structures on loose soils,

which were previously considered as unsuitable for construction (Jahanger et al., 2010). Loose sand packings have high compressibility and low shear strength (Terzaghi et al., 1996). One of the methods to improve the strength of the weak soil is to construct a suitable layer of granular material to decrease the overall compressibility. For instance, oil storage tanks and diesel power stations may be found on a thin layer of compacted granular fill (Jahanger et al., 2010). Unpaved roads are also built on the weak soil where the treated layers of sub base are used to spread the service loads applied by the passing vehicles (Jahanger et al., 2010). Shallow footings, when built on loose sandy soils, have a low load bearing capacity and undergo large settlements (Terzaghi et al., 1996). Construction on loose sands often requires the utilisation of ground improvement techniques (Das, 2009). Compacted soil layer is used under such foundation structures to improve the ultimate bearing capacity and corresponding displacement of soil. The ultimate bearing capacity equation according to Terzaghi (1943) for a surface footing (D_f =0) resting on the cohesionless soil (c=0) and subjected to a vertical load can be expressed by neglecting the N_q (bearing capacity factor) contribution (Dijkstra et al., 2013; Jahanger et al., 2018a; 2018b) is given as:

$$q_{\text{ult}} = 0.5\gamma B N_\gamma \tag{7.1}$$

Where

γ = Unit weight of the soil (kN/m^3), and

N_γ = Bearing capacity factor due to unit weight of soil.

In a recent study, digital particle image velocimetry (DPIV) was used to understand the displacement fields of strip footing interacting with homogeneous sand bed of different relative densities (Jahanger et al., 2018a). The experimental results compared favorably and validated the finite element method (FEM) simulations, which used experimentally measured constitutive relations of the sand grains. The current study deals with the specific case of the bearing capacity of a rigid plane-strain surface footing placed on a layered sand consisting of a dense sand layer overlying a homogeneous bed of loose sand. The study is restricted to cases where the thickness of the top sand layer, H, is quantified in terms of the width of the footing (B). A discussion is given of the various theoretical and the experimental work that have been proposed for this type of analysis. A detailed description is then given of a new proposed method that has been performed to investigate the ultimate bearing capacity and the failure mechanism of this problem.

7.2 Review of the Previous Work

Numerous researchers have investigated on the ultimate bearing capacity and settlement of the footings interacting with layered soil using theoretical and experimental approaches. Button (1953) was the first to analyse footings on the layered clayey soil. Likewise, many other investigations were conducted for the ultimate bearing capacity of a sand layer overlying a clay layer (Meyerhof and Adams, 1968; Khing et al., 1994; Michalowski and Shi, 1995; Al-Shenawy and Al-Karni, 2005; Fattah et al., 2011; Shoaei et al., 2012; Ramadan and Hussien, 2015). Similar were also conducted for the cases of layered cohesion-friction soils (Purushothamaraj et al., 1974; Azam et al., 1991). Furthermore, researchers have studied theoretically and numerically on the bearing capacity of footings interacting with two-layered granular soils (Farah, 2004; Ghazavi and Eghbali, 2008). Some experimental studies, for example Hanna (1982) focused on loose sand overlying on dense sand. Most of the aforementioned studies have used simplified failure mechanisms together with a reduction in the mobilized shear strength (ϕ_{mob}) of sand in their corresponding limit analysis and finite element method simulations. These simplified theoretical mechanisms comprise (i) projected area method (mode 1) that uses constant slip surface angle, β (as shown in **Figure 7.1**); (ii) a punching shear failure (mode 2) which assumes zero slip surface angle (as shown in **Figure 7.2**); (iii) the theory of bearing capacity by considering the top layer as surcharge (mode 3); and (iv) a variable slip surface method (modes 4 and 5) that assumes different values of β (**Figure 7.3 and Figure 7.4**). Large discrepancies between the measured and the predicted values of the ultimate bearing capacity have been observed. It is worth noting that existing studies either used a constant value of β (Yamaguchi, 1963) or set β =0 (Meyerhof, 1974), but in both cases β is independent of the thickness of the top layer (*H*). However, other conclusions from the previously mentioned studies are that the ultimate bearing capacity for the layered soils depends on the individual *c* and ϕ of each layer, *H*, *B*, *H/B*, D_f, and the shape of the footing embedment, as illustrated in **Figure 7.1**.

7.2.1 Theoretical Work

The most widely used methods to calculate the bearing capacity of layered soil are the projected area method (Yamaguchi, 1963) and the punching shear failure method (Meyerhof, 1974). The former method has been adopted by many researchers and used a constant value of β (**Figure 7.1**) in their studies; for example, 30° by Yamaguchi (1963),

30° and 45° by Myslivec and Kysela (1978) and considered equal to the angle of internal friction (ϕ_1) of the top layer of the soil by Baglioni et al. (1982). The latter, the punching shear failure, assumes as β=0 for the actual failure surface, but accounted for the shear strength of soil along the vertical wedge of the slip plane.

In the following, the principles behind the different methods are discussed briefly. In the projected area method, a rigid block of truncated cone under the footing was assumed in the top layer as well as a constant angle of the slip surface β (**Figure 7.1**). The shear strength along the slip surface of the top layer was neglected. The ultimate bearing capacity for the strip footing resting on the sand layer overlying clay could be estimated from the shear strength of the underlying clay soil and the dimension of the base of the trapezoidal failure pattern according to Yamaguchi (1963) as:

$$q_{\text{ult layered}} = (1 + 2H \tan \beta / B)\, q_{\text{ult 2}} \tag{7.2}$$

Where

$q_{\text{ult layered}}$ = Ultimate bearing capacity for footing on layered soil (kPa), and

$q_{\text{ult 2}}$ = Ultimate bearing capacity of the underlying clay soil (kPa) (**Figure 7.1**).

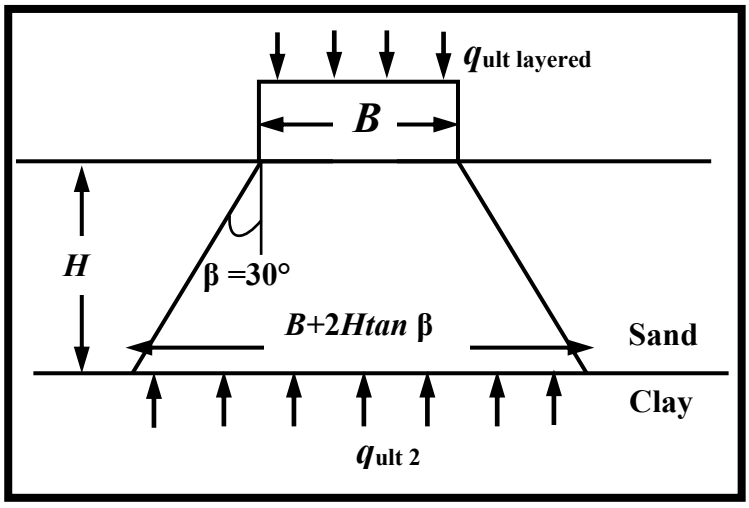

Figure 7.1 Schematic illustration of the projected area method (Yamaguchi, 1963)

Therefore, the ultimate bearing capacity for a surface strip footing resting on the layered granular soil of cohesion and subjected to the vertical load can be expressed by neglecting the N_q (bearing capacity factor) contribution (Dijkstra et al., 2013; Jahanger et al., 2018a).

Based on the mode 1, the bearing capacity for the dense sand on loose sand can be written as:

$$q_{\text{ult layered}} = 0.5\gamma_2 B N_{\gamma 2} + H\ tan\beta\ \gamma_2 N_{\gamma 2} \quad (7.3)$$

Where

β = Assumed as 30° (Yamaguchi, 1963),

γ_2 = Unit weight of the bottom soil layer (kN/m^3), and

$N_{\gamma 2}$ = Bearing capacity factor of the bottom soil layer.

The traditional analytical analysis according to Meyerhof (1974) studied the case of a dense sand resting on a soft clay. The failure of a rigid continuous footing punching through a thin layer of dense sand into a thick underlying deposit of clay was assumed as an inverted uplift problem. The failure mode 2 (**Figure 7.2**) considered a sand mass having an approximately truncated pyramidal shape, pushing into the lower layer in the direction of applied load. Similarly, Hanna (1981) studied mode 2 punching failure surface (β=0) of strip footing on a strong sand overlying weak sand deposit (**Figure 7.2**).

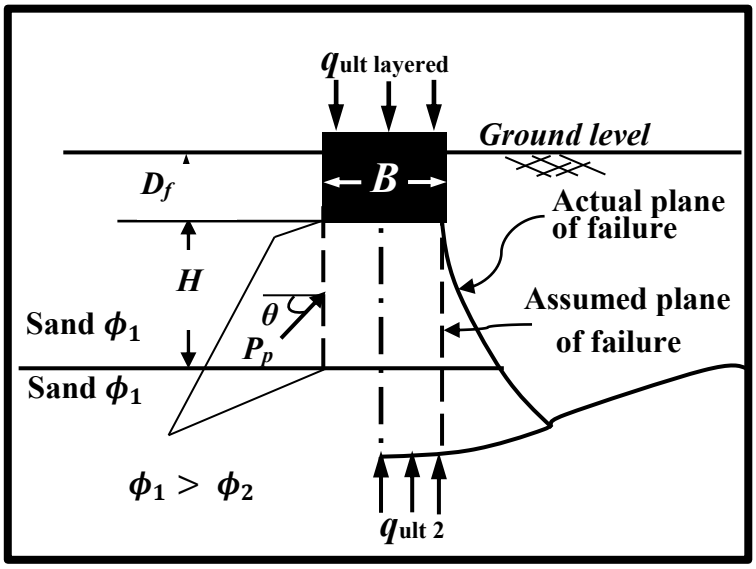

Figure 7.2 Failure mode of dense sand overlying loose sand deposit (Hanna, 1981)

Meyerhof (1974) proposed a theoretical equation for bearing capacity by considering the failure method using the assumed plane of failure, i.e. vertical side block (β =0) instead of the trapezoidal shape (P_p in **Figure 7.2** is the total passive earth pressure) for layered

dense sand overlying loose sand. The bearing capacity of the layered soil was evaluated from the force limit equilibrium of the sand block, and approximated as follows for mode 2:

$$q_{\text{ult layered}} = 0.5\,\gamma_2\,B\,N_{\gamma 2} + (\gamma_1 H^2\,K_s\,tan\,\phi_1)/B - \gamma_1 H \;\leq q_{\text{ult 1}} \qquad (7.4)$$

Where

$q_{\text{ult 1}}$ =Ultimate bearing capacity of the top soil layer (kPa).

γ_1 = Unit weight of the top soil layer (kN/m^3),

K_s = Coefficient of punching shear, and

ϕ_1 = Peak friction angle of the top soil layer (degree).

In this, $K_s \tan\phi_1 = Kp \tan\theta$ and ϕ_1 is experimentally value of the angle of internal friction for top layer. K_s=6.5 pertaining to the value of ϕ_1 and $q_{\text{ult 2}}/q_{\text{ult 1}}$. θ is the mobilized angle of shear resistance on the assumed failure zones (**Figure 7.2**). Kp is coefficient of passive earth pressure of the top soil.

Okamura et al. (1998) have proposed a new limit equilibrium method in order to verify the validity of the previous modes by comparing them to centrifuge test results **Figure 7.3**. They have adopted a failure mechanism (**Figure 7.3**) which is similar to the existing methods with accounting for the shear strength along the shear slips surfaces. In their analysis, β is calculated using the limit equilibrium method (Okamura et al., 1998).

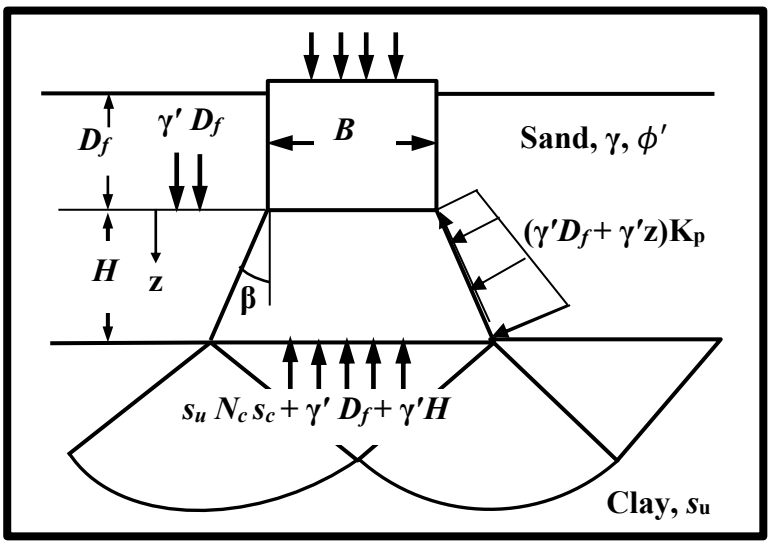

Figure 7.3 Failure mechanism assumed for sand overlying clay after (Okamura et al., 1998)

7.2.2 Experimental Work

Hanna (982) suggested to calculate the ultimate bearing capacity of the layered soil of weak sand overlying a strong deposit by considering the top layer as surcharge (mode 3) using the following:

$$q_{\text{ult layered}} = 0.5\,\gamma_2 B N_{\gamma 2} + \gamma_1 H N_{q2} \leq q_{\text{ult 1}} \tag{7.5}$$

In this, the ultimate bearing capacity of the layered soil (**Eq. 7.5**) is the sum of the bearing capacity of the lower layer 2, and the shearing resistance in the top sand layer 1 of thickness *H*. This can be considered as ultimate bearing capacity for the strip footing according to Terzaghi's bearing capacity equation (Terzaghi, 1943).

Farah (2004) has theoretically calculated β based on the experimental results of Meyerhof and Hanna (1978). In this, the angle β was correlated with the thickness ratio *H/B* for varying between 0.5 and 5, and the ratio $q_{\text{ult 2}}/q_{\text{ult 1}}$ =0.08. The variation of the angle β according to Farah (2004) analytical results is constant (89°) up to *H/B*=1.0, then β gradually decreases with depth to β =40.1° at *H/B* = 4.5, before β increases to 46.6° when *H/B*=5.0. It seems that β was overestimated as Prandtl (1920) and Terzaghi (1943) have showed that the maximum β is equal to $45 + \phi/2$ which results, β =68.85° even when *H/B* tends to zero.

In a preliminary study conducted by Jahanger et al. (2016), DPIV was used to investigate the failure plane of a soil system of a dense sand layer on loose sand. It was noted that the measured value of β significantly depended on the depth of the dense sand layer. The schematic diagram of their failure plane of the layered soil system is presented in **Figure 7.4**. However, no quantification of β as well as its use in evaluating the ultimate bearing capacity of layered system were reported either. These form the motivation of the current work. For this, a new methodology is presented below based on the experimentally measured β for the layered soil system considered in this paper. Furthermore, finite element analysis of the common cases was performed here for the purpose of comparisons.

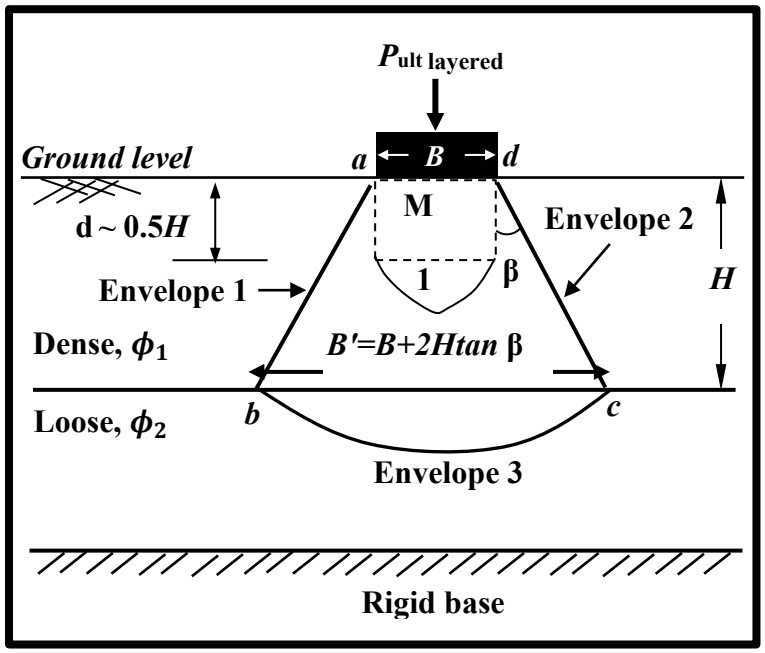

Figure 7.4 Schematic diagram of failure mechanism underneath the rigid footing on the layered sand using DPIV in the current study

7.3 Materials and Experimental Methods

7.3.1 Material

The soil used here are disturbed dry silica sand samples obtained in UK as detailed in **Section 5.2, Chapter 5**.

7.3.2 Experimental Setup

Bearing capacity of the rigid footing was tested using an aluminium planar test box of 460 mm in length, 250 mm in height and 39 mm in thickness, filled with dry sand, as illustrated **Figure 7.5**. The planar box had smooth and transparent Perspex front wall of 15 mm thickness and 10 mm aluminium back wall to eliminate any bending effects during the test in the plane strain direction. It is worth mentioning that it is also verified that under the ultimate load (P_{ult}) of the dense sand packing (H/B=6.5) did not lead to any remarkable out of plane movement of the container's face. More detailed could be found in **Section 5.4, Chapter 5**. It was verified during all the experimental tests that, under the ultimate loads (Pult) of the sand packing, no remarkable out of plane movement of the walls occurred along the thickness direction.

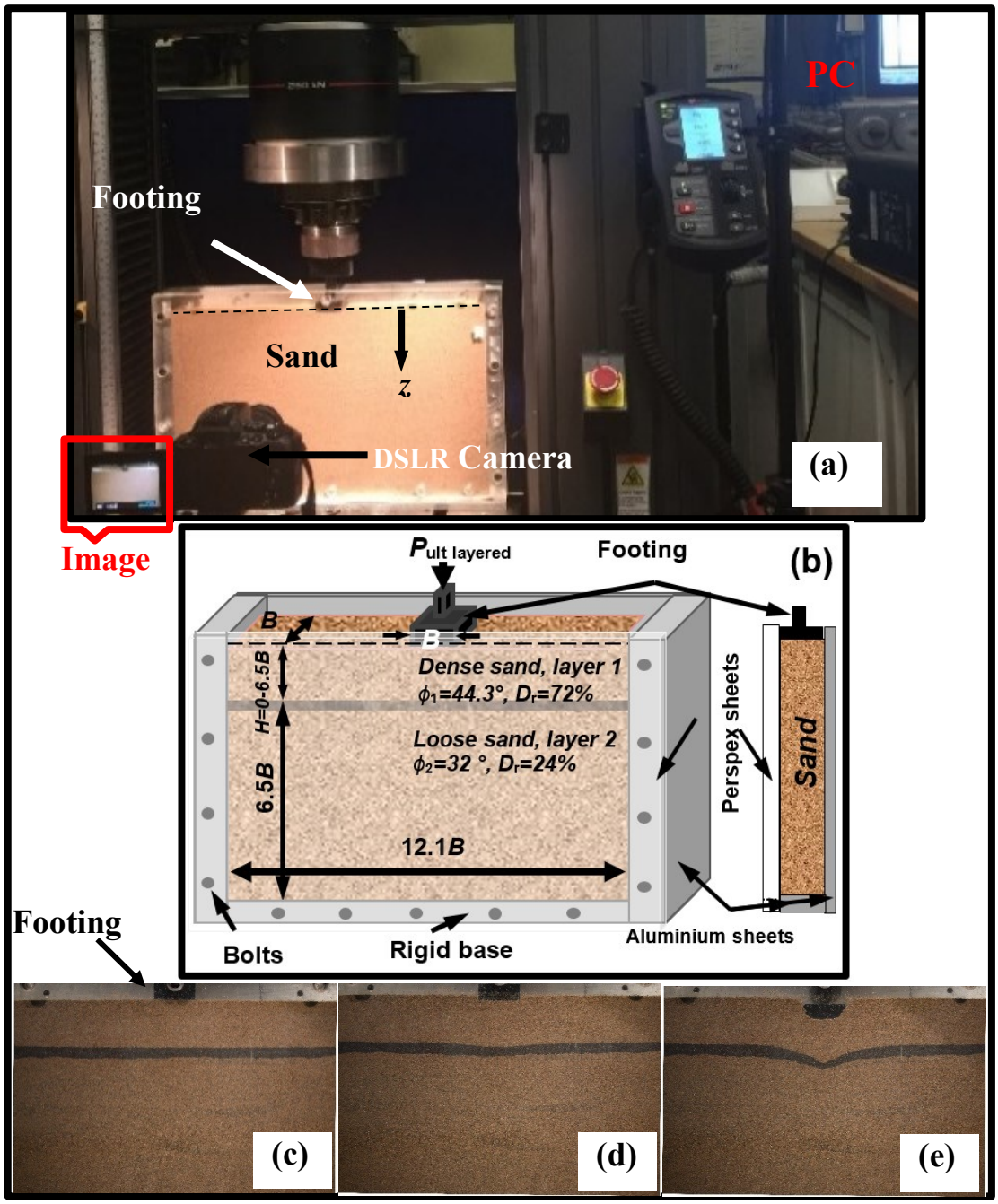

Figure 7.5 Experimental setup using DPIV (b) definition of the problem of rigid footing on layered soil, not to scale (c - e) images of the footing in contact with soil for H/B=1.0 at q= 0, q= q_{ult} and q> q_{ult} respectively

7.3.3 Preparation of the Layered Soil Samples

For the case of homogeneous packing (non-layered system), two cases of relative densities (D_r) of sand (loose and dense) were considered here. The loose granular packing (H/B=0 in **Figure 7.5b**, γ_{loose}=1500 kg/m^3, D_r= 24 % ± 2, e= 0.76) was prepared following the sample preparation detailed in **Section 3.3.3, Chapter 3**. The dense packing (H/B=6.5

in **Figure 7.5b**, γ_{dense}=1610 kg/m^3, D_r =74 % ± 2, e= 0.64) was achieved by using same procedure in **Section 3.3.3, Chapter 3.**

Layered samples of dense sand overlying loose sand were prepared by compacting the dense sand first inside the bottom of the test box. Then the loose sand was poured using pluviation technique (Kumar and Bhoi, 2009) after which the box was turned upside down using a simple mechanical apparatus designed for this purpose. A wide range of *H/B* was considered: 0.5 < *H/B* < 6.5. At first the dense sand layer was compacted into the bottom of the test box to the required depth *H/B*, as explained earlier (Cerato and Lutenegger, 2007; Lavasan and Ghazavi, 2012; Jahanger et al., 2018a). The bottom plate of the box has slightly smaller dimensions than the maximum available dimensions of the box, i.e., less by 1.5 mm from all three sides (except the front side through which DPIV measurements were made). This would help to remove the bottom plate from the box after turning the box upside down easily without much disturbances when required at a later stage. However, to avoid any leakage of sand grains when reversing the box, this small gap was initially covered using a cellophane type. One thin layer of dye sand was used. This used at the interface layer between the soil layers as colour coding technique (CCT), as illustrated in **Figure 7.5**. After this, the loose sand layer was poured in layers on the dense sand as discussed above. Then, the top plate (plan area is equal to the allowable plan area) was fixed to the box with screws. Then, the test box was turned upside down. Hence, the top layer of the sample contains the dense sand and the bottom layer contains the loose sand. It was also verified that there was no significant diffusion of sand particles from the top layer through the interface to the bottom layer of sand packing, by initially colour coating the interface region of the sand layers (**Figure 7.5c**). Even after reversing the test planner box as explained earlier, the level of the colour-coded interface layer of sand remained practically horizontal, as illustrated in **Figure 7.5c**. The footing was placed symmetrically on the top surface of the layered sand bed through which the axial loading applied in the experimental study. This study considered different cases of layered soil, viz., *H*/*B* = 0, 0.5, 1.0, 2.0, 3.0, 4.0, 6.5. For other cases of layered sand, the total sand depth (6.5*B*) was held constant, but the thickness of the dense sand layer (*H*) was varied systematically as *H*/*B* = 0.5, 1.0, 2.0, 3.0 and 4.0. Hence, any boundary effects from the bottom rigid wall of the box was practically negligible. Furthermore, the dimensions of the test box were kept much greater than that of the footing (**Figure 7.5b**) to minimize boundary effects.

7.3.4 DPIV Analysis

In the present study, the footing compression tests on homogenous and layered soil were performed under the same ambient laboratory conditions. The field of view of the DPIV camera focused on the footing-soil interaction region was 270 mm×180 mm, that was further, sub-divided into 375000 interrogation areas of 8×8 pixels each covering a zone of about 0.4 mm × 0.4 mm. Nikon D5500 high definition camera (6000 × 4000 pixels) was used here. This corresponds to a scale of ~ 0.045 mm per pixel in this study. Appling of DPIV technique to footing on a dense sand layer on loose sand, image capturing, and experimental setup are identical to those reported in detail in **Section 4.2, Chapter 4**.

7.3.5 Experimental Tests

An axial compression loading was applied slowly on the footing (0.05 mm/s penetration rate) using Instron loading machine with 5 kN/0.1N resolution (**Figure 7.5a**). The loading machine also had an inbuilt linear variable differential transformer (LVDT) to measure the settlement of the indenting footing on the layered packing. The macroscopic load and settlement of the footing were also recorded from the tests. The Nikon D5500 high definition camera (6000 × 4000 pixels) was fixed in front of the box and two light sources were used to illuminate the rig. However, as the loading condition is quasi-static in this study, an image at every 10 seconds was found to be adequate until reaching the failure load of the sand packing. DSSP was used to analyse the digital images acquired during test using DPIV (DantecDynamics, 2013). The distribution of velocity vectors of the grains was examined for which an adaptive interrogation area (IA) of maximum size 64 × 64 pixels (60 mean size particle) and of minimum 16 × 16 pixels size (4 mean size particle) resolution was employed in the image analysis. A typical mean size of sand grain (D_{50} = 0.37 mm) was represented by about 8 × 8 pixels (patch) to reduce DPIV error (DantecDynamics, 2013; Gollin et al., 2017). The mean number of particles per maximum IA should vary between 10 and 25 (DantecDynamics, 2013). Each of these patches was tracked using an adaptive PIV method, to identify the movement field of soil between consecutive images obtained from the front side of the Perspex sheet of the test rig, to a measurement precision of 0.045 mm for the field of view used during these experiments. The adaptive PIV iteratively adjust the size of the individual interrogation areas (IA) in order to adapt to local seeding densities (seeding with particles to create colour coded upon which image processing can operate) and flow gradients

(DantecDynamics, 2013; Gollin et al., 2017; Jahanger et al., 2018a). This space-pixel dimension of the measurement was calibrated by printing a known scale on the test box along the horizontal and vertical directions. White et al. (2003) have shown that the precision of the measurement (i.e., the random difference between multiple measurements of the same quantity) improves with larger DPIV patches and it is inversely proportional to the amount of the measurement resolution. This size of the mesh patch used here corresponds to a precision better than 1 pixel. It was verified that the variation in the image scale in both horizontal and vertical direction were not significantly different. Hence, the measurements made here are at the local-scale (close to discrete-grain scale) rather than a continuum measure. The tests were repeated at least twice to verify the repeatability and the consistency of the test data (Kumar and Bhoi, 2009).

Two standard cone penetration test tests (CPTs) were also conducted for each soil density, the loose and the dense sand layer, to verify the relative density of single layer sand using a 10 mm diameter model CPT, however, the results are presented in **Section 5.4, Chapter 5**. Therefore, for layered soil (H/B=1.0 and 2.0), the CPT was inserted at a penetration rate of 1 mm/s in the current experiments but using the identical filling procedure of the grains used in **Section 7.3.3**. The penetration resistance (q_c) profiles are plotted against the penetration depth (z) from the bottom level of the footing. The cone resistance of dense sand layer overlying loose sand samples (H/B=1.0 and 2.0) started to decrease when the cone penetrometer approached the underlying loose sand layer, as illustrated in **Figure 7.6**. As expected, the penetration resistance of dense sand is higher than loose sand. Once the cone penetrometer enters the loose sand layer, the cone resistance continues to decrease rapidly, thereafter the rate of decrease (kPa/mm) of the cone resistance decreases, until the cone tip q_c remained almost constant with depth, as illustrated in **Figure 7.6**. Accordingly, the prepared sand bed is homogenous dense sand (Jahanger et al. 2017a, 2017b; Jahanger et al. 2018a). The CPTs results show the average response of the two results (error within 5%).

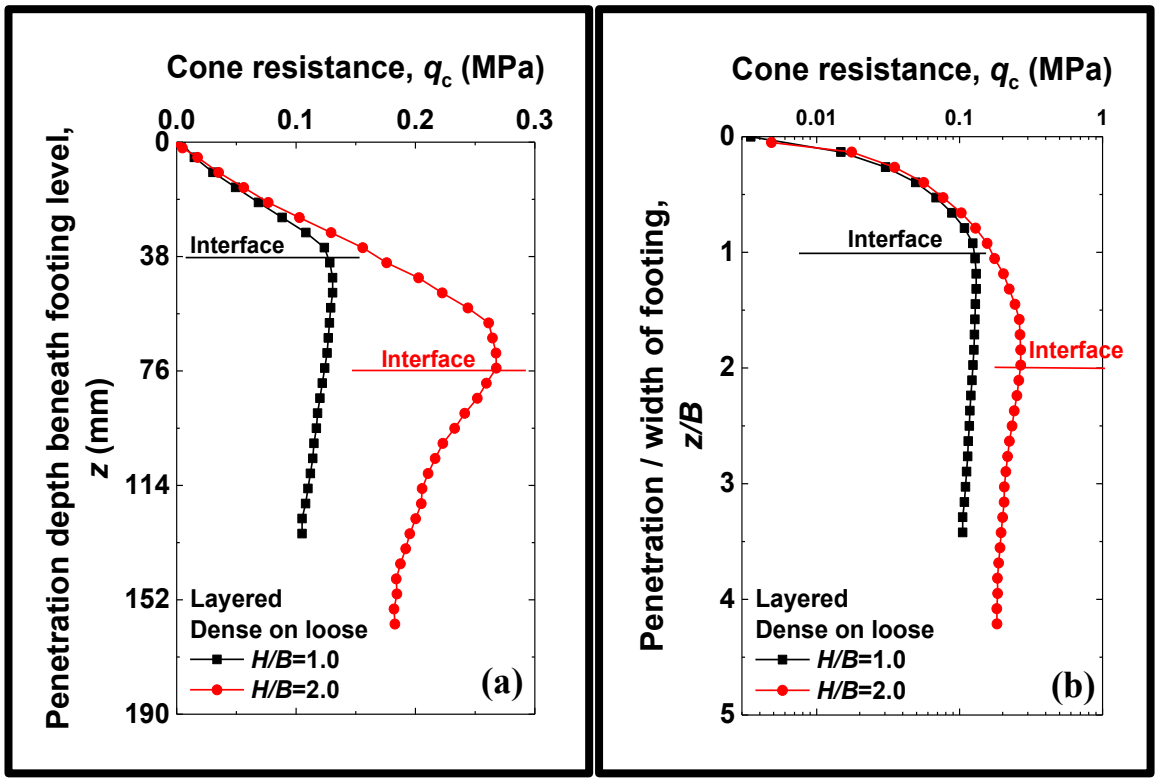

Figure 7.6 Cone resistance versus penetration depth profiles (a) and versus normalized penetration (b) for tests performed in dense sand over loose sand

7.4 FEM Simulations

In the present FEM study, the simulations were performed using ANSYS by creating a 2D solid geometry of the footing and the layered soil. The soil and the footing were modelled as under plane strain condition. The discretization of the footing and the layered soil were done using an eight-nodded quadratic solid element having two degrees of freedom at each node, i.e., translations in the nodal x and y directions (**Figure 7.7**). The nodes and element numbers are equal to about 80000 and 25000 respectively. The strip footing was discretised using nodes and element 309 and 76 respectively. The chosen domain along with applied boundary conditions and the size of the elemental geometry is shown in **Figure 7.7**.

The simulations were held under identical boundary conditions for footing indenting with different *H/B*. The contact regions between the sand layers were modelled as well bonded (Mohsenimanesh et al., 2009). A refined mesh was generated at the footing-soil interface where the largest stresses and strains would be expected. The material model for the soil describes the nonlinear plasticity behaviour that corresponds to the actual soil properties

in the current ANSYS simulations. For this, the experimentally characterised bulk stress-strain relationship corresponding to the load-displacement curves of loose and dense sand presented in (**Figure 7.8**) were discretised. Therefore, a large number of linear segments and fed as user defined digital input (Mohsenimanesh et al., 2009; Lee, 2015; ANSYS, 2016; Jahanger et al., 2018a) to account for the corresponding materials properties of the layered sand. The evolution of displacement components in the soil elements was tracked under different loading levels and compared with corresponding DPIV measures later. More details could be found in **Section 4.3.1, Chapter 4.**

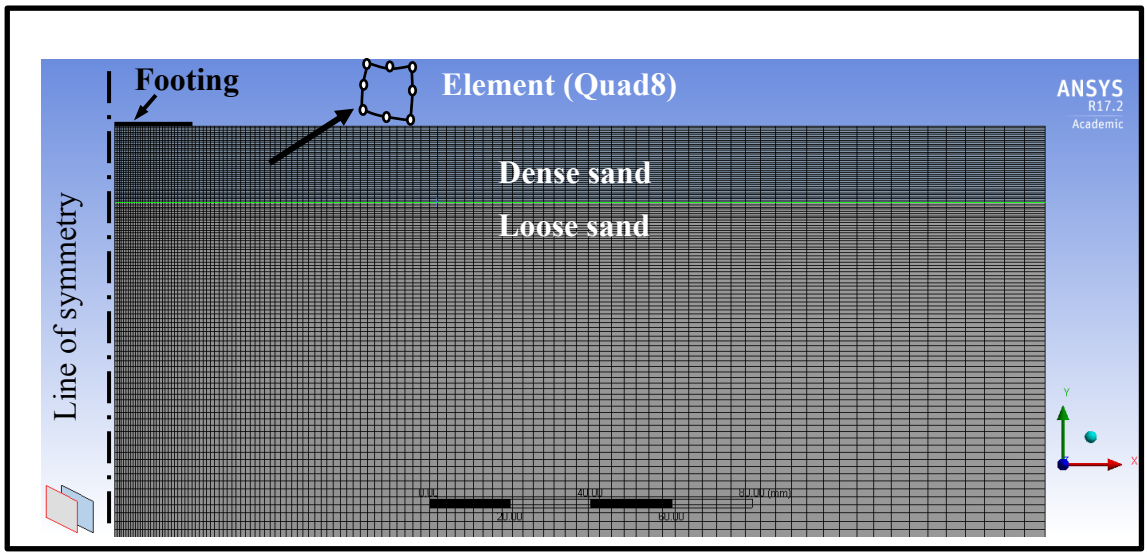

Figure 7.7 Finite element mesh, and element enlarged for *H/B*=0.5

7.5 Results and Discussions

The experimental axial load–settlement results for a typical footing interacting with homogeneous (single layer) and layered sand are presented in **Figure 7.8**. The load-settlement curves characterised here provide a consistent response with respect to an increase in the height of the dense sand layer (*H*). A well-defined peak is obtained for the case of *H/B*= 6.5 (practically a homogeneous dense sand packing). Using the load-settlement data, the tangent intersection method (Akbas and Kulhawy, 2009; Jahanger et al., 2018a) was applied to measure the value of the ultimate bearing capacity (**Figure 7.8**). This involves linear curve fittings for the initial loading and hardening phases of the load–settlement relations. The intersection point of these two lines thus corresponds to the q_{ult}. The ratio of the ultimate bearing capacity of the loose sand (*H/B*= 0) to the ultimate

bearing capacity of the dense sand (H/B= 6.5), $q_{ult\ 2}/q_{ult\ 1}$ =0.08. However, in the case where there was not a clear curvature in the shape of the load- settlement plots, the failure corresponds to punching failure (e.g. test H/B= 0 - 2) (Vesic, 1973). However, the failure surface was totally located in the dense soil layer if the depth H is relatively large (H/B > 2.0) and eventually resulted a soil rupture (Shaaban, 1983).

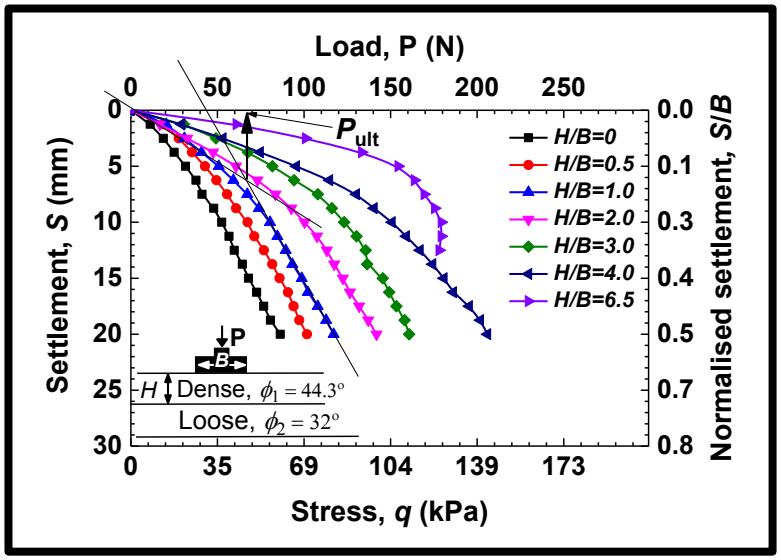

Figure 7.8 Experimental axial load-settlement curves. For convenience their corresponding stress and normalised settlement are also presented here

The ratios of ultimate vertical settlement of the footing (S_u) to footing width (B), S_u/B for the case of homogeneous sand (H/B= 0) are 6% and 8% for the dense and loose sand respectively. In the cases of layered sand, this varies between 14%-18% respectively. These measures and the nature of bulk load-settlement curves are consistent with Das (2009) for homogeneous sand, and Meyerhof and Hanna (1978) for layered sand.

Figure 7.9 presents the effect of depth of the dense sand layer overlying loose sand bed on the evolution of the mean resultant velocity vectors beneath a rigid footing subjected to the ultimate load were measured from DPIV data. It is evident that, for the homogeneous loose sand (H/B= 0), the slip planes occur in a triangular wedge shape through the punching shear failure mode (Vesic, 1973).

For the case of homogeneous dense sand ($H/B \geq 4.5$), the initial triangular wedge (punching failure) is followed by the formation of active and passive failure zones (marked as zones 1-3 in **Figure 7.9**). It is worth mentioning that it had also observed that

outside zone-1, the particles tended to move downward and sideward symmetrically until the ultimate bearing capacity was reached. Similar trends were noticed in other cases reported by Prandtl, (1920), Terzaghi (1943), Murthy et al. (2012) and Jahanger et al. (2018a). The depth of this plastic wedge at the ultimate bearing load is equal to about *B*, whose vertices (slip planes) intersect the horizontal at an angle (α) of about ($\phi < \alpha = 56° < 45 + \phi/2$). These are consistent with Terzaghi's assumption (1943) for relatively rough footing, which have not been confirmed using microscopic experiments, but using DPIV here. Furthermore, Kumar and Kouzer (2007) have assumed similar measures for using plasticity limit analysis of homogeneous soil using FEM. The current experimental study supports such an assumption. Surprisingly, in the case of layered packing, the slip planes are dominantly through the punching mode, but the shape of the slip planes contains a distinct rectangular wedge supported by a semi-circular (or simplified triangular) wedge (**Figure 7.9**). Furthermore, the sand surface does not heap noticeably on both sides of the footing (**Figure 7.9**) for the case of layered sand. This profile corresponds to the theory of punching shear failure that occurs in the top dense sand layer, followed by another punching shear failure in the bottom soil layer in the cases of $H/B \leq 1$. However, it is worth mentioning that it has observed that if $H/B \geq 4B$, then the failure mode was fully located within the top soil layer, which is the upper bound for the ultimate bearing capacity of dense sand (**Figure 7.8**, $H/B \geq 4.0$).

For the analysis of failure of wedge materials indented by a rigid footing, Prandtl (1920) assumed that the failure occurs along definite slip surfaces (lines) in the material beneath the indenter. Under plastic equilibrium, a rigid triangular wedge of soil was formed below the indenter with base angle $\alpha = 45 + \phi/2$, as illustrated in **Figure 7.9**. Further, the soil mass on the left and right of the rigid triangular wedge extended radially outwards (zone 2) and upward (zone 3) along the boundaries of the plastic flow, as shown in **Figure 7.9**. Therefore, Prandtl- type slip lines commonly appear in the tests on homogeneous sand if the footing is loaded greater than the ultimate load (Oda and Win, 1990). In the series of layered sand, however, two slip lines starting from the footing edges expand downward with angle β (**Figure 7.9**). It seems that the angle β depends on the angle of internal friction of the dense sand as well as its thickness *H* ($H/B \geq 1.0$), inconsistent with the theoretical work of Burd and Frydman (1997) for a uniform sand overlying a thick bed of clay ($H/B \leq 1.0$). Burd and Frydman (1997) stated that the value of β is insensitive to the top thickness of the sand layer.

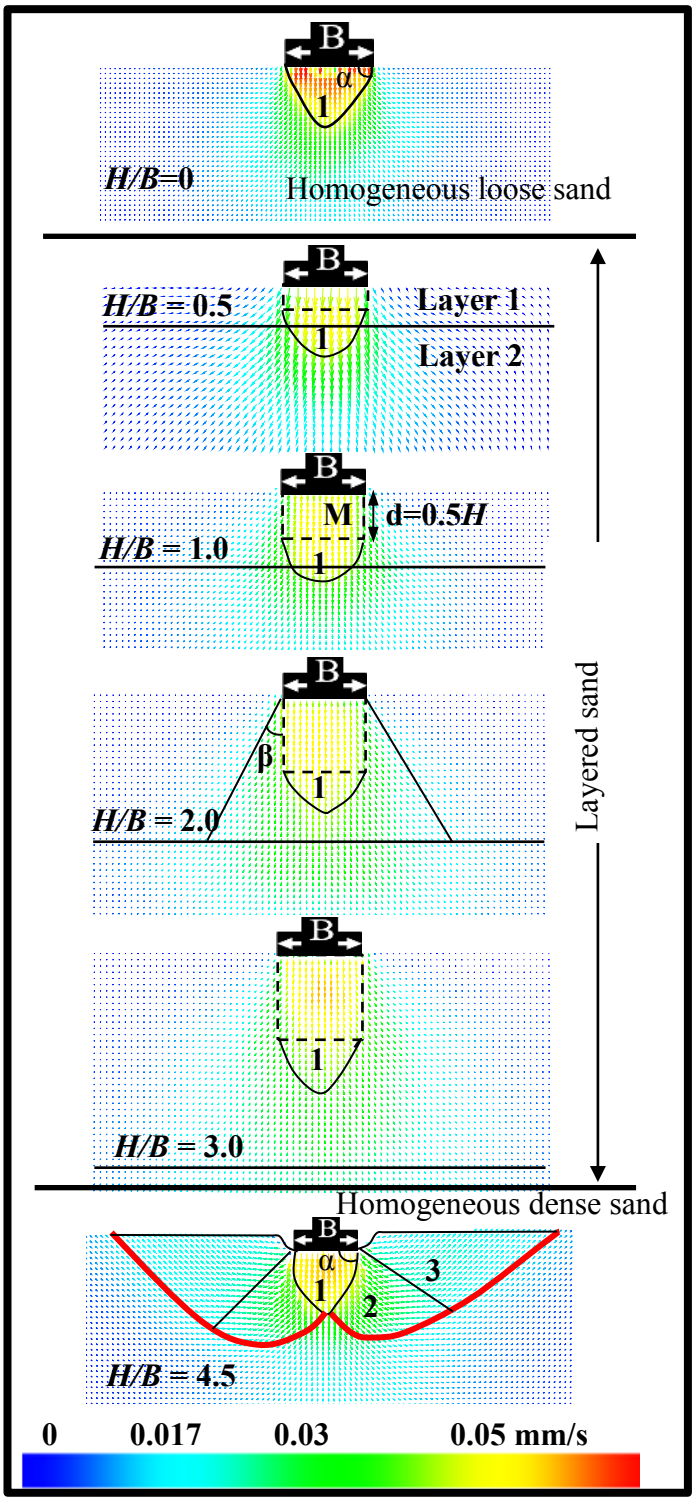

Figure 7.9 Effect of depth of dense sand layer overlying loose sand on the evolution of the mean resultant velocity vectors beneath a rigid footing subjected to the ultimate load P_{ult}. Active dead zone (1), radial shear zone (/transition zone) (2) and passive Rankine's zone (3)

The associated plastic strain in the rectangular mass sand is concentrated in a shallow zone right under the footing. The depth of such sand mass (M) is equal to about 0.3-0.5*H*. As the footing compresses, the displacement of the grains occurs generally downwards,

with the soil element trajectory moving towards the deeper loose soil interface. In contrast to ultimate bearing capacity theory, which comprises soil heave around footing edges to accommodate the punch volume, the mean resultant velocity vectors beneath the footing at ultimate load is dominantly downwards. Larger net downward displacement and less lateral displacement are observed in layered soil than in the case of homogeneous sand.

7.6 Comparison of the DPIV measurements with FEM analysis

Here the typical results are presented below for the case of rigid footing interacting with the layered soil of dense sand on loose sand packing for the case of H/B= 0.5 (**Figure 7.10**). This shows the comparison of mean resultant displacement profile and vertical displacement component contours using DPIV and FEM (ANSYS) analysis for the case of footing interacting with layered soil system under the ultimate load. The FEM simulation results are validated by DPIV results at localised scale. It is evident that a good level of agreement is obtained between the DPIV and FEM results both qualitatively and quantitatively.

Furthermore, though the figures are not presented here, it is worth mentioning that it had performed the FEM analysis for the other cases of soil profiles reported in this study, and a good level of agreement of the displacement measures were obtained with that of DPIV experiments. The results obtained from the current DPIV experiments with those obtained from ANSYS simulations are presented in **Table 7.1** for comparison purposes. As seen, the results obtained here from the current FEM analysis are in an excellent agreement with those obtained from ANSYS analysis for different cases of layered sand.

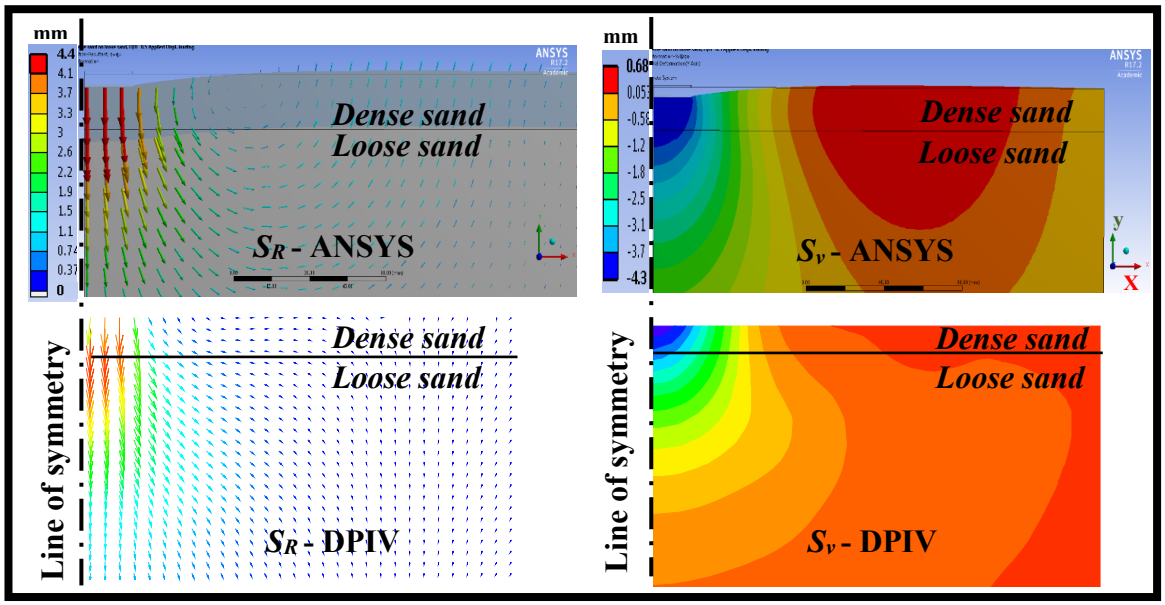

Figure 7.10 Comparison of DPIV-based measures with FEM (ANSYS) analysis in layered sand under ultimate load (identical colour codes are used) (left) mean resultant displacement profile (right) vertical displacement component (the field of view is 3B (horizontal) × 2.5B (vertical))

Table 7.1 Comparison of ultimate load results obtained from experiments with FEM

Width of footing (mm)	H (mm)	H/B	Ultimate load P_{ult} (N)		
			Dense sand on loose sand ($\phi_1 = 44.3°$ on $\phi_2 = 32°$)		
			Current experiments	FEM	Error %*
38	0	0	40	42	+5
	19	0.5	50	48	-4
	38	1.0	67	71	+5.9
	76	2.0	90	95	+5.5
	114	3.0	115	117	+1.7
	152	4.0	145	148	+2.1
	247	6.5	170	175	+3.0
$Error\ (\%) = (FEM - Exp./Exp.) \times 100$; (+) overestimated, (-) underestimated					

7.7 New Proposed Method

By taking advantage of the experimentally characterised failure surfaces using DPIV (**Figure 7.4**), here it is worth mentioning that a new method for evaluating bearing capacity of the layered soil system encountered here. The ultimate bearing capacity refers to the ability of the soil to sustain the maximum load on the footing before the soil collapses. The displacement of the loose sand located at shallow depth below the rigid footing is independent of the distribution of the pressure on the base of the footing itself, because the dense layer supporting the rigid footing acts as a natural raft that distributes the load from the footing to the loose sand layer (Terzaghi et al., 1996). Nevertheless, the displacement might be considerable at the interface of dense and loose layered sand media. This failure mechanism is kinematically realistic, as illustrated in **Figure 7.9**. The whole soil media (**Figure 7.4**) can be bounded by failure envelopes 1-3 (**Figure 7.4**, *abcd* region) through footing's corners and a semi-circle profile in the loose sand media. Inside zone *abcd*, the displacement occurs mostly vertically. Hence, this is the lower boundary of the zone of plastic equilibrium (Terzaghi, 1943).

As observed from **Figure 7.9**, β varies with the depth of the dense sand layer. Therefore, a relation between β and *H/B* from the DPIV measures (**Figure 7.11**) has been presented in Eq. (7.6). The lower bound solution is obtained when β = 0 which corresponds to no lateral dilatancy of the failure region (same as mode 2, Meyerhof, 1974). An upper bound solution is obtained when $\beta = \phi_1$ which corresponds to an associated flow rule where the angle of dilation (ψ) equals the angle of internal friction of dense sand. However, the plots of the mean resultant velocity vectors beneath the footing at ultimate load for different *H/B*, show that the angle β is variable and depending on *H/B* and the angle of internal friction of the top sand layer ϕ_1 (**Figure 7.11**). Therefore, from the test data used in **Figure 7.11**, a third order polynomial equation was obtained, as it was the best fit using the regression analysis as follows:

$$\beta / \phi_1 = -0.011\,(H/B)^3 + 0.115\,(H/B)^2 - 0.255\,(H/B) + 1.041 \qquad (7.6)$$

According to **Figure 7.4** and **Figure 7.11** and the analysis according to Terzaghi et al. (1996) for shallow foundation ($D_f/B \leq 4.0$ (Das, 2009)), it is worth mentioning that a new set of equations for mode 4 is presented for as:

$$q_{\text{ult layered}} = 0.5\,B\,\gamma_2 N_{\gamma 2} + \gamma_1 H N_{q2} \leq q_{ult\,1} \qquad (7.7)$$

By using $B = B'$ here (**Figure 7.4**)

$$q_{\text{ult layered}} = 0.5\,[B + 2H\tan\beta]\;\gamma_2 N_{\gamma 2} + \gamma_1 H N_{q2} \leq q_{ult\,1} \tag{7.8}$$

$$q_{\text{ult layered}} = 0.5\,B\,\gamma_2 N_{\gamma 2} + H\tan\beta\;\gamma_2 N_{\gamma 2} + \gamma_1 H N_{q2} \leq q_{ult\,1} \tag{7.9}$$

Where

$q_{\text{ult layered}}$ = Ultimate bearing capacity for footing on layered soil (kPa), and

B = Width of the footing (mm),

H = Thickness of the top layer (mm),

β = Slip surface angle as **Eq. 7.6** (degree),

γ_1 = Unit weight of the top soil layer (kN/m^3),

γ_2 = Unit weight of the bottom soil layer (kN/m^3),

$N_{\gamma 2}$ = Bearing capacity factor due to unit weight of the bottom soil layer.

N_{q2} = Bearing capacity factor for surcharge stress of the bottom soil layer.

$q_{\text{ult 1}}$ = Ultimate bearing capacity of the top soil (kPa) (**Figure 7.1**).

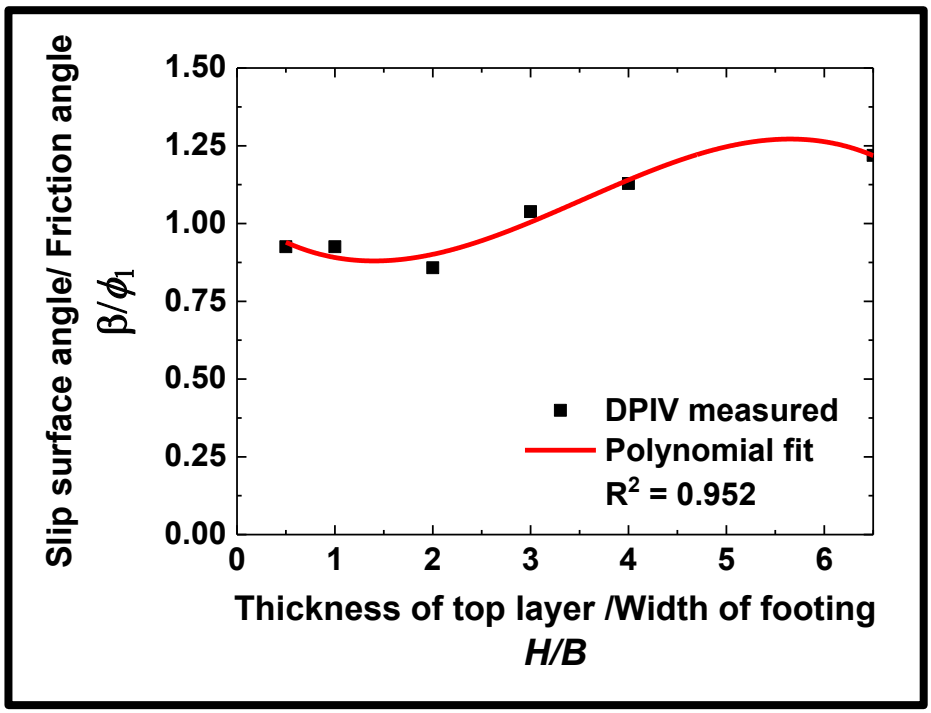

Figure 7.11 Variation of β with *H/B* for strip rigid footing on layered sand

For comparison purposes, it is worth mentioning that the analysis was also performed for mode 5, using **Eq. 7.2** (mode 1) but with variable slip surface angle β measured from the current DPIV test results. Here it is worth mentioning that a detailed comparison was presented of the bearing capacity of layered soil system based on modes 1-5 with the current DPIV-based experimental results in **Figure 7.12 (a)** and **(b)**. N_γ and N_q for loose and dense sand are obtained corresponding to their ϕ_{peak} using (Terzaghi, 1943). To compare the performance between each approach, a non-dimensional parameter, which is the ultimate bearing capacity ratio (UBCR), was used to analyse the results (Binquet and Lee, 1975). UBCR is defined as the ultimate loads ($q_{ult\ layered}$) of the rigid footing on layered soil system divided by the ultimate load of the same rigid footing on homogeneous dense sand ($q_{ult\ 1}$). It can be observed that the projected area method (mode 1) highly underestimates the bearing capacity of the layered media due to ignoring the shearing resistance of the soil along the sand slip surfaces and the use of a fixed slip surface angle β = 30° in mode 1.

The results based on mode 2 (Meyerhof, 1974) gives a conservative value for the bearing capacity due to use of an assumed plane of failure (with β = 0, **Figure 7.2**). The results based on mode 3 (Hanna, 1982) reveals a conservative estimate of the UBCR. However, the results based on the newly proposed method (mode 4) compare well with the current experimental values of UBCR.

It is interesting to note that mode 5 gives a relatively more comparable trend with the experimental results of UBCR than using modes 1-3. It is also interesting to note that, the UBCR reaches a value of 1.0 (**Figure 7.12b)** for different values of *H/B* of the layered sand (as well as depending on the mode of analysis used). For example, to achieve UBCR=1.0, modes 1-5 predicted the required value of *H/B* as ~11.5, 5.5, 6.0, 3.5 and 4.7 respectively. The results of mode 4 and mode 5 are closest to what is commonly considered in geotechnical engineering application (*H/B*= 4-5).

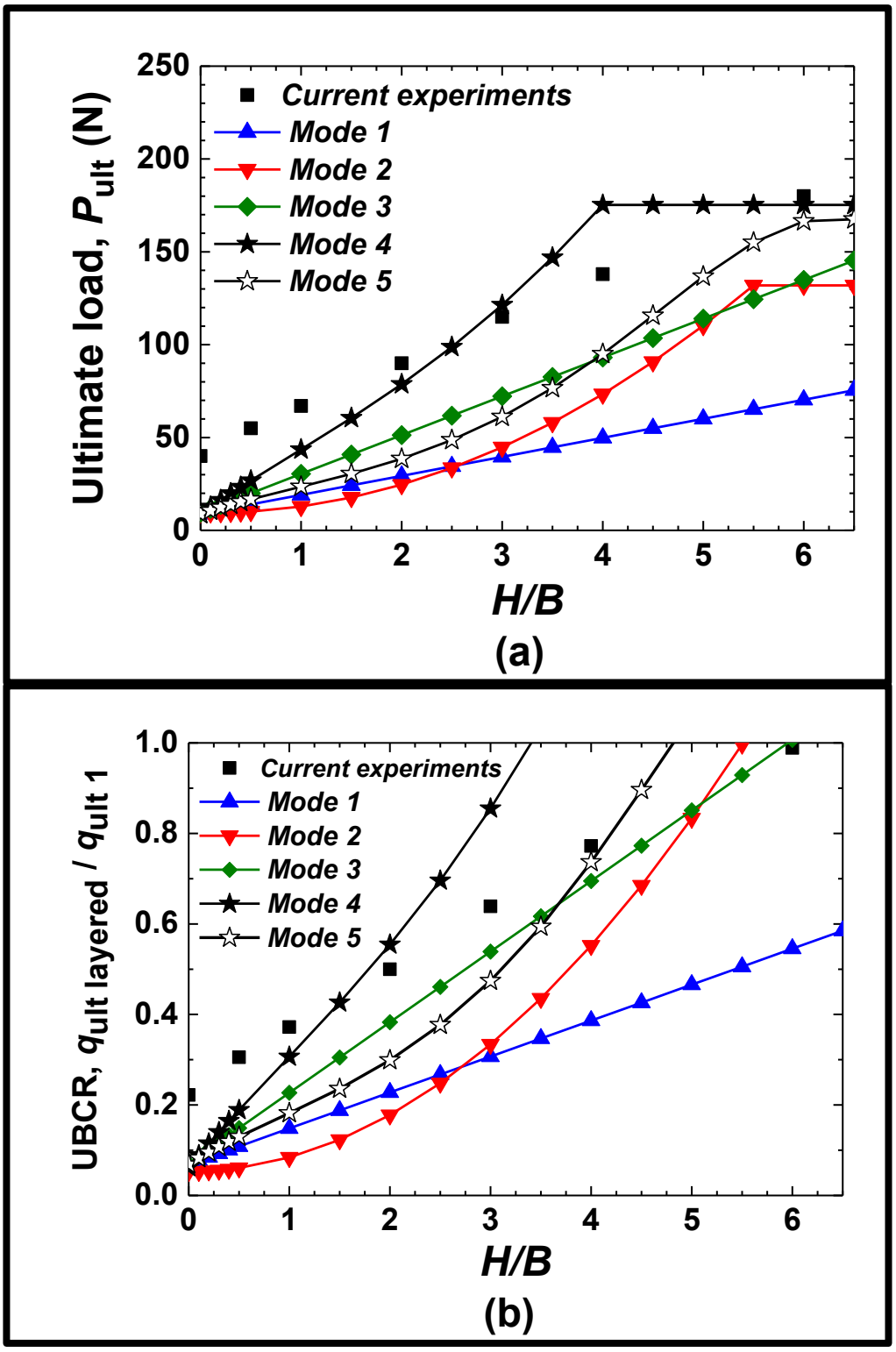

Figure 7.12 Effect of depth of dense sand layer on (a) ultimate load and (b) UBCR, and their comparison with the theoretical results using modes 1-5

7.8 Summary

Single layer is defined as a soil mass with same strength and properties within 4*B* deep under the footing while layered soil is defined as several different layers of soil with different strength within the depth of 4*B* to influence the ultimate failure load of shallow footing. In this study, DPIV is used to understand the local and global geomechanical characteristics of rigid footing interacting with layered sand deposit in a coherent manner. In sand-structure interaction problems, FEA based outputs of the displacement profiles in the sand bed to a level of accuracy of what happens in real experiments (e.g. using DPIV methodology here) is possible to obtain, as long as the input parameters of constitutive relations are also characterised realistically and fed as input in the FEM simulations. The FEM simulation results are validated by DPIV results at localised scale. Where possible, the displacement measures and generic characteristics of velocity fields in the layered sand are compared with FEM and a good level of agreement is obtained. Failure surfaces of homogeneous sand are consistent with Vesic (1973) but the advanced measurements reported here detect their evolutions more precisely. The boundaries of the zone of plastic flow in dense sand overlying loose sand at failure load measured here are remarkably similar to the shape of such intuitive diagrams suggested by Meyerhof (1974), but with different values of β.

The new modified **Eq. (7.9**) makes it possible to estimate the ultimate bearing capacity of the layered granular soil with quite a good level of accuracy. The ultimate bearing capacity refers to the ability of the soil to sustain the maximum load on the footing before the soil collapses. However, the results obtained from these model tests and new proposed approach (mode 4) can be applied for most strip prototype especially when $B \leq 1.0$ m (Jahanger and Antony, 2017a). Therefore, based on the results reported here, DPIV could be applied in future to develop robust failure surfaces for more complex soil profiles and types of foundation researches encounter in geotechnical engineering applications. The obtained layered failure mechanisms could be employed in related theoretical solutions in the future.

Chapter 8 Local Scale Displacement Fields in Footing-Sand Interactions under Cyclic Loading

Geotechnical engineers usually use design equations developed based on failure mechanism measured from experiments. However, investigations on the local scale measurement of displacements of the grain and failure patterns within the soil bed and their modelling of the strip footing interacting with sand under cyclic loading conditions are rather limited. Here, local displacement fields of a dense sand layer underneath a rigid footing are studied under plane-strain condition for three different types of cyclic loading. The study involves using the digital particle image velocimetry (DPIV) and the finite element method (FEM) simulations. In the FEM, experimentally characterised constitutive behaviour of the sand grains was fed as an input. The FEM simulation results are validated by DPIV results at localised scale. From the DPIV experiments, a wider and shallower displacement fields due to the effect of the types of the cyclic loading are observed compared with those from the static load test. Furthermore, it is shown that the shear failure planes are commenced and dissipated wider below the footing under the cyclic loading compared with those from the quasi-static load. Moreover, the vorticity regions are highly localized at the shear bands generated under the ultimate load. It is also observed that the value of maximum shear strain rate around the footing corner increases for the increase in the frequency of the applied cyclic loads. Failure of the soil is a function of the amplitude and the frequency of the cyclic loads. The test results suggest that the amplitude of the cyclic loading had significant effect on both the vertical and horizontal permanent deformation behaviour of the soil in which the deformations increase with the increase of the amplitude.

8.1 Introduction

Soils are periodically subjected to cyclic loading in situ in situations such as under earthquakes, machine vibrations and in the construction of foundations, pavements and railways ballast. The intensity of the cyclic loading (q_{cyc}) is generally small, as compared to the static load (q_s); $q_{cyc}/q_s \leq 0.5$. The value of 0.1-0.3 is likely to be measured in many

earthquakes while the ratio of 0.5 represents an extreme event (Das and Shin, 1996; Tafreshi et al., 2011). Under cyclic loading, foundations could experience a significant level of settlement that causes structure damage (Sabbar et al., 2016). Thus, it is important in the footing design that geotechnical engineers consider not only the static ultimate bearing capacity (q_{ult}) and settlement of the footings (S_u), but also the cyclic ultimate bearing capacity and settlement of the footings interacting. The ultimate bearing capacity refers to the ability of the soil to sustain the maximum load on the footing before the soil collapses. Cyclic softening can occur due to cyclic undrained loading, e.g. earthquake loading (Peralta, 2010). The design of the foundations under the cyclic loadings (q_{cyc}) becomes an essential and a challenging task for the geotechnical engineers due to lack of information on how failure occurs at local and global scale in soil bed under cyclic loadings.

The term cyclic loading is defined as a system of repeated loads, which shows a constancy rate in the amplitude and the frequency (Peralta, 2010). Different types of the environmental cyclic loadings encountered in practice such as due to the waves, wind and earthquakes. Man-made cyclic loading can occur from the traffic, blasting operations and rotating machinery (Shajarati et al., 2012). Traffic might generate vibrations of a periodic character and the blasting effects can be detrimental on foundation of an elevated railway (Terzaghi et al., 1967). Peralta (2010) has classified the types of loading cyclic loading according to the frequency; as cyclic, cyclic-dynamic and dynamic, as shown in **Table 8.1**.). Many researchers have studied on the effects of the cyclic loading on the failure of footings interacting with soil using different theoretical and experimental methods. Salem et al. (2013) have defined the cyclic loading failure of the footings interacting with the soil as the number of loading cycles required to reach liquefaction (quick condition) or when an axial strain of 5% is reached. Soil liquefaction defines a phenomenon when a saturated or partially saturated soil significantly loses their strength and stiffness in response to the cyclic loading, causing the sand to behave like a liquid (quick condition). Andersen (2009) suggested that the failure caused by cyclic loading is defined at a permanent shear strain of 15%.

Table 8.1 Classification of repeating loading of soils (Peralta, 2010)

Repeated loading of soils	Cyclic	Cyclic-dynamic	Dynamic
Frequency	0 to 1 Hz	1 to 10 Hz	>10 Hz
Strain accumulation	Mostly plastic	Plastic and elastic	Mostly elastic

Numerous researchers have studied on the behaviour of sand soil under cyclic loads using different materials and techniques (e.g. Raymond and Komos, 1978; Das and Shin, 1996; Tafreshi et al., 2011; Nguyen et al., 2014; Sabbar et al., 2016). They reported that excessive soil deformations are produced under cyclic loading and the strains accumulate with increasing number of cycles, causing damage to building foundations. The cyclic loading could have a significant effect on sandy soil. The strength of the sand under the cyclic loading could be less than that under the monotonic loading with the same level of stress amplitude. Raymond and Komos (1978) determined the relationship between the settlement of the foundation and the number of load cycles of a laboratory scale surface footings on sand subjected to cyclic loadings of low frequency. They reported a significant level of initial settlement of the footing during the first ten cycles of loading and that an equilibrium response was reached after about 20000 load cycles in which plastic strain was incrementally accumulated. Raymond (2002) studied the effect of geosynthetic reinforcement on the cumulative plastic settlement of a repeatedly loaded plane strain footing on ballast. The ballast reinforcement reduced the plastic settlements and the effect of reinforcement was more significant in the loose packing condition. Tafreshi et al. (2011) have investigated the response of the circular footings supported on the sand bed under incremental cyclic loads by using the laboratory model tests and the numerical analysis. They have shown that the value of the coefficient of elastic uniform compression (CEUC which is the elastic rebound displacement of the sand in unloading cycle) of sand was increased by increasing the relative density of the sand whereas it decreased with an increase in the area of the footing. Asakereh et al. (2103) have studied the cyclic response of footing on geogrid-reinforced sand with a void that modelled a tunnel. They stated that, the rate of settlement of the footing was significantly large during the initial loading cycles; thereafter the rate of settlement decreases significantly as number of the loading cycle increases. Sabbar et al. (2016) have found that the deformation of clayey soil under cyclic loading was less rapid than for sandy soil. Furthermore, the cyclic behaviour of sandy soils is influenced by factors such as the

frequency, stress level, load types and the relative density of the sand. Amrane and Messast (2017) have predicted the cyclic accumulation of deformations in non-cohesive soils using a numerical approach based on J. Lemaitre model. Amrane and Messast (2017) have shown that a good level of correlation exists between the predicted and experimental response of the cumulative volumetric strain resulting from cyclic loading in sand under the drained state.

In a recent study, digital particle image velocimetry (DPIV) was used to understand the displacement fields of strip footing interacting with homogeneous sand layer of different packing densities under static loading (Jahanger et al., 2018a). The experimental results compared favorably with finite element method (FEM) simulations, which used experimentally measured grain-scale properties and the constitutive relations of the sand grains (Jahanger et al., 2018a). However, experimental observations of the local scale kinematic failure mechanisms in silica sands beneath shallow footing under the vertical cyclic loading are sparse in the literature. Therefore, the current study deals with the specific case of the plane-strain surface footing interacting with dense sand subjected to different types of cyclic loading. The effects of the cyclic loading are studied with the help of DPIV and FEM. The aim is to understand the failure mechanism and deformation field in the dense sand under vertical cyclic loadings considered here. Furthermore, this paper provides insights into the effects of the cyclic loading on dense sands and a comparison between the results of the DPIV based results and FEM.

8.2 Material and Experimental Methods

8.2.1 Materials

The soil used in this study is a relatively uniform silica sand of grain sizes between 0.07 and 0.9 mm, which is, a disturbed dry sample obtained in UK. Its experimentally measured properties and size distribution are presented in **Table 3.1** and **Table 8.2**.

Table 8.2 Physical properties of the dense sand

Type of the test	Unit	Results	Standards
Dry density, γ_d	kN/m^3	16.2	ASTM C29/C29M
Void ratio, e_o		0.62	
Relative density, D_r	%	76	ASTM C128
Peak angle of internal friction, ϕ_{peak}	degree	44.8	ASTM D4767
Residual angle of internal friction, ϕ_{cr}	degree	36.3	

8.2.2 Experimental Setup

For conducting the DPIV experiments, a planar model box was designed and constructed to satisfy both the mechanical and optical requirements. The former requirement is that the granular box was able to sustain the external loading while minimising the out of plane deformation of the walls (including the front measuring side of the box) under the ultimate load. Furthermore, the dimension of the test box was kept much greater than that of the footing to minimize the boundary effects, as illustrated in **Figure 8.1**. The latter requirement pertains to enabling the image recording of the grains at the front face of the box model. The front face of the box was made of 15 mm thick Perspex sheet (rigid). The backside of the box was made of 10 mm thick smooth aluminium sheet whereas the side of the box was made of aluminium frames having the dimension of 25 mm × 39 mm as illustrated in **Figure 8.1**. The aluminium planar model has an internal dimension of 460 mm×300 mm×39 mm. Hence, any boundary effects from walls of the box were practically negligible. The footing dimensions were of 38 mm × 38 mm× 15 mm. A rigid footing model was constructed using aluminium. The experiments presented here have been performed as shown in **Figure 8.1**, wherein the planar box filled with sand is placed stationary while the footing model was indented in the sand bed.

Hence, any boundary effects from the bottom rigid wall of the box was practically negligible and the scale effects. The roughness of the walls was characterised and evaluated in a mechanical engineering laboratory and the results were also presented in **Section 3.3.2, Chapter 3**. Further discussions regarding the boundary condition, size effect arising from the relative sizes of the footing and sand grains, and frictions between the base surface of the footing and the sand grains were detailed in in **Section 5.4,**

Chapter 5. It is worth mentioning that it also verified during all tests that under the ultimate loads (P_{ult}) of the dense sand packing did not lead to any significant out of plane movement of the walls occurred along the thickness direction. This was checked using a dial gauge (0.01 mm resolution) mounted to the side walls from a magnetic base (though the picture of this arrangement is not included here).

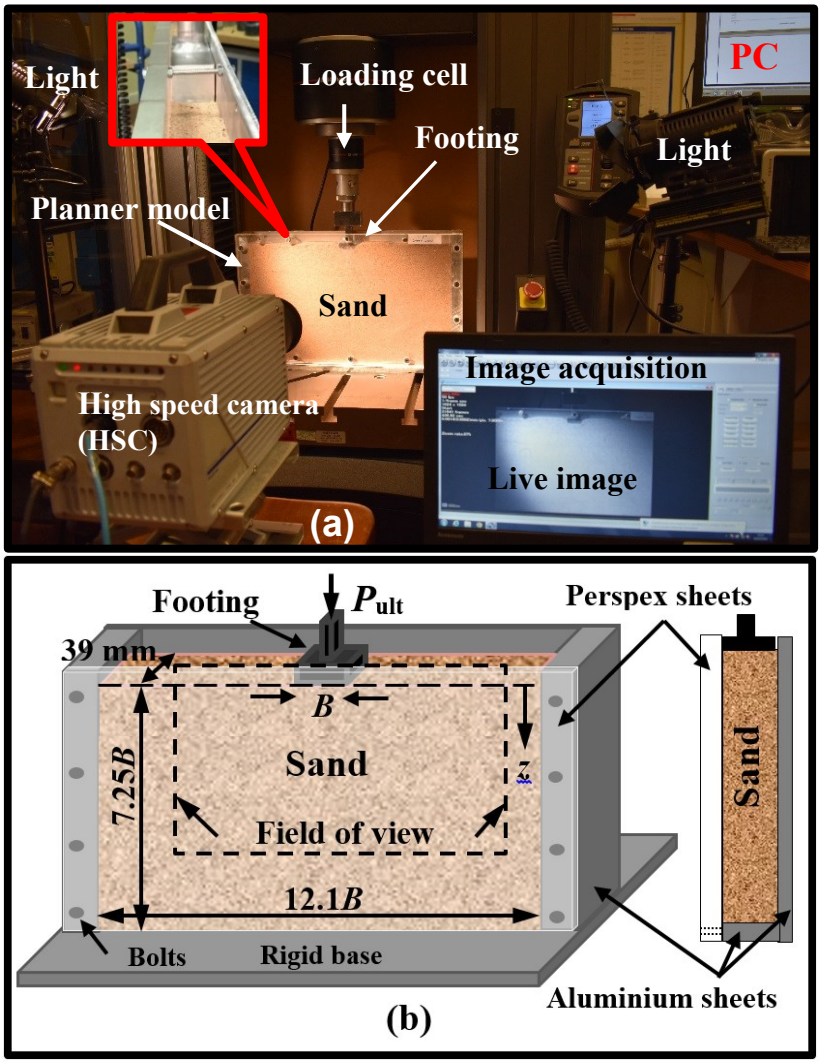

Figure 8.1 (a) Experimental setup using DPIV (b) Schematic

A small gap of 1 mm has set between the rear surface of the footing and the rear side of the aluminium wall to minimise any resisting frictional forces between these surfaces. This verified that no significant leakage of the grains occurred through this gap during the tests. The relative roughness of the side wall of the footing (δ_{bw}) in contact with

Perspex wall(δ_p); i.e., (δ_p/δ_{bw}) was 0.09, which was very small and negligible. **Figure 8.1** shows the complete setup of the footing test in the current study, which includes the Photron Fastcam SA5 high speed camera (HSC) in front of the designed planar model placed in the Instron 5kN loading machine (Instron, Norwood, Massachusetts, No. 5985L3398). The HSC with an allowable frame speed up to 100000 frames per second (fps) was used.

8.2.3 Preparation of the Dense Sand Packing

The homogeneous packing of the dense sand (γ= 16.2 kN/m^3, D_r= 76 ± 2%, e =0.62) was constructed in five layers. Each layer of the sample was constructed using five falling pouring technique method based on Kumar and Bhoi (2009) and Jahanger et al. (2018a), at a constant rate, such that the materials formed layers of ~55 mm thick each. The mass of sand grains laid in the box correspond to the required height and the packing density of the sand. Then the sand layer was compacted using 60 blows in 0.035 m lifts per layer with a 0.0016 m^2 (tamper base surface area) by a hand compaction tamper of 1.15 kg weight (Cerato and Lutenegger, 2007; Jahanger et al., 2018a; 2018b). The preparation of the sand test box was done directly on the loading machine baseplate to minimise any disturbing of the sand grains. The top surface of the sand layer was gently levelled off using a hand scraper. The footing was then placed symmetrically on the surface of the compacted dense sand layer, as illustrated in **Figure 8.1b**.

8.2.4 Cyclic Loading Types and Test Programme

Two types of tests were performed, and they are the static and the cyclic load tests. Details of the parameters of the model tests presented in **Table 8.3**. For studying the mechanical response of the footing-sand interactions, experiments were carried out to measure the static ultimate bearing capacity (q_{ult}) and the corresponding settlement of the footing (S_u). The quasi-static load was applied on the footing at a slow rate (0.05 mm/s) and up to 20 mm using the Instron machine with 0.1N resolution (**Figure 8.2**). The macroscopic load-settlement of the footing on the dense sand was measured at a frequency of 1 Hz. However, the quasi-static curve is drawn for the time as in the cyclic loading test, in reality the test continuous until the peak load was achieved as shown in the onset in

Figure 8.2. The cyclic load experiments were conducted using the Instron machine for the selected types of the cyclic load to measure the cyclic ultimate bearing capacity ($q_{ult\ cyc}$) and the corresponding settlement of the footing ($S_{u\ cyc}$). These are defined here to simulate different types of the machines cyclic loads, such as type 1 cyclic load selected which loading history consists of stepwise increasing load cycles as illustrated in **Figure 8.2**. Type 2 cyclic load was selected based on the cyclic plate loading test (PLT) in which the amplitudes increase with the increase of the cycles (Tafreshi et al., 2011). Type 3 of cyclic loading has staggered pattern that the amplitude of the same magnitude was used for two steps to simulate loads on the machine footing (Asakereh et al., 2013).

The tests were conducted by first applying the initial static settlement, $S = S_i = 2$ mm in with the corresponding initial static load (q_s) on the footing (Note that $q_s = q_{ult}/FS$ where FS is a factor of safety applied to the ultimate bearing capacity (Das, 2011)). Before applying the cyclic settlement (S_{cyc}), the initial static settlement (S_i) was applied (Tafreshi et al., 2011). Then after the cyclic loading was applied using a sinusoidal loading. The intensity of the load on the footing was then varied between the $S = S_i$ and $S = S_i + S_{cyc}$ ($q = q_s$ and $q = q_s + q_{cyc}$) with a frequency of 0.2-0.5 Hz (cycle/sec). Trapezoidal load cycles with a frequency of <1.0 Hz continue until excessive settlement and unstable behaviour (collapse of the soil) was observed. The cycles of the loading, unloading and reloading were continued until the ultimate load was reached. The resulting loading patterns are shown in **Figure 8.2**. Thus, the cyclic stress intensity varied between zero and the accumulative cyclic load (stress) q_{cyc}. Therefore, the footing was allowed to rebound to $S = 0$ (zero stress) or $S = S_i$ (static stress q_s) depending on the type of the applied cyclic load. The macroscopic load-settlement of the footing under the cycling load was measured for 10 load cycles.

Table 8.3 Details of the laboratory model for cyclic loading tests

Tests	q_s / q_{ult}	q_{cyc} / q_{ult}
Quasi-static	-	-
Type 1	0.59	0.155
Type 2	0.59	0.165
Type 3	0.65	0.09

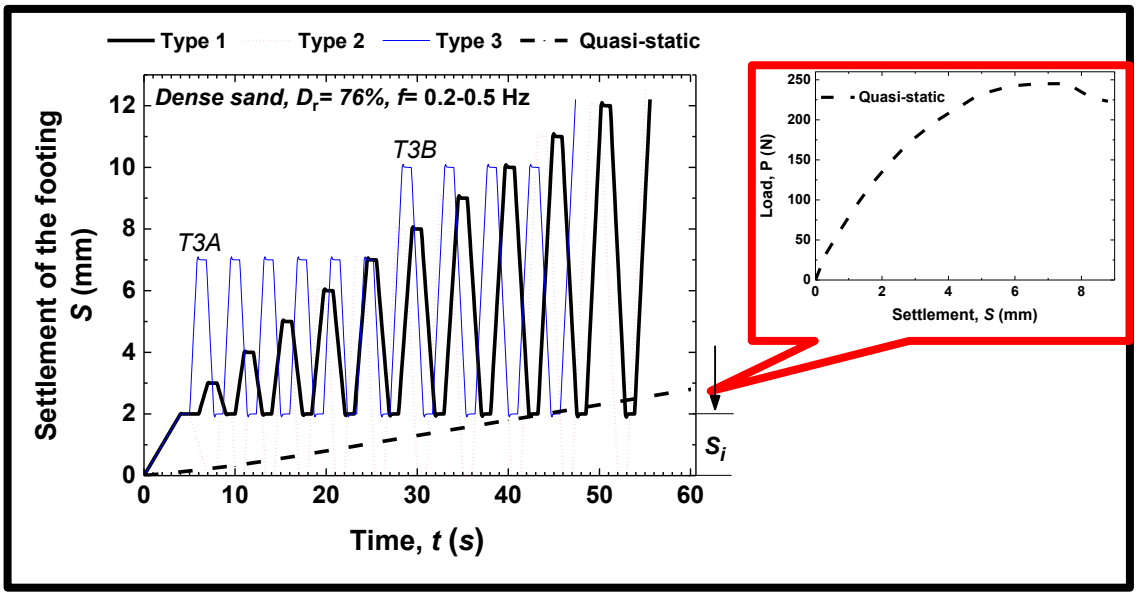

Figure 8.2 Pattern of cyclic loadings applied to the footing

8.2.5 DPIV Analysis and Experimental Work for DPIV

DPIV technique is applied to study the effect of the types of the cyclic loading on the deformation fields in dense sand layer under a strip footing. DPIV pertains to the digital platform of particle image velocimetry (Jahanger et al. 2018a; 2018b). Image capturing and experimental setup are identical to those reported in **Section 4.2, Chapter 4**.

An axial compression loading (q) was applied slowly on the footing under static loads using the loading machine (**Figure 8.1**). The macroscopic load-settlement of the footing on the dense sand were recorded from the tests. In the present study, the PIV camera lens was focused normal to the plane of the footing structures–soil interface region of ~ 273 mm × 154 mm. Two light sources were also used to illuminate the rig (on the front side of the test box, as illustrated in **Figure 8.1**) which was further sub-divided into 129600 interrogation areas (IA) of minimum 4×4 pixels each covering a zone of about 0.57 mm × 0.57 mm which contains about 3 grains in each IA. The HSC was used. The resolution of the images was 1920 × 1080 pixels. This corresponds to a scale of ~ 0.14 mm per pixel in this study. Hence, the DPIV experimental measurements made here are at the local-scale. However, as the loading condition is cyclic in this study and the storage capacity of the acquisition system (60 seconds of recording capacity), the recording at 250 fps was found to be adequate until soil failure was reached. This acquisition of 250 fps of the

recoded images were captured having spatial resolution of 0.028 mm (7 mms^{-1}/ 250 fps) - 0.0001 mm (1 mms^{-1}/ 250 fps).

DSSP was used to analyse the digital images acquired during test using DPIV (DantecDynamics, 2013). The distribution of velocity vectors of the grains examined for which an adaptive IA of maximum size 16 × 16 pixels resolution resolution (~36 particles). The mean number of particles per maximum IA should vary between 10 and 25 (DantecDynamics, 2013). The convergence limit equals 0.01 pixel was employed in the image analysis. A typical mean size of sand grain (D_{50} = 0.37 mm) was represented by about 3×3 pixel (patch) to reduce DPIV error (Gollin et al., 2017). Each of these patches was tracked using an adaptive PIV method, to identify the deformation field of sand grains between successive images obtained from the front side of the Perspex sheet of the test rig, to a measurement precision of 0.014 mm for the field of view used during these experiments. The adaptive PIV iteratively adjust the size of the individual IA in order to adapt to local seeding densities and flow gradients (to avoid gradient biasing) (DantecDynamics, 2013; Jahanger et al. 2016; Gollin et al. 2017; Jahanger and Antony 2017a, 2017b; Jahanger et al. 2018a; 2018b). The displacement measures i.e. horizontal displacement (S_h), vertical displacement (S_v), and resultant displacement (S_R) were calculated under a given load in total (i.e., between the reference image at zero load (q = 0) and the image at the required fractions of the ultimate static load) such as $0.34q_{ult}$ and q_{ult} and at maximum loading per each cycle of the cyclic loading test. It was also verified that the variation in the image scale in both vertical and horizontal direction were not significantly different.

8.3 Finite Element Method (FEM) Simulations

FEM were performed to investigate the behaviour of the relatively rough strip footing on dense sand under static and three different types of cyclic loads. The FEM simulations were used to evaluate the ultimate load, the failure fields and the CEUC. Non-linear elastic finite element simulations have been made for the cases of a single footing indenting on dense sand packing using ANSYS workbench 17.2 version (ANSYS, 2016).

In the present FEM study, ANSYS is used to create a two-dimensional solid geometry of the footing and the soil. The soil and the footing were modelled as under plane strain

condition. The discretization of the footing and the soil layer were done using an eight-nodded quadratic solid element having two degrees of freedom at each node, i.e., translations in the nodal x and y directions, as illustrated in **Figure 8.3**. The nodes and element numbers in the soil body are equal to 11500 and 3730 respectively. The strip footing was discretised using nodes and element 275 and 76 respectively. A refined mesh was generated at the footing-soil interface where the largest strains and stresses would be expected. It should be mentioned that Skewness mesh metric (a measure of mesh quality) of ~ 6×10^{-6} maximum value was obtained which is very well acceptable (Lee 2015). The size of the single-elemental geometry is also shown in **Figure 8.3**. The simulations were held under identical boundary conditions described in **Section 4.3, Chapter 4**.

The material model used here to describe the nonlinear behaviour is based on the experimentally characterised bulk stress-strain relationship corresponding to the hardening part of the load-displacement curves of the dense sand packing (**Figure 8.4**). These were discretised into a large number of linear segments and fed as user defined digital input (ANSYS, 2016; Lee, 2015; Jahanger et al., 2018a) in small increments as presented in **Table 8.3** and **Figure 8.3**. Furthermore, the experimentally measured material physical properties for dense sand were used as input to the simulations including bulk density (γ = 16.2 kN/m^2), initial modulus of elasticity (E = 50 MPa), Poisson's ratio (v= 0.35) as suggested by Das (2009) and the relative packing density of the sand of D_r= 76%. In the present analysis, ANSYS used the multilinear isotropic hardening of the stress-strain curve (Lee, 2015; Jahanger et al., 2018a). Geometrical non-linearity was also allowed in the simulation (ANSYS, 2016) by enabling the large deformation option. The axial loading was applied for the three types of the loads considered here on the rigid footing geometry elements of a length of 0.5B (**Figure 8.3**) of time step in the range of 0.001-0.1 seconds (~800 cumulative iteration) to achieve the convergence requirements of the simulation (ANSYS, 2016). The total duration of the loading cycle pertains to about 55 seconds. It is worth mentioning that such an approach applied to analyse the interaction behaviour of strip footing-sand interactions under the quasi-static loading. The results of the FEM were in a very good agreement with the DPIV experiments as reported in a previous work (Jahanger et al., 2018a). The evolution of displacement characteristics in the solid geometry (depicting the sand packing) was tracked under different loading levels and compared with corresponding DPIV measures later. The finite element model was

first calibrated by laboratory model footing under static tests based on DPIV test and then used to verify and to analyse the footing supported on sand.

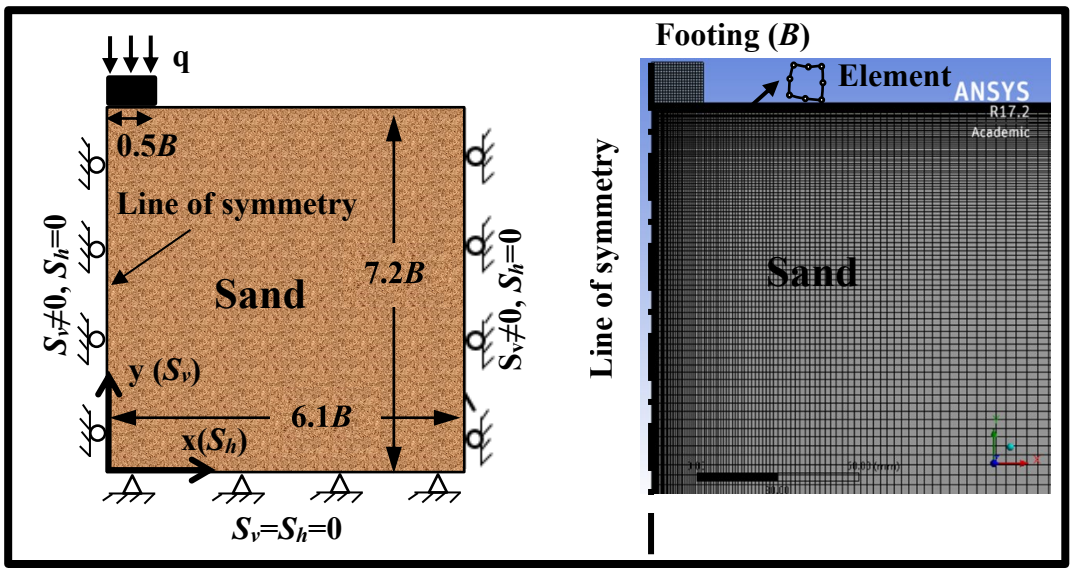

Figure 8.3 Chosen domain and boundary conditions (right) finite element mesh, and element enlarge

8.4 Results and Discussion

8.4.1 Quasi-static Tests

For the purpose of comparison presented later with cyclic loading test results, at first here the results of the footing-sand interactions under the quasi-static loading case were presented as illustrated in **Figure 8.4**. The results include the ultimate bearing capacity of the soil (q_{ult}) and the corresponding settlement of the model footing (S_u) (Jahanger et al., 2018a).

Using **Figure 8.4** the ultimate bearing capacity of the soil under the quasi-static loading (q_{ult}) was obtained. The ratio of the ultimate vertical settlement of the footing (S_u) to the width of the footing (B), i.e., S_u/B was obtained as 14.7%. It had also verified that this agreed very well the corresponding FEM results of 14.0% conducted here. By repeating the experiments, It had also verified that the variability in the experimental results between the tests were less than 10% and practically acceptable (Tafreshi et al., 2011; Jahanger et al., 2018a). Two standard cone penetrometer tests (CPTs) were performed to

characterize the shear strength of the dense sand (Teng et al., 2017; Jahanger et al., 2018a). It is worth mentioning that as expected, the penetration resistance of dense sand increased with depth at an increasing rate (kPa/mm). More details can be found in **Section 3.3.4, Chapter 3** and **Section 5.4, Chapter 5**.

8.4.2 Cyclic Load Tests

The experimental tests specimens were conducted under the three types of the cyclic loading sequences, i.e. types 1-3 cyclic loading. In addition, it depicts that the ultimate cyclic bearing capacity ($q_{\text{ult cyc}}$) occurs at higher settlement value compared to the quasi-static experiment due to the effect of the cyclic load. This agrees with the previous quasi-static and cyclic loading of sand (Tafreshi et al., 2011; Tafreshi and Dawson, 2012). In general, a well-defined peak is obtained for the cases of the cyclic loading tests and the failure corresponds to general shear failure (Terzaghi, 1943). Mostly, a peak value of the cyclic load response was obtained within the first 7 cycles of loading. The ratio of ultimate vertical cyclic settlement ($S_{\text{u cyc}}$) under the ultimate cyclic load to B, $S_{\text{u cyc}}/B$ is ~13-18% in all cases of the cyclic loading considered in the study. These measures are consistent with the results reported earlier for example, Andersen (2009). It can be attributed to the increase in the soil stiffness due to the increase in the loading cycles on sand that accommodates a large strain in soil beneath the footing, as illustrated in **Figure 8.4**. The test results here also suggest that the amplitude of the cyclic loading has a significant effect on both the vertical and horizontal permanent deformation behavior of the sand in which the deformations increase with the increase of the amplitude (Asakereh et al., 2103). However, contrary to the independent of the sand on the loading rate applied on the footing has mentioned previously (Liu and Evett, 2004). This reported conclusion could be applied only for the quasi-static loading type on the sand. It is worth mentioning that the ultimate load of the soil is a function of the amplitude and the frequency of the cyclic loads (Das, 2016).

The CEUC (in mm) was estimated in the range of 0.2 mm- 0.25 mm for all loading and unloading stages for under all types of cyclic loading in the current study. These results imply that the CEUC is dependent on the type of loading (Tafreshi et al., 2011). Particle crushing was not visually observed during loading of the footing for any of the cyclic types.

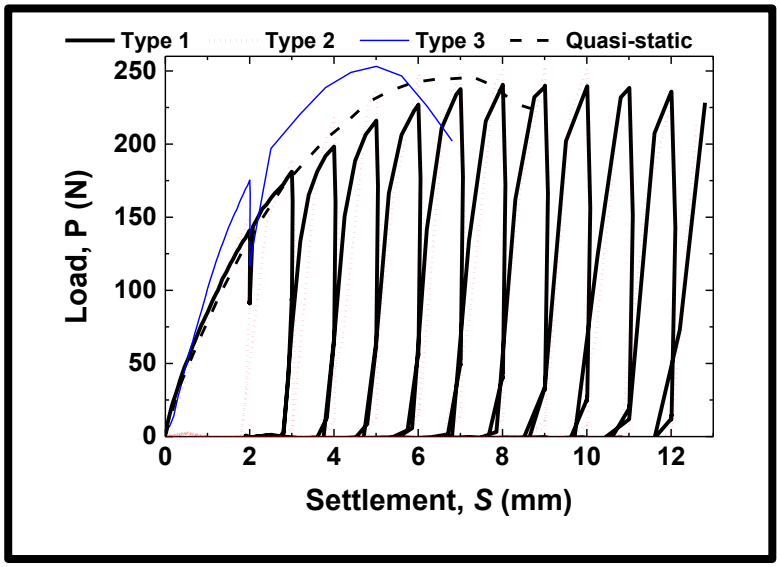

Figure 8.4 Cyclic load-settlement for different loading type

8.5 Local Displacements Obtained from the DPIV Analysis

The following analysis presents some useful results on the displacement fields and the failure mechanism of the strip footing- dense sand interactions subjected to the quasi-static and the cyclic loads considered in this study. Understanding this response is important to developing reliable design guidance in geotechnical engineering. Visualization of the failure mechanisms using DPIV under cyclic loading is entirely original and contributes to this understanding. Later, the local displacement measures are compared to FEM analysis.

8.5.1 Mean Resultant Displacement Vector Fields

Figure 8.5 compares the experimentally DPIV based measured of the mean resultant displacement vector under the ultimate load. In this, scalars contours of the vertical and horizontal displacements are superimposed for comparison purposes. In DSSP, the scalar contour is used for on-screen display of a number of data-types of available variables in the vector map. The numerical method is used to extract a scalar quantity from a dataset with multiple values (DantecDynamics, 2013). This visualization illustrates whether

horizontal or vertical soil displacements dominate the failure mechanism mobilised in the sand bed under the cyclic loads. The displacement fields are clearly very different for the cyclic loading compared with from the quasi-static loading. Under the ultimate load, approximately a triangular wedge of dead zone (with a constant amount of resultant displacement of the grains but has the highest vertical displacement (**Figure 8.5**) is formed beneath the base of the footing in all cases of loadings. It is worth mentioning that the dead zone does not mean that the grains are not moving at all but move as a block of grains with almost the same magnitude of displacement (Jahanger et al., 2018a). In granular mechanics, the dead-zone is characterised by the block of materials beneath the indenting objects with the granular materials and moving as if they are continuous extension of the indenter, i.e., no slip at the indenter-granular interface. The depth of this wedge at the ultimate bearing load is equal to about 0.6B, 0.8B, 0.7B and 0.95B for quasi-static, type1-3 respectively. The relatively higher value of the resultant displacement occurs in the case of footing subjected to the type 3 loading. This also correlates to the relatively higher value of the ultimate load for this case as presented in **Figure 8.4**. In these plots, the scalar contours of the corresponding displacements are superimposed.

As seen in **Figure 8.5**, there is considerably more horizontal displacement in the sand due to the cyclic loads than in the quasi-static load where the vertical soil displacement tends to dominate. Type 3 loading contributes to increase the ultimate bearing capacity through significantly changing the geometry of the failure mechanism (**Figure 8.5**). This is consistent that a 'general shear' type failure mechanism is more dominant in the dense sands bed under the loading conditions considered here. In general, the failure patterns are a conventional rigid plastic Terzaghi's failure wedges (**Figure 8.5**) in the analysis of foundation (Terzaghi, 1943). The boundaries of the zone of plastic flow at failure load profiled using the advanced DPIV here are remarkably similar to such intuitive diagrams suggested by Terzaghi's in 1940s (Terzaghi, 1943). In general, the vertical displacement component significantly diminished in magnitude at a depth of z/B>2.5.

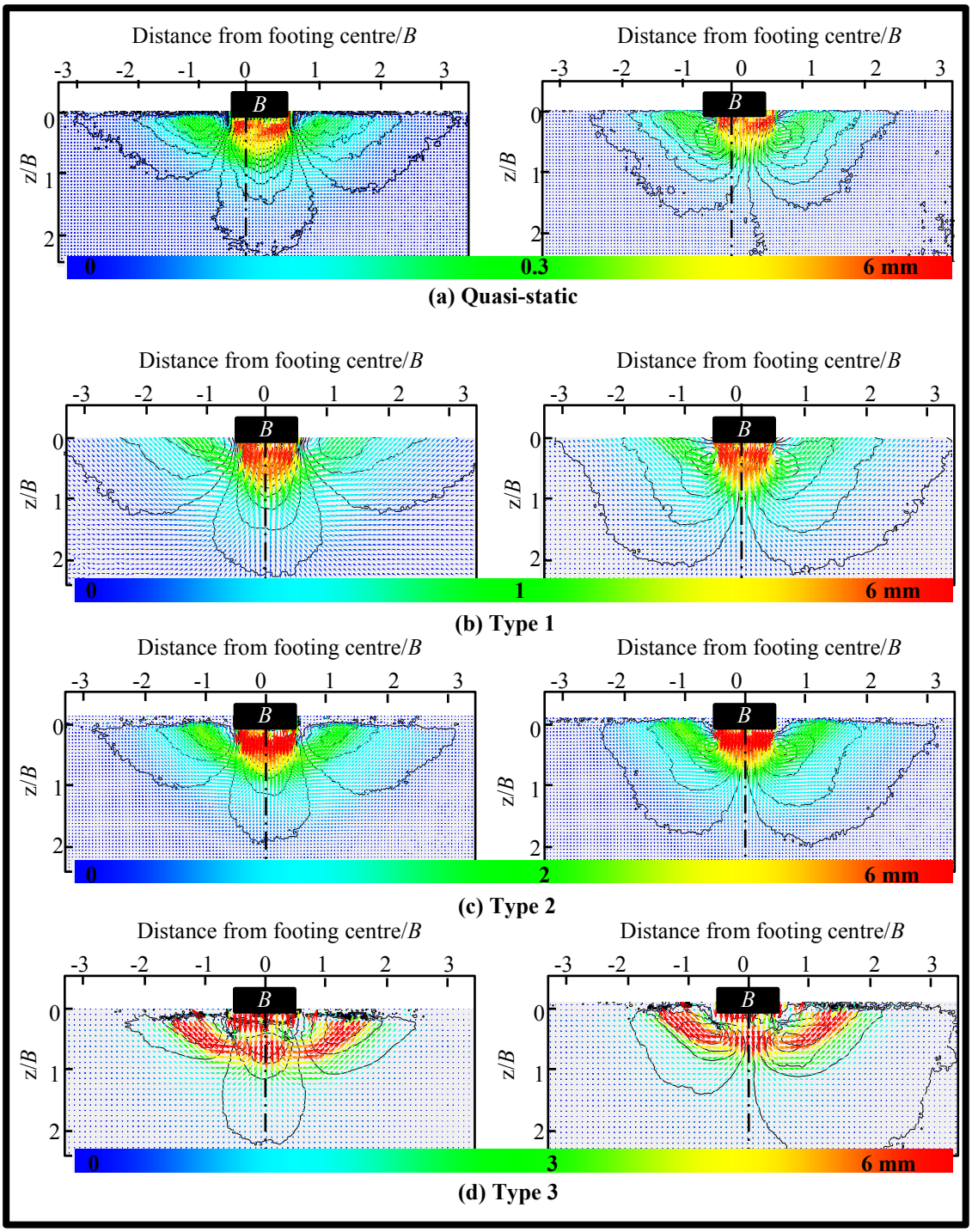

Figure 8.5 Map of the mean resultant displacement vector under the ultimate load for the quasi-static and cyclic tests (left) vertical displacement (right) horizontal displacement

8.5.2 Vorticity Fields

In order to further characterise the displacement patterns under the cyclic loading under the ultimate load, the mobilised vorticity zones or highly rotational flow during

compression of the footing in the dense sand are investigated by plotting the vorticity (ω_z) profiles for all loading cases, as illustrated in **Figure 8.6**. It is worth mentioning that for a planar data, only rotation around the z-axis can be determined (DantecDynamics, 2013) as follows:

$$\omega_z = \frac{\partial S_v}{\partial x} - \frac{\partial S_h}{\partial y} \tag{8.1}$$

where

$\frac{\partial S_v}{\partial x}$ = Gradient of vertical velocity in the x- direction, and

$\frac{\partial S_h}{\partial y}$ = Gradient of horizontal velocity in the y- direction.

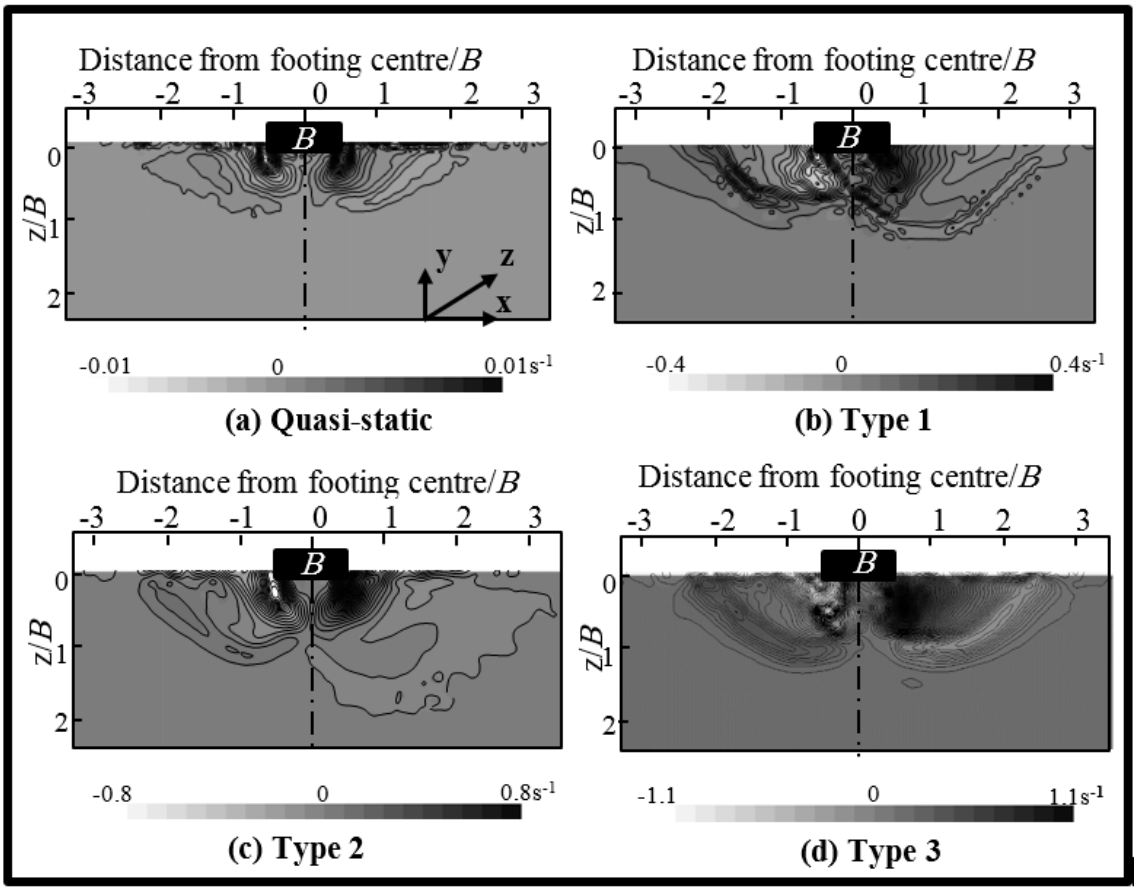

Figure 8.6 Average vorticity under the ultimate load for the quasi-static and cyclic tests

It can be clearly seen that the localized vorticity regions are developed more strongly around the corners of the footing under the ultimate load. This localization of vorticity is a result of concentration of the displacement at the corners of the footing influenced by

the rotational movement developed at the corners (Murthy et al., 2012; Jahanger et al. 2018a). Previous studies suggested that the higher localised vorticity regions could correlate to the shear bands (Hamm et al., 2011). According to Jahanger et al. (2018a), in reality, the local structural non-homogeneities could exist under the ultimate load and this subsequently triggers the non-symmetrical flow of grain (post-failure) under the loading conditions. Therefore, it is interesting to note that, the shear band profile is not exactly symmetric in the dense sand bed even under the symmetric cyclic loading conditions.

8.5.3 Distribution of the Maximum Shear Strain Rate under the Ultimate Load

The rate of maximum shear strain fields, derived from the displacement fields, are plotted in **Figure 8.7** to explore further the mechanisms of failure of dense sand under the ultimate load for the quasi-static and cyclic tests loading. The maximum shear strain rate ($\dot{\gamma}_{max}$) is derived from the velocity fields as follows:

$$\dot{\gamma}_{max} = \frac{1}{2}(\mathrm{J} + \mathrm{J}^{\mathrm{T}}) \tag{8.2}$$

Where $\mathrm{J} = S_{R_{\mathrm{x}'\mathrm{y}'}}$ is the velocity gradient tensor and $\mathrm{J}^{T} = S_{R_{\mathrm{y}'\mathrm{x}'}}$ where T is the time (s) and $(\mathrm{x}', \mathrm{y}')$ are orthogonal axes rotated at θ relative to (x, y) (Hamm et al., 2011; DantecDynamics, 2013). The negative value of the maximum shear strain rate can be used to identify vortex cores, while the positive value indicates the areas of the movement, where shear is present. In the all types of loading, a highly concentrated zone of shearing is seen at the corner of the footing. For the cyclic loading types, the shear strain rate fields are more and of generally higher magnitude than in the case of the quasi-static loading. The failure pattern in terms of the magnitude of shear strain rate can be identified as wider as and deeper for cyclic loading than in the case of the quasi-static loading (**Figure 8.5**).

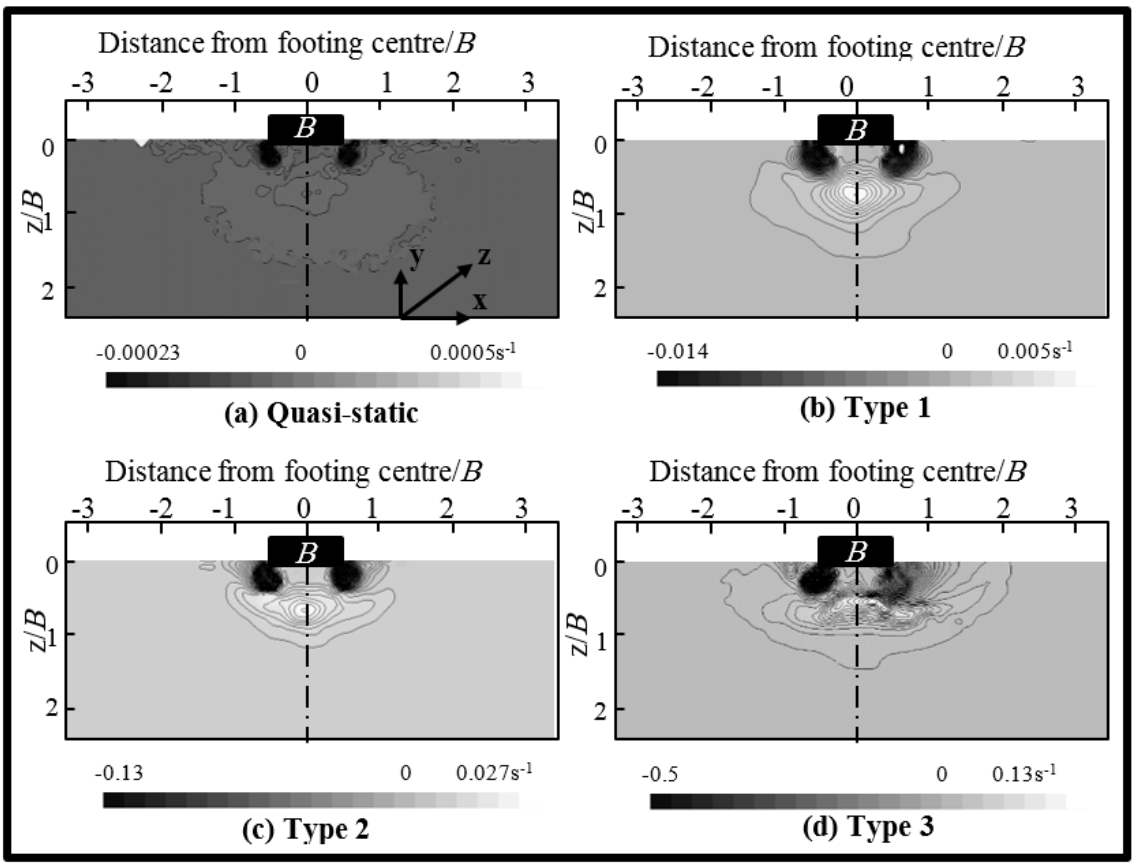

Figure 8.7 Maximum shear strain rate fields under the ultimate load for the quasi-static and cyclic tests

8.5.4 Plots of the Variation of the Displacements in the Sand Bed

The differences in displacement response between the cyclic loading and static tests at ultimate pressure level are further investigated by plotting the vertical displacement profiles along the line of symmetry of the footing centre line as illustrated in **Figure 8.8a**. Similarly, the horizontal displacement profiles at a horizontal cross section 0.5B below the footing using DPIV under the ultimate loading level are plotted in **Figure 8.8b**. The vertical displacement profiles show a nonlinear response for all cases of loading. They gradually decrease to a negligible value beyond~ z/B = 2.0-2.5 for all cases of the loading. Similar results have been reported for sand by Jahanger et al. (2018a) for the case of dense sand. The normalised vertical displacement (S_v/B) attains the peak at a depth of about 0.1B for the footing under quasi-static loading and about 0.15B for the cyclic loading. The profiles of S_h component presents S-like shape with a neutral point (zero value) occurring along the axis of symmetry of the footing. The sand along the vertical axis of symmetry is confined by the maximum vertical displacement and therefore $S_h \sim$ zero. The

S_v and S_h components in all types of the cyclic loading exhibit larger values than the case of the quasi-static loading was observed in the current study. This highlights the change in mechanism failure between the cyclic loading types and the quasi-static loading. The S_v and S_h components variations are relatively higher in the case of type3 loading.

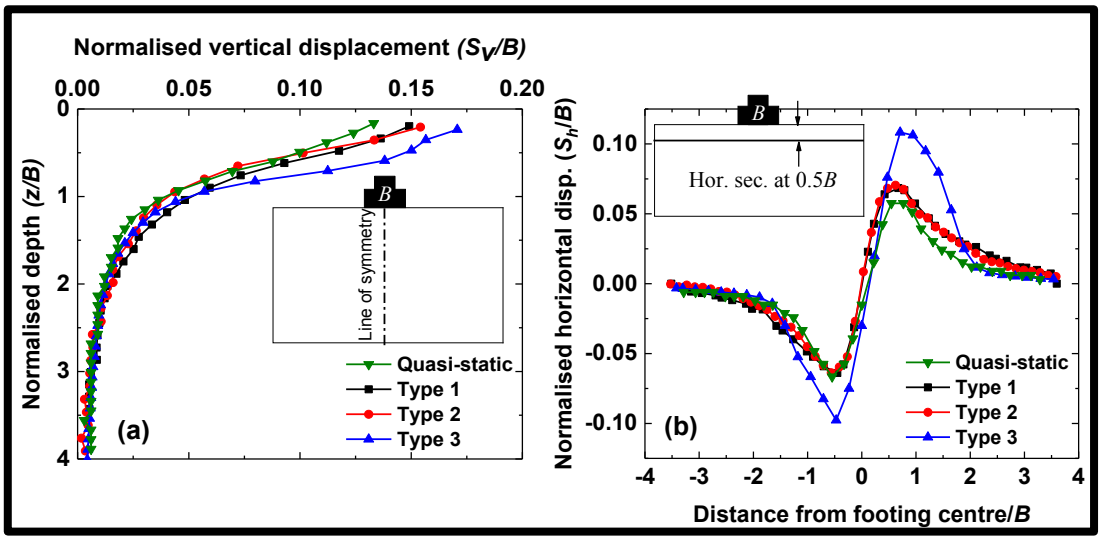

Figure 8.8 (a) Normalised vertical displacement component profiles with depth z from the bottom surface of the footing (b) normalised horizontal displacement component at a horizontal cross section 0.5B below footing

8.6 Comparison of the Displacement Fields Obtained from FEM and DPIV

Different displacement fields were presented below for the footing interacting with the dense sand packing under the ultimate load for all cases of loading considered here (**Figure 8.9**) This shows the variation of PIV-based resultant profiles on LHS compared with the FEM (ANSYS) analysis on RHS of the plots. The results are presented for a width of 2.5B from the edge of the footing (one-half portion is shown for the comparison purposes). It is evident that in general, an excellent level of agreement between the PIV and FEM approaches are obtained both qualitatively and quantitatively. Furthermore, quantitative comparisons between FEM and DPIV-based results of the variation S_v/B and S_h/B along a horizontal section at a depth of 0.5B below the level of footing under the

ultimate load were provided for different packing conditions of sand using (Jahanger et al. 2018a).

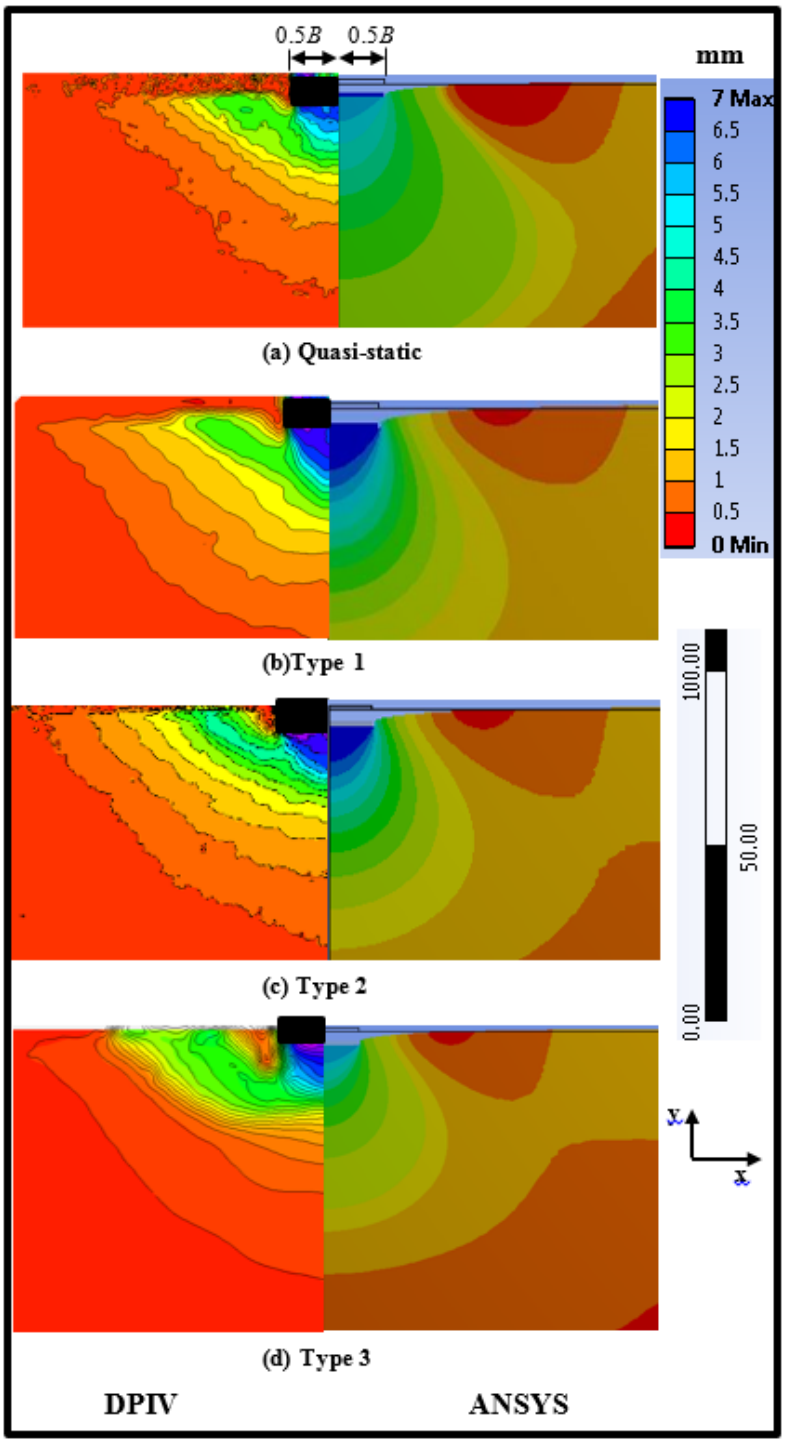

Figure 8.9 Resultant displacement contour field-DPIV (left) and mirrored corresponding contour field-FEM (right)

8.7 Analysis of Stress and Strain Distributions in the Sand Bed using FEM

Having validated the local displacement field of the sand bed using FEM with the DPIV experiment in the previous section, here the analysis is further exploited by presents the shear distribution characterised in the sand bed from the FEM analysis. **Figure 8.10** shows the variation of the normal stress contours on the LHS and the maximum elastic shear strain contours on the RHS under the ultimate bearing capacity load of dense sand under cyclic loading obtained from the FEM simulations.

It can be seen from the normal stress and the maximum elastic shear strain map that there is a maximum shear strain concentration around the corners of the footing. This trend is in agreement with the DPIV experiment results presented in the previous section. It can also be noticed that these shear values increase for an increase in the frequency of type 3 cyclic loading results. The higher values of the maximum elastic shear strain (regions with black colour) are as shown in **Figure 8.10**. Type 3 loading results the highest level of the distribution of the vertical stress and the corresponding shear strain. The results of the ultimate load of the footing obtained from FEM simulations and those the current DPIV experiments with are presented in **Table 8.4** for the comparison purposes.

Table 8.4 Comparison of the ultimate load obtained from the FEM and DPIV experiments

Tests	Ultimate load P_{ult} (N)		
	Current DIPV experiments	FEM	Error %*
Quasi-Static	244	229	-6.15
Type 1	237	214	-9.7
Type 2	249	273	+9.6
Type 3	253	294	+16.2
$*\ \text{Error}\ (\%) = ((\text{FEM} - \text{Exp.})/\text{Exp.}) \times 100$; (+) overestimated, (-) underestimated			

As seen, the results obtained here from the current FEM analysis are practically in an excellent agreement with those obtained from ANSYS analysis for different cases of loading considered in this study. The error becomes larger with increase in the amplitude of the loading. There seems to be a pattern here: error goes from -6% all the way up to

16% due to the effects of different types of cyclic loading; the contacts behave differently, and the error becomes larger with higher amplitude.

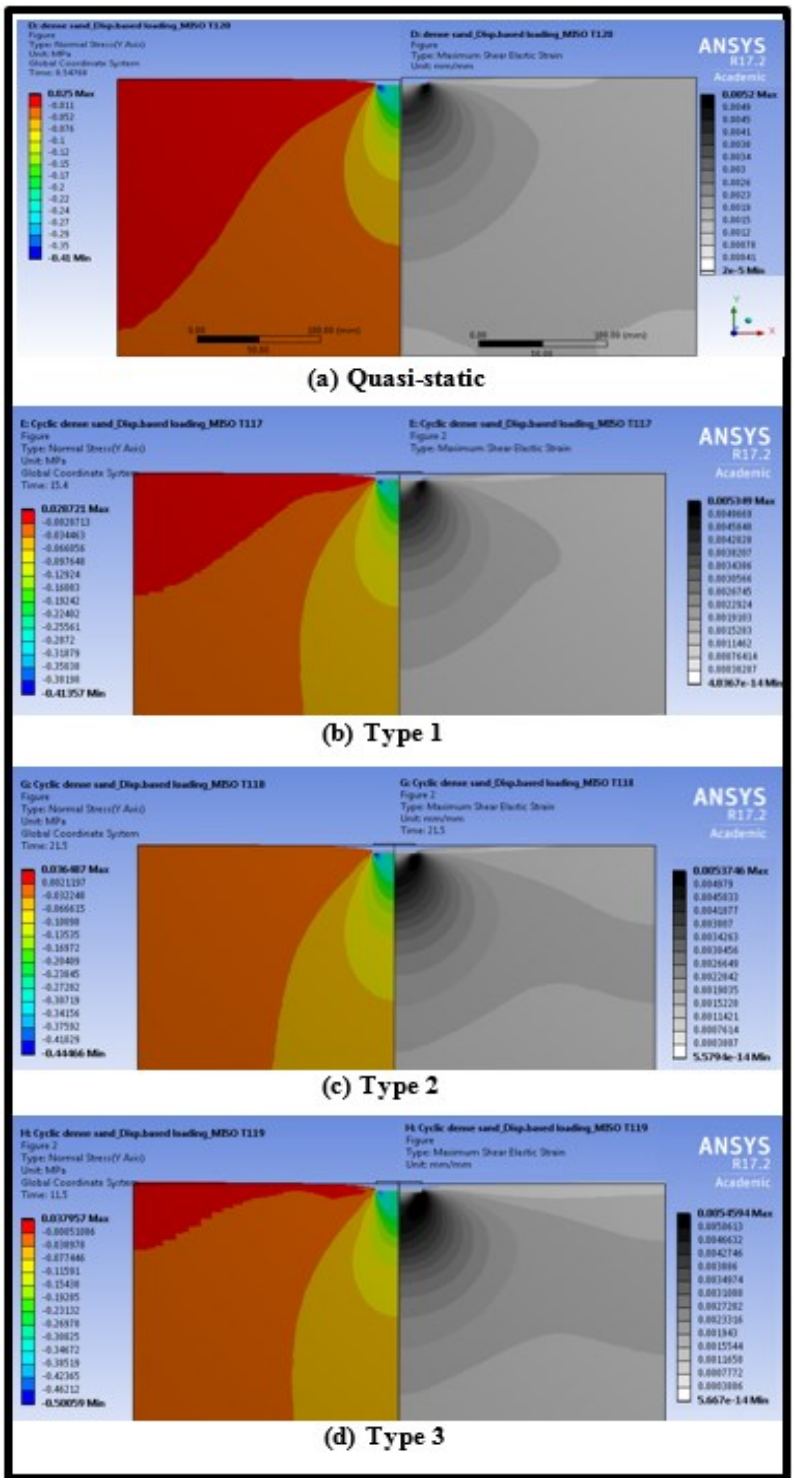

Figure 8.10 Variation of normal stress contours (left) and maximum shear elastic strain contours (right)

8.8 Summary

In this study, DPIV is used to understand the local and global geomechanical characteristics of an axially loaded rigid strip footing under different types of cyclic loading and quasi-static load using both DPIV and FEM simulations in a coherent manner. The displacement patterns in the sand are visualized using DPIV and studied qualitatively and quantitatively in terms of vertical and horizontal components of displacement, vorticity and maximum shear strain. Where possible, the displacement measures in the sand are compared with FEM analysis. In general, an excellent level of agreement is obtained between the FEM and DPIV results. The boundaries of the zone of plastic flow in the dense sand under the cyclic loads at failure load measured here are remarkably similar to the shape of such intuitive diagrams suggested by Terzaghi (1943), but much wider.

PIV clearly shows detailed descriptions of the stages of velocity discontinuities, vorticity and maxim shear strain rate for the dense sand media. There is significantly more horizontal displacement in the cyclic loading type 3 than in the quasi-static loading where vertical soil displacements tend to dominate. This is due to the increasing area of the active zones that pushed outward and upward to the ground surface as confirmed by DPIV here. The DPIV analyses show a classical general shear failure mechanism in the dense sand a deeper and wider distribution of the dead zone region under in the cyclic loading types. Cyclic loading types have considerable effect on the maximum ultimate load, settlement components and the failure mechanisms occurring beneath the footing under type 3 loading.

Local scale load-displacement of the results FEM is clearly validated using DPIV. In addition, the implementing of these users defined constitutive relation of load-displacement of the sand works very well in the FEM analysis. The simplicity in implementation of experimentally characterised constitutive relation of the sand grains are fed as an input, which can be applied easily for large-scale problems with small and large strain problems. As the DEM simulation of large-scale granules systems, such as those needed in foundation structures-sand interaction (hundreds of millions of particles) is computationally challenging and expensive.

Chapter 9 Conclusions and Recommendations for Future Work

9.1 Summary and Conclusions

An extensive experimental and numerical (FEM) simulation studies on different problems of foundation structures-granular soil interactions were performed. The study focused on the link between the micro (local)-macro (bulk) scale interactions using laboratory small-scale experiments and FEM simulations. Four different strip footing problem in geomechanics have been dealt with under the plane strain condition to systematically understanding the effects:

- The relative density of the sand grains (loose, medium-dense and dense) on both the internal and bulk mechanical properties for the strip footing interacting with sand bed.
- The interference of the nearby strip footings on the ultimate bearing capacity and the displacement field sand of three packing densities.
- The top dense sand layer on bottom loose sand layer on the measurement of ultimate bearing capacity, displacement field and the failure slip surface underneath the strip footing.
- Effects of types of cyclic loadings on the displacement field of the dense sand underneath the strip footing.

The present study provides both the spatial and temporal distribution of displacements in sands of different packing densities under key stages of loading elegantly. DPIV is shown to be effective and promising in understanding the local and global geomechanical characteristics of footing interacting with sand media of different relative densities in a coherent manner. The global measurements (stress-strain curve) from the compression test were fed to the FEM. Then, localised subsoil deformation measurements from FEM compared to DPIV outputs. Grain-scale (local scale) displacements of sand grains measured using DPIV are not fed as an input to FEM simulations. Rather, they are used to compare with corresponding outputs from the FEM simulations, and a good level of agreement is obtained between them. The objective of this thesis is to develop a new approach to use the experimentally characterised stress-strain curve from the DPIV-based

experiments as input to the FEM simulations and to validate the FEM based displacement fields using the DPIV methodology.

In sand-structure interaction problems, FEM based outputs of the displacement profiles in the sand bed to a level of accuracy of what happens in real experiments (e.g. using DPIV methodology here) is possible to obtain, if the input parameters of constitutive relations are also characterised realistically and fed as input in the FEM simulations. It is worth stating that, FEM simulations, when they work reliably are much more suited to simulate real-scale soil-structure interaction problems in future.

Based upon the work presented in the thesis, following conclusion are drawn:

- The depth of this elastic wedge at the ultimate bearing load is equal to about B, whose vertices (slip planes) intersect the horizontal at an angle (α = Angle of dead zone wedge/active zone 1, base angle under the footing) of about 62◦ ±2°. These are consistent with Prandtl's assumption for smooth footing ($\alpha = 45 + \phi/2$), which have not been confirmed using microscopic experiments, but using DPIV here. The boundaries of the zone of plastic flow in sand at failure load profiled using the advanced DPIV here are remarkably similar to such intuitive diagrams suggested by the forefathers of soil mechanics, for example Fröhlich in the 1930's. However, at or beyond the ultimate load, the DPIV experiments have shown non-symmetric flow of grains even under the symmetric loading conditions on the footing. However, here it is found that the absolute value of the vertical displacement (S_v) in the sand for a given depth increases for increase in the width of the footing as also referred in other studies. The depth at which the settlement vanishes in the sand decreases for increase in the relative density of sand. But, the grains resting beyond the influence zone of deformation (or velocity) do not move in the post-failure stage, which is beyond about 1.25B, 1.2B, and 1.1B for loose, medium-dense and dense sand respectively for both cases of footing width. The S_v component at horizontal section presents an inverted triangle-like profile that becomes deeper and narrower with increasing load level. The maximum value of S_v occurs along the footing centre, and then decreases gradually towards the footing edge. The profile of S_h component presents S-like shape with a neutral point (zero value) occurring along the axis of symmetry of the footing.

- The ratios of ultimate vertical settlement of footing (S_u) to footing breadth (B), S_u/B for single footing (B=38mm) and for adjacent footings of S/B=0, (B=76 mm) is 8%

and 16% respectively. These ratios increase with an increase in sand packings that the value S_u/B in dense sand is larger than in medium-dense and loose sand but decrease with the increase of the width of the footing. Results of this research presented that at a close spacing between the two footings, non-symmetrical triangular wedge was shown below the base of each footing and an invert arch can form beneath the footings. This could be the reason behind the increase in the bearing capacity with spacing up to a certain distance S_{opt}; however, such an incident does not take place for dense sand case. For different sand densities, at S/B=0, the deformation patterns are similar to an isolated footing under the ultimate load. The pairs of the footing acts as a single footing with the width=2B, and the total load on the one of the pairs is $1.0 < \xi\gamma < 1.6$ the load taken by single footing. The value of S_{opt}/B corresponding to which the value of ξ_γ becomes maximum $\xi_{\gamma\,max}$ is called as S_{opt}/B. As the spacing increases up to S_{opt}/B, they act as a single footing in which the breadth of the pairs of the footings (breadth=2B +S_{opt}) and $\xi_{\gamma\,max}$~1.4 and 1.75 for the loose and medium-dense respectively. It means that $\xi_{\gamma\,max}$ due to blocking (superposition of the displacement field) occurs in the loose and medium-dense sand between the footings of breadth =2B +S_{opt} (**Figure 6.6**, S/B=0.25, **Figure 6.7**, S/B=0.5). However, the blocking occurs at S_{opt}/B =0 for footing pairs on the dense sand when the footings touch each other, as illustrated in **Figure 6.8**. The results here showed that there could be some level of horizontal displacements S_h along the plane of symmetry (~20% of the S_{hmax} under the ultimate load) in practice due to nonuniformity of the sand grains (heterogeneity). This does not mean that the load was not applied symmetrically, nor the samples are not prepared uniformly. The boundaries of the zone of plastic flow in sand at failure load profiled using the advanced DPIV here are remarkably similar to such intuitive diagrams suggested by Stuart (1962) for interference effects.

- The investigation emphasises the influence of thicknesses of the top dense layer (H) on the evolution of grain-scale velocity fields and slip surfaces angle β in the sand for different loading levels. Different dense sand layers were used such as H/B=0, 0.5, 1.0, 2.0, 3.0, 4.5, and 6.5. The boundaries of the zone of plastic flow in dense sand overlying loose sand at failure load measured here are remarkably similar to the shape of such intuitive diagrams suggested in the literature, but with different values of the failure slip surface β. By taking advantage of the experimentally characterised slip failure surfaces (β) using DPIV, here it is worth mentioning that β is correlated with

thicknesses of the top dense layer (*H*). The new modified **Equation 7.9** makes it possible to estimate the bearing capacity of the layered granular soil with quite a good level of accuracy. It is also interesting to note that, the UBCR reaches a value of 1.0 for different values of *H/B* of the layered sand (as well as depending on the mode of analysis used). For example, to achieve UBCR=1.0, modes 1-5 predicted the required value of *H/B* as ~11.5, 5.5, 6.0, 3.5 and 4.7 respectively. The results of mode 4 and mode 5 are closest to what is commonly considered in geotechnical engineering application (*H/B*= 4-5). However, the results obtained from these model tests and new proposed approach (mode 4) can be applied for most strip prototype especially when $B \leq 1.0$ m. Therefore, based on the results reported here, the obtained layered failure mechanisms could be employed in related theoretical solutions in the future.

- In this study, DPIV is used to understand the local and global geomechanical characteristics of an axially loaded rigid strip footing under different types of cyclic loading and quasi-static load using both DPIV and FEM simulations in a coherent manner. The displacement patterns in the sand are visualized using DPIV and studied qualitatively and quantitatively in terms of vertical and horizontal components of displacement, vorticity and maximum shear strain. Where possible, the displacement measures in the sand are compared with FEM analysis. In general, an excellent level of agreement is obtained between the FEM and DPIV results. The boundaries of the zone of plastic flow in the dense sand under the cyclic loads at failure load measured here are remarkably similar to the shape of such intuitive diagrams suggested by Terzaghi (1943), but much wider. There is significantly more horizontal displacement in the cyclic loading type 3 than in the quasi-static loading where vertical soil displacements tend to dominate. This is due to the increasing area of the active zones that pushed outward and upward to the ground surface as confirmed by DPIV here. Cyclic loading types have considerable effect on the maximum ultimate load, settlement components and the failure mechanisms occurring beneath the footing under type 3 loading. Local scale load-displacement of the results FEM is clearly validated using DPIV. The simplicity in implementation of experimentally characterised constitutive relation of the sand grains are fed as an input, which can be applied easily for large-scale problems with small and large strain problems.

9.2 Limitations and Recommendations for Further Research

It is acknowledged that the scale effects of the footing model could affect the estimations of their strength characteristics (Jahanger et al., 2018a). Though the small-scale model is widely used to investigate the behaviour of the full-scale foundation, there could be some differences between the results of the experiments using laboratory models and the prototype (Vesic, 1973). To minimize the scaling effect, it was suggested that the packing density of the tested sample should not pertain too close to its maximum void ratio (e_{max}) and minimum void ratio (e_{min}) (Altaee and Fellenius, 1994). However, these suggestions were accounted for in the current study to minimise the scale effects.

Furthermore, Zuhair and Antony (2017b) have applied the DPIV in the analysis of scale effects in sand of different packings interacting with footing. They reported scale effect for the strip surface footing interacting with sand packings. The bearing capacity factors (N_γ) rapidly decreased from 98.5, 246 and 443 to 13.6, 60 and 52 for footing widths increased from 0.038 m to B=0.65 m for loose, medium-dense and dense sand respectively, after which there is no substantial decrease in the N_γ. It means that the scale effects are minimised beyond certain sizes of the footing. Even though that scaling effects cannot be ignored in small scale test and the test results are of limited use in predicting the behaviour of a particular prototype, by minimising the side effects, the study is useful and provide insights into the basic failure patterns and local displacement of the sand. Though, the settlement of footings could depend on their width for a given soil (Das, 2011), the ultimate bearing capacity of sand is less dependent on footing width (B) when B is less than 1 m as reported by Terzaghi and Peck (1967).

- The current study is limited to strip footings interacting with sand.
- The research outlined here is to be expanded to other types of foundations and soil constitutive in future including different soil (clay, sand, sandy clay and or clayey sand) and using different footing shapes such as square and circular.
- Applying the cyclic loading to different sand packing densities such as loose sand and medium-dense sand.
- Through a dynamic analysis of the soil type (the frequency of dynamic loading is greater than 10 Hz) effects on the foundation structures-soil interactions over an extended time should be studied in future. This is to find the accumulative elastic strain

over thousands of cycles, which may be relevant to practical problems where loading sustains for a longer period than considered in the current study.

- To employ new numerical modelling concepts that involves coupling numerical methods such as the finite element method (FEM) and the discrete element method (DEM) to model the behaviour of the foundation structures-granular soil interactions. This could result detailed information on displacement of granular materials often they interact with different foundation structures and under complex loading environment in future.

References

Adrian, R.J. 1991. Particle-imaging techniques for experimental fluid mechanics. *Annual review of fluid mechanics.* **23**(1), pp.261-304.

Adrian, R.J. 2005. Twenty years of particle image velocimetry. *Experiments in Fluids.* **39**(2), pp.159-169.

Ahmed, A.A. 2014. Effect of tunneling in cohesive soils on existing structures. *Enginerring and Technology Journal.* **32**(10), pp.2475-2490.

Akbas, S.O. and Kulhawy, F.H. 2009. Axial compression of footings in cohesionless soils. I: Load-settlement behaviour. *Journal of Geotechnical and Geoenvironmental Engineering.* **135**(11), pp.1562-1574.

Al-Ashou, M., Sulaiman, R. and Mandal, J. 1994. Effect of number of reinforcing layers on the interference between footings on reinforced sand. *Indian Geotechnical Journal.* **24**(3), pp.285-301.

Al-Shenawy, A.O. and Al-Karni, A.A. 2005. Derivation of bearing capacity equation for a two layered system of weak clay layer overlaid by dense sand layer. *Pertanika Journal of Science & Technology.* **13**(2), pp.213-235.

Albaraki, S. and Antony, S.J. 2014. How does internal angle of hoppers affect granular flow? Experimental studies using Digital Particle Image Velocimetry. *Powder Technology.* **268**, pp.253-260.

Albaraki, S.M.A. 2015. *Micromechanical analysis of pharmaceutical granules using advanced experimental imaging methodologies*. PhD thesis, University of Leeds.

Altaee, A. and Fellenius, B.H. 1994. Physical modeling in sand. *Canadian Geotechnical Journal.* **31**(3), pp.420-431.

Amrane, M. and Messast, S. Modeling the behaviour of geotechnical constructions Under cyclic loading with a numerical approach based on J. Lemaitre model. *Indian Geotechnical Journal.* Available from: https://doi.org/10.1007/s40098-017-0275-1.

Andersen, K.H. 2009. Bearing capacity under cyclic loading—offshore, along the coast, and on land. The 21st Bjerrum Lecture presented in Oslo, 23 November 2007. *Canadian Geotechnical Journal.* **46**(5), pp.513-535.

ANSYS17.2. 2016. ANSYS theory manual. *ANSYS, Inc., Canonsburg, Pennsylvania, USA*.

Antony, S. 2007. Link between single-particle properties and macroscopic properties in particulate assemblies: role of structures within structures. *Philosophical Transactions of the Royal Society A: Mathematical, Physical and Engineering Sciences.* **365**(1861), pp.2879-2891.

Armin, A., Fotouhi, R. and Szyszkowski, W. 2014. On the FE modeling of soil–blade interaction in tillage operations. *Finite Elements in Analysis and Design.* **92**, pp.1-11.

Asakereh, A., Ghazavi, M. and Tafreshi, S.M. 2013. Cyclic response of footing on geogrid-reinforced sand with void. *Soils and Foundations.* **53**(3), pp.363-374.

ASTM. 1989. Soil and rock, building, stores, geotextiles. *American Society for Testing and Materials , ASTM Standard.* **04.08**.

Atkinson, J. 2007. *The mechanics of soils and foundations.* 2nd ed. London, UK: CRC Press.

Azam, G., Hsieh, C. and Wang, M. 1991. Performance of strip footing on stratified soil deposit with void. *Journal of geotechnical engineering.* **117**(5), pp.753-772.

Baglioni, V.P., Chow, G.S. and Endley, S.N. 1982. Jack-up rig foundation stability in stratified soil profiles. In: *Offshore Technology Conference*: Offshore Technology Conference.

Binquet, J. and Lee, K.L. 1975. Bearing capacity tests on reinforced earth slabs. *Journal of the geotechnical Engineering Division.* **101**(12), pp.1241-1255.

Bjerrum, L. and Eggestad, A. 1963. Interpretation of loading test on sand. In: *Proceedings of European Conference in Soil Mechanics, Weisbaden, West Germany.* pp.199-203.

Bolton, M. 1986. The strength and dilatancy of sands. *Geotechnique.* **36**(1), pp.65-78.

Boussinesq, J. 1885. *Application des potentiels à l'étude de l'équilibre et du mouvement des solides élastiques.* Gauthier-Villars.

Bowles, J.E. 1996. *Foundation analysis and design.* 5th ed. Singapore: McGraw-Hill.

Budhu, M. 2011. *Soil mechanics and foundations.* 3rd ed. UK: John Wiley & Sons.

Burd, H. and Frydman, S. 1997. Bearing capacity of plane-strain footings on layered soils. *Canadian Geotechnical Journal.* **34**(2), pp.241-253.

Button, S.J. 1953. The bearing capacity of footings on a two-layer cohesive subsoil. In: *Proc. 3rd International Conference on Soil Mechanics and Foundation Engineering, Zurich*. pp.332-335.

Cerato, A.B. and Lutenegger, A.J. 2007. Scale effects of shallow foundation bearing capacity on granular material. *Journal of Geotechnical and Geoenvironmental Engineering.* **133**(10), pp.1192-1202.

Chen, Z., Li, K., Omidvar, M. and Iskander, M. 2017. Guidelines for DIC in geotechnical engineering research. *International Journal of Physical Modelling in Geotechnics.* **17**(1), pp.3-22.

Cheng, Y., White, D., Bowman, E., Bolton, M. and Soga, K. 2001. The observation of soil microstructure under load. *4th International Conference on Micromechanics of Granular Media, Powders and Grains, Sendai, Japan*. pp.69-72.

Cicek, E., Guler, E. and Yetimoglu, T. 2014. Comparison of measured and theoretical pressure distribution below strip footings on sand soil. *International Journal of Geomechanics.* **14**(5), p06014009.

Cicek, E., Guler, E. and Yetimoglu, T. 2018. Stress distribution below a continuous footing on geotextile-reinforced soil. *International Journal of Geomechanics.* **18**(3), p06018005.

Cinicioglu, O., Altunbas, A., Soltanbeigi, B. and Gezgin, A.T. 2014. Dilatancy based similitude of small-scale 1g models and prototypes for cohesionless soils. *Geomechanics from Micro to Macro.* CRC Press, pp.1641-1645.

DantecDynamics. 2013. DynamicStudio user's guide. DantecDynamics, Skovlunde, Denmark.

Das, B.M. 1999. *Shallow foundations: bearing capacity and settlement.* London, UK: CRC press.

Das, B.M. 2006. *Principles of geotechnical engineering.* 5th ed. USA: Brooks/Cole.

Das, B.M. 2009. *Shallow foundations: bearing capacity and settlement.* London, UK: CRC Press.

Das, B.M. 2011. *Principles of foundation engineering.* 7th ed. UK: Cengage Learning.

Das, B.M. 2016. *Principles of foundation engineering.* 8th ed. India: Cengage Learning.

Das, B.M. and Larbi-Cherif, S. 1983. Bearing capacity of two closely-spaced shallow foundations on sand. *Soils and Foundations.* **23**(1), pp.1-7.

Das, B.M. and Shin, E.C. 1996. Laboratory model tests for cyclic load-induced settlement of a strip foundation on a clayey soil. *Geotechnical & Geological Engineering.* **14**(3), pp.213-225.

Davoudi, S., Alimardani, R., Keyhani, A. and Atarnejad, R. 2008. A two dimensional finite element analysis of a plane tillage tool in soil using a non-linear elasto-plastic model. *American-Eurasian Journal of Agricultural and Environmental Sciences.* **3**(3), pp.498-505.

De Beer, E.E. 1965. Bearing capacity and settlement of shallow foundations on sand. In: *Proc. of Symp. Bearing Capacity and Settlement of Foundation*, *Duke University, Durham, NC, USA*. pp.15-33.

Desrues, J. and Viggiani, G. 2004. Strain localization in sand: an overview of the experimental results obtained in Grenoble using stereophotogrammetry. *International Journal for Numerical and Analytical Methods in Geomechanics.* **28**(4), pp.279-321.

Díaz, E. and Tomás, R. 2016. A simple method to predict elastic settlements in foundations resting on two soils of differing deformability. *European Journal of Environmental and Civil Engineering.* **20**(3), pp.263-281.

Dijkstra, J., Gaudin, C. and White, D.J. 2013. Comparison of failure modes below footings on carbonate and silica sands. *International Journal of Physical Modelling in Geotechnics.* **13**(1), pp.1-12.

Duran, J. 2000. *Sands, powders, and grains-an introduction to the physics of granular materials.* Springer Science & Business Media.

Duran, J. 2012. *Sands, powders, and grains: an introduction to the physics of granular materials.* Springer Science & Business Media.

Efretuei, E.O. 2013. *Thermal impact on soil-structure interaction for integral bridges*. PhD thesis, University of Leeds.

El Sawwaf, M.A. and Nazir, A.K. 2012. Cyclic settlement behavior of strip footings resting on reinforced layered sand slope. *Journal of Advanced Research.* **3**(4), pp.315-324.

Fang, H.-Y. 1991. *Foundation engineering handbook.* 2nd ed. New York, USA: Chapman and Hall.

Farah, C.A. 2004. *Ultimate bearing capacity of shallow foundations of layered soils*. M.Sc. thesis, Concordia University.

Fattah, M.Y., Rahil, F.H. and Turki, M.A. 2011. Determination of the adequate thickness of granular subbase beneath foundations. *Engineering and Technical Journal.* **29**(9), pp.1845-1869.

Ghazavi, M. and Eghbali, A.H. 2008. A simple limit equilibrium approach for calculation of ultimate bearing capacity of shallow foundations on two-layered granular soils. *Geotechnical and Geological Engineering.* **26**(5), pp.535-542.

Ghazavi, M. and Lavasan, A.A. 2008. Interference effect of shallow foundations constructed on sand reinforced with geosynthetics. *Geotextiles and Geomembranes.* **26**(5), pp.404-415.

Gollin, D., Brevis, W., Bowman, E.T. and Shepley, P. 2017. Performance of PIV and PTV for granular flow measurements. Granular Matter. **19**(3), p42.

Gordan, B., Adnan, A. and Aida, M.A. 2014. Soil saturated simulation in embankment during strong earthquake by effect of elasticity modulus. *Modelling and Simulation in Engineering.* **2014**, p7.

Griffiths, D., Fenton, G.A. and Manoharan, N. 2006. Undrained bearing capacity of two-strip footings on spatially random soil. *International Journal of Geomechanics.* **6**, pp.421-427.

Gupta, A., Dutta, R.K., Shrivastava, R. and Khatri, V.N. 2017. Ultimate bearing capacity of square/rectangular footing on layered soil. *Indian Geotechnical Journal.* **47**(3), pp.303-313.

Hamm, E., Tapia, F. and Melo, F. 2011. Dynamics of shear bands in a dense granular material forced by a slowly moving rigid body. *Physical Review E.* **84**(4), p041304.

Hanna, A. 1982. Bearing capacity of foundations on a weak sand layer overlying a strong deposit. *Canadian Geotechnical Journal.* **19**(3), pp.392-396.

Hanna, A.M. 1981. Foundations on strong sand overlying weak sand. *Journal of Geotechnical and Geoenvironmental Engineering.* **107**(ASCE 16367).

Hansbo, S. 1994. *Foundation engineering.* London, UK: Elsevier.

Head, K. 2006. *Manual of soil laboratory test. Volume 1: Soil classification and compaction tests*. Florida, USA: CRC Press.

Hryciw, R.D., Zheng, J. and Shetler, K. 2016. Particle Roundness and Sphericity from Images of Assemblies by Chart Estimates and Computer Methods. *Journal of Geotechnical and Geoenvironmental Engineering.* **142**(9), p04016038.

Ismael, N.F. and Ahmad, A.H.N. 1990. Bearing capacity of footings on calcareous sands. *Soil and Foundations.* **30**(3), pp.81-90.

Jaeger, H.M., Nagel, S.R. and Behringer, R.P. 1996. Granular solids, liquids, and gases. *Reviews of Modern Physics.* **68**(4), p1259.

Jahanger, Z.K., Ahmad, A.A. and Jahanger, Q.K. 2010. Effect of plate load test curve shape on modulus of subgrade reaction of compacted subbase soil. In: *In 2nd Annual Scientific Conference of the College of Engineering, University of Babylon, Babylon, Iraq*. pp.1-12.

Jahanger, Z.K., Antony, S.J. and Richter, L. 2016. Displacement patterns beneath a rigid beam indenting on layered soil. In: *8th Americas Regional Conference of International Society for Terrain-Vehicle Systems, Michigan, USA*. ISTVS, paper no. 67.

Jahanger, Z.K. and Antony, S.J. 2017a. Application of digital particle image velocimetry in the analysis of scale effects in granular soil. In: *Proceedings Proceeding of 19th International Conference on Soil Mechanics and Dynamics,* **19**(7) part X, Rome. pp.1134-1139.

Jahanger, Z.K. and Antony, S.J. 2017b. Application of particle image velocimetry in the analysis of scale effects in granular soil. *International Journal of Civil, Environmental, Structural, Construction and Architectural Engineering.* **11**(7), pp.832-837.

Jahanger, Z.K., Sujatha, J. and Antony, S.J. 2018a. Local and global granular mechanical characteristics of grain–structure interactions. *Indian Geotechnical Journal.* Available from: https://doi.org/10.1007/s40098-018-0295-5.

Jahanger, Z.K., Antony, S.J., Martin, E. and Richter, L. 2018b. Interaction of a rigid beam resting on a strong granular layer overlying weak granular soil: Multi-Methodological Investigations. *Journal of Terramechanics*, **79**, pp.23-32.

Jassim, S.Z. and Goff, J.C. 2006. *Geology of Iraq.* London, UK: DOLIN

Javid, A.H., Fahimifar, A. and Imani, M. 2015. Numerical investigation on the bearing capacity of two interfering strip footings resting on a rock mass. *Computers and Geotechnics.* **69**, pp.514-528.

Jewell, R. 1989. Direct shear tests on sand. *Geotechnique.* **39**(2), pp.309-322.

Jha, P. and Kumar, S. 2015. Simplified approach to estimate lateral load on drilled shafts resulting from a heavily loaded adjacent shallow foundation using horizontal stress isobars. *International Journal of Geomechanics.* **16**(1), p04015032.

Kardani, M. *Large deformation analysis in geomechanics using adaptive finite element methods*. 2012. Available from: http://hdl.handle.net/1959.13/928191

Kempfert, H.-G., Thomas, S. and Gebreselassie, B. 2010. Observation of pile-soil-interaction during cyclic axial loading using particle image velocimetry. In: *Proceedings of the GeoShanghai 2010 International Conference, Deep Foundations and Geotechnical In situ Testing, Shanghai, China*, pp.67-72.

Khing, K., Das, B., Puri, V., Yen, S. and Cook, E. 1994. Foundation on strong sand underlain by weak clay with geogrid at the interface. *Geotextiles and Geomembranes.* **13**(3), pp.199-206.

Krumbein, W. C., and Sloss, L. L. (1951). Stratigraphy and sedimentation, W. H. Freeman and Company, San Francisco.

Kruyt, N. and Antony, S. 2007. Force, relative-displacement, and work networks in granular materials subjected to quasistatic deformation. *Physical Review E.* **75**(5), p051308.

Kumar, A. and Saran, S. 2003. Closely spaced footings on geogrid-reinforced sand. *Journal of Geotechnical and Geoenvironmental Engineering.* **129**(7), pp.660-664.

Kumar, J. and Bhoi, M.K. 2009. Interference of two closely spaced strip footings on sand using model tests. *Journal of Geotechnical and Geoenvironmental Engineering.* **135**(4), pp.595-604.

Kumar, J. and Ghosh, P. 2007. Ultimate bearing capacity of two interfering rough strip footings. *International Journal of Geomechanics.* **7**(1), pp.53-62.

Kumar, J. and Kouzer, K. 2007. Effect of footing roughness on bearing capacity factor N γ. *Journal of Geotechnical and Geoenvironmental Engineering.* **133**(5), pp.502-511.

Kumar, J. and Kouzer, K. 2008. Bearing capacity of two interfering footings. *International Journal for Numerical and Analytical Methods in Geomechanics.* **32**(3), pp.251-264.

Lambe, T.W. and Whitman, R.V. 1979. *Soil mechanics, SI version.* New York, USA: Wiley.

Lau, C.K. 1988. *Scale effects in tests on footings*. PhD thesis, University of Cambridge.

Lavasan, A.A. and Ghazavi, M. 2012. Behavior of closely spaced square and circular footings on reinforced sand. *Soils and Foundations.* **52**(1), pp.160-167.

Lavasan, A.A. and Ghazavi, M. 2014. Failure mechanism and soil deformation pattern of soil beneath interfering square footings. *Numerical Methods in Civil Engineering.* **1**(2), pp.48-56.

Lavasan, A.A., Ghazavi, M., von Blumenthal, A. and Schanz, T. 2018. Bearing capacity of interfering strip footings. *Journal of Geotechnical and Geoenvironmental Engineering.* **144**(3), p04018003.

LaVision. 2018. Digital image correlation. *Available at*: *https://www.lavision.de/en/techniques/piv-ptv/index.php*.

Lee, H.-H. 2015. *Finite element simulations with ANSYS workbench 16.* SDC publications, Kansas, USA.

Lee, J., Eun, J., Prezzi, M. and Salgado, R. 2008. Strain influence diagrams for settlement estimation of both isolated and multiple footings in sand. *Journal of Geotechnical and Geoenvironmental Engineering.* **134**(4), pp.417-427.

Lee, K., Cassidy, M. and Randolph, M. 2013a. Bearing capacity on sand overlying clay soils: experimental and finite-element investigation of potential punch-through failure. *Géotechnique.* **63**(15), p1271.

Lee, K., Randolph, M. and Cassidy, M. 2013b. Bearing capacity on sand overlying clay soils: A simplified conceptual model. *Géotechnique.* **63**(15), pp.1285-1297.

Lemmen, H., Jacobsz, S. and Kearsley, E.P. 2017. The influence of foundation stiffness on the behaviour of surface strip foundations on sand. *Journal of the South African Institution of Civil Engineering.* **59**(2), pp.19-27.

Leshchinsky, D. and Marcozzi, G.F. 1990. Bearing capacity of shallow foundations: rigid versus flexible models. *Journal of Geotechnical Engineering.* **116**(11), pp.1750-1756.

Likitlersuang, S., Teachavorasinskun, S., Surarak, C., Oh, E. and Balasubramaniam, A. 2013. Small strain stiffness and stiffness degradation curve of Bangkok clays. *Soils and Foundations.* **53**(4), pp.498-509.

Lini Dev, K., Pillai, R.J. and Robinson, R.G. 2016. Drained angle of internal friction from direct shear and triaxial compression tests. *International Journal of Geotechnical Engineering.* **10**(3), pp.283-287.

Liu, C. and Evett, J.B. 2004. *Soils and foundations.* 6th ed. New Jersey, USA: Pearson Prentice Hall.

Liu, J. and Iskander, M. 2004. Adaptive cross correlation for imaging displacements in soils. *Journal of Computing in Civil Engineering.* **18**(1), pp.46-57.

Lombardi, D., Bhattacharya, S., Hyodo, M. and Kaneko, T. 2014. Undrained behaviour of two silica sands and practical implications for modelling SSI in liquefiable soils. *Soil Dynamics and Earthquake Engineering.* **66**, pp.293-304.

Lutenegger, A.J. and Adams, M.T. 1998. Bearing capacity of footings on compacted sand. In: *Proceedings of the 4th International Conference on Case Histories in Geotechnical Engineering, St. Louis, Missouri, USA*. pp.1216–1224.

Lutenegger, A.J. and DeGroot, D.J. 1995. *Settlement of shallow foundations on granular soils.* Report no. 6332, University of Massachusetts Transportation Center.

Lyamin, A.V. and Sloan, S. 2002. Upper bound limit analysis using linear finite elements and non-linear programming. *International Journal for Numerical and Analytical Methods in Geomechanics.* **26**(2), pp.181-216.

MAGICgeo. 2018. MAGICGEO. *Available at https://wp.nyu.edu/magicgeo/.*

Majmudar, T., Sperl, M., Luding, S. and Behringer, R.P. 2007. Jamming transition in granular systems. *Physical Review Letters.* **98**(5), p058001.

Majmudar, T.S. and Behringer, R.P. 2005. Contact force measurements and stress-induced anisotropy in granular materials. *Nature.* **435**(7045), pp.1079-1082.

Mayne, P.W. and Poulos, H.G. 1999. Approximate displacement influence factors for elastic shallow foundations. *Journal of Geotechnical and Geoenvironmental Engineering.* **125**(6), pp.453-460.

Meyerhof, G. 1974. Ultimate bearing capacity of footings on sand layer overlying clay. *Canadian Geotechnical Journal.* **11**(2), pp.223-229.

Meyerhof, G. and Adams, J. 1968. The ultimate uplift capacity of foundations. *Canadian Geotechnical Journal.* **5**(4), pp.225-244.

Meyerhof, G. and Hanna, A. 1978. Ultimate bearing capacity of foundations on layered soils under inclined load. *Canadian Geotechnical Journal.* **15**(4), pp.565-572.

Michalowski, R.L. and Shi, L. 1995. Bearing capacity of footings over two-layer foundation soils. *Journal of Geotechnical Engineering.* **121**(5), pp.421-428.

Mohsenimanesh, A., Ward, S.M., Owende, P.O. and Javadi, A. 2009. Modelling of pneumatic tractor tyre interaction with multi-layered soil. *Biosystems Engineering.* **104**(2), pp.191-198.

Mosadegh, A. and Nikraz, H. 2015. Bearing capacity evaluation of footing on a layeredâ soil using ABAQUS. *Journal of Earth Science and Climatic Change.* **6**(3), p1000264.

Mulungye, R., Owende, P. and Mellon, K. 2007. Finite element modelling of flexible pavements on soft soil subgrades. *Materials and Design.* **28**(3), pp.739-756.

Murthy, T.G., Gnanamanickam, E. and Chandrasekar, S. 2012. Deformation field in indentation of a granular ensemble. *Physical Review E.* **85**(6), p061306.

Myslivec, A. and Kysela, Z. 1978. *The bearing capacity of building foundations.* Amsterdam, The Netherlands: Elsevier.

Naderi, E. and Hataf, N. 2014. Model testing and numerical investigation of interference effect of closely spaced ring and circular footings on reinforced sand. *Geotextiles and Geomembranes.* **42**(3), pp.191-200.

Nainegali, L.S., Basudhar, P.K. and Ghosh, P. 2013. Interference of two asymmetric closely spaced strip footings resting on nonhomogeneous and linearly elastic soil bed. *International Journal of Geomechanics.* **13**(6), pp.840-851.

Ng, C.W.W., Choi, C.E., Goodwin, G.R. and Cheung, W.W. 2017. Interaction between dry granular flow and deflectors. *Landslides.* **14**(4), pp.1375-1387.

Nguyen, N.-S., François, S. and Degrande, G. 2014. Discrete modeling of strain accumulation in granular soils under low amplitude cyclic loading. *Computers and Geotechnics.* **62**, pp.232-243.

O'Loughlin, C. and Lehane, B. 2010. Nonlinear cone penetration test-based method for predicting footing settlements on sand. *Journal of Geotechnical and Geoenvironmental Engineering.* **136**(3), pp.409-416.

Oda, M. and Iwashita, K. 1999. *An Introduction mechanics of granular materials.* Rotterdam, The Netherlands: AA BALKEMA.

Oda, M. and Win, S. 1990. Ultimate bearing capacity tests on sand with clay layer. *Journal of Geotechnical Engineering.* **116**(12), pp.1902-1906.

Okamura, M., Takemura, J. and Kimura, T. 1998. Bearing capacity predictions of sand overlying clay based on limit equilibrium methods. *Soils and Foundations.* **38**(1), pp.181-194.

Peralta, P. 2010. *Investigations on the behavior of large diameter piles under long-term lateral cyclic loading in cohesionless soil.* Germany: IGtH.

Potts, D.M. and Zdravkovic, L. 2001. *Finite element analysis in geotechnical engineering: application.* London, UK: Thomas Telford.

Powrie, W. 2014. *Soil mechanics: concepts and applications.* 3rd ed. London, UK: CRC Press.

Prandtl, L. 1920. Über die härte plastischer körper (On the hardness of plastic bodies). *Nachrichten von der Gesellschaft der Wissenschaften zu Göttingen, Mathematisch-Physikalische Klasse.* pp.74-85.

Purushothamaraj, P., Ramiah, B. and Rao, K.V. 1974. Bearing capacity of strip footings in two layered cohesive-friction soils. *Canadian Geotechnical Journal.* **11**(1), pp.32-45.

Radjai, F., Wolf, D.E., Jean, M. and Moreau, J.-J. 1998. Bimodal character of stress transmission in granular packings. *Physical Review Letters.* **80**(1), p61.

Ramadan, M.I. and Hussien, M.H. 2015. Bearing capacity of sand overlying clay–strip footing. *International Journal of Science and Research (IJSR).* **4**(11), pp.1852-1859.

Raymond, G.P. 2002. Reinforced ballast behaviour subjected to repeated load. *Geotextiles and Geomembranes.* **20**(1), pp.39-61.

Raymond, G.P. and Komos, F.E. 1978. Repeated load testing of a model plane strain footing. *Canadian Geotechnical Journal.* **15**(2), pp.190-201.

Sabbar, A., Chegenizadeh, A. and Nikraz, H. 2016. Review of the experimental studies of the cyclic behaviour of granular materials: Geotechnical and pavement engineering. *Australian Geomechanics Journal.* **51**(2), pp.89-103.

Salem, M., Elmamlouk, H. and Agaiby, S. 2013. Static and cyclic behavior of North Coast calcareous sand in Egypt. *Soil Dynamics and Earthquake Engineering.* **55**, pp.83-91.

Saran, S. and Agarwal, V. 1974. Interference of surface footings on sand. *Indian Geotechnical Journal.* **4**(2), pp.129-139.

Schanz, T., Vermeer, P. and Bonnier, P. 1999. The hardening soil model: formulation and verification. In: *Proc., Plaxis Symposium Beyond 2000 in Computational Geotechnics, Amsterdam, The Netherlands*. pp.281-296.

Schmertmann, J.H., Brown, P.R. and Hartman, J.P. 1978. Improved strain influence factor diagrams. *Journal of the Geotechnical Engineering Division.* **104**(8), pp.1131-1135.

Selvadurai, A. 1979. Elastic analysis of soil–foundation interaction. Amsterdam, The Netherlands: Elsevier.

Shaaban, S. 1983. Evolution of the bearing capacity of dry sand with its density. *Journal of Terramechanics.* **20**(3), pp.129-138.

Shoaei, M.D., Alkarni, A., Noorzaei, J., Jaafar, M.S. and Huat, B.B. 2012. Review of available approaches for ultimate bearing capacity of two-layered soils. *Journal of Civil Engineering and Management.* **18**(4), pp.469-482.

Shajarati, A., Sørensen, K.W., Nielsen, S.K. and Ibsen, L.B. 2012. *Behaviour of cohesionless soils during cyclic loading.* [Manuscript]. At*:* Department of Civil Engineering, Aalborg University, Denmark. 14.

Sloan, S. 1988. Lower bound limit analysis using finite elements and linear programming. *International Journal for Numerical and Analytical Methods in Geomechanics.* **12**(1), pp.61-77.

Stanier, S.A., Blaber, J., Take, W.A. and White, D. 2016. Improved image-based deformation measurement for geotechnical applications. *Canadian Geotechnical Journal.* **53**(5), pp.727-739.

Stuart, J. 1962. Interference between foundations, with special reference to surface footings in sand. *Géotechnique.* **12**(1), pp.15-22.

Tafreshi, S.M. and Dawson, A. 2012. A comparison of static and cyclic loading responses of foundations on geocell-reinforced sand. *Geotextiles and Geomembranes.* **32**, pp.55-68.

Tafreshi, S.M., Mehrjardi, G.T. and Ahmadi, M. 2011. Experimental and numerical investigation on circular footing subjected to incremental cyclic loads. *International Journal of Civil Engineering.* **9**(4), pp.265-274.

Taib, S.N.L., Hung, L.S. and Kolay, P.K. 2013. Laboratory measurement of displacement on shallow foundation in uniform sand using particle image velocimetry technique. *Jurnal Teknologi.* **61**(3).

Tehrani, F.S., Arshad, M.I., Prezzi, M. and Salgado, R. 2017. Physical modeling of cone penetration in layered sand. *Journal of Geotechnical and Geoenvironmental Engineering.* **144**(1), p04017101.

Teng, Y., Stanier, S. and Gourvenec, S. 2017. Analysis of failure mechanisms in silica and carbonate sands beneath a strip foundation under vertical loading. In: *ASME 2017 36th International Conference on Ocean, Offshore and Arctic Engineering, Trondheim, Norway*. American Society of Mechanical Engineers, pp.V009T010A016-V009T010A016.

Terzaghi, K. 1943. *Theoretical soil mechanics.* New York: John Wiley & Sons, Inc.

Terzaghi, K. and Peck, R.B. 1967. *Soil mechanics in engineering practice.* 2nd ed. New York: John Wiley & Sons, Inc.

Terzaghi, K., Peck, R.B. and Mesri, G. 1996. *Soil mechanics in engineering practice.* 3rd ed. New York: John Wiley & Sons, Inc.

Thornton, C. and Antony, S. 1998. Quasi-static deformation of particulate media. *Philosophical Transactions-Royal Society of London Series a Mathematical Physical and Engineering Sciences.* pp.2763-2782.

Ti, K.S., Huat, B.B., Noorzaei, J., Jaafar, M.S. and Sew, G.S. 2009. A review of basic soil constitutive models for geotechnical application. *Electronic Journal of Geotechnical Engineering.* **14**, pp.1-18.

Vangla, P. and Latha, G.M. 2015. Influence of particle size on the friction and interfacial shear strength of sands of similar morphology. *International Journal of Geosynthetics and Ground Engineering.* **1**(1), p6.

Vesic, A.S. 1973. Analysis of ultimate loads of shallow foundations. *Soil Mechanics and Foundation Division.* **99**(SM1), pp.45-73.

Wadell, H. 1932. Volume, Shape, and Roundness of Rock Particles. *The Journal of Geology.* **40**(5), pp.443-451.

White, D. and Bolton, M. 2004. Displacement and strain paths during plane-strain model pile installation in sand. *Géotechnique.* **54**(6), pp.375-397.

White, D., Take, W. and Bolton, M. 2001a. Measuring soil deformation in geotechnical models using digital images and PIV analysis. In: *10th International Conference on Computer Methods and Advances in Geomechanics, Tucson, Arizona*. pp.997-1002.

White, D., Take, W. and Bolton, M. 2003. Soil deformation measurement using particle image velocimetry (PIV) and photogrammetry. *Géotechnique.* **53**(7), pp.619-631.

White, D., Take, W., Bolton, M. and Munachen, S. 2001b. A deformation measurement system for geotechnical testing based on digital imaging, close-range photogrammetry, and PIV image analysis. In: *15th International Conference on Soil Mechanics and Geotechnical Engineering, Istanbul, Turkey*. pp.539-542.

Wieneke, B. and Pfeiffer, K. 2010. Adaptive PIV with variable interrogation window size and shape. In: *15th International Symposium on Applications of Laser Techniques to Fluid Mechanics, Lisbon, Portugal*. pp.1-8.

Willert, C.E. and Gharib, M. 1991. Digital particle image velocimetry. *Experiments in fluids.* **10**(4), pp.181-193.

Yadav, R.K., Saran, S. and Shanker, D. 2017. Interference between two adjacent footings located in seismic region. *Geosciences.* **7**(4), pp.129-140.

Yamaguchi, H. 1963. Practical formula of bearing value for two layered ground. In: *Proceedings of the 2nd Asian Regional Conference on Soil Mechanics and Foundation Engineering, Tokyo, Japan*. pp.176-180.

Zhou, C. 2011. *Investigation of micro-and macro-phenomena in densely packed granular media using the discrete element method*. PhD thesis, The University of Edinburgh.

Zhu, D., Lee, C. and Jiang, H. 2001. A numerical study of the bearing capacity factor N γ. *Canadian Geotechnical Journal.* **38**(5), pp.1090-1096.

Ziccarelli, M., Valore, C., Muscolino, S.R. and Fioravante, V. 2017. Centrifuge tests on strip footings on sand with a weak layer. *Geotechnical Research.* **4**(1), pp.47-64.